

NOVEL AROMATIC DENDRITIC-CO-POLY(3- HEXYLTHIOPHENE) COMPOSITES FOR PHOTOVOLTAIC CELL APPLICATION



UNIVERSITY *of the*
WESTERN CAPE

By

Morongwa Emmanuel Ramoroka

BSc Chemistry Honours (University of Limpopo)

MSc Nanoscience (Cum Laude, University of the Western Cape)

A thesis submitted in partial fulfilment of the requirements for the degree
of

Philosophiae Doctor

in the Department of Chemistry

Faculty of Natural Science

University of the Western Cape

Supervisor: Prof. Emmanuel I. Iwuoha

Co-supervisors: Dr. Vivian Suru John-Denk

Prof Kwena D. Modibane (University of Limpopo)

November 2021

Abstract

Fossil fuels are part of fuels that are formed from natural processes and they are called non-renewable sources of energy. These include natural gas, coal and oil. They have been used for decades to produce energy globally. However, there are some factors that related with the use of fossil fuels which results in an increase in the requirement of large amounts of energy. In addition, the use of fossil fuels as energy source has a negative impact on the environment and they cannot be reused. It is expected that at some point they will run out. Thus, a need for a renewable, clean and plentiful source of energy is urgent. Solar energy is one of the energy sources that may overcome fossil fuel drawbacks. The use of solar energy has attracted a lot of researchers to perform their investigations focused on utilizing solar energy to generate electricity. In this regard, photovoltaic cells play an important role. To date, most photovoltaic cells that are commercially available are based on inorganic materials and they are costly to fabricate while also using toxic elements. These make organic based photovoltaic cells advantageous over inorganic ones. In this work, we focus on developing novel donor materials for organic photovoltaic cells application. The synthesized compounds in this work were confirmed by a variety of characterization techniques. The synthesis of polypropylenimine tetra(thiophene), polypropylenimine tetra(N-methylpyrrole) and polypropylenimine tetra(5-bromosalicylaldehyde) were confirmed by nuclear magnetic resonance spectroscopy, Fourier-transform infrared spectroscopy and mass spectroscopy, while hexathienylbenzene and tetrathienylthiophene were confirmed by nuclear magnetic resonance spectroscopy and Fourier-transform infrared spectroscopy. After the synthesis of polypropylenimine tetra(thiophene), polypropylenimine tetra(N-methylpyrrole), polypropylenimine tetra(5-bromosalicylaldehyde), hexathienylbenzene and tetrathienylthiophene, they were all decorated by growing poly(3-hexylthiophene-2,5-diyl) on their surface. The resulting composites namely; polypropylenimine tetra(thiophene)-co-poly(3-hexylthiophene-2,5-diyl), polypropylenimine tetra(N-methylpyrrole)-co-poly(3-hexylthiophene-2,5-diyl), polypropylenimine tetra(5-bromosalicylaldehyde)-co-poly(3-hexylthiophene-2,5-diyl), hexathienylbenzene-co-poly(3-hexylthiophene-2,5-diyl) and tetrathienylthiophene-co-poly(3-hexylthiophene-2,5-diyl) were characterized using different characterization techniques and the effect of reaction time, molar ratio and solvents were performed on different composites. The

finding revealed that as the reaction time, molar ratios and solvent changes, the spectroscopic and electrochemical properties of composites also changes. The properties of tetrathienylthiophene-co-poly(3-hexylthiophene-2,5-diyl) were compared to those of poly(3-hexylthiophene-2,5-diyl). Tetrathienylthiophene-co-poly(3-hexylthiophene-2,5-diyl) was found to have wider band gap and poor organic photovoltaic cell performance than poly(3-hexylthiophene-2,5-diyl). We also used electrochemical methods to study the degree at which poly(3,4-ethylenedioxythiophene) polystyrene sulfonate blocks electrons from the active layer using electrochemical methods. The study revealed that poly(3,4-ethylenedioxythiophene) polystyrene sulfonate does not block electrons completely. It was also revealed in this work that the presence of poly(3-hexylthiophene-2,5-diyl) on the surface of polypropylenimine tetra(5-bromosalicylaldehyde) turn to improve the thermal, optical and conductivity properties of polypropylenimine tetra(5-bromosalicylaldehyde). Organic photovoltaic cells of the polymers synthesized in this study as donor materials were fabricated. The effect of solvent, molar ratio and reaction time were investigated. It was revealed that polypropylenimine tetra(thiophene)-co- poly(3-hexylthiophene-2,5-diyl) synthesized using molar ratio of 1 polypropylenimine tetra(thiophene): 40 3-hexylthiophene gave highest power conversion efficiency when compared to other molar ratios because of its narrow optical band gap and small distance between the LUMO energy levels of donor and acceptor materials. Hexathienylbenzene-co-poly(3-hexylthiophene-2,5-diyl) was used as a donor material to study the effect of solvent on photovoltaic parameters such as fill factor, open circuit voltage, short circuit current and power conversion efficiency. The highest photovoltaic parameters were obtained in chlorobenzene due to faster electron transfer confirmed by electrochemical impedance spectroscopy. It was also revealed that polypropylenimine tetra(N-methylpyrrole)-co- poly(3-hexylthiophene-2,5-diyl) synthesized for 24 h has highest power conversion efficiency and open circuit voltage when compared to 48 and 72 h which were attributed to sufficient electron-hole separation at the donor:acceptor interface revealed by photoluminescence studies and its high crystallinity. Polypropylenimine tetra(5-bromosalicylaldehyde)-co-poly(3-hexylthiophene-2,5-diyl) as a donor material gave power conversion efficiency of 0.21%.

Keywords

[6,6]-Phenyl C71 butyric acid methyl ester

Cyclic voltammetry

Dendrimers

Electrochemical impedance spectroscopy

Hexathienylbenzene-co-poly(3-hexylthiophene-2,5-diyl)

Organic Photovoltaic cells

Photoluminescence

Poly(3,4-ethylenedioxythiophene) polystyrene sulfonate

Poly(3-hexylthiophene-2,5-diyl)

Polypropylenimine tetra(5-bromosalicylaldehyde)-co-poly(3-hexylthiophene-2,5-diyl)

Polypropylenimine tetra(N-methylpyrrole)-co- poly(3-hexylthiophene-2,5-diyl)

Polypropylenimine tetra(thiophene)-co- poly(3-hexylthiophene-2,5-diyl)

Schiff base condensation reaction

Tetrathienylthiophene-co-poly(3-hexylthiophene-2,5-diyl)

Ultraviolet-visible spectroscopy




Declaration

I declare that the work titled: NOVEL AROMATIC DENDRITIC-CO-POLY(3-HEXYLTHIOPHENE) COMPOSITES FOR PHOTOVOLTAIC CELL APPLICATION has never been submitted before for any kind of examination, is my own work and all the sources or quotes I used have been well referenced and acknowledged.

Names and Surname: Morongwa Emmanuel Ramoroka

Date: November 2021

Signed: 



Acknowledgements

I would like to take this opportunity and gratefully thank my supervisor Prof. Emmanuel I. Iwuoha for your support through guidance and encouragement. Your contribution in my life has turned me into a very confident researcher and a leader. I will always be grateful and thankful for what you have done in my life. Working with you was very joyful and thank you very much. May God almighty bless you.

I would like to thank my Co-supervisor, Dr Vivian Suru John-Denk for the beneficial discussions and support you gave towards the completion of this thesis. And also thank Prof Kwena D. Modibane (University of Limpopo) for the productive discussions we had. Your contributions made it easier for me to complete this work and I will forever be thankful.

I would like to thank Dr Tesfaye Waryo and Mr Timothy Lesch who made sure that characterization techniques in the chemistry department are available and working. Also thank Mrs Wilhelmina Jackson who made sure that chemicals I need for my research are paid. Your contribution in this study is highly appreciated.

I would like to thank SensorLab researchers for their very helpful ideas during hard times encountered in this work. More especially Mr Siyabonga B. Mdluli, Mr Kelechi Nwambaekwe, Mr Sodiq T. Yussuf, Mr Samuel Mkhehlane and Mr Hayelom H. Tesfay for very productive meetings and discussions we had. I really thank you for your support.

I would also like to thank my father Mr David N. Ramoroka, my mother Mr Rosina R. Ramoroka and my brothers (Michael M. Ramoroka, Kenneth L. Ramoroka, Obed K. Ramoroka and Lethabo K. Ramoroka) for the love, care, support and prayers they gave me during my entire journey as a student. May almighty God be with you and bless you all the time.

During this study, I had chance to go visit Helmholtz-Zentrum Berlin in Berlin, Germany. I would like to express my sincere gratitude to Prof. Dr. Susan Schorr for the warm welcome, for providing valuable guidance and support during my visit at HZB. I would also like to thank Dr. Galina

Gurieva for her valuable assistance and support. Also, I would like to thank Dr Sara Niedenzu together with the whole research team for their kind assistance during my visit.

I would like to thank National Research Foundation of South African (113803) and European Union H2020 RISE (2017) INFINITE-CELL-DVL-777998 project for their financial support.



Dedication

I dedicate this work to

My parents

Mr David N Ramoroka and Mrs. Rosina R Ramoroka

&

My Brothers: Michael M. Ramoroka, Kenneth L. Ramoroka, Obed K. Ramoroka and Lethabo K.
Ramoroka



List of Publications

- [1] Mashao, G., Ramohlola, K.E., Mdluli, S.B., Monama, G.R., Hato, M.J., Makgopa, K., Molapo, K.M., **Ramoroka, M.E.**, Iwuoha, E.I. and Modibane, K.D., 2019. Zinc-based zeolitic benzimidazolate framework/polyaniline nanocomposite for electrochemical sensing of hydrogen gas. *Materials Chemistry and Physics*, 230, pp.287-298.
- [2] Nwambaekwe, K.C., Masikini, M., Mathumba, P., **Ramoroka, M.E.**, Duoman, S., John-Denk, V.S. and Iwuoha, E.I., 2021. Electronics of anion hot injection-synthesized Te-functionalized kesterite nanomaterial. *Nanomaterials*, 11(3), p.794.
- [3] **Ramoroka, M.E.**, Mdluli, S.B., John-Denk, V.S., Modibane, K.D., Arendse, C.J. and Iwuoha, E.I., 2021. Synthesis and photovoltaics of novel 2, 3, 4, 5-tetrathienylthiophene-co-poly (3-hexylthiophene-2, 5-diyl) donor polymer for organic solar cell. *Polymers*, 13(1), p.2.
- [4] Memela, M., Feleni, U., Mdluli, S., **Ramoroka, M.E.**, Ekwere, P., Douman, S. and Iwuoha, E., 2020. Electro-photovoltaics of polymer-stabilized copper–indium selenide quantum dot. *Electroanalysis*, 32(12), pp.3086-3097.
- [5] Teffu, D., **Ramoroka, M.**, Makhafola, M., Makgopa, K., Maponya, T., Hato, M.J., Iwuoha, E., Modibane, K., 2021. High performance asymmetric supercapattery based on reduced graphene oxide/metal organic framework nanocomposite decorated with palladium nanoparticles. *Electrochimica Acta*: EA21-3819 (Submitted).
- [6] **Ramoroka, M.E.**, Mdluli, S.B., John-Denk, V.S., Modibane, K.D., Nwambaekwe, K.C., Yussuf, S.T. and Iwuoha, E., 2021. Polypropylenimine tetra(thiophene)-co-poly(3-hexylthiophene-2,5-diyl): synthesis, characterization, electrochemical and photovoltaic studies. *International Journal of Molecular Sciences* (Submitted).

List of Conferences and Workshops

- South African Nanoscience and Nanotechnology Summer School 2016, “*Nanotechnology health, safety and environmental risk research: A necessity and not an impediment in the advancement of nanotechnology benefits*”, Conference, North-west University, Potchefstroom, South Africa.
- The 9th International Conference of the African Materials Research Society 2017, “*Photovoltaics of Copper Telluride Dendritic Core-Shell Nanoparticles*”, Conference, Gaborone International Convention Centre, Gaborone, Botswana.
- The 9th International Conference of the African Materials Research Society 2017, “*Free liquid surface electrospinning on nanospider technology workshop*”, Pre-conference workshop, Gaborone, Botswana.
- Thin Film Photovoltaics Workshop 2017, “*Thin film silicon solar cells and Tandem and triple junction cells, including hybrids*”, Workshop, University of the Western Cape, Cape Town, South Africa.
- Thin Film Photovoltaics Workshop 2017, “*Potential of hot-wire chemical vapour deposition (HWCVD) and flexible silicon solar cells*”, Workshop, University of the Western Cape, Bellville, South Africa.
- Rheometer workshop 2017, “*Basics and different techniques of Rheometer*”, Workshop, University of the Western Cape, Bellville, South Africa.
- 70th Annual International Society of Electrochemistry Meeting 2019, “*Copper Telluride Nanoparticles for Solar Cells*”, Conference, Inkosi Albert Luthuli International Convention Centre Complex, Durban, South Africa.
- 5th International Symposium on Electrochemistry 2019, Conference, University of the Western Cape, Cape Town, South Africa.
- 10th European Kesterite + Workshop & PhD Day 2019, “*Kesterite+ Workshop day*”, Uppsala University, Uppsala, Sweden.

Table of Content

Abstract	i
Keywords	iii
Declaration	iv
Acknowledgements	v
Dedication	vii
List of Publications	viii
List of Conferences and Workshops	ix
Table of Content	x
List of Figures	xviii
List of Tables	xxiii
List of Schemes	xxv
Chapter 1	1
1.1. Introduction	1
1.2. Aim and Objectives	2
1.3. Thesis outline	3
References	5
Chapter 2	8
Literature review: Operating Mechanism and Factors Affecting the Performance of Organic Photovoltaic Cells	8
Abstract	8
2.1. Introduction	9
2.2. Operating principle of OPVs and active layer processes	10
2.2.1. Light absorption	11



2.2.2.	Exciton diffusion.....	12
2.2.3.	Exciton separation.....	13
2.2.4.	Charge Transportation	14
2.2.5.	Charge collection	14
2.3.	OPVs active layer Materials.....	15
2.3.1.	Electron donating materials based on thiophene derivatives polymers	16
2.3.2.	Electron donating materials based on phthalocyanine derivatives	17
2.3.3.	Electron accepting materials based on fullerenes	18
2.3.4.	Electron accepting materials based on non-fullerenes.....	20
2.4.	Factors affecting OPVs performance during fabrication	21
2.4.1.	Thickness of the active layer.....	21
2.4.2.	Solvent and Additives.....	23
2.4.3.	Molecular weight of donor materials	25
2.4.4.	Annealing temperature.....	27
2.5.	Stability and lifetime of OPVs	29
2.6.	Conclusion.....	30
	References	32
Chapter 3.....		48
	Experimental: Characterization techniques and mechanisms used for synthesis	48
3.1.	Characterization techniques and purification methods	48
3.1.1.	Purification methods	48
3.1.1.1.	Thin layer chromatography (TLC).....	48
3.1.1.2.	Column chromatography	48
3.1.1.3.	Liquid-liquid extraction.....	48
3.1.2.	Characterization techniques	49

3.1.2.1.	Nuclear magnetic resonance spectroscopy (NMR)	49
3.1.2.2.	Fourier-transform infrared spectroscopy (FTIR)	49
3.1.2.3.	Mass spectroscopy.....	50
3.1.2.4.	Size exclusion chromatography	50
3.1.2.5.	Thermal gravimetric analysis	51
3.1.2.6.	Transmission electron microscopy	51
3.1.2.7.	Ultra-Violet visible spectroscopy (UV-Vis)	51
3.1.2.8.	Scanning electron microscope (SEM).....	52
3.1.2.9.	X-ray diffraction (XRD).....	52
3.1.2.10.	Cyclic voltammetry (CV).....	52
3.1.2.11.	Electrochemical impedance spectroscopy (EIS).....	53
3.1.2.12.	Photoluminescence (PL)	53
3.2.	Fabrication of photovoltaic cells.....	53
3.3.	Mechanism of the synthetic methods used in this study	54
3.3.1.	Schiff base reaction.....	54
3.3.2.	Stille coupling reaction	54
3.3.3.	Suzuki coupling reaction.....	55
3.3.4.	Grignard reaction	57
3.3.5.	Chemical oxidation polymerization.....	57
	References	59
	Chapter 4.....	61
	Polypropylenimine Tetra(thiophene)-co-Poly(3-hexylthiophene-2,5-diyl): Synthesis, characterization, electrochemical and photovoltaic studies	61
	Abstract	61
4.1.	Introduction	62

4.2. Materials and Methods	63
4.2.1. Materials	63
4.2.2. Synthesis of PPI-Th	64
4.2.3. Synthesis of PPI-Th-co-P3HT	65
4.2.4. Characterization techniques	66
4.2.5. Fabrication of OPVs	67
4.3. Results and Discussion.....	67
4.3.1. NMR analysis.....	67
4.3.2. FTIR analysis	71
4.3.3. TGA analysis	72
4.3.4. UV-Vis studies.....	73
4.3.5. TEM studies	74
4.3.6. SEM and elemental analysis of PPI-Th-co-P3HT	75
4.3.7. CV studies.....	77
4.3.8. EIS studies	78
4.3.9. Photoluminescence studies of PPI-Th-co-P3HT	81
4.3.10. XRD analysis of PPI-Th-co-P3HT	83
4.3.11. Photovoltaic performance of PPI-Th-co-P3HT	84
4.4. Conclusion.....	85
References	87
Chapter 5.....	94
Effect of Reaction Time on the Optical, Electrochemical and Photovoltaic Properties of Polypropylenimine Tetra(pyrrole)-co-Poly(3-hexylthiophene-2,5-diyl)	94
Abstract	94
5.1. Introduction	95



5.2.	Materials and Methods	96
5.2.1.	Materials	96
5.2.2.	Synthesis of PPI-Py.....	97
5.2.3.	Synthesis of PPI-Py-co-P3HT.....	98
5.2.4.	Characterization techniques	99
5.2.5.	Fabrication of OPVs	99
5.3.	Results and discussion.....	100
5.3.1.	NMR analysis of PPI-Py and PPI-Py-co-P3HT.....	100
5.3.2.	FTIR studies of PPI-Py and PPI-Py-co-P3HT	102
5.3.3.	TGA spectra of PPI-Py and PPI-Py-co-P3HT	103
5.3.4.	UV-Vis studies of PPI-Py and PPI-Py-co-P3HT	104
5.3.5.	TEM studies of PPI-Py-co-P3HT	106
5.3.6.	SEM analysis of PPI-Py-co-P3HT.....	107
5.3.7.	CV studies of PPI-Py-co-P3HT.....	108
5.3.8.	EIS studies of PPI-Py, PPI-Py-co-P3HT and PPI-Py-co-P3HT:PC ₇₁ BM composite	109
5.3.9.	Photoluminescence studies of PPI-Py-co-P3HT.....	111
5.3.10.	XRD analysis of PPI-Py-co-P3HT.....	113
5.3.11.	Photovoltaic performance	114
5.4.	Conclusion.....	115
	References	117
Chapter 6.....		124
	Electrochemical studies of Polypropylenimine Tetra(salicylalimine)-co-Poly(3- hexylthiophene-2,5-diyl Composite Synthesized by Grignard method	124
	Abstract	124
6.1.	Introduction	125

6.2.	Materials and Methods	126
6.2.1.	Materials	126
6.2.2.	Synthesis of PPI-Sal.....	127
6.2.3.	Synthesis of PPI-Sal-co-P3HT.....	128
6.2.4.	Characterization techniques	131
6.2.5.	Fabrication of OPVs	131
6.3.	Results and Discussions	132
6.3.1.	NMR analysis of PPI-Sal and PPI-Sal-co-P3HT	132
6.3.2.	FTIR analysis of PPI-Sal and PPI-Sal-co-P3HT	133
6.3.3.	TGA studies of PPI-Sal and PPI-Sal-co-P3HT.....	134
6.3.4.	UV-Vis studies of PPI-Sal and PPI-Sal-co-P3HT	135
6.3.5.	SEM images of PPI-Sal-co-P3HT	136
6.3.6.	TEM studies of PPI-Sal-co-P3HT	137
6.3.7.	CV studies of PPI-Sal and PPI-Sal-co-P3HT	138
6.3.8.	EIS studies of PPI-Sal and PPI-Sal-co-P3HT	140
6.3.9.	Photoluminescence of PPI-Sal-co-P3HT.....	143
6.3.10.	Photovoltaic properties of PPI-Sal-co-P3HT	144
6.4.	Conclusion.....	145
	Reference.....	146
CHAPTER 7	152
	Hexathienylthiophene-co-Poly(3-hexylthiophene) as Donor Material for Organic Photovoltaic Cell	152
	Abstract	152
7.1.	Introduction	153
7.2.	Materials and Methods	154

7.2.1.	Materials	154
7.2.2.	Synthesis of HTB	154
7.2.3.	Synthesis of HTB-co-P3HT	155
7.2.4.	Characterization Techniques.....	156
7.2.5.	OPVs fabrication.....	157
7.3.	Results and Discussions	158
7.3.1.	NMR studies of HTB and HTB-co-P3HT	158
7.3.2.	FTIR analysis of HTB and HTB-co-P3HT.....	160
7.3.3.	TGA studies of HBT-co-P3HT.....	160
7.3.4.	UV-Vis studies of HTB and HTB-co-P3HT in different solvents.....	161
7.3.5.	TEM studies of HTB-co-P3HT.....	162
7.3.6.	SEM studies of HTB-co-P3HT.....	163
7.3.7.	Photoluminescence of HTB-co-P3HT	164
7.3.8.	CV studies of HTB-co-P3HT.....	166
7.3.9.	EIS studies of HTB and HTB-co-P3HT	167
7.3.10.	Photovoltaic properties of HTB-co-P3HT	169
7.4.	Conclusion.....	170
	References	172
Chapter 8.....		179
	Synthesis and Photovoltaics of Novel 2,3,4,5-Tetrathienylthiophene-co-poly(3-hexylthiophene-2,5-diyl) Donor Polymer for Organic Photovoltaic cells	179
	Abstract	179
8.1.	Introduction	180
8.2.	Experimental Section	181
8.2.1.	Materials	181

8.2.2.	Synthesis of 2,3,4,5-Tetrathienylthiophene (TTT)	181
8.2.3.	Synthesis of TTT-co-P3HT.....	182
8.2.4.	Characterization Techniques.....	182
8.2.5.	Fabrication of OPVs	183
8.3.	Results and Discussion.....	184
8.3.1.	Optical and Electrochemical Characterization.....	188
8.3.2.	Photovoltaic Properties	191
8.3.3.	Characterization of OPVs with Electrochemical Methods	193
8.4.	Conclusion.....	197
	References	198
Chapter 9	204
9.1.	Conclusion.....	204
9.2.	Recommendations	207
Appendix	209



List of Figures

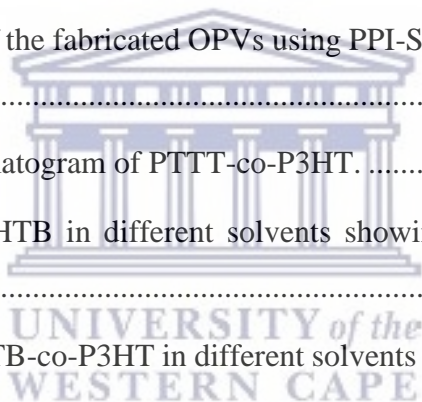
Figure 2.1: Schematic diagram of typical OPV cell.	11
Figure 2.2: Schematic diagram of light absorption process in OPVs cell.	11
Figure 2.3: Schematic diagram of exciton diffusion process in OPVs cell.	12
Figure 2.4: Schematic diagram of exciton separation process in OPVs cell.	13
Figure 2.5: Schematic diagram of charge transportation process in OPVs cell.....	14
Figure 2.6: Schematic diagram of charge collection process in OPVs cell.	15
Figure 2.7: (A) P3HT, (B) J51 and (C) PffBT4T-2OD.	17
Figure 2.8: (A) Phthalocyanine derivatives and (B) metal-phthalocyanine derivatives.	18
Figure 2.9: (A) PC ₆₁ BM, (B) PC ₇₁ BM and (C) ICMA.	20
Figure 2.10: (A) Perylene diimide and (B) Naphthalene diimide.	21
Figure 4.1: (A) ¹ H-NMR and (B) ¹³ C-NMR of PPI-Th.	69
Figure 4.2: ¹ H-NMR of PPI-Th-co-P3HT (A) 1:40, (B)1:60 and (C) 1:80.	70
Figure 4.3: ¹³ C-NMR of PPI-Th-co-P3HT (A) 1:40, (B)1:60 and (C) 1:80.	71
Figure 4.4: FTIR spectra of PPI-Th and PPI-Th-co-P3HT synthesized using 1:40, 1:60 and 1: 80 molar ratios.	72
Figure 4.5: TGA thermograms of PPI-Th and PPI-Th-co-P3HT synthesized using different molar ratio.	73
Figure 4.6: UV–Vis absorption spectra of PPI-Th and PPI-Th-co-P3HT synthesized using different molar ratios. Onset wavelength of PPI-Th-co-P3HT synthesized using molar ratio of 1:40, 1:60 and 1:80 are determined on spectra B, C and D, respectively.	74
Figure 4.7: TEM micrographs of PPI-Th-co-P3HT synthesized using different ratios of (A) 1:40, (B) 1:60 and (C) 1:80 molar ratios.....	75
Figure 4.8: SEM images of PPI-Th-co-P3HT synthesized using molar ratio A) 1:40, B) 1:60 and C) 1:80 with their EDS spectra on D, E and F, respectively.	76

Figure 4.9: (A) CV of PPI-Th-co-P3HT and (B) energy levels diagram.....	78
Figure 4.10: (A) Nyquist plot, (B) Bode-phase plots and (C) Bode-impedance of PPI-Th compared PPI-Th-co-P3HT synthesized using molar ratios.	80
Figure 4.11: (A) Nyquist plots, (B) Bode-phase plots and (C) Bode-impedance of PPI-Th-co-P3HT compared with and without PC ₆₁ BM.....	81
Figure 4.12: Photoluminescence spectra of PPI-Th-co-P3HT synthesized using molar ratios of (A) 1:40, (B) 1:60 and (C) 1:80. D) Comparison of emission spectra of PPI-Th-co-P3HT synthesized using different molar ratios.....	83
Figure 4.13: XRD pattern of PPI-Th-co-P3HT with different molar ratios.	84
Figure 4.14: J–V characteristics of the fabricated OPVs using PPI-Th-co-P3HT synthesized using different molar ratio as donor materials.....	85
Figure 5.1:(A) ¹ H-NMR and (B) ¹³ C-NMR of PPI-Py.....	101
Figure 5.2: ¹ H-NMR of PPI-Py-co-P3HT (A) 24 h, (B) 48 h and (C) 72 h.....	102
Figure 5.3: FTIR spectra of PPI-Py and PPI-Py-co-P3HT synthesized at 24, 48 and 72 h.....	103
Figure 5.4: TGA thermograms of PPI-Py and PPI-Py-co-P3HT synthesized for 24, 48 and 72 h.	104
Figure 5.5: (A) UV–Vis absorption spectra and Tauc plots of (B) PPI-Py and PPI-Py-co-P3HT synthesized for (C) 24 h, (D) 48 h and (E) 72 h.	106
Figure 5.6: TEM micrographs of PPI-Py-co-P3HT synthesized for (A) 24 h and (B) 72 h.....	107
Figure 5.7: SEM images of PPI-Py-co-P3HT synthesized for (A) 24 h, (B) 48 h and (C) 72 h with their EDS spectra D, E and F, respectively.....	108
Figure 5.8: (A) CV of PPI-Py-co-P3HT synthesized using different reaction times and (B) energy levels diagram.	109
Figure 5.9: Nyquist plot of (A) PPI-Py compared with PPI-Py-co-P3HT and (B) PPI-Py-co-P3HT with and without PC ₇₁ BM. Bode plot of (C) PPI-Py compared with PPI-Py-co-P3HT and (D) PPI-Py-co-P3HT with and without PC ₇₁ BM.	111

Figure 5.10: Photoluminescence studies of PPI-Py-co-P3HT synthesized for (A) 24, (B) 48 and (C) 72 h. (D) Comparison of emission spectra of PPI-Py-co-P3HT synthesized with different polymerization times.....	113
Figure 5.11: XRD pattern of PPI-Py-co-P3HT synthesized using different reaction time.....	114
Figure 5.12: J–V characteristics of the fabricated OPVs using PPI-Py-co-P3HT synthesized using different polymerization time as donor materials.	115
Figure 6.1: (A) ¹ H-NMR and (B) ¹³ C-NMR of PPI-Sal.	133
Figure 6.2: ¹ H NMR of PPI-Sal-co-P3HT.	133
Figure 6.3: FTIR spectra of PPI-Sal and PPI-Sal-co-P3HT.	134
Figure 6.4: TGA thermograms of PPI-Sal and PPI-Sal-co-P3HT.	135
Figure 6.5: (A) UV-Vis spectra and Tauc plots of (B) PPI-Sal and (C) PPI-Sal-co-P3HT.....	136
Figure 6.6: SEM images of PPI-Sal-co-P3HT with different magnifications of (A) 500 nm, B) 1 μm and (C) 5 μm. (D) EDS spectrum of PPI-Sal-co-P3HT.	137
Figure 6.7: TEM image of PPI-Sal-co-P3HT.	138
Figure 6.8: (A) CV of PPI-Sal and PPI-Sal-co-P3HT, (B) CV of PPI-Sal-co-P3HT and (C) energy level diagram.....	139
Figure 6.9: (A) Nyquist plots, (B) Bode-phase plots and (C) Bode-impedance of PPI-Sal and PPI-Sal-co-P3HT obtained at bias potential of -1.5 V.....	141
Figure 6.10: (A) Nyquist plots, (B) Bode-phase plots and (C) Bode-impedance of PPI-Sal-co-P3HT obtained at different bias potentials. (D) plot of R _{ct} and τ against bias potential.....	142
Figure 6.11: Photoluminescence spectra of (A) PPI-Sal and (B) PPI-Sal-co-P3HT in chlorobenzene.	144
Figure 6.12: J–V characteristics of the fabricated OPVs using PPI-Sal-co-P3HT as donor materials.	145
Figure 7.1: (A) ¹ H-NMR and (B) ¹³ C-NMR of HTB.....	159
Figure 7.2: ¹ H-NMR of HTB-co-P3HT.....	159
Figure 7.3: FTIR spectra of HTB and HTB-co-P3HT.....	160

Figure 7.4: TGA thermogram of HTB-co-P3HT.....	161
Figure 7.5: UV-Vis spectra of HTB and HTB-co-P3HT in different solvents.....	162
Figure 7.7: SEM images of HTB-co-P3HT films prepared using (A) chlorobenzene, (B) chloroform and (C) toluene.....	164
Figure 7.8: EDS spectra of HTB-co-P3HT films prepared using (A) chlorobenzene, (B) chloroform and (C) toluene as solvents.	164
Figure 7.9: (A) Photoluminescence spectra of HTB in different solvents. Photoluminescence spectra of HTB-co-P3HT in (B) chlorobenzene, (C) toluene and (D) chloroform.....	166
Figure 7.10: (A) Cyclic voltammograms and (B) energy levels HTB-co-P3HT obtained in different solvents compared with PC ₇₁ BM energy levels.....	167
Figure 7.11: (A) Nyquist plot, (B) Bode-phase plot and (C) Bode-impedance plot of HTB and HTB-co-P3HT prepared in different solvents.....	169
Figure 7.12: J–V characteristics of the fabricated OPVs using HTB-co-P3HT as donor material in different solvents.....	170
Figure 8.1: (A) ¹ H-NMR of TTT in CDCl ₃ and the insertion is ¹ H-NMR of TTT.....	186
Figure 8.1: (C) ¹ H-NMR of TTT-co-P3HT and (D) ¹ H-NMR of P3HT in CDCl ₃	187
Figure 8.2: FTIR of P3HT, TTT-co-P3HT, and TTT.....	188
Figure 8.3: (A) Absorption spectra, (B) CV and (C) energy levels diagram of P3HT and TTT-co-P3HT.....	190
Figure 8.4: Photoluminescence spectra of (A) TTT-co-P3HT and TTT-co-P3HT:PC ₇₁ BM and (B) P3HT and P3HT:PC ₇₁ BM.....	191
Figure 8.5: J–V plots of (A) P3HT:PC ₇₁ BM and (B) TTT-co-P3HT:PC ₇₁ BM devices.....	192
Figure 8.6: (A) CV (measured at 100 mVs ⁻¹ scan rate) and (B) Nyquist plots of 1 mM ferrocene obtained using bare ITO and ITO/PEDOT:PSS as working electrodes in 0.1 M TBAPF ₆ /acetonitrile solution. The Nyquist plots were attained at bias potential of 0.45 V vs Ag/Ag ⁺ . The equivalent circuit used for impedance data fitting is shown as an inset on B.....	195

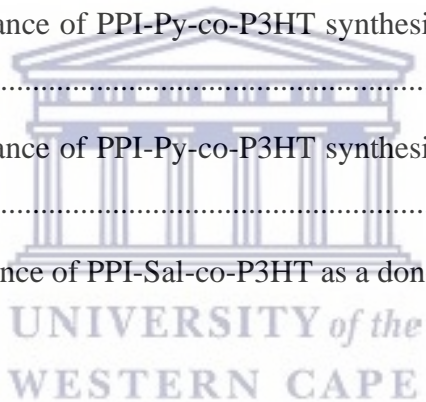
Figure 8.7: CV of (A) TTT-co-P3HT:PC ₇₁ BM, (B) TTT-co-P3HT:PC ₇₁ BM/ZnO, (C) P3HT:PC ₇₁ BM and (D) P3HT:PC ₇₁ BM/ZnO thin films coated on ITO substrate with/without PEDOT:PSS interlayer at 100 mVs ⁻¹ in 0.1 M TBAPF ₆ /acetonitrile solution.	196
Figure A1: Mass spectrum of PPI-Th.	209
Figure A2: J–V characteristics of the fabricated OPVs using PPI-Th-co-P3HT synthesized using molar ratio of A) 1:40, B) 1:60 and C) 1:80 as donor materials.	210
Figure A3: Mass spectrum of PPI-Py.	211
Figure A4: J–V characteristics of the fabricated OPVs using PPI-Py-co-P3HT synthesized for (A) 24h, (B) 48h and (C) 72h as donor materials.	212
Figure A5: Mass spectrum of PPI-Sal.	213
Figure A6: J–V characteristics of the fabricated OPVs using PPI-Sal-co-P3HT as donor materials.	214
Figure A7: Size-exclusion chromatogram of PTTT-co-P3HT.	214
Figure A8: UV-Vis spectra of HTB in different solvents showing how onset wavelength was determined.	215
Figure A9: UV-Vis spectra of HTB-co-P3HT in different solvents showing how onset wavelength was determined.	216
Figure A10: UV-Vis spectra of HTB-co-P3HT films prepared in different solvents showing how onset wavelength was determined.	217
Figure A11: UV-Vis spectra of TTT-co-P3HT and P3HT in chlorobenzene and as thin films showing how onset wavelength was determined.	218



List of Tables

Table 2.1: OPVs performance with different active layer thickness.	23
Table 2.2: OPVs performance in different solvents and additives.	25
Table 2.3: Effect of molecular weight of donor polymers on the performance of OPVs.	27
Table 2.4: Effect of annealing conditions on the performance of OPVs.	29
Table 4.1: EDS data of PPI-Th-co-P3HT synthesized using different molar ratios.	77
Table 4.2: Electrochemical responses of PPI-Th-co-P3HT synthesized using different molar ratios.	78
Table 4.3: Photovoltaic performance of PPI-Th-co-P3HT as donor material.	85
Table 5.1: EDS data of PPI-Py-co-P3HT synthesized using different reaction times.	108
Table 5.2: Electrochemical responses of PPI-Py-co-P3HT synthesized at different reaction times.	109
Table 5.3: Photovoltaic performance of PPI-Py-co-P3HT as donor material.	115
Table 6.1: Electrochemical results of PPI-Sal and PPI-Sal-co-P3HT.	139
Table 6.2: Electrochemical data of PPI-Sal and PPI-Sal-co-P3HT.	143
Table 7.1: UV-Vis response of HTB and HTB-co-P3HT in various solvents.	162
Table 7.2: Electrochemical properties of HTB and HTB-co-P3HT in different solvents.	167
Table 7.3: EIS results of HTB and HTB-co-P3HT prepared in various solvents.	169
Table 7.4: Photovoltaic performance of HTB-co-P3HT as donor material.	170
Table 8.1: Size exclusion chromatography analysis of TTT-co-P3HT.	185
Table 8.2: Optical and Electrochemical responses of TTT-co-P3HT and P3HT.	190
Table 8.3: Response of the TTT-co-P3HT:PC ₇₁ BM and P3HT:PC ₇₁ BM devices.	193
Table 8.4: Results obtained from fitting electrochemical impedance data of bare ITO and ITO/PEDOT:PSS.	195

Table 8.5: Cathodic and anodic peak currents obtained from CV used to study the effect of PEDOT:PSS interlayer.....	196
Table A1: Photovoltaic performance of PPI-Th-co-P3HT synthesized using molar ratio of 1:40 as donor material.	210
Table A2: Photovoltaic performance of PPI-Th-co-P3HT synthesized using molar ratio of 1:60 as donor material.	210
Table A3: Photovoltaic performance of PPI-Th-co-P3HT synthesized using molar ratio of 1:80 as donor material.	211
Table A4: Photovoltaic performance of PPI-Py-co-P3HT synthesized for 24h as donor material.	212
Table A5: Photovoltaic performance of PPI-Py-co-P3HT synthesized for 48h as donor material.	212
Table A6: Photovoltaic performance of PPI-Py-co-P3HT synthesized for 72h as donor material.	213
Table A7: Photovoltaic performance of PPI-Sal-co-P3HT as a donor material.	214



List of Schemes

Scheme 3.1: Shows Schiff base mechanism.....	54
Scheme 3.2: Stille coupling reaction	54
Scheme 3.3: Stille coupling mechanism.....	55
Scheme 3.4: Suzuki coupling reaction.....	56
Scheme 3.5: Suzuki coupling reaction mechanism.	56
Scheme 3.6: Grignard reaction method.	57
Scheme 3.7: Grignard reaction mechanism.....	57
Scheme 3.8: Mechanism of chemical oxidation polymerization.....	58
Scheme 4.1: Synthetic route of PPI-Th. (i). MeOH, 48 h.....	64
Scheme 4.2: Synthetic route of PPI-Th-co-P3HT. (i). FeCl ₃ , Chloroform, 60°C. n= 40, 60 and 80.	66
Scheme 5.1: Synthetic route of PPI-Py. (i). MeOH, 48 h.....	97
Scheme 5.2: Synthetic route of PPI-Py-co-P3HT. (i). FeCl ₃ , chloroform, 60°C.....	98
Scheme 6.1: Synthetic route of PPI-Sal. (i). MeOH, 48 h.....	128
Scheme 6.2: Synthesis of PPI-Sal-co-P3HT. (i) 2 M tertbutylmagnesium chloride solution, THF, 2 h, 60 °C, (ii) 2 M tertbutylmagnesium chloride solution, THF, 2 h, 60 °C, and (iii) Ni(dppp)Cl ₂ , 3 h, 60 °C.	130
Scheme 7.1: Synthetic route of HTB. (i). 5% Pd(PPh ₃) ₄ , K ₂ CO ₃ , CuI, Toluene, 120 h, 110°C.	155
Scheme 7.2: Synthetic route of HTB-co-P3HT. (i) FeCl ₃ , chloroform, 24 h, 60°C.....	156
Scheme 8.2: Synthetic of TTT-co-P3HT. i) FeCl ₃ , 60 °C, 24 h.	185

Chapter 1

1.1. Introduction

With increasing population and economic development, communities need a large amount of energy to create a good living condition. We depend more on energy required services such as heating, hospitals, refrigeration and transportation to maintain our way of living which makes it impossible to imagine life without electricity. More energy is generated by the burning of fossil fuels which leads to serious problems to the environment such as acid rain, air pollution, climate change, and global warming [1–5]. To overcome these challenges of environmental pollution and energy shortage, there is an urgent need to develop technologies which produce renewable energy especially photovoltaic cells.

To date, there are already commercially available photovoltaic cells but they are based on inorganic materials such as polycrystalline silicon [6,7], copper indium gallium selenide (CIGS) [8,9] and cadmium telluride (CdTe) [10]. As for silicon based photovoltaic cells, they are very costly manufacture because of very challenging manufacturing processes, expensive wafer and high thermal budget [11,12]. As for CIGS, the problem is the cost of indium. Estimated amount of about 27 000 kg is required to manufacture approximately 1 GW of CIGS based photovoltaic cells [8,9]. For large scale production of CIGS based photovoltaic cells, the price may be unbalanced because of high demand [12]. Much effort has been done to find alternative materials to replace CIGS. Copper zinc tin sulphide (CZTS) has been found as an alternative material because is composed of plentiful and nontoxic elements. However, this material suffers many challenges such as structural defects, presence of secondary phases and formation of multiple quaternary phases during synthesis [13–15]. CdTe on the other hand suffers drawbacks such as extreme rarity of tellurium and high toxicity of cadmium [16,17]. Therefore, these drawbacks make organic based photovoltaic cells advantageous over inorganic one.

In the recent years, the improvement of photovoltaic cells based on organic materials is the most investigated way to produce solar devices owing to the favourable combination of an easy manipulation in the production process [18–22]. In addition, they are studied due to their light

weight and possible low fabrication costs because they can be processed from solution [23–25]. The disadvantage of the organic-based photovoltaics (OPVs) is that they have low light conversion efficiency which limits them from being economically interesting alternative of expensive and toxic inorganic based photovoltaic cells especially when using poly(3-hexylthiophene-2,5-diyl) (P3HT). The improvement in organic based photovoltaic cells is achieved by modification of either donor or acceptor materials.

1.2. Aim and Objectives

The aim of this work is to synthesize a variety of modified P3HT based organic donor materials for use in photovoltaic cells. The synthesized materials were characterized with different analytical techniques to study their structural and photophysical properties for potential use in organic photovoltaic cells. In order to accomplish these aims, the following objectives were set:

- Synthesis of polypropylenimine tetra(thiophene) (PPI-Th), polypropylenimine tetra(N-methylpyrrole) (PPI-Py), polypropylenimine tetra(5-bromosalicylaldehyde) (PPI-Sal), hexathienylbenzene (HTB) and tetrathienylthiophene (TTT).
- Characterization of PPI-Th, PPI-Py and PPI-Sal by nuclear magnetic resonance (NMR), Fourier-transform infrared spectroscopy (FTIR), mass spectroscopy, thermogravimetric analysis (TGA) and electrochemical impedance spectroscopy (EIS) analysis.
- Characterization of HTB and TTT with NMR and FTIR.
- Synthesis of polypropylenimine tetra(thiophene)-co-poly(3-hexylthiophene-2,5-diyl) (PPI-Th-co-P3HT), polypropylenimine tetra(N-methylpyrrole)-co-poly(3-hexylthiophene-2,5-diyl) (PPI-Py-co-P3HT), polypropylenimine tetra(5-bromosalicylaldehyde)-co-poly(3-hexylthiophene-2,5-diyl) (PPI-Sal-co-P3HT), hexathienylbenzene-co-poly(3-hexylthiophene-2,5-diyl) (HTB-co-P3HT) and tetrathienylthiophene-co-poly(3-hexylthiophene-2,5-diyl) (TTT-co-P3HT) composites.
- The synthesized composites are characterized using NMR, FTIR, TGA, EIS, CV, size-exclusion chromatography, UV-Vis, scanning electron microscope (SEM) and transmission electron microscope (TEM).
- The synthesized donor materials are blended with acceptor materials [6,6]-Phenyl C71 butyric acid methyl ester and [6,6]-phenyl-C61-butyrac acid methyl ester.

- After blending, the blends were analyzed with electrochemical impedance spectroscopy, and photoluminescence.
- The organic photovoltaic cells were fabricated.

1.3. Thesis outline

This thesis is divided into nine chapters. The following presents summary of each chapter:

Chapter 1: highlights the importance of photovoltaic cells and gives the challenges with the current photovoltaic cells that are already commercially available. It indicates why organic photovoltaic cells are advantageous than inorganic based ones. In addition, it also gives objectives that must be met in order for this work to be complete.

Chapter 2: provides the operation mechanism of photovoltaic cells and also explain in details how the parameter such as open circuit voltage, short circuit current and fill factor are affected when organic materials are modified and preparation factors changes.

Chapter 3: gives the description of the characterization techniques and mechanisms of the synthetic methods used in this study.

Chapter 4: reports on the synthesis and characterization of PPI-Th-co-P3HT composite. The effect of molar ratio on optical, morphology and electrochemical properties were investigated.

Chapter 5: the effect of the reaction time during synthesis of PPI-Py-co-P3HT composite were investigated. Electrochemical, thermal and spectroscopic methods were used to study the effect of reaction time.

Chapter 6: reports on the comparison of PPI-Sal and PPI-Sal-co-P3HT to study the effect of P3HT on the surface of PPI-Sal.

Chapter 7: this chapter presents the synthesis and characterization of HTB-co-P3HT. The effect of solvent on the optical and electrochemical response of HTB-co-P3HT composite were investigated.

Chapter 8: reports on the synthesis of TTT-co-P3HT composite, its characterization and photovoltaic performance. It also shows how electrochemical methods can be used to study the layer of photovoltaic cells.

Chapter 9: this chapter summarizes the overall findings of this work.

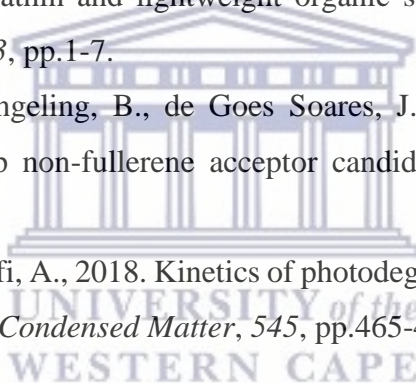


References

- [1] Tahri, F., Tahri, A. and Oozeki, T., 2018. Performance evaluation of grid-connected photovoltaic systems based on two photovoltaic module technologies under tropical climate conditions. *Energy Conversion and Management*, 165, pp.244-252.
- [2] Lee, J., Lee, K. and Park, S.S., 2016. Environmentally friendly preparation of nanoparticle-decorated carbon nanotube or graphene hybrid structures and their potential applications. *Journal of Materials Science*, 51, pp.2761-2770.
- [3] Desideri, U., Proietti, S., Zepparelli, F., Sdringola, P. and Bini, S., 2012. Life Cycle Assessment of a ground-mounted 1778 kWp photovoltaic plant and comparison with traditional energy production systems. *Applied Energy*, 97, pp.930-943.
- [4] Peng, J., Lu, L. and Yang, H., 2013. Review on life cycle assessment of energy payback and greenhouse gas emission of solar photovoltaic systems. *Renewable and Sustainable Energy Reviews*, 19, pp.255-274.
- [5] Rwenyagila, E.R., 2017. A review of organic photovoltaic energy source and its technological designs. *International Journal of Photoenergy*, 2017, pp.1-12.
- [6] Kruse, C.N., Schäfer, S., Haase, F., Mertens, V., Schulte-Huxel, H., Lim, B., Min, B., Dullweber, T., Peibst, R. and Brendel, R., 2021. Simulation-based roadmap for the integration of poly-silicon on oxide contacts into screen-printed crystalline silicon solar cells. *Scientific Reports*, 11, pp.1-14.
- [7] Yang, X., Kang, J., Liu, W., Zhang, X. and De Wolf, S., 2021. Solution-Doped Polysilicon Passivating Contacts for Silicon Solar Cells. *ACS Applied Materials & Interfaces*, 13, pp.8455–8460.
- [8] Misra, P., Atchuta, S.R., Mandati, S., Sarada, B.V., Rao, T.N. and Sakthivel, S., 2021. A non-vacuum dip coated SiO₂ interface layer for fabricating CIGS solar cells on stainless steel foil substrates. *Solar Energy*, 214, pp.471-477.
- [9] Uličná, S., Welch, L.M., Abbas, A., Togay, M., Tsai, V., Betts, T.R., Malkov, A.V., Walls, J.M. and Bowers, J.W., 2021. Sodium doping of solution-processed amine-thiol based CIGS solar cells by thermal evaporation of NaCl. *Progress in Photovoltaics: Research and Applications*, pp.1-12.

- [10] Watts, M.J., Hatton, P., Smith, R., Fiducia, T., Abbas, A., Greenhalgh, R., Walls, J.M. and Goddard, P., 2021. Chlorine passivation of grain boundaries in cadmium telluride solar cells. *Physical Review Materials*, 5, p.035403.
- [11] Wang, K., Liu, C., Meng, T., Yi, C. and Gong, X., 2016. Inverted organic photovoltaic cells. *Chemical Society Reviews*, 45, pp.2937-2975.
- [12] Ramanujam, J. and Singh, U.P., 2017. Copper indium gallium selenide based solar cells—a review. *Energy & Environmental Science*, 10, pp.1306-1319.
- [13] Prabeesh, P., Sajeesh, V.G., Selvam, I.P. and Potty, S.N., 2021. Influence of thiourea in the precursor solution on the structural, optical and electrical properties of CZTS thin films deposited via spray coating technique. *Journal of Materials Science: Materials in Electronics*, 32, pp.1-11.
- [14] Padhy, S., Mannu, R. and Singh, U.P., 2021. Graded band gap structure of kesterite material using bilayer of CZTS and CZTSe for enhanced performance: A numerical approach. *Solar Energy*, 216, pp.601-609.
- [15] Niedenzu, S., Gurieva, G. and Schorr, S., 2019. $\text{Cu}_2\text{ZnGe}(\text{S}_{1-x}\text{Se}_x)_4$ – The challenge to synthesize single phase material. *Thin Solid Films*, 669, pp.625-628.
- [16] Bousselmi, G., Khemiri, N., Ahmadi, S., Cantarero, A. and Kanzari, M., 2021. Cation Substitution of Copper by Silver in the Earth-Abundant Compound $\text{Cu}_2\text{ZnSnS}_4$: Comparative Study of Structural, Morphological, and Optical Properties. *Journal of Electronic Materials*, 50, pp.1-8.
- [17] Soleimani, Z., Zoras, S., Ceranic, B., Shahzad, S. and Cui, Y., 2021. The cradle to gate life-cycle assessment of thermoelectric materials: A comparison of inorganic, organic and hybrid types. *Sustainable Energy Technologies and Assessments*, 44, p.101073.
- [18] Wu, J., Fan, Q., Xiong, M., Wang, Q., Chen, K., Liu, H., Gao, M., Ye, L., Guo, X., Fang, J. and Guo, Q., 2021. Carboxylate substituted pyrazine: A simple and low-cost building block for novel wide bandgap polymer donor enables 15.3% efficiency in organic solar cells. *Nano Energy*, 82, p.105679.
- [19] Wan, J., Xia, Y., Fang, J., Zhang, Z., Xu, B., Wang, J., Ai, L., Song, W., Hui, K.N., Fan, X. and Li, Y., 2021. Solution-Processed Transparent Conducting Electrodes for Flexible Organic Solar Cells with 16.61% Efficiency. *Nano-Micro Letters*, 13, pp.1-14.

- [20] Fu, H., Li, Y., Yu, J., Wu, Z., Fan, Q., Lin, F., Woo, H.Y., Gao, F., Zhu, Z. and Jen, A.K.Y., 2021. High Efficiency (15.8%) All-Polymer Solar Cells Enabled by a Regioregular Narrow Bandgap Polymer Acceptor. *Journal of the American Chemical Society*, 143, pp.2665-2670.
- [21] Liu, X., Wei, Y., Zhang, X., Qin, L., Wei, Z. and Huang, H., 2021. An ADA'-DA type unfused nonfullerene acceptor for organic solar cells with approaching 14% efficiency. *Science China Chemistry*, 64, pp.228-231.
- [22] Guo, X., Fan, Q., Wu, J., Li, G., Peng, Z., Su, W., Lin, J., Hou, L., Qin, Y., Ade, H. and Ye, L., 2021. Optimized active layer morphologies via ternary copolymerization of polymer donors for 17.6% efficiency organic solar cells with enhanced fill factor. *Angewandte Chemie International Edition*, 60, pp.2322-2329.
- [23] Kaltenbrunner, M., White, M.S., Głowacki, E.D., Sekitani, T., Someya, T., Sariciftci, N.S. and Bauer, S., 2012. Ultrathin and lightweight organic solar cells with high flexibility. *Nature Communications*, 3, pp.1-7.
- [24] Lopez, S.A., Sanchez-Lengeling, B., de Goes Soares, J. and Aspuru-Guzik, A., 2017. Design principles and top non-fullerene acceptor candidates for organic photovoltaics. *Joule*, 1, pp.857-870.
- [25] Arshad, M.A. and Maaroufi, A., 2018. Kinetics of photodegradation mechanisms in organic photovoltaics. *Physica B: Condensed Matter*, 545, pp.465-474.



Chapter 2

Literature review: Operating Mechanism and Factors Affecting the Performance of Organic Photovoltaic Cells

Abstract

Due to the negative impact and possible run out of fossil fuels, the use of an alternative source of energy which is plentiful, it is crucial. The use of sunlight to produce energy by means of photovoltaic cell devices is the perfect approach to deal with the disadvantages of fossil fuels. Now, the photovoltaics that are already in market because of their power conversion efficiency (PCE) and stability are based on inorganic materials with drawbacks such as use of toxic substances during manufacturing, and expensive to manufacture. Changing inorganic materials to organic photovoltaic cells (OPVs), it is very important to overcome those drawbacks. The problem with the OPVs is the low PCE and stability. For over a decade now, researchers have been trying to improve the performance of OPVs with the PCE of over 11% reached. Here, we report the general mechanism of OPVs, materials that can be used as donor or acceptor materials and review recent work done on factors affecting the performance of the OPVs during fabrication.

2.1. Introduction

OPVs have fascinated significant attention recently because of their advantages such as their great ability of producing flexible, low-cost, simple preparation process and light weight devices [1–3]. New organic materials have been developed for use in OPVs in order to improve their PCE [4,5]. Most important that should be taken into consideration during fabrication of OPVs, it is the appropriate choice of an electron acceptor and electron donor materials. It is believed that factors like light absorption, exciton diffusion, charge separation, charge transportation and morphology which lead to poor charge collection by metal electrode in organic active layer limits the PCE of the device [6–9]. OPVs with over 11% PCE have been reported based on fullerenes and non-fullerenes acceptor materials together with thiophene derivatives donor materials [10–13].

Currently, fullerene derivative materials are dominating in OPVs as electron acceptors. However, fullerene derivatives acceptors have a relatively narrow absorption region which results to poor harvesting of sunlight and have advantages such as sufficient charge separation and good electron transportation [14,15]. Therefore, donor materials with wide absorption properties are required for sufficient excitons generation which are directly proportional to the performance of the device.

Donor-Acceptor organic active layers for OPVs have been widely studied in order to achieve a way of regulating band gap and energy levels [7,16–18]. Nevertheless, to attain good organic donor materials is still a problem since it must have a good balance with all the OPVs device parameters such as short circuit current (J_{SC}), fill factor (FF) and open circuit voltage (V_{OC}) which are related to PCE by Equation 2.1 below:

$$PCE = \frac{J_{sc} \times V_{oc} \times FF}{P_{in}} \dots\dots\dots 2.1$$

where P_{in} is the input light power. Understanding of the degradation mechanism in OPVs and how the OPVs parameters are affected are essential factors in order to improve their lifespan as well as donor and acceptor materials properties [19].

Therefore, fabrication conditions such as active layer thickness, donor-acceptor materials ratio, solvents, annealing temperature and annealing time were investigated on how they affect photovoltaic parameters [20–23]. Studies have been carried out to determine the optimal

fabrication conditions using fullerene derivative acceptor materials together with P3HT donor material and revealed that even a small change in those conditions causes a huge change in photovoltaic parameters [23–28]. To date, a lot of researchers still attempt to find optimal fabrication conditions and are also developing novel donor-acceptor materials hoping for high OPVs performance. However, a significant progress has been achieved in OPVs but their performances are still low as compared to other commercial photovoltaic cells such as silicon-based photovoltaic cells. We believe that OPVs performance can reach the target through researching.

In this chapter, we highlight the general operation mechanism of OPVs and discuss the processes that take place in the organic active layer of the device. Also, this chapter presents different materials that can be used as acceptor materials and donor materials as well as how the fabrication conditions affect the photovoltaics parameters. We trust that understanding how OPVs works together with fabrication conditions may help a lot in improving the performance of the devices. Stability and lifetime of the OPVs are also discussed.

2.2. Operating principle of OPVs and active layer processes

The working principle of OPVs is one of the most debated and researched issue. The devices use organic donor and organic acceptor materials which are sandwiched between transparent and metal electrodes. Transparent electrode allows the light to pass through it and strike the active layer of the device and the most commonly used material is indium tin oxide (ITO) which is supported on a glass substrate. For the metal electrode, they mostly use metals such as aluminium (Al), gold (Au) and silver (Ag) as opaque electrodes [29]. The structure of OPVs is shown in Figure 2.1. In OPVs, the acceptor material can be mixed with or deposited onto the donor material to form an active layer. In the active layer, several processes are taking place and are discussed below.

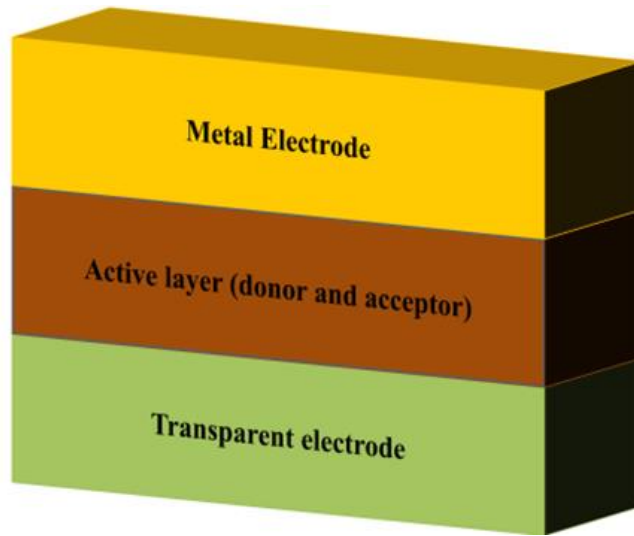


Figure 2.1: Schematic diagram of typical OPV cell.

2.2.1. Light absorption

This process is the first one that takes place in the organic active layer. The light travels through the transparent electrode to the active layer. After striking the active layer, light get absorbed leading to the production of electron-hole pairs. Due to high band gap of organic materials, utilization of visible-near infrared region of solar spectrum is a problem. The schematic of this process is shown in Figure 2.2. The metal electrode reflects light that was not absorbed by the donor material in the active layer. The reflected light can be trapped to be absorbed by introducing inorganic materials in the active layer [30,31].

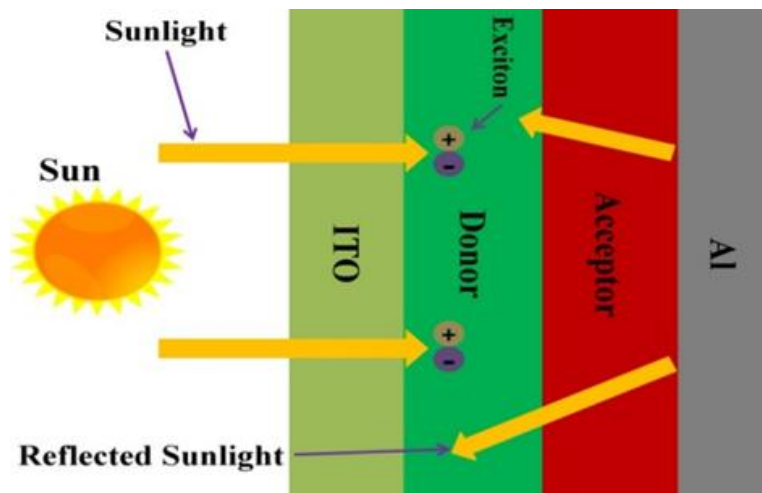


Figure 2.2: Schematic diagram of light absorption process in OPV's cell.

2.2.2. Exciton diffusion

After generation of electron-hole pair, they move to donor/acceptor interface. A schematic of this process is shown in Figure 2.3. The electron-hole pairs with large diffusion length can travel to donor/acceptor interface and thus contribute to PCE if the coulombic bound electron-hole pairs are not dissociated within their lifetime [32]. The electron-hole pair diffusion length (L_D) is a physical quantity known by Equation 2.2 below:

$$L_D = (D\tau)^{\frac{1}{2}} \dots\dots\dots 2.2$$

where D is diffusion coefficient and τ is an electron-hole pairs lifetime. The lifetime of most conjugated polymers is typically less than 1 ns, limiting the diffusion lengths to 20 nm. As a result, limited part of the electron-hole pair generated will diffuse to donor/acceptor interface in bilayer OPVs. Therefore, bulk heterojunction OPVs are introduced in order to harvest more electron-hole pairs at donor/acceptor interface. Electron-hole pairs can easily reach the interface once the domain size of acceptor and donor materials is less than the diffusion length. Therefore, understanding the exciton diffusion dynamics can help to further optimize active layer thickness and develop new donor materials with high electron-hole transportation properties to improve OPVs performance [33]. Studies revealed that exciton diffusion length can be increased by use of donor materials which contains heavy atoms that permits intersystem crossing and by doping active layer with triple sensitizers [34].

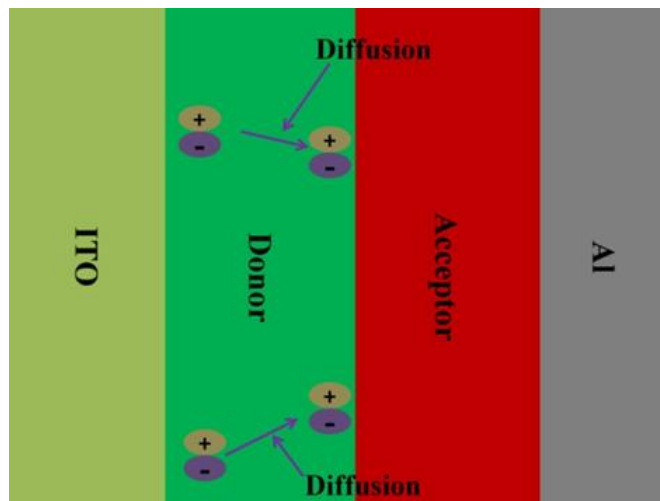


Figure 2.3: Schematic diagram of exciton diffusion process in OPVs cell.

2.2.3. Exciton separation

During exciton separation, the coulombically bound electron-hole pair separate into free charges (an electron and a hole). This separation takes place at the donor/acceptor interface which facilitates electron transfer from donor material to acceptor material by construction of charge transfer state leaving a hole in the donor material. This process is shown schematically in Figure 2.4. The lowest unoccupied molecular orbitals (LUMO) of the donor material must be higher than those of acceptor material for successful electron-hole separation. The difference in LUMO energy levels of donor and acceptor materials must be around 0.2-0.3 eV and must be higher than the electron-hole pair binding energy for sufficient electron-hole separation [35]. At the charge transfer state, electron and hole that are next to each other have a chance to recombine and drop to the ground state. If recombination takes place, there will be a loss in terms of charge separation process which is one of the reasons why OPVs have low efficiency [36,37]. The OPVs performance can be improved by increasing charge transfer rate, increasing charge separation rate and decreasing charge recombination rate.

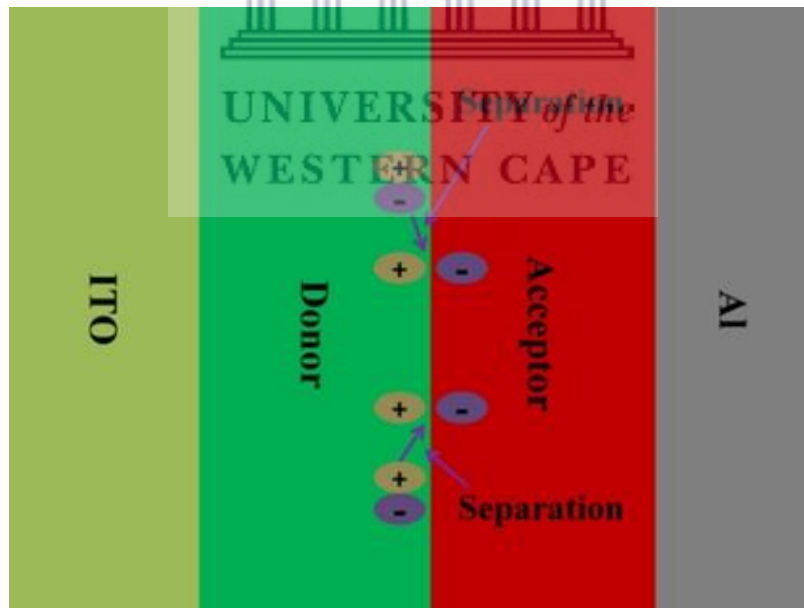


Figure 2.4: Schematic diagram of exciton separation process in OPV's cell.

2.2.4. Charge Transportation

After separation of exciton at donor/acceptor interface, electrons will travel through the acceptor material to the active layer/cathode (metal electrode) interface while holes will travel through donor material to active layer/anode (ITO electrode) interface (Figure 2.5). The charge transport is also affected by recombination and the interaction of charges with atoms or other charges that may decrease the rate they travel will lead to decrease in PCE of OPVs. Zhu *et al.* [38] achieved an efficiency of 16.88% using PM6:Y6 blends as an active layer. They concluded that this high PCE was achieved by fine tuning crystallinity within a proper morphology framework using annealing temperature which led to improvement of charge transportation. Omidvar *et al.* [7] studied novel thiophene-linked porphyrin donor and furan-linked porphyrin donor containing metals such as cobalt, nickel, copper, zinc and iron by density functional theory calculations. Their findings revealed that thiophene-linked porphyrin donor-cobalt and furan-linked porphyrin donor-cobalt possessed suitable energy levels with PCBM acceptor and good charge transport properties.

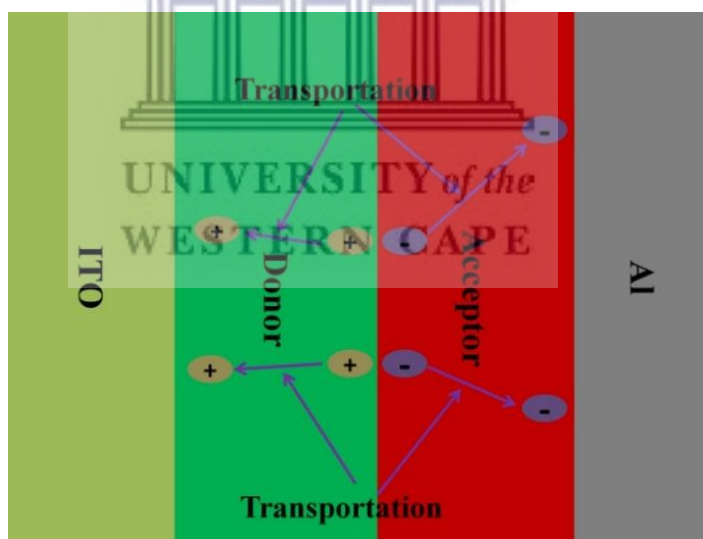


Figure 2.5: Schematic diagram of charge transportation process in OPVs cell.

2.2.5. Charge collection

To generate current, the holes must be collected at the anode while electrons must be collected at the cathode. The current is flow of electrons and connecting conductor on the anode and cathode of the OPV draw current off for external use as shown on Figure 2.6. The cell voltage which results from cell build-in electric together with the cell current defines the cell power produced. The

current flow is directed by employing electrodes with dissimilar work functions. Anode is elected to have a high work function while cathode is elected to have low work function. Electrons will travel through the low work function cathode while holes will travel through high work function anode. Mostly, modified layers such as PEDOT:PSS are inserted between the active layer and anode while metal oxides such as zinc oxide and titanium oxide are inserted between cathode and organic active layer. These modified layers permit only specific carrier charges type to pass through to the matching electrode [39–41]. Hou *et al.* [40] used PEDOT:PSS hole transport layer and they further incorporated titanium carbide ($\text{Ti}_3\text{C}_2\text{T}_x$) MXene into it. Their results revealed that the OPV with PEDOT:PSS- $\text{Ti}_3\text{C}_2\text{T}_x$ hole transport layer achieved an efficiency of 14.55% and a device with PEDOT:PSS achieved 13.10%. They believe that the presence of $\text{Ti}_3\text{C}_2\text{T}_x$ improve the hole collection and transfer through forming a hole transfer path between PEDOT by interacting with PSS. Their work shows that the properties of charge collecting can be improved by forming their composites with appropriate materials.

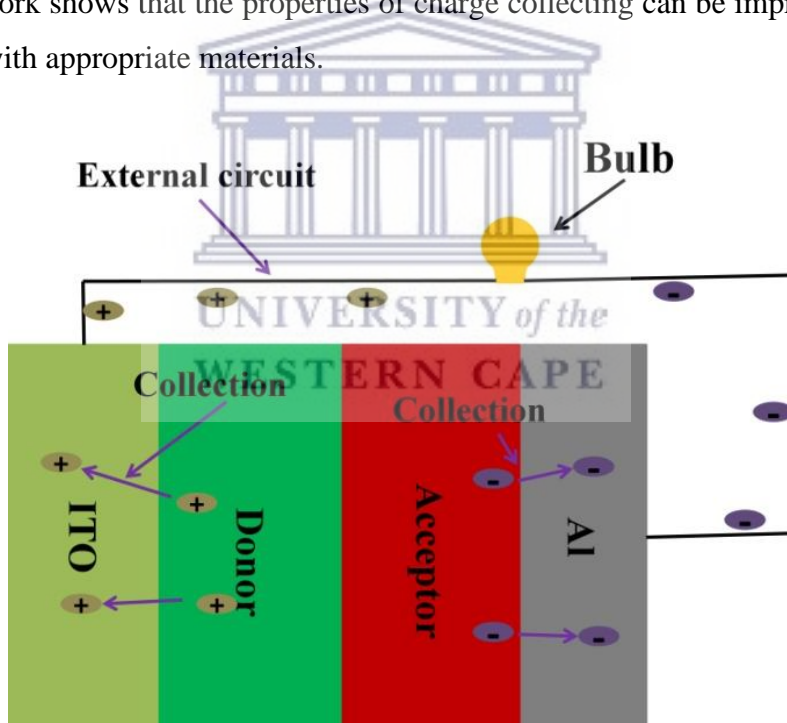


Figure 2.6: Schematic diagram of charge collection process in OPVs cell.

2.3. OPVs active layer Materials

In OPVs, the active layer either in bulk heterojunction or bilayer, is composed of organic materials. The organic materials that are used in active layers must have either electron-accepting or electron-

donating properties. Mostly used electron-accepting materials are either as fullerene-based or non-fullerene-based materials while the electron-donating materials are based on thiophene derivatives polymers and phthalocyanine derivatives. In this section, we are going to discuss some of those materials based on their application in OPVs.

2.3.1. Electron donating materials based on thiophene derivatives polymers

Over the past decades, researchers tried to develop novel thiophene derivative donor materials to improve the performance of OPVs [42–45]. Several factors have been taken into consideration to design and synthesize novel donor materials that have a narrow band gap, high solubility, high mobility, suitable energy level against those of acceptor materials and optimal phase separated morphology [46–48]. Thiophene-based donor material systems are the most promising as compared to other classes of systems due to their moderate band gap, efficient electron transfer, environmental stability, and can be easily modified leading to new properties [49]. Introduction of electron withdrawing groups such as fluorine and alkyl groups such as hexyl on the backbone of thiophene-based donor material turns to improve light absorption, stronger intermolecular interactions, fine-tune energy levels, and enhanced hole mobility properties. These properties lead to the development in performance of OPVs [50], [51]. Some of the developed thiophene-based donor materials are shown in Figure 2.7 which are P3HT, Poly[(5,6-difluoro-2-octyl-2*H*-benzotriazole-4,7-diyl)-2,5-thiophenediyl][4,8-bis[5-(2-hexyldecyl)-2-thienyl]benzo[1,2-*b*:4,5-*b'*]dithiophene-2,6-diyl]-2,5-thiophenediyl] (J51), and Poly[(5,6-difluoro-2,1,3-benzothiadiazol-4,7-diyl)-*alt*-(3,3''-di(2-octyldodecyl)-2,2',5',2'',5'',2''' quaterthiophen-5,5'''-diyl)] (PffBT4T-2OD).

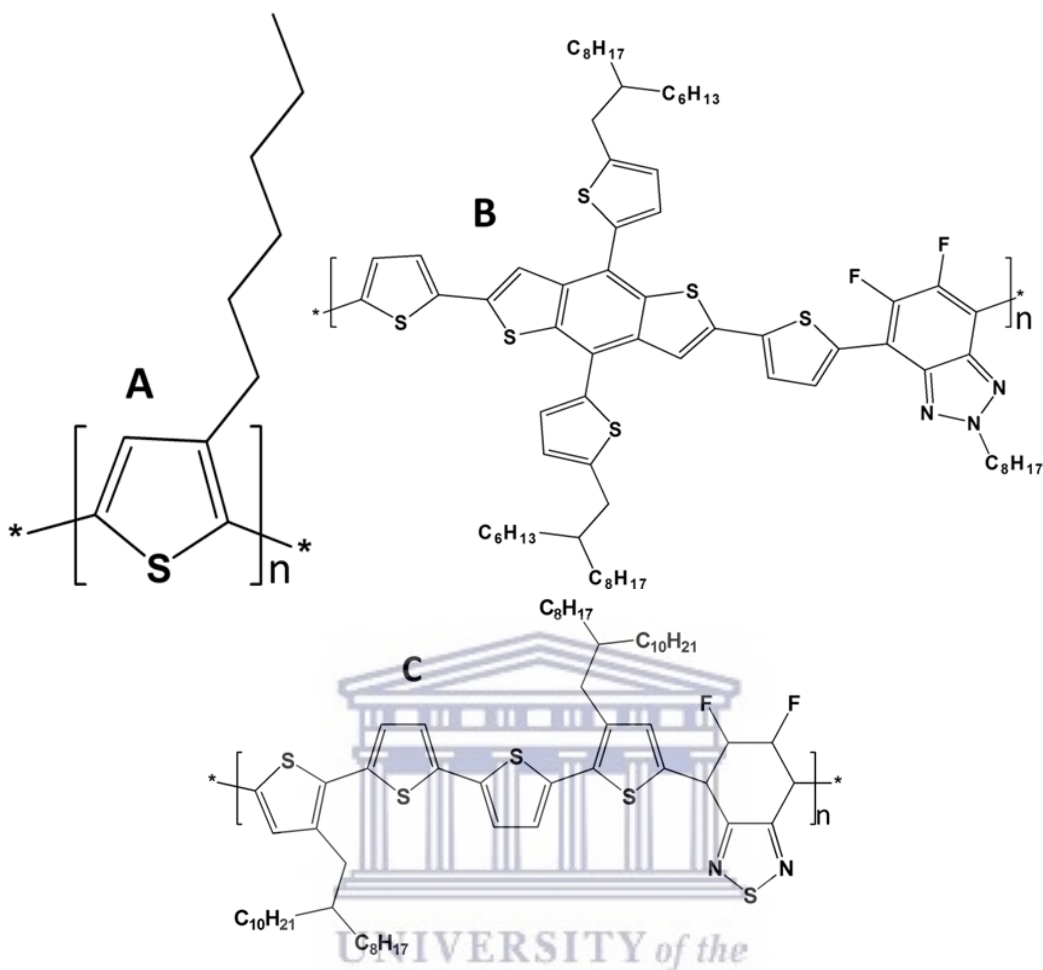


Figure 2.7: (A) P3HT, (B) J51 and (C) PffBT4T-2OD.

2.3.2. Electron donating materials based on phthalocyanine derivatives

Phthalocyanine derivatives have been widely used because of their chemical, physical and spectral properties. These properties give them advantages for utilization in different fields such as optoelectronics [52], gas sensors [53,54], and photodynamic therapy [55,56]. The properties of phthalocyanine derivatives are believed to arise from their efficient electron transfer capabilities. Their conjugated system produces intense absorption spectra giving two main bands: solet B band lies at ~ 350 nm and Q band lies between 600-800 nm [57]. The light absorption properties of phthalocyanine can be further adjusted by introduction of a metal such as copper into the core and peripheral substitution with different groups. This modification of phthalocyanine also plays a crucial role in improving the performance of OPVs by altering with its energy levels with a PCE of 13% reported [58,59]. Use of different metals and peripheral groups results in different π - π

stacking in phthalocyanine which can modify the hole mobility, solubility and stability in phthalocyanine [57,60,61]. Figure 2.8 shows the structures of phthalocyanine derivatives.

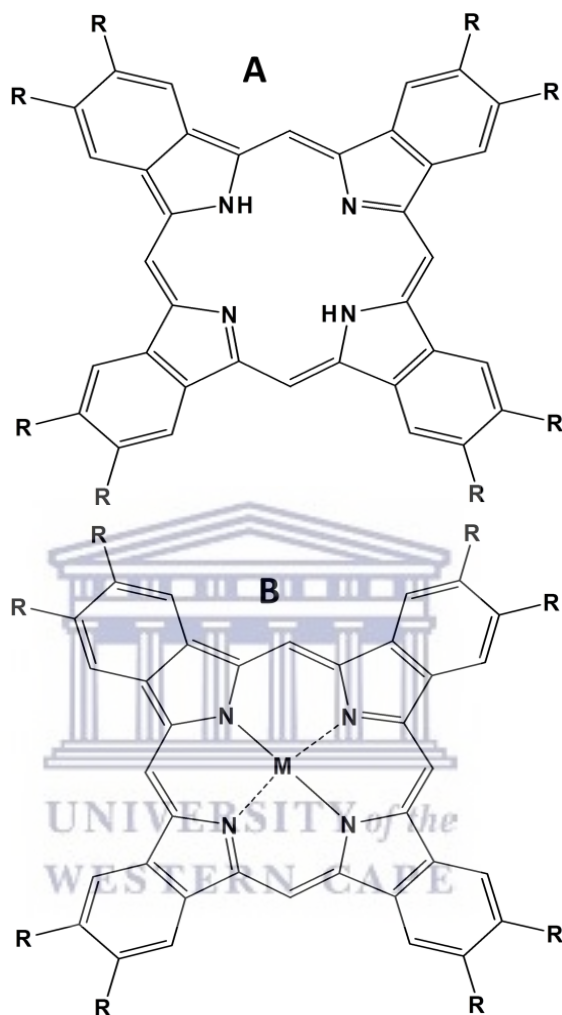
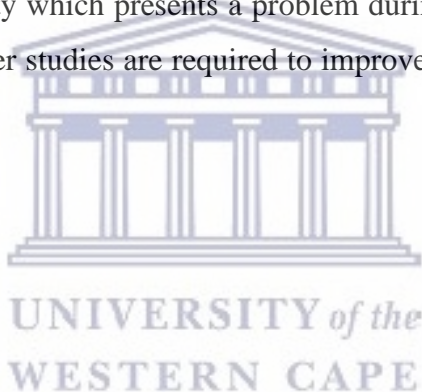


Figure 2.8: (A) Phthalocyanine derivatives and (B) metal-phthalocyanine derivatives.

2.3.3. Electron accepting materials based on fullerenes

Fullerene derivatives such as [6,6]-phenyl-C₆₁-butyric acid methyl ester (PC₆₁BM), [6,6]-phenyl-C₇₁-butyric acid methyl ester (PC₇₁BM) and 1',4'-Dihydro-naphtho[2',3':1,2][5,6]fullerene-C₆₀, C₆₀ derivative, indene-C₆₀ monoadduct (ICMA) shown in Figure 2.9 are most widely used as acceptor materials in OPVs [62–64]. They have an outstanding electron transporting properties which contribute a lot towards the performance of the devices. The main challenge in fullerene derivatives as acceptor materials is limited absorption spectrum and large energy losses which lead to lower J_{sc} and V_{oc} [65]. Studies revealed that organic donor material with band gap between

1.2-1.8 eV and acceptor material with a LUMO level which is 0.3 eV lower than that of donor material results to PCE of about 10% when external quantum efficiency is 65% [66]. The poor PCE of OPVs is believed to be due to lower LUMO levels of fullerene derivatives which results to a decrease in V_{OC} [67]. There are several ways that can be used to increase the LUMO levels of fullerene-based acceptor materials. The first way is by introducing more substituents on fullerene and this approach decreases the double bonds resulting in destruction of conjugation, thus the LUMO level of the acceptor material increases. However, the charge mobility will be negatively affected results in lower J_{SC} [68,69]. The second way is by employing endohedralfullerene as starting material during synthesis of fullerene derivatives. But endohedralfullerene has poor solubility which can be improved by introduction of alkyl group substituents. These substituents turn to decrease the electron mobility [70]. The last way is by forming a metal-fullerene complex. However, they have poor stability which presents a problem during optimization processes such as thermal annealing [71]. Further studies are required to improve use of fullerene derivatives as acceptor materials in OPVs.



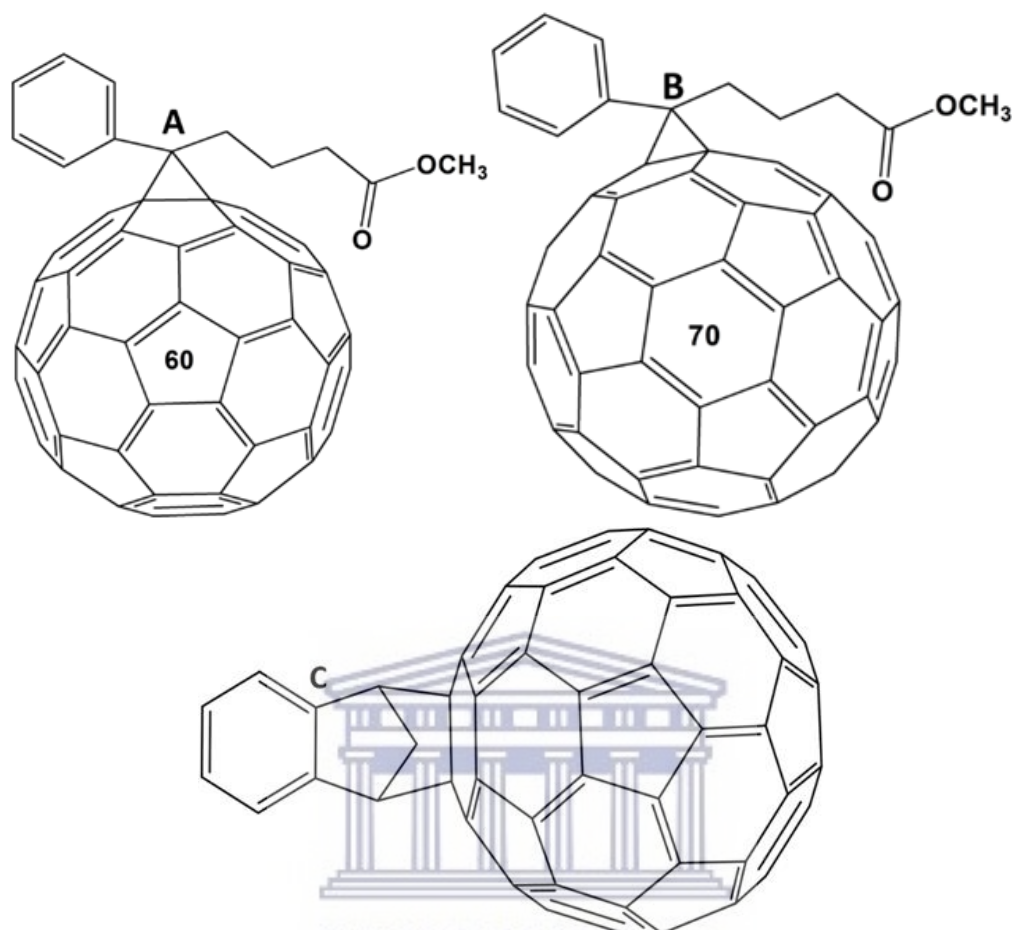


Figure 2.9: (A) PC₆₁BM, (B) PC₇₁BM and (C) ICMA.

2.3.4. Electron accepting materials based on non-fullerenes

Recently, non-fullerene acceptor materials have fascinated much interest because of their good absorption properties, better stability and tunable energy levels [72–75]. OPVs based on non-fullerene acceptor materials have been reported [74–77]. Perylene diimides and naphthalene diimide (Figure 2.10) are some of the mostly used non-fullerene acceptors either as polymers or small molecules due to the presence of two electron withdrawing imide groups in their structures which lead to high electron affinity. Their π -conjugated double bonds systems allow a strong intermolecular interaction that enhances the electron mobility [78]. However, these diimide containing acceptors have some disadvantages. They tend to aggregate in a blend and have poor solubility in common solvents. Aggregation allows formation of excimer which limits the diffusion length and traps the electron-hole pairs leading to poor performance in OPVs [79]. Studies revealed that the

use of more polar aromatic solvents can prevent aggregation at the early time during preparation of a film. Also, structural variation is important for developing the crystallinity of the bulk, blend morphology, charge transportation, and molecular orbitals energy levels (HOMO and LUMO) [80–82]. Bridging of either perylene diimide or naphthalene diimide dimers by different aromatic rings and substitution by alkoxy group at the bay-region or core position turns to improve the aggregation of the molecule [83,84].

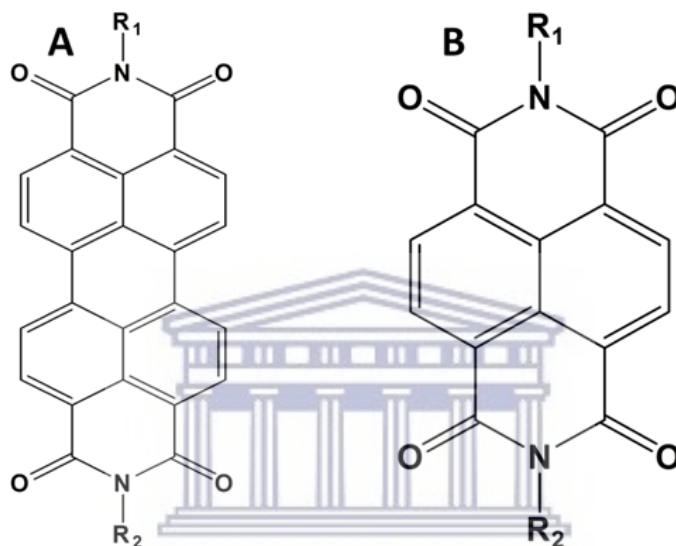


Figure 2.10: (A) Perylene diimide and (B) Naphthalene diimide.

2.4. Factors affecting OPVs performance during fabrication

2.4.1. Thickness of the active layer

An active layer is inserted between two electrodes that have dissimilar work functions. Investigations revealed that as the active layer thickness is tampered, the performance of the device dramatically changes. As the active layer thickness increases, more light is absorbed resulting to high J_{SC} which is due to generation of sufficient electron-hole pairs [85]. But since PCE of OPVs does not depend only on J_{SC} , some parameters are affected as the thickness of the active layer increases. As the thickness increase, charge carrier transport and collection are affected due to an increase in interface defect states and low charge mobility resulting in an increase in charge carrier recombination. These lower the FF and V_{OC} which are the reason for dramatical decrease in PCE as the thickness of the active layer increases [86]. To overcome these challenges, donor and

acceptor material with high charge mobility, ordered molecular structure, high light absorption abilities and good morphology need to be developed. Table 2.1 below shows recent studies based on how active layer thickness influence the OPVs performance. From the Table 2.1 below, the high performance of OPVs were achieved when the active layer thickness is ~100 nm. As the thickness of the active layer changes, photovoltaic parameters such as J_{SC} , V_{OC} , FF and PCE also changes. The optimal conditions were achieved when the active layer thickness is close to 100 nm. At an active layer close to 100 nm, maximum PCE and FF are achieved. While at thinner active layer, J_{SC} is low indicating the reduction of the amount of light absorbed and generation of small number of excitons. Thicker active layer films can absorb more photons; but this could bring larger resistance that will obstruct charge transportation in the organic active layer decreasing the PCE of OPVs [87]. The charge mobility of organic donor/acceptor materials limits the active layer thickness to approximately 100 nm.



Table 2.1: OPVs performance with different active layer thickness.

Active layer	Active layer thickness (nm)	PCE (%)	Jsc (mA/cm ²)	FF	Voc (V)	Ref
PTB7:PC ₇₁ BM	70	5.89	14.19	0.61	0.68	[87]
	90	6.99	16.33	0.62	0.69	
	100	7.23	16.39	0.63	0.70	
	120	6.73	15.93	0.61	0.69	
	130	6.21	14.95	0.62	0.76	
PM6:IT-4F	79	9.86	16.02	0.71	0.87	[88]
	103	11.78	18.99	0.71	0.88	
	149	10.72	17.92	0.68	0.88	
	186	9.94	17.68	0.65	0.87	
	233	9.27	17.24	0.61	0.85	
	330	7.30	16.72	0.51	0.85	
	398	5.62	14.63	0.49	0.83	
PTB7-Th:PC ₇₁ BM	480	4.52	12.68	0.44	0.83	[89]
	99	8.02	16.78	0.60	0.80	
	133	9.13	17.82	0.62	0.82	
	149	8.78	17.35	0.62	0.81	
PBDB-T:IT-M	165	8.58	16.88	0.62	0.82	[90]
	50	6.17	9.90	0.68	0.93	
	100	11.34	16.69	0.70	0.96	
	225	9.21	18.17	0.54	0.94	
	250	9.09	18.13	0.54	0.95	
	305	9.03	18.44	0.53	0.94	
	390	8.73	18.66	0.51	0.94	

Abbreviations: PTB7, Poly([2,6'-4,8-di(5-ethylhexylthienyl)benzo[1,2-b;3,3-b]dithiophene][3-fluoro-2(2-ethylhexyl)carbonyl]thieno[3,4-b]thiophenediyl)). PM6, Poly[(2,6-(4,8-bis(5-(2-ethylhexyl)-3-fluoro)thiophen-2-yl)-benzo[1,2-b:4,5-b']dithiophene))-alt-(5,5-(1',3'-di-2-thienyl-5',7'-bis(2-ethylhexyl)benzo[1',2'-c:4',5'-c']dithiophene-4,8-dione)]. IT-4F, (3,9-bis(1-oxo-2-methylene-3-(1,1-dicyanomethylene)-5,6-difluoroindanone)-5,5,11,11-tetrakis(4-n-hexylphenyl)-dithieno[2,3d:2',3'd']-s-indaceno[1,2b:5,6b'] dithiophene). PBDB-T, (poly[(2,6-(4,8-bis(5-(2-ethylhexyl)thiophen-2-yl)-benzo[1,2-b:4,5-b']dithiophene))-alt-(5,5-(10,30-di-2-thienyl-15,70-bis(2-ethylhexyl)benzo[10,20-c:40,50-c']dithiophene-4,8-dione))]). IT-M, 3,9-bis(2-methylene-((3-(1,1-dicyanomethylene)-6/7-methyl)-indanone))-5,5,11,11-tetrakis(4-hexylphenyl)-dithieno[2,3-d:2',3'-d']-s-indaceno[1,2-b:5,6-b']dithiophene.

2.4.2. Solvent and Additives

During the preparation of the active layer of OPVs, it is important to choose a good solvent in order to study the properties of the active layer which can help in predicting what is affecting the performance of the device. There are several factors that must be taken into consideration when choosing the solvent. These factors include ability to dissolve donor and acceptor materials to allow proper mixing, inability to form a complex with either donor or acceptor material and should not have very high boiling point [99]. Mostly used solvents for preparation of the active layer are chlorinated for example chlorobenzene (CB), dichlorobenzene (DCB), o-dichlorobenzene (o-

DCB), dichloromethane (DCM) and chloroform (CF). It was revealed that solvent cause dramatic change on the performance of the device [98]. Solvents affect the morphology of the active layer which turns to affect the OPVs parameters and crystallinity which determines the charge carrier mobility. The use of solvents with low drying speed (high boiling point) like CB improves the FF and J_{SC} by increasing the crystallinity of the active layer [91]. The use of additives such as 1, 8-diiodooctane and mixing of solvents are methods employed to improve the solute affinity [92]. Additives also play a crucial role in charge carrier mobility, crystallinity, morphology and PCE depending on their interaction with the donor or acceptor materials [93]. The effect of solvents and additives on the performance of OPVs are given and compared in Table 2.2. The studies reveal that after the addition of additives in the active layer, the PCE of OPVs improve, whereas for studies done using PTB7-Th:FNIC1 and PTB7-Th:FNIC2 active layers, OPVs performance decreases after the addition of additives [71,94-100]. The OPVs prepared in ODCB results to lower V_{OC} , J_{SC} and PCE after the addition of additives. The presence of additive in the blend prepared in ODCB exhibit films larger domain size and rough surface. The films with rough surface and larger domain contribute to insufficient electron/hole dissociation and charge transportation between donor/acceptor interface thus reducing V_{OC} and J_{SC} [71]. In other solvents such as CB, DCM and CF, the J_{SC} and PCE increases after the addition of additives. The presence of additives produces better phase separation in the active layer which offers improved J_{SC} and decrease in non-germinate recombination losses. While the presence of GO in an active layer improve light absorption resulting to an improved J_{SC} [94-99].

Table 2.2: OPVs performance in different solvents and additives.

Active layer	Solvent	Additive	PCE %	J _{sc} (mA/cm ²)	FF	V _{oc} (V)	Ref
PTB7-Th:PC ₇₁ BM	CB	w/o DDO: w/o DIO	5.72	14.01	0.54	0.78	[94]
		w/o DDO: 3% DIO	9.26	18.26	0.66	0.78	
		w/o DDO: 1% DIO	8.98	17.96	0.63	0.79	
		0.3% DDO: w/o DIO	8.52	16.47	0.66	0.79	
		0.4% DDO: w/o DIO	9.46	17.69	0.67	0.79	
		0.5% DDO: w/o DIO	9.74	18.07	0.67	0.81	
		0.6% DDO: w/o DIO	9.11	18.79	0.60	0.81	
		0.5% DDO: 0.5% DIO	10.29	19.65	0.65	0.81	
		0.5% DDO: 1% DIO	11.35	19.74	0.71	0.81	
		0.5% DDO: 2% DIO	10.51	19.43	0.68	0.80	
PTB7-Th: P(NDI2OD-T2)	CB	w/o	4.51	11.92	0.47	0.80	[95]
		DIO	5.40	11.96	0.56	0.81	
		CN	5.26	11.96	0.54	0.81	
		DPE	5.56	12.64	0.55	0.80	
P3HT:PCBM	CF	w/o	2.00	9.60	0.41	0.52	[96]
		GO	4.40	18.21	0.43	0.57	
PffBT4T-2OD:PC ₇₁ BM	CB:DCB	w/o	8.83	18.42	0.63	0.77	[97]
		CN	10.50	18.85	0.71	0.78	
		DPE	9.87	18.89	0.68	0.78	
		CN:DPE	10.93	20.07	0.69	0.78	
PBDTBT-COOR:PC ₇₁ BM	o-DCB	w/o	3.08	9.57	0.37	0.87	[71]
		DIO	2.83	8.89	0.39	0.82	
J71:N2200	CB	w/o	5.50	8.87	0.67	0.93	[98]
		1%DIO	7.28	10.45	0.77	0.91	
		CF	w/o	7.48	12.17	0.66	
PBDB-TF:IT-4F	CB	1% DIO	9.34	13.19	0.78	0.91	[99]
		w/o	10.93	17.60	0.71	0.87	
		0.5% DIO	12.29	19.91	0.76	0.81	
		0.5% DIO: 1% CN	12.72	20.07	0.72	0.88	
PTB7-Th:FNIC1	o-DCB	w/o	8.91	18.27	0.63	0.77	[100]
		DIO	7.83	15.35	0.66	0.78	
		CN	2.93	8.81	0.44	0.76	
PTB7-Th:FNIC2	o-DCB	w/o	11.10	21.42	0.72	0.73	
		DIO	9.81	19.00	0.70	0.74	
		CN	7.68	15.68	0.67	0.73	

Abbreviations: CB, Chlorobenzene. DDO, 1,10-decanediol. DIO, 1,8-diiodooctane. CN, 1-chloronaphthalene. DPE, diphenylether. P(NDI2OD-T2), Poly{[N,N'-bis(2-octyldecyl)-naphthalene-1,4,5,8-bis(dicarboximide)-2,6-diyl]-alt-5,5'-(2,2'-bithiophene)}. GO, Graphene oxide. PffBT4T-2OD, poly[(5,6-difluoro-2,1,3-benzothiadiazol-4,7-diyl)-alt-(3,3''-di(2-octyldecyl) 2,2';5',2'';5'',2''''-quaterthiophen-5,5''''-diyl)]. PBDTBT-COOR, Poly[(4,8-bis(5-(2-ethylhexyl)thiophen-2-yl)benzo [1,2-b:4,5-b']dithiophene)-alt-(diethyl 4,7-di(thiophen-2-yl)benzo[c][1,2,5]thiadiazole-5,6-dicarboxylate)]. J71, Poly [[5,6-difluoro-2-(2-hexyldecyl)-2H-benzotriazole-4,7-diyl]-2,5-thiophenediyl[4,8-bis[5-(tripropylsilyl)-2-thienyl]benzo[1,2-b:4,5-b']dithiophene-2,6-diyl]-2,5-thiophenediyl]. N2200, (poly[[N,N-9-bis(2-octyldecyl)-naphthalene-1,4,5,8- bis(dicarboximide)-2,6-diyl]-alt-5,50 -(2,20 -bithiophene)]). o-DCB, ortho-Dichlorobenzene. CF, Chloroform. FNIC1, benzo[1,2-b:4,5-b0]dithieno[3,2-b]thiophene fused with diarylcyclopentadienylthiophene. FNIC2, benzo[1,2-b:4,5-b0]dithiophene fused with diarylcyclopentadienylthieno[3,2-b]thiophene.

2.4.3. Molecular weight of donor materials

The main idea in OPVs field is to understand the relation between the structural properties that rule the performance of the material. The changes in chemical structure of a donor material have

shown to affect properties such as light absorption [101], charge carrier transport [102], [103], morphology [104] and electronic agreement with acceptor materials [105]. However, inclusion of substituents like alkyl chains and fluorine turn to further improve these properties. However, they turn to affect the conduction properties and decrease the crystallinity of the donor materials [106,107]. To overcome the OPVs performance limitations, optimization and development of new organic donor materials are required. Therefore, understanding the relationship between the donor material structures and the OPVs performance is necessary. Therefore, the effect of molecular weight of donor material on OPVs performance has been investigated. Table 2.3 shows the studies done to understand how molecular weight of the donor materials affect OPVs performance. Better performance of OPVs were achieved when donor material molecular weight was between 36 kDa to 215 kDa. PCE of OPVs increases as the molecular weight of polymer increases. These findings were attributed to more favored morphology of the active layer, decrease in series resistance and an increase in interconnectivity. The molecular weight range of polymers are limited. The maximum PCE can be reached at a specific molecular weight of a certain donor polymer and beyond this molecular weight no further increase in device performance. The OPVs fabrication conditions such as spin coating speed and substrate temperature were investigated using donor material with high molecular weight and it was revealed that no improvement in photovoltaic parameters [110].

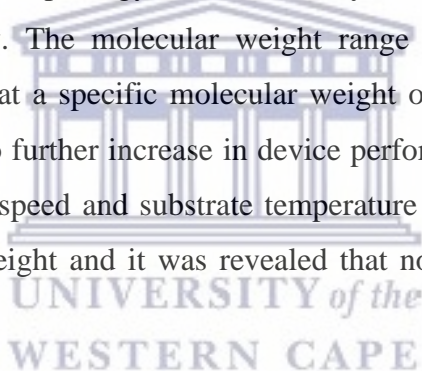


Table 2.3: Effect of molecular weight of donor polymers on the performance of OPVs.

Donor	Molecular weight (kDa)	PCE (%)	J _{sc} (mA/cm ²)	FF	V _{oc} (V)	Ref
J51	8	1.56	5.42	0.40	0.72	[108]
	16	3.52	8.35	0.58	0.72	
	21	4.20	9.31	0.62	0.73	
	36	5.97	12.18	0.65	0.75	
PTB7-Th	50	8.44	13.50	0.62	1.01	[103]
	100	8.68	14.20	0.61	1.00	
	200	9.57	15.20	0.63	1.00	
	300	7.73	15.10	0.52	0.99	
PTB7	41.20	4.02	10.10	0.55	0.73	[105]
	83.30	4.92	12.10	0.56	0.73	
	109.90	6.04	13.90	0.62	0.71	
	215.70	6.71	15.70	0.61	0.70	
DTBDT	9.60	0.85	2.00	0.45	0.94	[109]
	17.10	1.25	3.50	0.40	0.89	
	32.00	3.35	7.40	0.47	0.92	
	72.90	4.10	9.90	0.45	0.89	
	138.90	3.80	8.60	0.48	0.92	
PffBT4T-2OD	41.80	9.40	20.80	0.62	0.72	[110]
	43.80	9.30	18.80	0.68	0.72	
	54.90	8.80	18.60	0.66	0.72	
P _{SiSe}	8	1.03	4.27	0.39	0.62	[111]
	11	1.38	5.57	0.42	0.58	
	18	1.64	6.72	0.45	0.55	
P _{GeSe}	5	1.21	5.78	0.41	0.51	
	16	2.02	9.48	0.44	0.48	
	24	1.82	7.80	0.52	0.45	
PTB7	28	5.41	13.96	0.520	0.75	[101]
	40	6.27	15.27	0.540	0.76	
	128	8.50	18.51	0.600	0.76	

Abbreviation: DTBDT, 4,8-di(2-(2-ethylhexyl)-3-hexyl-thiophen-5-yl)-benzo[1,2-b:4,5-b']dithiophene. PTB7, poly[[4,8-bis(2-ethylhexyl)oxy]benzo[1,2-b:4,5-b']dithiophene-2,6-diyl][3-fluoro-2-[(2-ethylhexyl)carbonyl]thieno[3,4-b]-thiophenediyl]]. P_{SiSe}, Poly[(4,40-bis(2-ethylhexyl)dithieno[3,2-b:2',3'-d]silole)-2,6-diyl-alt-(2,1,3-benzoselenadiazole)-4,7-diyl]. P_{GeSe}, Poly[(4,40-bis(2-ethylhexyl)dithieno[3,2-b:2',3'-d]germole)-2,6-diyl-alt-(2,1,3-benzoselenadiazole)-4,7-diyl].

2.4.4. Annealing temperature

The performance of the OPVs can also be affected by fabrication conditions such as annealing time and annealing temperature. Annealing temperature alters with active layer morphology which consequently changes the PCE. Morphology of the active layer should be tuned in such a way that it allows efficient separation of electron-hole pair at donor/acceptor materials interface. The way of tuning the morphology is by annealing where it facilitates the aggregations that depend on the annealing temperature of the active layer [112,113]. Therefore, appropriate optimization of annealing temperature is important for overall performance of OPVs and the optimum conditions of annealing are different depending on the materials used in the active layer. Table 2.4 shows the results obtained trying to find optimum annealing conditions. It was reported that for P3HT:PCBM

active layer appropriate annealing temperature is 150°C since it creates bi-continuous morphology within seconds with crystalline polymers leading to enhancement in PCE [114]. After annealing at 150°C, stable performance of OPVs is obtained. This indicates the formation of thermally stable nanoscale active layer [115]. Amorphous polymers such as PTB7 requires no annealing to achieve high PCE. The use of additive such as DIO in this device assists to form thin active layer that helps to improve exciton harvesting in the acceptor materials and charge separation in the donor material. [116]. The results shown in Table 2.4 reveals that the best performance of OPVs is achieved when the annealing temperature is between 80 and 150 °C. The champion performance of OPVs is achieved at a certain annealing temperature depending on the acceptor and donor organic materials. The decrease in the PCE of OPVs is due to major reduction of FF as the annealing temperature increase above certain temperature. For example, FF of the PBDB-T:ITIC device decreases above 80 °C [117].



Table 2.4: Effect of annealing conditions on the performance of OPVs.

Active layer	Annealing temperature (°C)	PCE (%)	Jsc (mA/cm ²)	FF	Voc (V)	Ref
PBDB-T:ITIC	w/o	10.55	18.91	0.61	0.90	[117]
	80	11.35	18.59	0.66	0.91	
	100	10.23	18.05	0.62	0.90	
	120	8.01	16.00	0.56	0.86	
	140	6.03	16.79	0.50	0.72	
	160	5.74	18.04	0.48	0.64	
PTB7:PC ₇₁ BM	70	7.51	17.31	0.62	0.70	[87]
	90	8.82	18.10	0.61	0.75	
	110	7.09	16.31	0.58	0.75	
	140	6.47	15.89	0.56	0.73	
BQR:PC ₇₁ BM	w/o	4.70	10.70	0.46	0.95	[118]
	90	5.10	11.30	0.47	0.96	
	120	7.30	12.80	0.62	0.95	
	140	5.50	9.50	0.61	0.95	
	150	4.30	8.70	0.52	0.95	
	160	2.10	5.90	0.38	0.93	
PBDT4TBT:PC ₇₁ BM	w/o	3.04	10.10	0.52	0.57	[119]
	200	4.23	9.72	0.68	0.64	
PBDT4TffBT:PC ₇₁ BM	w/o	3.84	11.90	0.54	0.59	
	150	4.74	11.40	0.65	0.65	
PBDB-T: PMI-F-PMI	w/o	3.09	6.54	0.45	0.11	[120]
	135	4.34	8.13	0.49	0.11	
PBDB-T: PMI-FSi-PMI	w/o	2.69	6.08	0.43	0.11	
	150	4.67	7.88	0.53	0.11	
PBDB-T: PMI-FN-PMI	w/o	3.07	7.08	0.40	0.11	
	150	4.45	9.10	0.44	0.11	
PffBT4T-2OD:PC ₇₁ BM	w/o	7.17	15.45	0.64	0.73	[121]
	60	8.01	15.98	0.68	0.74	
	80	8.56	17.04	0.67	0.75	
	100	7.55	15.54	0.64	0.76	
	120	7.11	15.76	0.58	0.78	

Abbreviations: PBDB-T, poly[(2,6-(4,8-bis(5-(2-ethylhexyl)thiophen-2-yl)-benzo[1,2-b:4,5-b']dithiophene))-alt-(5,5-(1',3'-di-2-thienyl-5',7'-bis(2-ethylhexyl)benzo[1',2'-c:4',5'-c']dithiophene-4,8-dione))]. ITIC, 3,9-bis(2-methylene-(3-(1,1-dicyanomethylene)-indanone))-5,5,11,11-tetrakis(4-hexylphenyl)-dithieno[2,3-d:2',3'-d']-s-indaceno[1,2-b:5,6-b']dithiophene. BQR, Benzodithiophene-quaterthiophene-rhodanine. PBDT4TBT, composed of 4,8-di-2-thienylbenzo[1,2-b:4,5-b']dithiophene and 4,7-bis([2,2'-bithiophen]-5-yl)-benzo-2-1-3-thiadiazole. PBDT4TffBT, composed from benzo[1,2-b:4,5-b']dithiophene and difluoro-substituted 4,7-bis([2,20 -bithiophen]-5-yl)-benzo-2-1-3-thiadiazole. PMI-F-PMI, Perylene monoimide-fluorene-Perylene monoimide. PMI-FN-PMI, Perylene monoimide-carbazole-Perylene monoimide. Silafluorene.

2.5. Stability and lifetime of OPVs

Beside the PCE of the OPVs, the stability and lifetime of the device are the main challenges that affect the commercialization of the OPVs. The materials used for fabrication of the device are those that determines the stability and lifetime of the OPVs. To improve the stability of the organic active layer which decides the lifetime of the device, the mechanisms of the degradation process taking place at the active layer need to be understood. Understanding this process will help with

ideas on how the materials can be modified sequentially to improve their stability. There are several challenges identified which are said to be responsible for poor stability (short lifetime) of OPVs such as visible-near infrared light, UV light, moisture and air [122]. In air, photo-oxidation of crystalline polymers film takes place slower than amorphous film of similar materials because of the less chemically reactive ability due to the confinement of molecules [123]. Oxygen can be conquered by the use of encapsulations likewise to moisture. The use of encapsulation agents and UV filters can result in OPVs with lifetime of over 15 years [124]. In encapsulated OPVs, degradation is taking place around glass transition temperature (T_g). Above T_g , organic donor and acceptor materials can move leading to a blockage layer at the interface or increase in the diffusion length causing FF to drop [125]. Photo-degradation in encapsulated OPVs takes place at the active layer because of the photochemical processes causing a decrease in V_{oc} [126]. The photo-degradation seems to be in relationship with the donor/acceptor interface. To further improve the stability and performance of the OPVs, interfacial engineering is the main issue to address. Recently, OPVs comprising of either donor:acceptor:acceptor or donor:donor:acceptor as active layer have received a lot of attention. These types of OPVs composed of three materials in the active layer are termed ternary OPVs. The reason for studying ternary OPVs is to improve the PCE and stability. Yang *et al.* [127] studied the photovoltaic response and stability test of donor:acceptor:acceptor using PM6 as a donor material and Y6 and PIDTC-T as acceptor materials. They obtained an efficiency of 16.76 % and an improvement in thermal stability, photo-stability and shelf-like stability. They believe that their improved performance in terms of PCE and stability is due to the presence of PIDTC-T acceptor material which lead to enhancement in charge mobilities, reduced recombination, improved absorption and reasonable phase separation and redistributed composition in active layers. Therefore, this study revealed that developing and combining novel materials and device engineering to provide a way towards highly efficient and more stable OPVs.

2.6. Conclusion

In this chapter, we outlined the processes that takes place in OPVs. Understanding how OPVs works can help with developing new donor and acceptor materials with improved properties. It was revealed that substituting electron withdrawing groups on donor materials turns to improve hole mobility and light absorption properties. The use of fullerene derivatives as acceptor material

leads to a low V_{OC} since its LUMO energy is lower. It requires a donor material with engineered energy levels for good performance. Perylene diimide or naphthalene diimide acceptor materials have a problem with aggregation which can be improved by substituting alkoxy group on their core position or bay-region. We also reviewed factors that have an effect on the performance of OPVs such as active layer thickness, solvents and additives, molecular weight of donor material and annealing temperature. It is difficult to tune these factors since they are very sensitive and as new materials are developed; the optimal condition consequently changes. Further understanding on how these factors changes as the structure of a donor or acceptor material changes is still required. The other problem with OPVs is stability; the development of photochemical and thermally stable polymers is crucial in order to achieve better lifetimes that can participate with that of inorganic materials based photovoltaic cells. Recently, stable OPV with an efficiency of 16.76 % was achieved. This fast improvement will propose that the commercialization of OPVs will be realized soon.



References

- [1] Zhang, Y., Cai, G., Li, Y., Zhang, Z., Li, T., Zuo, X., Lu, X. and Lin, Y., 2021. An Electron Acceptor Analogue for Lowering Trap Density in Organic Solar Cells. *Advanced Materials*, 33, p.2008134.
- [2] Chen, Y., Bai, F., Peng, Z., Zhu, L., Zhang, J., Zou, X., Qin, Y., Kim, H.K., Yuan, J., Ma, L.K. and Zhang, J., 2021. Asymmetric Alkoxy and Alkyl Substitution on Nonfullerene Acceptors Enabling High-Performance Organic Solar Cells. *Advanced Energy Materials*, 11, p.2003141.
- [3] Armin, A., Li, W., Sandberg, O.J., Xiao, Z., Ding, L., Nelson, J., Neher, D., Vandewal, K., Shoaee, S., Wang, T. and Ade, H., 2021. A History and Perspective of Non-Fullerene Electron Acceptors for Organic Solar Cells. *Advanced Energy Materials*, 11, p.2003570.
- [4] Belverdi, A.R., Jamshidi, M.B., Taherpour, A.A., Jamshidi, M. and Rezaei, O., 2018. Novel donor-acceptor non-fullerene metal-organic solar cells: A first DFT and TD-DFT study. *Physica B: Condensed Matter*, 542, pp.37-43.
- [5] Rostami, Z., Saedi, L., Beheshti, K.S., Vahabi, V. and Ostadhosseini, N., 2019. Design of a novel series of small molecule donors for application in organic solar cells. *Solar Energy*, 186, pp.72-83.
- [6] Caliskan, M., Erer, M.C., Aslan, S.T., Udum, Y.A., Toppare, L. and Cirpan, A., 2020. Narrow band gap benzodithiophene and quinoxaline bearing conjugated polymers for organic photovoltaic applications. *Dyes and Pigments*, 180, p.108479.
- [7] Omidvar, A. and Mohajeri, A., 2020. Fine-tuning of charge transport properties of porphyrin donors for organic solar cell. *Journal of Molecular Liquids*, 312, p.113403.
- [8] Jahantigh, F., Ghorashi, S.B. and Belverdi, A.R., 2018. A first principle study of benzimidazobenzophenanthrolin and tetraphenyldibenzoperiflanthene to design and construct novel organic solar cells. *Physica B: Condensed Matter*, 542, pp.32-36.
- [9] Singh, A., Dey, A. and Iyer, P.K., 2018. Collective effect of hybrid Au-Ag nanoparticles and organic-inorganic cathode interfacial layers for high performance polymer solar

- cell. *Solar Energy*, 173, pp.429-436.
- [10] Hu, D., Yang, Q., Chen, H., Wobben, F., Le Corre, V.M., Singh, R., Liu, T., Ma, R., Tang, H., Koster, L.J.A. and Duan, T., 2020. 15.34% Efficiency All-Small-Molecule Organic Solar Cells with Improved Fill Factor Enabled by A Fullerene Additive. *Energy & Environmental Science*, 13, pp. 2134-2141.
- [11] Zhan, L., Li, S., Lau, T.K., Cui, Y., Lu, X., Shi, M., Li, C.Z., Li, H., Hou, J. and Chen, H., 2020. Over 17% efficiency ternary organic solar cells enabled by two non-fullerene acceptors working in an alloy-like model. *Energy & Environmental Science*, 13, pp.635-645.
- [12] Liu, Q., Jin, K., Li, W., Xiao, Z., Cheng, M., Yuan, Y., Shi, S., Jin, Z., Hao, F., Yang, S. and Ding, L., 2020. An efficient medium-bandgap nonfullerene acceptor for organic solar cells. *Journal of Materials Chemistry A*, 8, pp.8857-8861.
- [13] Firdaus, Y., He, Q., Lin, Y., Nugroho, F.A.A., Le Corre, V.M., Yengel, E., Balawi, A.H., Seitkhan, A., Laquai, F., Langhammer, C. and Liu, F., 2020. Novel wide-bandgap non-fullerene acceptors for efficient tandem organic solar cells. *Journal of Materials Chemistry A*, 8, pp.1164-1175.
- [14] Wang, H., Zhang, Z., Yu, J., Lin, P.C., Chueh, C.C., Liu, X., Guang, S., Qu, S. and Tang, W., 2020. Over 15% Efficiency in Ternary Organic Solar Cells by Enhanced Charge Transport and Reduced Energy Loss. *ACS Applied Materials & Interfaces*, 12, pp.21633-21640.
- [15] Doumon, N.Y., Houard, F.V., Dong, J., Christodoulis, P., Dryzhov, M.V., Portale, G. and Koster, L.J.A., 2019. Improved photostability in ternary blend organic solar cells: the role of [70] PCBM. *Journal of Materials Chemistry C*, 7, pp.5104-5111.
- [16] Al-horaibi, S.A., Alrabie, A.A., Alghamdi, M.T., Al-Ostoot, F.H., Garoon, E.M. and Rajbhoj, A.S., 2020. Novel hemicyanine sensitizers based on benzothiazole-indole for dye-sensitized solar cells: Synthesis, optoelectrical characterization and efficiency of solar cell. *Journal of Molecular Structure*, 1224, p.128836.
- [17] Bogdan, A., Szolga, L., Giurgi, G.I., Crişan, A.P., Bogdan, D., Hadsadee, S., Jungsuttiwong,

- S., Po, R., Grosu, I. and Roncali, J., Structure-properties relationships in triarylamine-based push-pull systems-C₆₀ dyads as active material for single-material organic solar cells. *Dyes and Pigments*, 184, p.108845.
- [18] Siddique, S.A., Siddique, M.B.A., Hussain, R., Liu, X., Mehboob, M.Y., Irshad, Z. and Adnan, M., 2020. Efficient Tuning of Triphenylamine-Based Donor Materials for High-Efficiency Organic Solar Cells. *Computational and Theoretical Chemistry*, 1191, p.113045.
- [19] Mohankumar, V., Pounraj, P., Pandian, M.S. and Ramasamy, P., 2019. Tuning the lifetime from molecular engineering of carbazole donor based metal-free organic dyes for dye sensitized solar cells–A computational approach. *Journal of Molecular Structure*, 1195, pp.494-505.
- [20] Hoang, M.H., Park, G.E., Choi, S., Park, C.G., Park, S.H., Van Nguyen, T., Kim, S., Kwak, K., Cho, M.J. and Choi, D.H., 2019. High-efficiency non-fullerene polymer solar cell fabricated by a simple process using new conjugated terpolymers. *Journal of Materials Chemistry C*, 7, pp.111-118.
- [21] Heiber, M.C., Okubo, T., Ko, S.J., Luginbuhl, B.R., Ran, N.A., Wang, M., Wang, H., Uddin, M.A., Woo, H.Y., Bazan, G.C. and Nguyen, T.Q., 2018. Measuring the competition between bimolecular charge recombination and charge transport in organic solar cells under operating conditions. *Energy & Environmental Science*, 11, pp.3019-3032.
- [22] Sun, R., Deng, D., Guo, J., Wu, Q., Guo, J., Shi, M., Shi, K., Wang, T., Xue, L., Wei, Z. and Min, J., 2019. Spontaneous open-circuit voltage gain of fully fabricated organic solar cells caused by elimination of interfacial energy disorder. *Energy & Environmental Science*, 12, pp.2518-2528.
- [23] Lin, B., Zhou, X., Zhao, H., Yuan, J., Zhou, K., Chen, K., Wu, H., GUO, R., Scheel, M.A., Chumakov, A. and Roth, S.V., 2020. Balancing the Pre-aggregation and Crystallization Kinetics Enables High Efficiency Slot-Die Coated Organic Solar Cells with Reduced Non-radiative Recombination losses. *Energy & Environmental Science*. 13, pp. 2467–2479.
- [24] Yuan, K., Chen, L. and Chen, Y., 2014. Photovoltaic performance enhancement of

- P3HT/PCBM solar cells driven by incorporation of conjugated liquid crystalline rod-coil block copolymers. *Journal of Materials Chemistry C*, 2, pp.3835-3845.
- [25] Bubnov, A., Iwan, A., Cigl, M., Boharewicz, B., Tazbir, I., Wójcik, K., Sikora, A. and Hamplová, V., 2016. Photosensitive self-assembling materials as functional dopants for organic photovoltaic cells. *RSC Advances*, 6, pp.11577-11590.
- [26] Kadem, B., Alfahed, R.F., Al-Asadi, A.S. and Badran, H.A., 2020. Morphological, structural, optical, and photovoltaic cell of copolymer P3HT:ICBA and P3HT:PCBM. *Optik*, 204, p.164153.
- [27] Kumar, S., Kim, H., Kim, D.K. and Iyer, S.S.K., 2020. Spin and doctor-blade coated PEDOT: PSS back electrodes in inverted organic solar cells. *Solar Energy*, 204, pp.64-70.
- [28] Li, P., Jiang, Z., Huang, H., Tian, S., Hu, X., Li, W., Bao, X. and Wang, Y., 2020. Improving electron transport by using a NaCl/polyethylenimine ethoxylated double layer for high-efficiency polymer solar cells. *Materials Science in Semiconductor Processing*, 116, p.105150.
- [29] Kumar, M.S. and Balachander, K., 2016. Performance analysis of different top metal electrodes in inverted polymer solar cells. *Optik*, 127, pp.2725-2731.
- [30] Mohan, M., Sekar, R. and Namboothiry, M.A., 2020. Understanding the effects of shape, material and location of incorporation of metal nanoparticles on the performance of plasmonic organic solar cells. *RSC Advances*, 10, pp.26126-26132.
- [31] Phetsang, S., Nootchanat, S., Lertvachirapaiboon, C., Ishikawa, R., Shinbo, K., Kato, K., Mungkornasawakul, P., Ounnunkad, K. and Baba, A., 2020. Enhancement of organic solar cell performance by incorporating gold quantum dots (AuQDs) on a plasmonic grating. *Nanoscale Advances*, 2, pp. 2950–2957.
- [32] Sajjad, M.T., Ruseckas, A., Jagadamma, L.K., Zhang, Y. and Samuel, I.D., 2020. Long-range exciton diffusion in non-fullerene acceptors and coarse bulk heterojunctions enable highly efficient organic photovoltaics. *Journal of Materials Chemistry A*, 8, pp.15687-15694.
- [33] Tamai, Y., Ohkita, H., Benten, H. and Ito, S., 2015. Exciton diffusion in conjugated

- polymers: from fundamental understanding to improvement in photovoltaic conversion efficiency. *The Journal of Physical Chemistry Letters*, 6, pp.3417-3428.
- [34] Luppi, B.T., Majak, D., Gupta, M., Rivard, E. and Shankar, K., 2019. Triplet excitons: improving exciton diffusion length for enhanced organic photovoltaics. *Journal of Materials Chemistry A*, 7, pp.2445-2463.
- [35] Athanasopoulos, S., Tscheuschner, S., Bäessler, H. and Köhler, A., 2017. Efficient charge separation of cold charge-transfer states in organic solar cells through incoherent hopping. *The Journal of Physical Chemistry Letters*, 8, pp.2093-2098.
- [36] Karki, A., Vollbrecht, J., Gillett, A.J., Xiao, S.S., Yang, Y., Peng, Z., Schopp, N., Dixon, A.L., Yoon, S., Schrock, M. and Ade, H., 2020. The role of bulk and interfacial morphology in charge generation, recombination, and extraction in non-fullerene acceptor organic solar cells. *Energy & Environmental Science*, 13, pp.3679-3692.
- [37] Pelzer, K.M. and Darling, S.B., 2016. Charge generation in organic photovoltaics: a review of theory and computation. *Molecular Systems Design & Engineering*, 1, pp.10-24.
- [38] L. Zhu, L., Zhang, M., Zhou, G., Hao, T., Xu, J., Wang, J., Qiu, C., Prine, N., Ali, J., Feng, W. and Gu, X., 2020. Efficient Organic Solar Cell with 16.88% Efficiency Enabled by Refined Acceptor Crystallization and Morphology with Improved Charge Transfer and Transport Properties. *Advanced Energy Materials*, 10, pp. 1–9.
- [39] Son, H.J., Park, H.K., Moon, J.Y., Ju, B.K. and Kim, S.H., 2020. Thermal degradation related to the PEDOT: PSS hole transport layer and back electrode of the flexible inverted organic photovoltaic module. *Sustainable Energy & Fuels*, 4, pp.1974-1983.
- [40] Hou, C. and Yu, H., 2020. Modifying the nanostructures of PEDOT:PSS/Ti₃C₂T_x composite hole transport layers for highly efficient polymer solar cells. *Journal of Materials Chemistry C*, 8, pp.4169-4180.
- [41] Fan, X., Song, W., Lei, T., Xu, B., Yan, F., Wang, N., Cui, H. and Ge, Z., 2019. High-efficiency robust organic solar cells using transfer-printed PEDOT:PSS electrodes through interface bonding engineering. *Materials Chemistry Frontiers*, 3, pp.901-908.
- [42] Fan, Q., Zhu, Q., Xu, Z., Su, W., Chen, J., Wu, J., Guo, X., Ma, W., Zhang, M. and Li, Y.,

2018. Chlorine substituted 2D-conjugated polymer for high-performance polymer solar cells with 13.1% efficiency via toluene processing. *Nano Energy*, *48*, pp.413-420.
- [43] Liu, D., Yang, B., Jang, B., Xu, B., Zhang, S., He, C., Woo, H.Y. and Hou, J., 2017. Molecular design of a wide-band-gap conjugated polymer for efficient fullerene-free polymer solar cells. *Energy & Environmental Science*, *10*, pp.546-551.
- [44] Li, Z., Xu, X., Zhang, W., Meng, X., Genene, Z., Ma, W., Mammo, W., Yartsev, A., Andersson, M.R., Janssen, R.A. and Wang, E., 2017. 9.0% power conversion efficiency from ternary all-polymer solar cells. *Energy & Environmental Science*, *10*, pp.2212-2221.
- [45] Sun, C., Wu, Z., Hu, Z., Xiao, J., Zhao, W., Li, H.W., Li, Q.Y., Tsang, S.W., Xu, Y.X., Zhang, K. and Yip, H.L., 2017. Interface design for high-efficiency non-fullerene polymer solar cells. *Energy & Environmental Science*, *10*, pp.1784-1791.
- [46] Heo, H., Ban, L., Nam, G., Kim, H., Jang, S. and Lee, Y., 2018. Regioregular polymers containing benzodithiophene and thienothiophene segments with different electron donating side chains for high-performance polymer solar cells. *Dyes and Pigments*, *158*, pp.249-258.
- [47] Zhao, J., Zhao, S., Xu, Z., Qiao, B., Huang, D., Zhao, L., Li, Y., Zhu, Y. and Wang, P., 2016. Revealing the effect of additives with different solubility on the morphology and the donor crystalline structures of organic solar cells. *ACS Applied Materials & Interfaces*, *8*, pp.18231-18237.
- [48] Wan, X., Li, C., Zhang, M. and Chen, Y., 2020. Acceptor–donor–acceptor type molecules for high performance organic photovoltaics—chemistry and mechanism. *Chemical Society Reviews*, *49*, pp.2828-2842.
- [49] Kumaresan, P., Vegiraju, S., Ezhumalai, Y., Yau, S.L., Kim, C., Lee, W.H. and Chen, M.C., 2014. Fused-thiophene based materials for organic photovoltaics and dye-sensitized solar cells. *Polymers*, *6*, pp.2645-2669.
- [50] Wang, K., Song, X., Guo, X., Wang, Y., Lai, X., Meng, F., Du, M., Fan, D., Zhang, R., Li, G. and Kyaw, A.K.K., 2020. Efficient as-cast thick film small-molecule organic solar cell with less fluorination on the donor. *Materials Chemistry Frontiers*, *4*, pp.206-212.

- [51] Li, C., Cai, M., Bao, X., Liu, Y., Yang, R. and Wan, X., 2019. N-Alkylation vs. O-alkylation: influence on the performance of the photovoltaic cells based on a tetracyclic lactam polymer donor. *RSC Advances*, 9, pp.12310-12318.
- [52] Ghadari, R., Saei, P.S., Sabri, A., Ghasemi, Z. and Kong, F., 2020. Enhanced phthalocyanine-sensitized solar cell efficiency via cooperation of nitrogen-doped carbon dots. *Journal of Cleaner Production*, 268, p. 122236.
- [53] Kumar, S., Sharma, A.K., Sohal, M.K., Sharma, D.P., Debnath, A.K., Aswal, D.K. and Mahajan, A., 2020. Room temperature highly sensitive chlorine sensor based on reduced graphene oxide anchored with substituted copper phthalocyanine. *Sensors and Actuators B: Chemical*, 327, p. 128925.
- [54] Huang, J., Jiang, D., Zhou, J., Ye, J., Sun, Y., Li, X., Geng, Y., Wang, J., Du, Y. and Qian, Z., 2020. Visible light-activated room temperature NH₃ sensor base on CuPc-loaded ZnO nanorods. *Sensors and Actuators B: Chemical*, 327, p.128911.
- [55] Santos, K.L.M., Barros, R.M., da Silva Lima, D.P., Nunes, A.M.A., Sato, M.R., Faccio, R., de Lima Damasceno, B.P.G. and Junior, J.A.O., 2020. Prospective application of phthalocyanines in the photodynamic therapy against microorganisms and tumor cells: a mini-review. *Photodiagnosis and Photodynamic Therapy*, p.102032.
- [56] Motlounq, B.M., Babu, B., Prinsloo, E. and Nyokong, T., 2020. The photophysical properties and photodynamic therapy activity of In and Zn phthalocyanines when incorporated into individual or mixed Pluronic® micelles. *Polyhedron*, 188, p.114683.
- [57] Dalkılıç, Z., Lee, C.B., Choi, H., Nar, I., Yavuz, N.K. and Burat, A.K., 2020. Tetra and octa substituted Zn(II) and Cu(II) phthalocyanines: Synthesis, characterization and investigation as hole-transporting materials for inverted type-perovskite solar cells. *Journal of Organometallic Chemistry*, 922, p.121419.
- [58] Torabi, N., Rahnamanic, A., Amrollahi, H., Mirjalili, F., Sadeghzade, M.A. and Behjat, A., 2017. Performance enhancement of perovskite solar cell by controlling deposition temperature of copper phthalocyanine as a dopant-free hole transporting layer. *Organic Electronics*, 48, pp.211-216.

- [59] Guo, J., Sun, M., Meng, X., Zhu, H., Ma, C., Hu, S., Shen, J., Wang, Q. and Gao, J., 2020. Impact of peripheral groups on novel asymmetric phthalocyanine-based hole-transporting materials for perovskite solar cells. *Dyes and Pigments*, 177, p.108301.
- [60] Lu, X. and Zhang, X.F., 2020. Phosphorous tetrabenzocorrolazine from its metal-free phthalocyanine precursor: Its facile synthesis, high fluorescence emission, efficient singlet oxygen formation, and promising hole transporting material. *Dyes and Pigments*, 179, p. 108421.
- [61] Şahin, S. and Açar, E., 2020. A3B type unsymmetrical and amphiphilic phthalocyanines: Synthesis, characterization, thermal stability and aggregation studies. *Spectrochimica Acta Part A: Molecular and Biomolecular Spectroscopy*, 227, p.117694.
- [62] Trapalis, C., Lidorikis, E. and Papageorgiou, D.G., 2020. Structural and energetic properties of P3HT and PCBM layers on the Ag (1 1 1) surface. *Computational and Theoretical Chemistry*, 1190, p.112997.
- [63] Xing, Z., Li, S.H., Hui, Y., Wu, B.S., Chen, Z.C., Yun, D.Q., Deng, L.L., Zhang, M.L., Mao, B.W., Xie, S.Y. and Huang, R.B., 2020. Star-like hexakis [di (ethoxycarbonyl) methano]-C60 with higher electron mobility: An unexpected electron extractor interfaced in photovoltaic perovskites. *Nano Energy*, 74, p.104859.
- [64] Sun, Y., Yang, C., Li, Q., Liu, K., Xue, X., Zhang, Y., Azam, M., Ren, K., Chen, Y., Wang, Z. and Qu, S., 2020. The route and optimization of charge transport in ternary organic solar cells based on O6T-4F and PC₇₁BM as acceptors. *Journal of Power Sources*, 449, p.227583.
- [65] Li, X., Xu, Z., Guo, X., Fan, Q., Zhang, M. and Li, Y., 2018. Synthesis and photovoltaic properties of a simple non-fused small molecule acceptor. *Organic Electronics*, 58, pp.133-138.
- [66] He, Y., Shao, M., Xiao, K., Smith, S.C. and Hong, K., 2013. High-performance polymer photovoltaics based on rationally designed fullerene acceptors. *Solar Energy Materials and Solar Cells*, 118, pp.171-178.
- [67] Xiao, B., Zhao, Y., Tang, A., Wang, H., Yang, J. and Zhou, E., 2017. PTB7-Th based organic solar cell with a high V_{OC} of 1.05 V by modulating the LUMO energy level of

- benzotriazole-containing non-fullerene acceptor. *Science Bulletin*, 62, pp.1275-1282.
- [68] Calderon-Cerquera, K., Parra, A., Madrid-Úsuga, D., Cabrera-Espinoza, A., Melo-Luna, C.A., Reina, J.H., Insuasty, B. and Ortiz, A., 1920. Synthesis, characterization and photophysics of novel BODIPY linked to dumbbell systems based on Fullerene [60] pyrrolidine and Fullerene [60] isoxazoline. *Dyes and Pigments*, 184, p.108752.
- [69] Lenes, M., Wetzelaer, G.J.A., Kooistra, F.B., Veenstra, S.C., Hummelen, J.C. and Blom, P.W., 2008. Fullerene bisadducts for enhanced open-circuit voltages and efficiencies in polymer solar cells. *Advanced Materials*, 20, pp.2116-2119.
- [70] Liedtke, M., Sperlich, A., Kraus, H., Baumann, A., Deibel, C., Wirix, M.J., Loos, J., Cardona, C.M. and Dyakonov, V., 2011. Triplet exciton generation in bulk-heterojunction solar cells based on endohedral fullerenes. *Journal of the American Chemical Society*, 133, pp.9088-9094.
- [71] Park, J., Ha, J.W., Kim, H.S. and Hwang, D.H., 2018. Synthesis and characterization of a donor-acceptor type copolymer containing ester-functionalized benzo [c][1, 2, 5] thiadiazole as an accepting building block for organic photovoltaics. *Thin Solid Films*, 663, pp.56-61.
- [72] Wadsworth, A., Moser, M., Marks, A., Little, M.S., Gasparini, N., Brabec, C.J., Baran, D. and McCulloch, I., 2019. Critical review of the molecular design progress in non-fullerene electron acceptors towards commercially viable organic solar cells. *Chemical Society Reviews*, 48, pp.1596-1625.
- [73] Yang, C., Zhang, S., Ren, J., Gao, M., Bi, P., Ye, L. and Hou, J., 2020. Molecular design of a non-fullerene acceptor enables a P3HT-based organic solar cell with 9.46% efficiency. *Energy & Environmental Science*, 13, pp.2864-2869.
- [74] Zhu, C., Yuan, J., Cai, F., Meng, L., Zhang, H., Chen, H., Li, J., Qiu, B., Peng, H., Chen, S. and Hu, Y., 2020. Tuning the electron-deficient core of a non-fullerene acceptor to achieve over 17% efficiency in a single-junction organic solar cell. *Energy & Environmental Science*, 13, pp.2459-2466.
- [75] Speller, E.M., Clarke, A.J., Luke, J., Lee, H.K.H., Durrant, J.R., Li, N., Wang, T., Wong,

- H.C., Kim, J.S., Tsoi, W.C. and Li, Z., 2019. From fullerene acceptors to non-fullerene acceptors: prospects and challenges in the stability of organic solar cells. *Journal of Materials Chemistry A*, 7, pp.23361-23377.
- [76] Pascual-San-José, E., Rodríguez-Martínez, X., Adel-Abdelaleim, R., Stella, M., Martínez-Ferrero, E. and Campoy-Quiles, M., 2019. Correction: Blade coated P3HT: non-fullerene acceptor solar cells: a high-throughput parameter study with a focus on up-scalability. *Journal of Materials Chemistry A*, 7, pp.21523-21523.
- [77] Strohm, S., Machui, F., Langner, S., Kubis, P., Gasparini, N., Salvador, M., McCulloch, I., Egelhaaf, H.J. and Brabec, C.J., 2018. P3HT: non-fullerene acceptor based large area, semi-transparent PV modules with power conversion efficiencies of 5%, processed by industrially scalable methods. *Energy & Environmental Science*, 11, pp.2225-2234.
- [78] Liu, Z., Zeng, D., Gao, X., Li, P., Zhang, Q. and Peng, X., 2019. Non-fullerene polymer acceptors based on perylene diimides in all-polymer solar cells. *Solar Energy Materials and Solar Cells*, 189, pp.103-117.
- [79] Lin, H. and Wang, Q., 2018. Non-fullerene small molecule electron acceptors for high-performance organic solar cells. *Journal of Energy Chemistry*, 27, pp.990-1016.
- [80] Al Kurdi, K., Gregory, S.A., Jhulki, S., Conte, M., Barlow, S., Yee, S.K. and Marder, S.R., 2020. Electron transport in a sequentially doped naphthalene diimide polymer. *Materials Advances*, 1, pp.1829-1834.
- [81] Schmidt, S.B., Biskup, T., Jiao, X., McNeill, C.R. and Sommer, M., 2019. Controlling intermolecular redox-doping of naphthalene diimides. *Journal of Materials Chemistry C*, 7, pp.4466-4474.
- [82] Gao, X., Gao, J., Xue, Z., Wang, H., Wang, J., Cheng, Y., Li, Z., Zhu, F., Huettner, S., Li, H. and Tao, Y., 2019. Benzodithiophene-modified terpolymer acceptors with reduced molecular planarity and crystallinity: improved performance and stability for all-polymer solar cells. *Journal of Materials Chemistry C*, 7, pp.10338-10351.
- [83] Sharma, S., Kolhe, N.B., Gupta, V., Bharti, V., Sharma, A., Datt, R., Chand, S. and Asha, S.K., 2016. Improved all-polymer solar cell performance of n-type naphthalene diimide-

- bithiophene P (NDI2OD-T2) copolymer by incorporation of perylene diimide as coacceptor. *Macromolecules*, 49, pp.8113-8125.
- [84] Wang, X., Huang, J., Niu, Z., Zhang, X., Sun, Y. and Zhan, C., 2014. Dimeric naphthalene diimide based small molecule acceptors: synthesis, characterization, and photovoltaic properties. *Tetrahedron*, 70, pp.4726-4731.
- [85] Morvillo, P., Bobeico, E., Esposito, S. and Diana, R., 2012. Effect of the active layer thickness on the device performance of polymer solar cells having [60] PCBM and [70] PCBM as electron acceptor. *Energy Procedia*, 31, pp.69-73.
- [86] Zang, Y., Xin, Q., Zhao, J. and Lin, J., 2018. Effect of active layer thickness on the performance of polymer solar cells based on a highly efficient donor material of PTB7-Th. *The Journal of Physical Chemistry C*, 122, pp.16532-16539.
- [87] Zhang, Y., Li, X., Dai, T., Xu, D., Xi, J. and Chen, X., 2019. Charge transport and extraction of PTB7: PC 71 BM organic solar cells: effect of film thickness and thermal-annealing. *RSC Advances*, 9, pp.24895-24903.
- [88] Zhang, L., Zhao, H., Lin, B., Yuan, J., Xu, X., Wu, J., Zhou, K., Guo, X., Zhang, M. and Ma, W., 2019. A blade-coated highly efficient thick active layer for non-fullerene organic solar cells. *Journal of Materials Chemistry A*, 7, pp.22265-22273.
- [89] R. Gupta, R.K., Garai, R., Afroz, M.A. and Iyer, P.K., 2020. Regulating active layer thickness and morphology for high performance hot-casted polymer solar cells. *Journal of Materials Chemistry C*, 8, pp.8191-8198.
- [90] Liu, X., Ye, L., Zhao, W., Zhang, S., Li, S., Su, G.M., Wang, C., Ade, H. and Hou, J., 2017. Morphology control enables thickness-insensitive efficient nonfullerene polymer solar cells. *Materials Chemistry Frontiers*, 1, pp.2057-2064.
- [91] Jo, J., Na, S.I., Kim, S.S., Lee, T.W., Chung, Y., Kang, S.J., Vak, D. and Kim, D.Y., 2009. Three-Dimensional Bulk Heterojunction Morphology for Achieving High Internal Quantum Efficiency in Polymer Solar Cells. *Advanced Functional Materials*, 19, pp.2398-2406.
- [92] Vongsaysy, U., Bassani, D.M., Servant, L., Pavageau, B., Wantz, G. and Aziz, H., 2014.

Formulation strategies for optimizing the morphology of polymeric bulk heterojunction organic solar cells: a brief review. *Journal of Photonics for Energy*, 4, p.040998.

- [93] Xu, B., Sai-Anand, G., Gopalan, A.I., Qiao, Q. and Kang, S.W., 2018. Improving photovoltaic properties of P3HT:IC₆₀BA through the incorporation of small molecules. *Polymers*, 10, pp. 1–10.
- [94] Du, X., Li, X., Lin, H., Zhou, L., Zheng, C. and Tao, S., 2019. High performance opaque and semi-transparent organic solar cells with good tolerance to film thickness realized by a unique solid additive. *Journal of Materials Chemistry A*, 7, pp.7437-7450.
- [95] Tran, H.N., Kim, D.H., Park, S. and Cho, S., 2018. The effect of various solvent additives on the power conversion efficiency of polymer-polymer solar cells. *Current Applied Physics*, 18, pp.534-540.
- [96] Amollo, T.A., Mola, G.T. and Nyamori, V.O., 2018. High-performance organic solar cells utilizing graphene oxide in the active and hole transport layers. *Solar Energy*, 171, pp.83-91.
- [97] Zhao, J., Song, D., Qiao, B., Xu, Z., Huang, D., Wang, M., Zhang, X., Li, Y., Zhu, Y. and Zhao, S., 2018. Regulating the polymer crystallize behavior via the synergistic additives towards high-performance bulk heterojunction solar cells. *Organic Electronics*, 58, pp.178-184.
- [98] Liu, X., Li, X., Wang, L., Fang, J. and Yang, C., 2020. Synergistic effects of the processing solvent and additive on the production of efficient all-polymer solar cells. *Nanoscale*, 12, pp.4945-4952.
- [99] Yang, Q., Li, X., Tang, H., Li, Y., Fu, Y., Li, Z. and Xie, Z., 2020. Ultrafast spectroscopic investigation of the effect of solvent additives on charge photogeneration and recombination dynamics in non-fullerene organic photovoltaic blends. *Journal of Materials Chemistry C*, 8, pp.6724-6733.
- [100] Xiao, T., Wang, J., Yang, S., Zhu, Y., Li, D., Wang, Z., Feng, S., Bu, L., Zhan, X. and Lu, G., 2020. Film-depth-dependent crystallinity for light transmission and charge transport in semitransparent organic solar cells. *Journal of Materials Chemistry A*, 8, pp.401-411.

- [101] Liu, C., Wang, K., Hu, X., Yang, Y., Hsu, C.H., Zhang, W., Xiao, S., Gong, X. and Cao, Y., 2013. Molecular weight effect on the efficiency of polymer solar cells. *ACS Applied Materials & Interfaces*, 5, pp.12163-12167.
- [102] Koch, F.P.V., Rivnay, J., Foster, S., Müller, C., Downing, J.M., Buchaca-Domingo, E., Westacott, P., Yu, L., Yuan, M., Baklar, M. and Fei, Z., 2013. The impact of molecular weight on microstructure and charge transport in semicrystalline polymer semiconductors—poly (3-hexylthiophene), a model study. *Progress in Polymer Science*, 38, pp.1978-1989.
- [103] Hoefler, S.F., Rath, T., Pastukhova, N., Pavlica, E., Scheunemann, D., Wilken, S., Kunert, B., Resel, R., Hobisch, M., Xiao, S. and Bratina, G., 2018. The effect of polymer molecular weight on the performance of PTB7-Th: O-IDTBR non-fullerene organic solar cells. *Journal of Materials Chemistry A*, 6, pp.9506-9516.
- [104] Spoltore, D., Vangerven, T., Verstappen, P., Piersimoni, F., Bertho, S., Vandewal, K., Van den Brande, N., Defour, M., Van Mele, B., De Sio, A. and Parisi, J., 2015. Effect of molecular weight on morphology and photovoltaic properties in P3HT:PCBM solar cells. *Organic Electronics*, 21, pp.160-170.
- [105] Ding, Z., Kettle, J., Horie, M., Chang, S.W., Smith, G.C., Shames, A.I. and Katz, E.A., 2016. Efficient solar cells are more stable: the impact of polymer molecular weight on performance of organic photovoltaics. *Journal of Materials Chemistry A*, 4, pp.7274-7280.
- [106] He, X., Cao, B., Hauger, T.C., Kang, M., Gusarov, S., Lubner, E.J. and Buriak, J.M., 2015. Donor–Acceptor Small Molecules for Organic Photovoltaics: Single-Atom Substitution (Se or S). *ACS Applied Materials & Interfaces*, 7, pp.8188-8199.
- [107] Yiu, A.T., Beaujuge, P.M., Lee, O.P., Woo, C.H., Toney, M.F. and Frechet, J.M., 2012. Side-chain tunability of furan-containing low-band-gap polymers provides control of structural order in efficient solar cells. *Journal of the American Chemical Society*, 134, pp.2180-2185.
- [108] Zhang, Y., Xu, X., Lu, J. and Zhang, S., 2019. Effect of polymer molecular weight on J51 based organic solar cells. *RSC Advances*, 9, pp.14657-14661.
- [109] Xiao, Z., Sun, K., Subbiah, J., Qin, T., Lu, S., Purushothaman, B., Jones, D.J., Holmes, A.B.

- and Wong, W.W., 2015. Effect of molecular weight on the properties and organic solar cell device performance of a donor–acceptor conjugated polymer. *Polymer Chemistry*, 6, pp.2312-2318.
- [110] Pirotte, G., Agarkar, S., Xu, B., Zhang, J., Lutsen, L., Vanderzande, D., Yan, H., Pollet, P., Reynolds, J.R., Maes, W. and Marder, S.R., 2017. Molecular weight tuning of low bandgap polymers by continuous flow chemistry: Increasing the applicability of PffBT4T for organic photovoltaics. *Journal of Materials Chemistry A*, 5, pp.18166-18175.
- [111] Gibson, G.L., Gao, D., Jahnke, A.A., Sun, J., Tilley, A.J. and Seferos, D.S., 2014. Molecular weight and end capping effects on the optoelectronic properties of structurally related ‘heavy atom’ donor–acceptor polymers. *Journal of Materials Chemistry A*, 2, pp.14468-14480.
- [112] Bagui, A., Gupta, V., Maurya, K.K. and Singh, S.P., 2016. High-performance non-fullerene acceptor derived from diathiafulvalene wings for solution-processed organic photovoltaics. *The Journal of Physical Chemistry C*, 120, pp.24615-24622.
- [113] Yi, Z., Ni, W., Zhang, Q., Li, M., Kan, B., Wan, X. and Chen, Y., 2014. Effect of thermal annealing on active layer morphology and performance for small molecule bulk heterojunction organic solar cells. *Journal of Materials Chemistry C*, 2, pp.7247-7255.
- [114] Milanovich, M., Sarkar, T., Popowski, Y., Low, J.Z., Campos, L.M., Kenig, S., Frey, G.L. and Amir, E., 2020. Enhancing P3HT/PCBM blend stability by thermal crosslinking using poly (3-hexylthiophene)-S, S-dioxide. *Journal of Materials Chemistry C*, 8, pp.7698–7707.
- [115] Liu, J., Zhu, X., Li, J., Shen, J. and Tu, G., 2016. Enhancing the thermal stability of the bulk-heterojunction photovoltaics based on P3HT/PCBM by incorporating diblock amphipathic P3HT–PEO at D/A interface. *RSC advances*, 6, pp.61934-61943.
- [116] Collins, B.A., Li, Z., Tumbleston, J.R., Gann, E., McNeill, C.R. and Ade, H., 2013. Absolute measurement of domain composition and nanoscale size distribution explains performance in PTB7:PC₇₁BM solar cells. *Advanced Energy Materials*, 3, pp.65-74.
- [117] Upama, M.B., Elumalai, N.K., Mahmud, M.A., Wright, M., Wang, D., Xu, C. and Uddin, A., 2018. Effect of annealing dependent blend morphology and dielectric properties on the

- performance and stability of non-fullerene organic solar cells. *Solar Energy Materials and Solar Cells*, 176, pp.109-118.
- [118] Bourque, A.J., Engmann, S., Fuster, A., Snyder, C.R., Richter, L.J., Geraghty, P.B. and Jones, D.J., 2019. Morphology of a thermally stable small molecule OPV blend comprising a liquid crystalline donor and fullerene acceptor. *Journal of Materials Chemistry A*, 7, pp.16458-16471.
- [119] Más-Montoya, M., Li, J., Wienk, M.M., Meskers, S.C. and Janssen, R.A., 2018. Effects of fluorination and thermal annealing on charge recombination processes in polymer bulk-heterojunction solar cells. *Journal of Materials Chemistry A*, 6, pp.19520-19531.
- [120] Weber, S., Hofinger, J., Rath, T., Reinfelds, M., Pfeifer, D., Borisov, S.M., Fürk, P., Amenitsch, H., Scharber, M.C. and Trimmel, G., 2020. Comparison of fluorene, silafluorene and carbazole as linkers in perylene monoimide based non-fullerene acceptors. *Materials Advances*, 1, pp.2095-2106.
- [121] Duan, L., Zhang, Y., Yi, H., Haque, F., Xu, C., Wang, S. and Uddin, A., 2020. Thermal annealing dependent dielectric properties and energetic disorder in PffBT4T-2OD based organic solar cells. *Materials Science in Semiconductor Processing*, 105, p.104750.
- [122] Cheacharoen, R., Mateker, W.R., Zhang, Q., Kan, B., Sarkisian, D., Liu, X., Love, J.A., Wan, X., Chen, Y., Nguyen, T.Q. and Bazan, G.C., 2017. Assessing the stability of high performance solution processed small molecule solar cells. *Solar Energy Materials and Solar Cells*, 161, pp.368-376.
- [123] Mateker, W.R., Heumueller, T., Cheacharoen, R., Sachs-Quintana, I.T., McGehee, M.D., Warnan, J., Beaujuge, P.M., Liu, X. and Bazan, G.C., 2015. Molecular packing and arrangement govern the photo-oxidative stability of organic photovoltaic materials. *Chemistry of Materials*, 27, pp.6345-6353.
- [124] Mateker, W.R., Sachs-Quintana, I.T., Burkhard, G.F., Cheacharoen, R. and McGehee, M.D., 2015. Minimal long-term intrinsic degradation observed in a polymer solar cell illuminated in an oxygen-free environment. *Chemistry of Materials*, 27, pp.404-407.
- [125] Sachs-Quintana, I.T., Heumüller, T., Mateker, W.R., Orozco, D.E., Cheacharoen, R.,

- Sweetnam, S., Brabec, C.J. and McGehee, M.D., 2014. Electron Barrier Formation at the Organic-Back Contact Interface is the First Step in Thermal Degradation of Polymer Solar Cells. *Advanced Functional Materials*, 24, pp.3978-3985.
- [126] Fraga Dominguez, I., Topham, P.D., Bussiere, P.O., Bégué, D. and Rivaton, A., 2015. Unravelling the photodegradation mechanisms of a low bandgap polymer by combining experimental and modeling approaches. *The Journal of Physical Chemistry C*, 119, pp.2166-2176.
- [127] Yang, T., Ma, R., Cheng, H., Xiao, Y., Luo, Z., Chen, Y., Luo, S., Liu, T., Lu, X. and Yan, H., 2020. A compatible polymer acceptor enables efficient and stable organic solar cells as a solid additive. *Journal of Materials Chemistry A*, 8, pp.17706-17712.



Chapter 3

Experimental: Characterization techniques and mechanisms used for synthesis

3.1. Characterization techniques and purification methods

3.1.1. Purification methods

3.1.1.1. Thin layer chromatography (TLC)

Silica gel coated plates (Merck (Pty) Ltd., Johannesburg, South Africa) were used for thin layer chromatography profiling. The spot on the silica gel coated plates were viewed using ultra-violet lamp (254 nm and 366 nm) followed by immersing the plates into vanillin (Merck (Pty) Ltd.)/sulphuric acid (Merck (Pty) Ltd.) and lastly heating with a heat gun. Thin layer chromatography was used to determine the solvent system to be used to perform column chromatography.

3.1.1.2. Column chromatography

To perform column chromatography for separation of product from impurities, wet packing method was used. Silica gel 60 Å (230–400 mesh, Merck (Pty) Ltd.) was dispersed in the chosen solvent system, then transferred to a glass column (2-3 cm diameter). After transferring silica gel, it was allowed to settle on its own before the sample was transferred into the column. Column chromatography was used to purify synthesized core materials.

3.1.1.3. Liquid-liquid extraction

After performing Schiff base condensation, methanol was removed and the product was dissolved in dichloromethane or chloroform. After dissolving the product, it was washed with water to remove the reagent used in excess.

3.1.2. Characterization techniques

3.1.2.1. Nuclear magnetic resonance spectroscopy (NMR)

NMR is a technique that is mostly used for structural determination of organic compounds. When organic compounds are exposed to a strong magnetic field, the nuclei of atoms start to behave like small magnets. The nuclei resonance frequency is measured and changed into the NMR spectrum that provide information about the structure. NMR can be performed either in a liquid or solid form. During this work, liquid state NMR was performed to confirm the structure of synthesized organic compounds. Only ^1H -NMR and ^{13}C NMR were performed in this study. The positions of the peaks were referenced using deuterated chloroform. It was used for structural analysis of the synthesized organic materials. For NMR studies, Bruker 400 MHz Avance III HD Nanobay spectrometer, Karlsruhe, Germany was used.

3.1.2.2. Fourier-transform infrared spectroscopy (FTIR)

FTIR is a characterization technique that is used to determine functional groups present in the organic molecule. This technique can be used to measure the spectrum of transmittance of either gas, liquid or solid. In this study, characterization of the synthesized materials was performed using liquid-based analysis for some samples and solid based method for other samples. For liquid-based method, the attenuated total reflectance was used. The samples were dissolved in chlorobenzene (Merck (Pty) Ltd.) and before any measurement of the samples were recorded, chlorobenzene was used to run background. As for solid based method, the samples were mixed with potassium bromide pellet using mortar and pestle and before any measurement of the samples were recorded, potassium bromide was used to run background. FTIR analysis were performed in the wavenumber range of 4000 to 450 cm^{-1} and the scan was set to 10 times. After the scan was complete, the baseline was corrected by subtracting the background spectrum of chlorobenzene or potassium bromide depending on the method used. FTIR (Spectrum-100 FTIR spectrometer from PerkinElmer (Pty) Ltd., Midrand, South Africa) was used to identify the functional groups present in the synthesized monomers and polymers.

3.1.2.3. Mass spectroscopy

Quadrupole time-of-flight mass spectrometer (Waters Synapt G2 Quadrupole time-of-flight (QTOF) mass spectrometer (MS) connected to a Waters Acquity ultra-performance liquid chromatograph (UPLC) (Waters, Milford, MA, USA)) was used for direct infusion high-resolution mass spectrometer analysis. Electrospray ionization was used in positive mode with a cone voltage of 15 V, desolvation temperature of 275 °C, desolvation gas at 650 L/h, and the rest of the MS settings optimized for best resolution and sensitivity. Data were acquired by scanning from m/z 150 to 1500 m/z in resolution mode. Leucine enkaphalin was used as lock mass for accurate mass determination and the instrument was calibrated with sodium formate. A 2µL injection volume was used to introduce the sample into a flow stream consisting of 40% of 0.1% formic acid in water (solvent A) and 60% acetonitrile containing 0.1% formic acid as solvent B. This solvent conveyed the samples to the high-definition Quadrupole time-of-flight mass spectrometer which due to its high mass resolution, allows accurate mass elemental composition to be determined. Mass spectroscopy was used to determine molecular weight of synthesized monomers.

3.1.2.4. Size exclusion chromatography

Size exclusion chromatography is one of the characterization techniques for polymers. It is used to determine their polydispersity, molar mass distribution and molar mass. The separation of the polymers is based on the effective molecular size and the extent they interact with the stationary phase. A size exclusion chromatography instrument equipped with a Waters 717plus Autosampler, Waters 600E system controller and a Waters 610 fluid unit were used to perform size exclusion chromatography analyses. A Waters 2414 differential refractometer was used for detection. Two PLgel 5 mm Mixed-C columns (300×8 mm i.d.) and a PLgel 5 mm guard column were used. The oven temperature was maintained at 30 °C and 100 mL of 2 mg/mL sample in THF was injected into the column set. THF (HPLC grade, BHT stabilised) was used as the eluent for the analyses at a flow rate of 1 mL/min. Narrow polystyrene standards with molar masses ranging from 800 to 2×10^6 g mol⁻¹ were used to calibrate the instrument. Data obtained from size exclusion is reported as polystyrene equivalents. Agilent 1260 Infinity series HPLC instrument from Agilent Technologies, Waldbronn, Germany, was used to determine polydispersity and molecular weight of the polymers.

3.1.2.5. Thermal gravimetric analysis

Thermal gravimetric analysis (TGA) is a characterization technique that is used to determine the changes in the composition of materials by monitoring the weight loss as the temperature increases. The weight loss of compounds can be due to oxidation, decomposition or loss of moisture content. Prior to analyses, 5 mg of the sample was placed in the crucible supported on an analytical balance. Thermal gravimetric analysis was performed in the temperature range of 50 to 650 °C under nitrogen atmosphere using a flow rate of 20 mL/min at the heating rate of 10°Cmin⁻¹. The thermal analyzer Perkin Elmer STA 6000 instrument (PerkinElmer (Pty) Ltd.) was used to study thermal stability properties of monomers and polymers.

3.1.2.6. Transmission electron microscopy

Transmission electron microscopy (TEM) is a technique mostly used for structural features of nanoscale samples. It uses electron beam which is focused by the condenser lenses directly to the samples. The beam of electrons passes through the samples to the screen which reveal the information of the sample in the form of images. For sample preparation, the samples were dissolved in chlorobenzene and drop coated on the copper grid. And lastly, the grid was placed on the path of the electron beam inside the instrument for analysis. TEM analysis was performed using FEI Tecnai T20 TEM from FEI company, Hillsboro, OR, USA, to study the morphological properties of polymers.

3.1.2.7. Ultra-Violet visible spectroscopy (UV-Vis)

Ultra-Violet visible spectroscopy is one of the mostly used analytical technique in the research field. During the use of UV-Vis, light is allowed to pass through the sample at a certain wavelength in the ultraviolet or visible region of the spectrum. All the incident light will not pass through the sample if some of the light is absorbed within the sample. The UV-Vis can be used to quantitatively determine the concentration of the sample and qualitatively to identify a compound by matching the absorbance with the published data. In this study, the synthesized materials were dissolved in different solvents (chlorobenzene, chloroform and toluene) for UV-Vis analysis. Some of the synthesized materials were analysed as thin films on indium tin oxide (ITO) and others in liquid form. Nicolet Evolution 100 from Thermo Electron Corporation, Altrincham, UK, was used to determine optical band-gaps of the polymers.

3.1.2.8. Scanning electron microscope (SEM)

SEM is an analytical technique that uses a focused high energy electron beam to generate an array of signals at the surface of solid sample. These signals are derived from the interaction between the electrons and sample. They reveal an important information about the sample such as the chemical composition, external morphology, and crystalline structure. The samples can be analyzed with SEM in powder form or as films. In this work, SEM studies were done as thin films to investigate morphological properties of the synthesized polymers. SEM analysis was done using Tescan MIRA3 RISE SEM from Tescan, Brno, Czech Republic and elemental analysis was done using FEI NovaNano SEM from FEI company, hillsboro, OR, USA.

3.1.2.9. X-ray diffraction (XRD)

XRD is an analytical instrument that is used to study the crystallographic structure of a sample. XRD works by directing incident X-rays to a sample. Scattered angles and intensities of X-rays leave the sample while containing structural information of the sample are measured. XRD is mostly used to identify crystalline phases and orientation, determine structural structure such as grain size, phase composition and lattice parameters, and determine the arrangement of atoms. It was used to confirm the findings from PL studies by investigating crystallinity of the polymers. XRD analysis were performed using D8-Advanced diffractometer from Bruker AXS, Billerica, MA, USA.

3.1.2.10. Cyclic voltammetry (CV)

CV is an electrochemical technique that utilizes a change in applied potential of a working electrode where the current is being controlled. This is done in both forward and reverse direction while observing the change in current. The set up consist of an electrolyte with three electrodes immersed in the electrolyte. The working electrode use in this study is indium tin oxide (ITO, 14–16 Ω /square resistance, Oscilla, Sheffield, UK), counter electrode is platinum wire (Goodfellow Cambridge Ltd., Huntingdon, UK) and the reference electrode used is silver-silver chloride (Ag/AgCl, from BASi® in West Lafayette, IN, USA). In this study, cyclic voltammetry was used to determine the energy levels of the polymers synthesized. The cyclic voltammograms were obtained using CHI700E-potentiostat (CH instruments, Inc, Bee Cave, TX, USA).

3.1.2.11. Electrochemical impedance spectroscopy (EIS)

EIS is an electrochemical method that is used to investigate the charge transfer and it measures the resistance of the charge transfer between the electrolyte and electrode interface. This method has the same setup of electrochemical cell as CV. In this study, EIS was used to determine the conductivity of the synthesized polymers using certain or different values of bias potentials. EIS measurements were obtained using CHI700E-potentiostat (CH instruments, Inc, Bee Cave, TX, USA).

3.1.2.12. Photoluminescence (PL)

This technique is based on the measurements of the energy emitted when electrons are from the excited state move back to the ground state. It is mostly used in photovoltaic cells to study electron transfer from donor material to the acceptor material by observing the reduction of emission intensity (quenching effect). PL measurements were obtained using NanoLog from Horiba Jobin Yvon, Edison, NJ, USA.

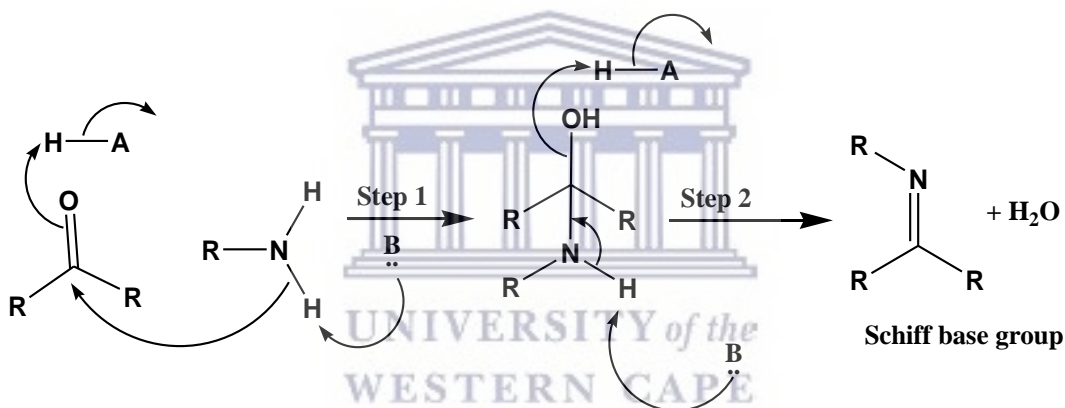
3.2. Fabrication of photovoltaic cells

During fabrication of the photovoltaic cells, the ITO substrate was washed with 1% hellmanex solution in hot water, isopropanol and acetone for 5 min in each. The ITO substrate was dried using nitrogen gas. PEDOT:PSS was sonicated and filtered using 0.45 μm filters. It was spun coated for 30 sec at the rate of 4000 rpm using the amount of 40 μL . The thin film was wiped at the cathode using cotton bud and baked at 150 $^{\circ}\text{C}$ for 5 min. The donor and acceptor materials were blended at 60 $^{\circ}\text{C}$ for overnight. The solution was spun coated onto the PEDOT:PSS coated ITO at the spin rate of 2000 rpm for 30 sec. The film was annealed at 100 $^{\circ}\text{C}$ for 5 min. The final layer of aluminium was deposited thermally at the pressure of 10^{-5} mbar. While for other devices, silver paste was coated using micro-pipette tip. The photovoltaic parameters were determined from the current as a function of voltage obtained under light illumination of AM 1.5G, 100 mW cm^{-2} supplied by a solar simulator from Sciencetech Inc., London, ON, Canada, using a source meter (X200 Source Meter Unit from Ossila, Sheffield, UK).

3.3. Mechanism of the synthetic methods used in this study

3.3.1. Schiff base reaction

Schiff base reaction is named after Prof. Hugo Schiff and are identified by the secondary aldimines or ketimines functional group. They are synthesized by reacting primary amines and carbonyl groups. Firstly, an amine nitrogen act as a nucleophile by attacking the electron poor carbon of the carbonyl of either aldehydes or ketones. In the following step, the nitrogen losses a proton and the pair of electrons from the N–H bond force oxygen to de-attach from the carbon resulting in C=N functional group (an imine) and water as by-product [1–4]. The schematic of the mechanism is shown in Scheme 3.1.



Scheme 3.1: Shows Schiff base mechanism.

3.3.2. Stille coupling reaction

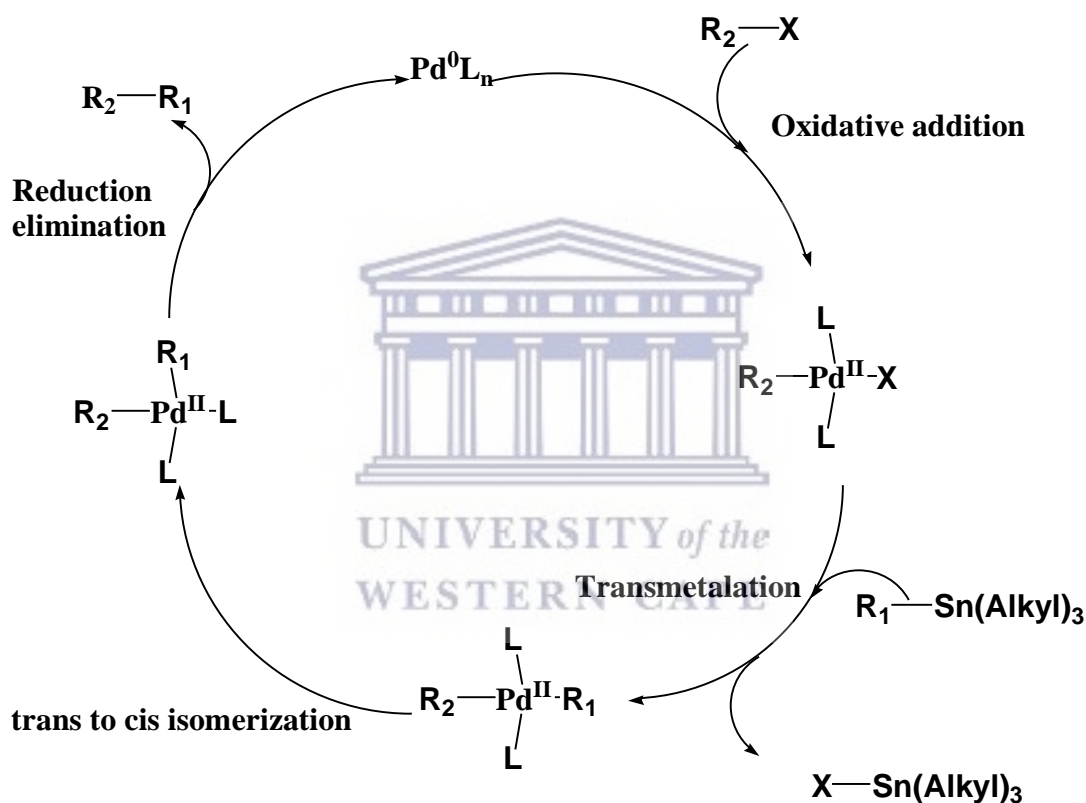
It is a chemical reaction that involves the use of organotin compounds and halogenated compounds to form carbon–carbon bond in the presence of palladium (Pd) based catalyst. The Stille coupling reaction is shown in Scheme 3.2.



Scheme 3.2: Stille coupling reaction

R₁ and R₂ can be either alkenyl, benzyl, allyl, aryl or acyl. X represent the halogens (bromine, chlorine and iodine). The reaction mechanism of this method is given in Scheme 3.3. In details, the first step is the oxidative addition of R₂–X to the palladium-based catalyst (Pd⁰) resulting in an

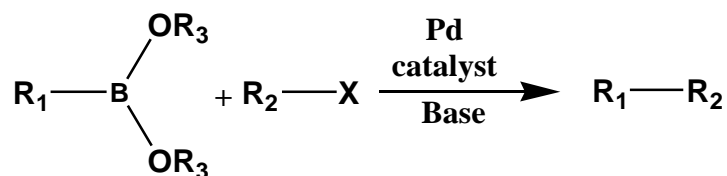
intermediate Pd^{II} with 16-electron transition state. The second step is called trans-metalation. During this step, organotin compound is used as trans coupling reagent. The organotin compound together with R_1 will form a four membered ring with the Pd^{II} intermediate and X forming transition state of 18-electron. Then, organotin will leave with the X. This results in the intermediate of Pd^{II} bonded to R_1 and R_2 . Finally, the R_1 and R_2 will isomerize into cis-conformation before undergoing reductive elimination [5–7]. These steps are shown in scheme 3.3.



Scheme 3.3: Stille coupling mechanism.

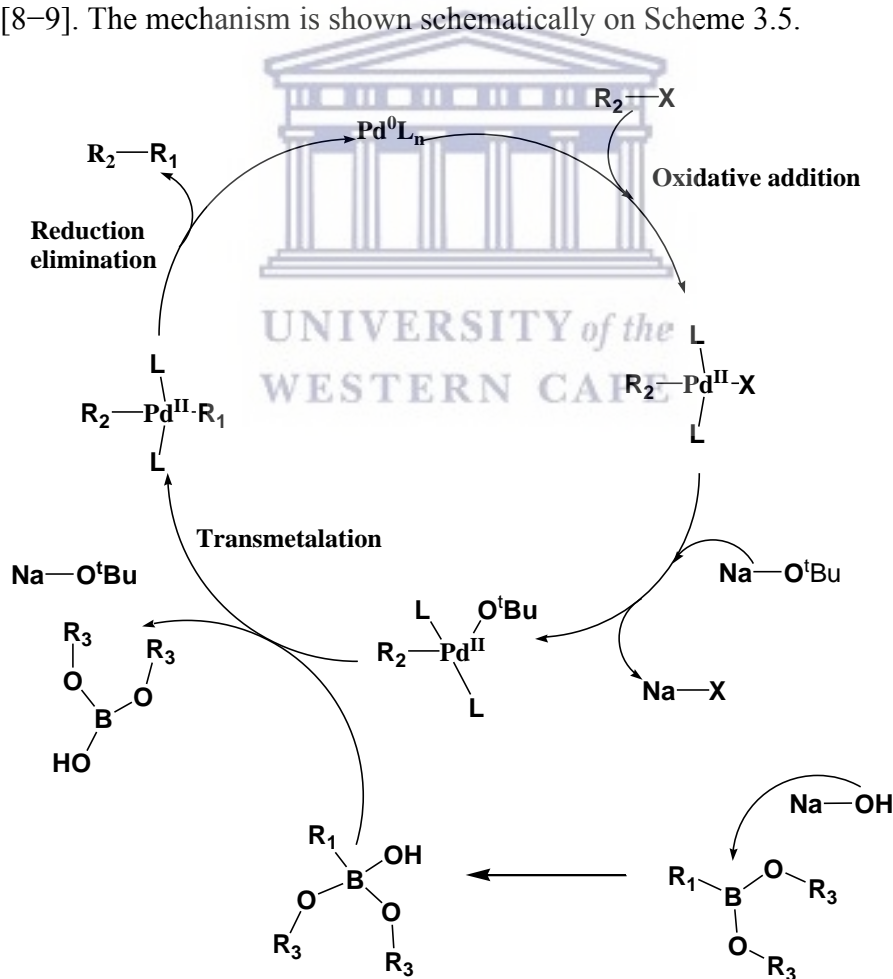
3.3.3. Suzuki coupling reaction

This method is the reaction between the boronic acid and an organohalide in the presence of Pd based catalyst and base to form carbon-carbon bond. The difference between Suzuki coupling and Stille coupling is that, during Suzuki coupling, boronic acid requires to be activated by base while in Stille coupling, organotin is used and it does not require any activation. The reaction of Suzuki coupling is shown in Scheme 3.4



Scheme 3.4: Suzuki coupling reaction.

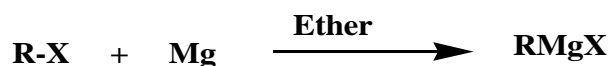
where R_3 can be either H or an alkyl group. R_1 and R_2 can be either aryl, alkyl or alkenyl. Base like sodium hydroxide can be used. The mechanism starts with the oxidative addition of organohalide to Pd^0 catalyst to form Pd^{II} complex. In the second step, base replaces the halide from the Pd^{II} complex and base also adds to the boronic acid to form a reagent that makes R_1 a nucleophile. In the third step (transmetalation), R_1 attacks where the halide has been replaced on the Pd^{II} complex. The reductive elimination step then regenerates the Pd catalyst and gives the final product [8–9]. The mechanism is shown schematically on Scheme 3.5.



Scheme 3.5: Suzuki coupling reaction mechanism.

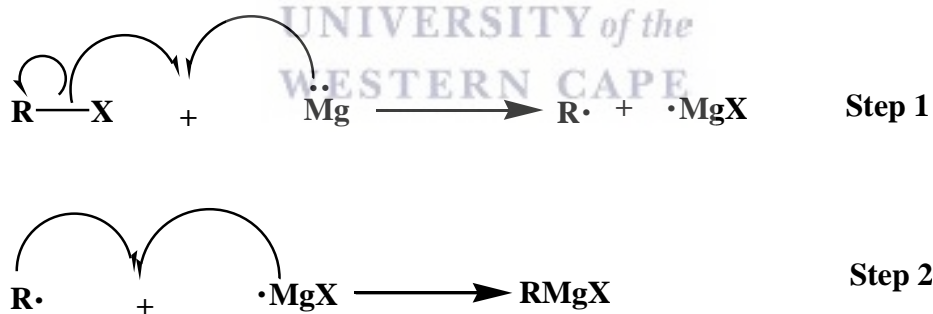
3.3.4. Grignard reaction

This reaction method uses magnesium (Mg) which is defined by the formula RMgX, where R can be an aryl or alkyl group and X is a halogen. This method is used to form new carbon-carbon bond by joining two aryl or alkyl groups. Grignard reaction takes place well in ether as a solvent and requires to be kept in dry conditions since the reaction can react with moisture. The Grignard reaction is shown in Scheme 3.6.



Scheme 3.6: Grignard reaction method.

The Grignard reaction mechanism takes place by the free radical reaction. In this mechanism, radical chain or chain generation are not involved. The electrons move singly during the formation of the product and the mechanism takes place in two steps. First step, an electron from the Mg is transferred to the RX resulting in the formation of free radicals R and MgX. In the second step, MgX couples with R to form Grignard reagent [10,11]. This mechanism is shown schematically in Scheme 3.7.

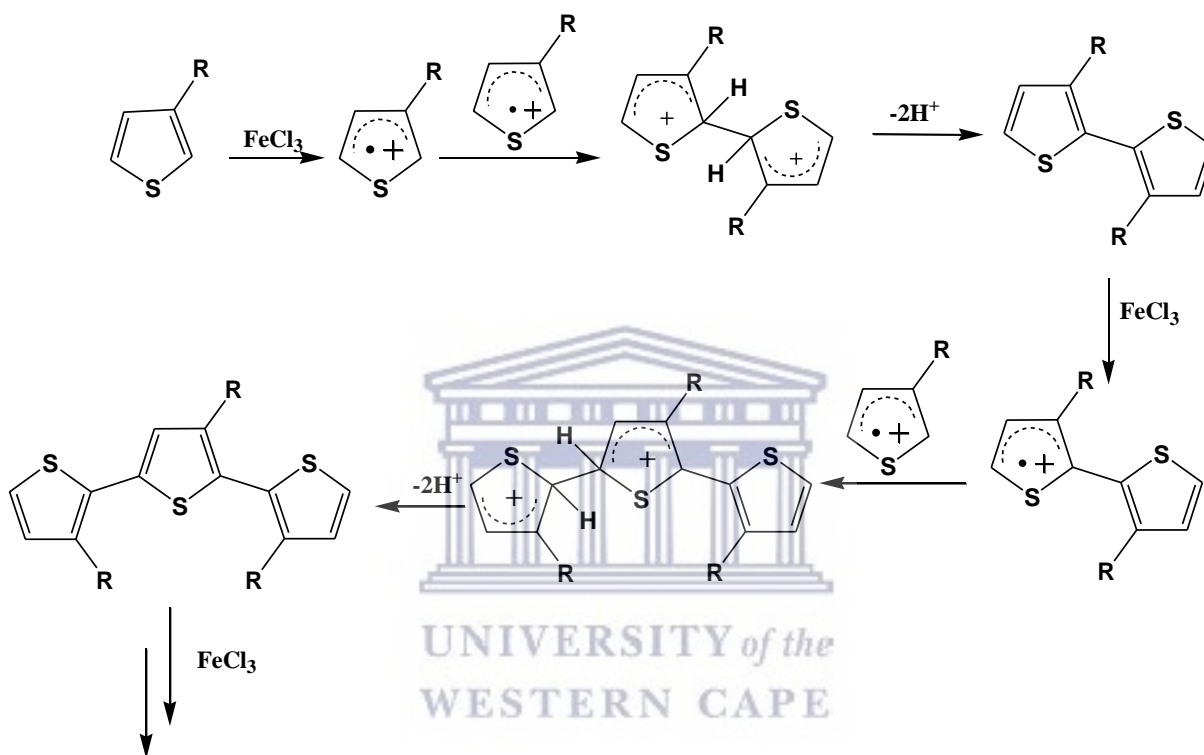


Scheme 3.7: Grignard reaction mechanism.

3.3.5. Chemical oxidation polymerization

This method is used for synthesis of polymers from aromatic starting materials such as phenols, thiophene, pyrrole and diphenyl sulphide in the presence of inorganic oxidizing agent [12]. During chemical oxidation method, cation radicals are generated in the aromatic starting material to initiate polymerization. Scheme 3.8 shows the suggested mechanism of chemical oxidation polymerization using thiophene based starting material and FeCl₃ as an oxidizing agent. The first

step is the cation radical formation and the reduction of the oxidant for Fe^{III} to Fe^{II} . During propagation step, there is a dimerization process of the two formed cation radicals, two protons elimination and resulting to dimer re-aromatization. The formed dimer is oxidized to the corresponding cation radical and reacts with cation radical to form a trimer. The process continues in this manner until a polymer is formed [13–15].



Scheme 3.8: Mechanism of chemical oxidation polymerization.

References

- [1] Mahato, S., Meheta, N., Kotakonda, M., Joshi, M., Shit, M., Choudhury, A.R. and Biswas, B., 2021. Synthesis, structure, polyphenol oxidase mimicking and bactericidal activity of a zinc-schiff base complex. *Polyhedron*, 194, p.114933.
- [2] Abu-Dief, A.M., El-Metwaly, N.M., Alzahrani, S.O., Bawazeer, A.M., Shaaban, S. and Adam, M.S.S., 2021. Targeting ctDNA binding and elaborated in-vitro assessments concerning novel Schiff base complexes: Synthesis, characterization, DFT and detailed in-silico confirmation. *Journal of Molecular Liquids*, 322, p.114977.
- [3] Lima, L., Murakami, H., Gaebler, D.J., Silva, W.E., Belian, M.F., Lira, E.C. and Crans, D.C., 2021. Acute Toxicity Evaluation of Non-Innocent Oxidovanadium (V) Schiff Base Complex. *Inorganics*, 9, p.42.
- [4] Wei, Z., Zhang, Y., Ma, X. and Wang, W., 2021. Insight into the high-efficiency adsorption of pyrene by Schiff base porous polymers: Modelling and mechanism. *Polymer*, 220, p.123576.
- [5] Heravi, M.M., Hashemi, E. and Azimian, F., 2014. Recent developments of the Stille reaction as a revolutionized method in total synthesis. *Tetrahedron*, 70, pp.7-21.
- [6] Chang, Y.T., Liu, L.J., Peng, W.S., Lin, L.T., Chan, Y.T. and Tsai, F.Y., 2021. Stille coupling for the synthesis of isoflavones by a reusable palladium catalyst in water. *Journal of the Chinese Chemical Society*, 68, pp.469-475.
- [7] Cordovilla, C., Bartolomé, C., Martínez-Ilarduya, J.M. and Espinet, P., 2015. The Stille reaction, 38 years later. *Acs Catalysis*, 5, pp.3040-3053.
- [8] Suzuki, A., 2004. Organoborane coupling reactions (Suzuki coupling). *Proceedings of the Japan Academy, Series B*, 80, pp.359-371.
- [9] Biswas, B. and Kuls, G., 2016. Solving the Riddle-the Mechanism of Suzuki Cross Coupling: A Review. *Asian Journal of Advanced Basic Sciences*, 4, pp.131-140.
- [10] Rogers, H.R., Hill, C.L., Fujiwara, Y., Rogers, R.J., Mitchell, H.L. and Whitesides, G.M., 1980. Mechanism of formation of Grignard reagents. Kinetics of reaction of alkyl halides

- in diethyl ether with magnesium. *Journal of the American Chemical Society*, 102, pp.217-226.
- [11] Kobayashi, Y., Takashima, Y., Motoyama, Y., Isogawa, Y., Katagiri, K., Tsuboi, A. and Ogawa, N., 2021. α -and γ -Regiocontrol and Enantiospecificity in the Copper-catalyzed Substitution Reaction of Propargylic Phosphates with Grignard Reagents. *Chemistry–A European Journal*, 27, pp.3779-3785.
- [12] Higashimura, H. and Kobayashi, S., 2002. Oxidative polymerization. *Encyclopedia of Polymer Science and Technology*, pp.1-37.
- [13] Liu, S., Du, C., Zhang, Y., Xie, M., Chen, J. and Wan, L., 2021. Oxidative-polymerization and deoxygenation of mixed phenols to faradaic-oxygen modified mesoporous carbon and its supercapacitive performances. *Journal of Energy Storage*, 34, p.102198.
- [14] Fukumoto, H., Omori, Y. and Yamamoto, T., 2013. Effects of solvent and temperature on regioregularity of poly(3-hexylthiophene-2,5-diyl) prepared by chemical oxidative polymerization. *Polymer Journal*, 45, pp.462-465.
- [15] Abu-Thabit, N.Y., 2016. Chemical oxidative polymerization of polyaniline: A practical approach for preparation of smart conductive textiles. *Journal of Chemical Education*, 93, pp.1606-1611.

Chapter 4

Polypropylenimine Tetra(thiophene)-co-Poly(3-hexylthiophene-2,5-diyl): Synthesis, characterization, electrochemical and photovoltaic studies

Abstract

In recent years, new conjugated polymers have been developed with improved properties using existing synthetic methods. In this work, we report synthesis of polypropylenimine tetra(thiophene)-co-poly(3-hexylthiophene-2,5-diyl) (PPI-Th-co-P3HT) using chemical oxidation co-polymerization method. The polymers (PPI-Th-co-P3HT) was synthesized using different molar ratios of polypropylenimine tetra(thiophene) (PPI-Th) and 3-hexylthiophene (3HT). The molar ratios used were 1 PPI-Th:40 3HT, 1 PPI-Th:60 3HT and 1 PPI-Th:80 3HT. The synthesized PPI-Th-co-P3HT was characterized using nuclear magnetic resonance spectroscopy (NMR), Fourier-transform infrared spectroscopy (FTIR) spectroscopy, ultraviolet-visible (UV-Vis) spectroscopy, transmission electron microscopy (TEM), scanning scanning microscopy (SEM), cyclic voltammetry (CV), thermal gravimetric analysis (TGA) and electrochemical impedance spectroscopy (EIS). The spectroscopic, microscopic and electrochemical properties of PPI-Th-co-P3HT changes as the molar ratios change. These changes are attributed to highly possible difference in molecular weight achieved as the molar ratios change. Organic photovoltaic cells (OPVs) of PPI-Th-co-P3HT synthesized using different molar ratios were fabricated. Maximum performance conversion efficiency was achieved for PPI-Th-co-P3HT synthesized using molar ratio of 1 PPI-Th:40 3HT due its narrow optical band gap, high crystallinity and small distance between the lowest unoccupied molecular orbital (LUMO) of PPI-Th-co-P3HT and [6,6]-phenyl-C₆₁-butyric acid methyl ester (PC₆₁BM).

4.1. Introduction

Conjugated polymers have attracted a lot of research interest in the research areas of Physics and Chemistry because of their properties can be beneficial for optoelectronics and sensors [1–4]. Interestingly, the properties of polymers can be easily modified by introduction of different functional groups on the polymer chain. It was discovered that modification of a polymer chain with alkyl groups turn to improve the solubility [5]. The presence of alkyl group also provides control of crystallinity and molecular packing behaviour which influence the charge carrier mobility [6,7]. It also permits control over intermolecular aggregation and morphology of the thin film while sustaining properties such as electrochemical and optical [8,9]. Some studies have been reported on the use of halogens such as fluorine to modify polymers [10–11]. The role of fluorine on the properties of the polymers have been well studied [12] and showed to narrow the optical band gap [13,14]. Additionally, the internal noncovalent interaction (F–S and F–H) might be advantageous to develop the intermolecular packing leading to improvement in morphology and charge transportation properties [15,16].

Poly(3-hexylthiophene-2,5-diyl) (P3HT) and its derivatives are a class of conjugated polymers used in different research field such as energy storage [17], organic light-emitting diodes [18], organic transistors [19] and organic photovoltaic cells [20]. To date, there are several methods that have been used to synthesize P3HT namely: oxidation polymerization [21], electrochemical method [22] and Grignard reaction [23]. Oxidation polymerization is the most preferred synthetic method for P3HT by researchers because of its mild reaction conditions. In most cases, iron (III) chloride (FeCl_3) is used as oxidants during oxidation polymerization [21]. It was suggested that during synthesis of P3HT using oxidation polymerization, the molar ratio of the 3-hexylthiophene and FeCl_3 should be 1:4 in chloroform [24]. The percentage yield of P3HT varies according to the change in FeCl_3 and 3-hexylthiophene molar ratio. High percentage yield is obtained when the molar ratio of 1 3-hexylthiophene: 4 FeCl_3 .

Oxidation polymerization is an easy and economical method for large production of P3HT because it does not need removal of by-products [25]. But the properties of P3HT such as molecular weight and regioregularity degree can affect the formation of thin films [24]. These properties depend strongly on the synthetic conditions of the oxidation polymerization method. Studies showed that

slow addition of oxidant at low temperature results to low molecular weight and regioregularity of up to 80% [26], while a fast addition of oxidant results to broad distribution of the molecular weight [27]. Understanding how synthesis conditions affects the properties of polymers in general, can help in improving the performance of polymers in various applications.

Here we report our findings on the synthesis of novel PPI-Th-co-P3HT synthesized using chemical oxidation polymerization method and different molar ratios of PPI-Th and 3-hexylthiophene. The effect of molar ratios of the optical, thermal, morphological and electrochemical properties were investigated. The LUMO energy levels of the synthesized PPI-Th-co-P3HT using different molar ratios were compared with those of PC₆₁BM. These was done to understand electron dynamics at the interface of PPI-Th-co-P3HT:PC₆₁BM and the effect of molar ratio on the performance of OPVs. Maximum PCE of OPVs was achieved when the molar ratio of 1 PPI-Th: 40 3HT was used. The performance was attributed to smaller LUMO offset and narrow optical band gap.

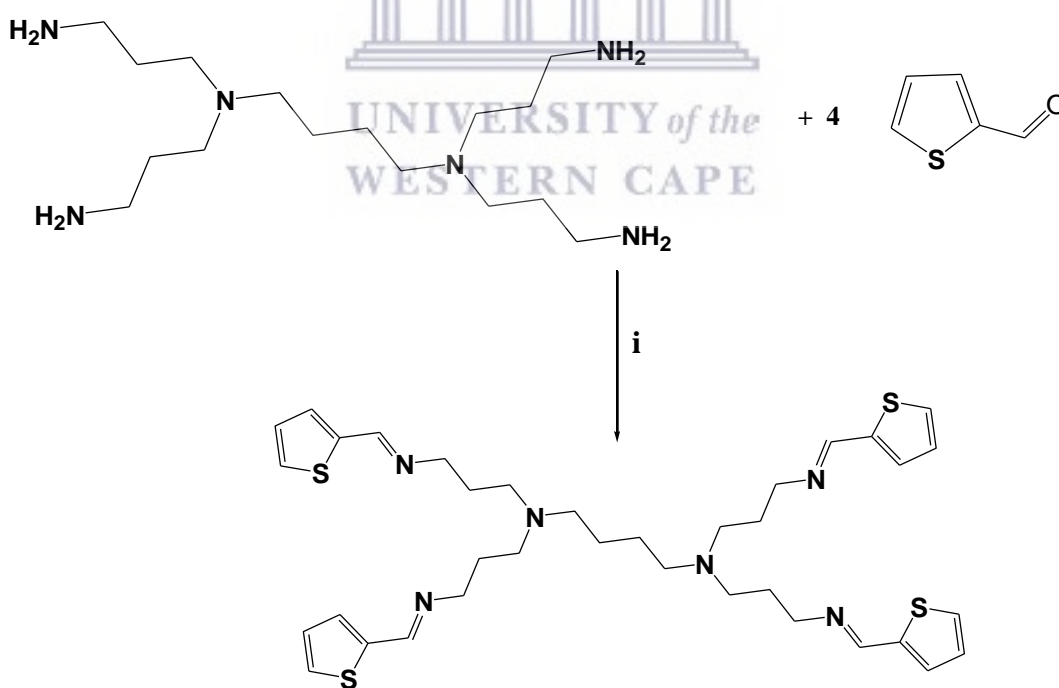
4.2. Materials and Methods

4.2.1. Materials

The following reagents were procured from Merck (Pty) Ltd., Johannesburg, South Africa and used without further purification: generation 1 poly(propylene imine) tetramine (DAB-Am4) dendrimer (pH 12, 25 wt % aq. soln), thiophene-2-carboxaldehyde (98%), methanol (MeOH, 99.5%), dichloromethane (DCM, 99.9%), deuterated chloroform (CDCl₃, ≥99%), magnesium sulphate (MgSO₄, ≥99.5%), 3-hexylthiophene (3HT, ≥99%), FeCl₃ (≥99.99%), chloroform (≥99%), acetone (99.3%), [6,6]-phenyl-C₆₁-butyric acid methyl ester (PC₆₁BM, >99.5%), tetrabutylammonium hexafluorophosphate (TBAPF₆, ≥99%), poly(3,4-ethylenedioxythiophene) polystyrene sulfonate (PEDOT:PSS, 0.5-1.0% in H₂O, high-conductivity grade), acetonitrile (99.8%), chlorobenzene (99.9%), Hellmanex III, 2-propylalcohol (99.5%) and silver (Ag) conductive paste. Indium tin oxide (ITO, 20 Ω/square resistance, Ossila Ltd., Sheffield, UK) coated substrates were used for characterization and fabrication. Deionized water used in this study was obtained from a Millipore Direct Q3 system (Millipore, Milford, MA, USA).

4.2.2. Synthesis of PPI-Th

Schiff base condensation reaction was used to synthesize PPI-Th as shown in Scheme 4.1 [28,29]. In details, 0.5 g of DAB-Am4 was added into a round bottom flask containing a solution of 0.6 mL of thiophene-2-carboxyaldehyde in 50 mL MeOH. The mixture was stirred at room temperature for 48 h under nitrogen atmosphere. After 48 h, the MeOH was removed with rotary evaporator and the resulting oily product was dissolved in DCM and washed three times with deionized water. MgSO_4 powder was added into the mixture and its suspensions were later removed by filtration method. The DCM was removed by rotary evaporator resulting in a yellow oily product with actual yield of 0.55 g and percentage yield of 52%. $^1\text{H-NMR}$ (CDCl_3 , 400 MHz): δH 1.39 (tt, 4H), 1.78-1.82 (tt, 8H), 2.38-2.48 (m, 12H), 3.56-3.59(t, 8H), 7.03 (dd, 4H), 7.25 (dd, 4H), 7.35 (dd, 4H), 8.35 (s, 8H). $^{13}\text{C-NMR}$ (CDCl_3 , 400 MHz): δC 25.13 (4C), 28.16 (2C), 51.49 (4C), 53.96 (4C), 59.32 (2C), 127.30 (4C), 128.57 (4C), 130.13 (4C), 142.60 (4C), 154.31 (4C). HRMS (m/z): Calc. 693.044: 62.39% C, 6.98% H, 12.13% N, 18.50% S. Exp. 693.289: 62.36% C, 6.98% H, 12.13% N, 18.50% S.

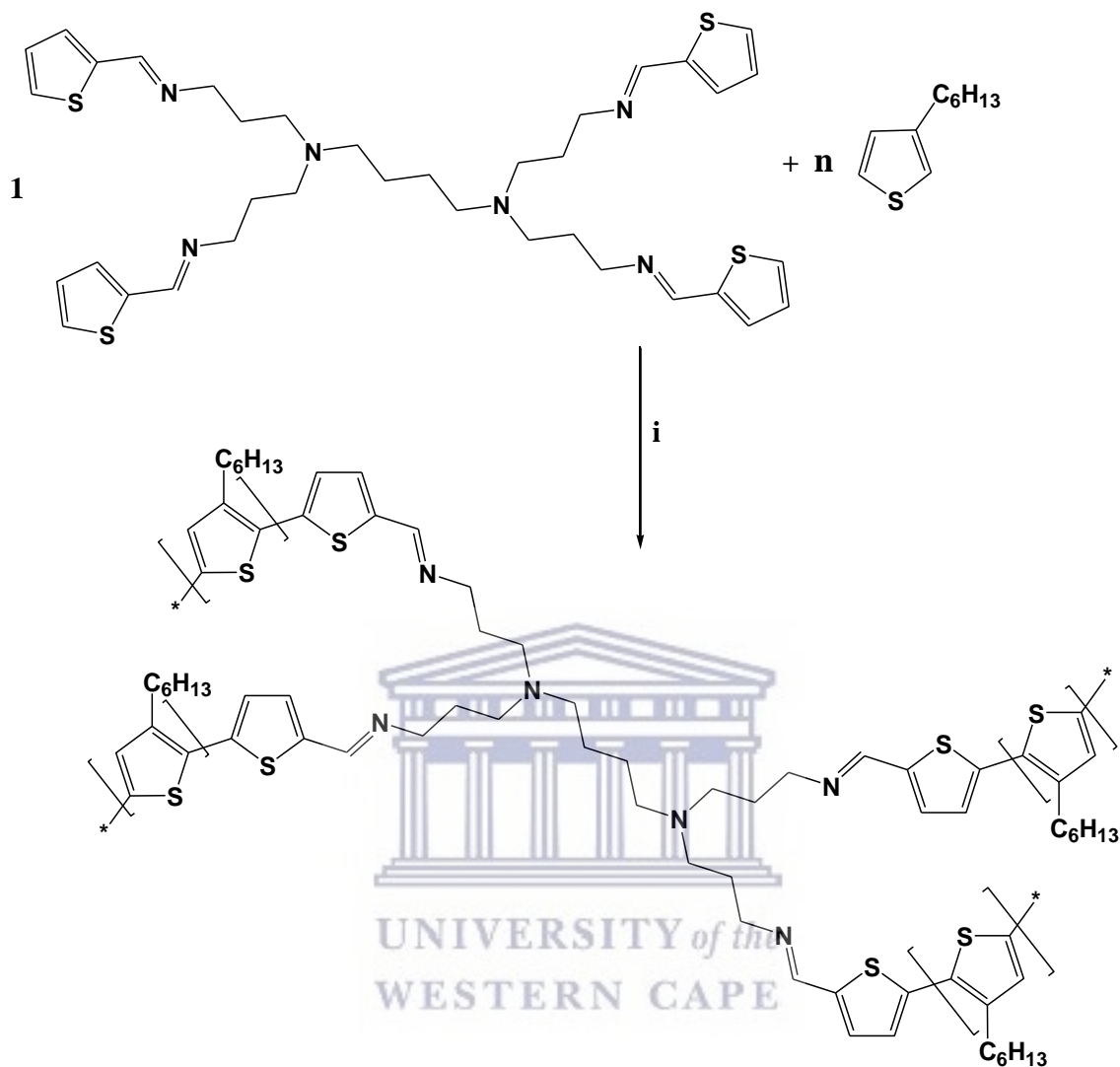


Scheme 4.1: Synthetic route of PPI-Th. (i). MeOH, 48 h.

4.2.3. Synthesis of PPI-Th-co-P3HT

Synthesis of PPI-Th-co-P3HT was performed with chemical oxidation polymerization method as shown in Scheme 4.2 [28] and three different molar ratios between PPI-Th and 3HT were used. The molar ratios used were 1 PPI-Th:40 3HT, 1 PPI-Th:60 3HT, and 1 PPI-Th:80 3HT. In details, PPI-Th and 3-HT which were dissolved in 100 mL chloroform under nitrogen atmosphere for 30 min while stirring. After, the mixture of 50 mL chloroform and FeCl₃ was added, the resulting mixture was stirred for 24 h at 60 °C. After 24 h, the resulting mixture was poured into a thimble which was transferred into a Soxhlet extractor (size large, 200 mL extractor volume, Merck (Pty) Ltd.) for purification. The mixture was washed with MeOH and acetone each for 24 h. Finally, the product was extracted with DCM for 24 h and dried in an oven for 24 h resulting to 0.55, 0.52 and 0.66 g for PPI-Th-co-P3HT synthesized using molar ratio of 1:40, 1:60 and 1:80, respectively.





Scheme 4.2: Synthetic route of PPI-Th-co-P3HT. (i). $FeCl_3$, chloroform, $60^\circ C$. $n = 40, 60$ and 80 .

4.2.4. Characterization techniques

NMR studies were done using A Bruker 400 MHz Avance III HD Nanobay Spectrometer equipped with a 5 mm BBO Probe at 298 K from Bruker, Karlsruhe, Germany. FTIR studies were performed with Spectrum-100 FTIR Spectrometer from (Perkin Elmer, Waltham, Massachusetts, US). Mass spectroscopy analysis was performed using Waters Synapt G2 Quadrupole Time-of-Flight (QTOF) Mass Spectrometer (MS) connected to a Waters Acquity Ultra-Performance Liquid Chromatograph (UPLC) (Waters, Milford, MA, USA). TGA studies were performed using Simultaneous Thermal Analyzer (STA) 6000 (PerkinElmer Pty Ltd.). TEM images were done using FEI Tecnai T20 TEM from FEI company, Hillsboro, OR, USA. SEM images were obtained using

Tescan MIRA3 RISE SEM from Tescan, Brno, Czech Republic and elemental analysis was performed using FEI NovaNano SEM from FEI company, Hillsboro, OR, USA. Photoluminescence spectra were obtained using NanoLog Spectrofluorometer from HORIBA Scientific, Cedex, France. X-ray diffraction (XRD) analysis was obtained using D8-Advanced Diffractometer from Bruker AXS, Billerica, MA, USA. The UV-Vis measurements were performed with Nicolet Evolution 100 UV-Vis Spectrophotometer (Thermo Electron Corporation, Waltham, MA, USA). Electrochemical studies were conducted with a CHI 760E Electrochemical Analyzer (CH Instruments Inc., Bee Cave, TX, USA, using ITO glass substrate working electrode from Ossila Ltd., Sheffield, UK, platinum wire counter electrode from Goodfellow Cambridge Ltd., Huntingdon, UK, silver/silver chloride reference electrode from Bioanalytical Systems Incorporated (BASi) in West Lafayette, IN, USA and electrolyte consisting of 0.1 M TBAPF₆/acetonitrile solution.

4.2.5. Fabrication of OPVs

8 pixels ITO substrates were sonicated in Hellmanex III solution, acetone and 2-propylalcohol. Filtered PEDOT:PSS was spun coated onto cleaned ITO substrate and baked for 5 min at 150 °C. Blended PPI-Th-co-P3HT:PC₆₁BM active layers in chlorobenzene were spun coated onto the PEDOT:PSS/ITO glass substrates. The PPI-Th-co-P3HT:PC₆₁BM coated substrates were annealed at 100°C for 5 min. Lastly, Ag conductive paste was coated using micropipette tip. After coating Ag with a micropipette tip, the device was annealed for 5 min at 100 °C. Device characteristics (current density–voltage) were measured with X200 Source Meter Unit from Ossila Ltd., Sheffield, UK using an illumination of AM 1.5G, 100 mW cm⁻² supplied by a SciSun-150 Solar Simulator, Class AAA from Sciencetech Inc., London, ON, Canada.

4.3. Results and Discussion

4.3.1. NMR analysis

The ¹H-NMR spectrum of PPI-Th is shown in Figure 4.1A. The number of protons obtained from the spectrum of PPI-Th through integration, are the same as the number of protons from the structure of PPI-Th. These findings confirm that PPI-TH was successfully synthesized. The signals at 1.39 ppm and 1.78-1.82 ppm are due to C–CH₂–C protons, 2.38-2.48 ppm are assigned to C–

CH₂-N protons, 3.56-3.59 ppm are attributed to C-CH₂=N protons, 7.03 ppm and 7.25 ppm are for =CH-CH= protons (β -position) of thiophene, 7.35 ppm signal is ascribed to =CH-S- proton (α -position) of thiophene and finally, 8.35 ppm signal is for -HC=N- proton [28]. PPI-Th was also analyzed with ¹³C-NMR. The signals at 25.13 and 28.16 ppm are attributed to the methylene carbons bonded to other two carbons (C-CH₂-C). The signals at 51.49, 53.96 and 59.32 ppm are assigned to methylene carbons bonded to nitrogen (-CH₂-N). The signals at 127.30 and 130.13 ppm are due to the β -position carbons of thiophene ring, while 128.57 ppm is for α -position carbon of thiophene ring [21]. The signal at 154.31 ppm is ascribed to the imine group carbon [28]. Synthesis of PPI-Th was also confirmed by mass spectroscopy. The theoretical molar mass of PPI-Th is 693.044 g.mol⁻¹ and the experimental molar mass is 693.289 g.mol⁻¹ (Figure A1). The molar masses are close to each other confirming successful synthesis of PPI-Th. Figure 4.2 shows the ¹H-NMR of PPI-Th-co-P3HT synthesized using different molar ratios. The interactions of hexyl group with the PPI-Th protons and dominating concentration of P3HT protons over the protons of PPI-Th causes the PPI-Th signals intensity to decrease leading to the dominance of P3HT signals in the ¹H-NMR of PPI-Th-co-P3HT. It was seen that the ¹H-NMR signals of PPI-Th-co-P3HT are broad because they are different chain lengths of P3HT attached to the α -position of the thiophene in PPI-Th compound. The change in molar ratios during synthesis of PPI-Th-co-P3HT does influence the ¹H-NMR spectra since the signals have different shapes. The change in the signal shape can be explained by the different chain lengths of P3HT attached to PPI-Th [28]. Figure 4.3 shows the ¹³C-NMR of different PPI-Th-co-P3HT. The ¹³C-NMR of all PPI-Th-co-P3HT synthesized under different conditions show no peaks. This is because of lack of nuclear Overhauser effect and slow relaxation of PPI-Th-co-P3HT carbons [48].

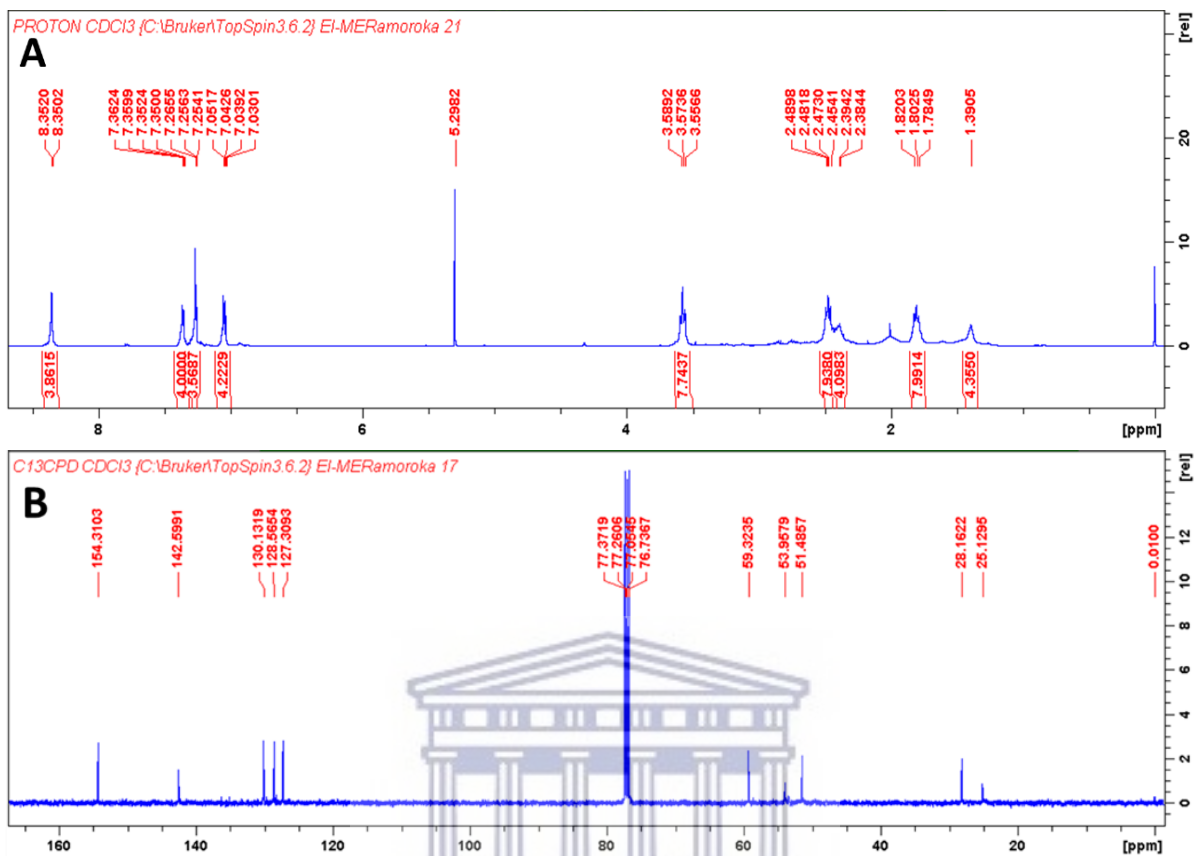


Figure 4.1: (A) ^1H -NMR and (B) ^{13}C -NMR of PPI-Th.

UNIVERSITY of the
 WESTERN CAPE

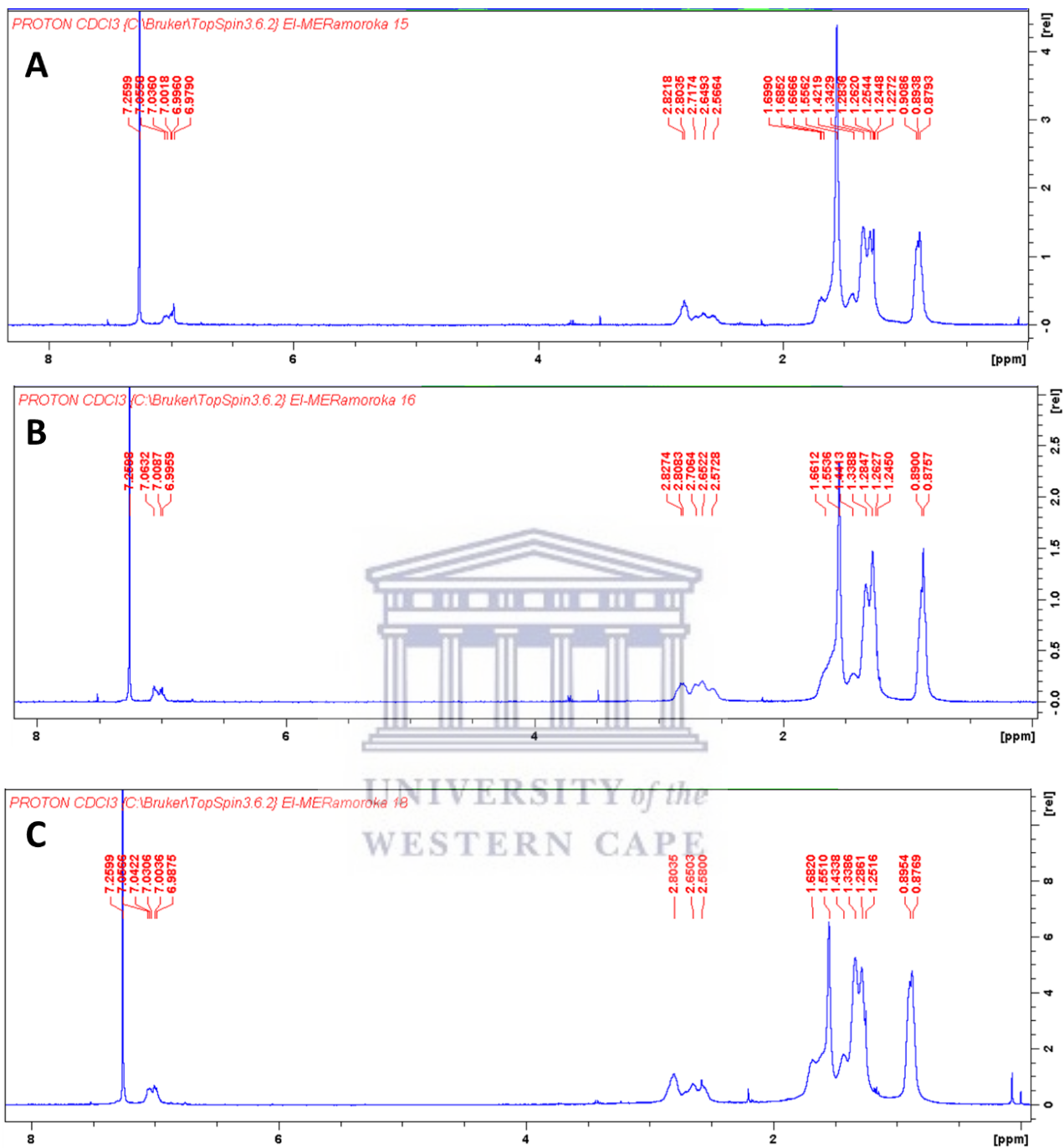


Figure 4.2: ¹H-NMR of PPI-Th-co-P3HT (A) 1:40, (B)1:60 and (C) 1:80.

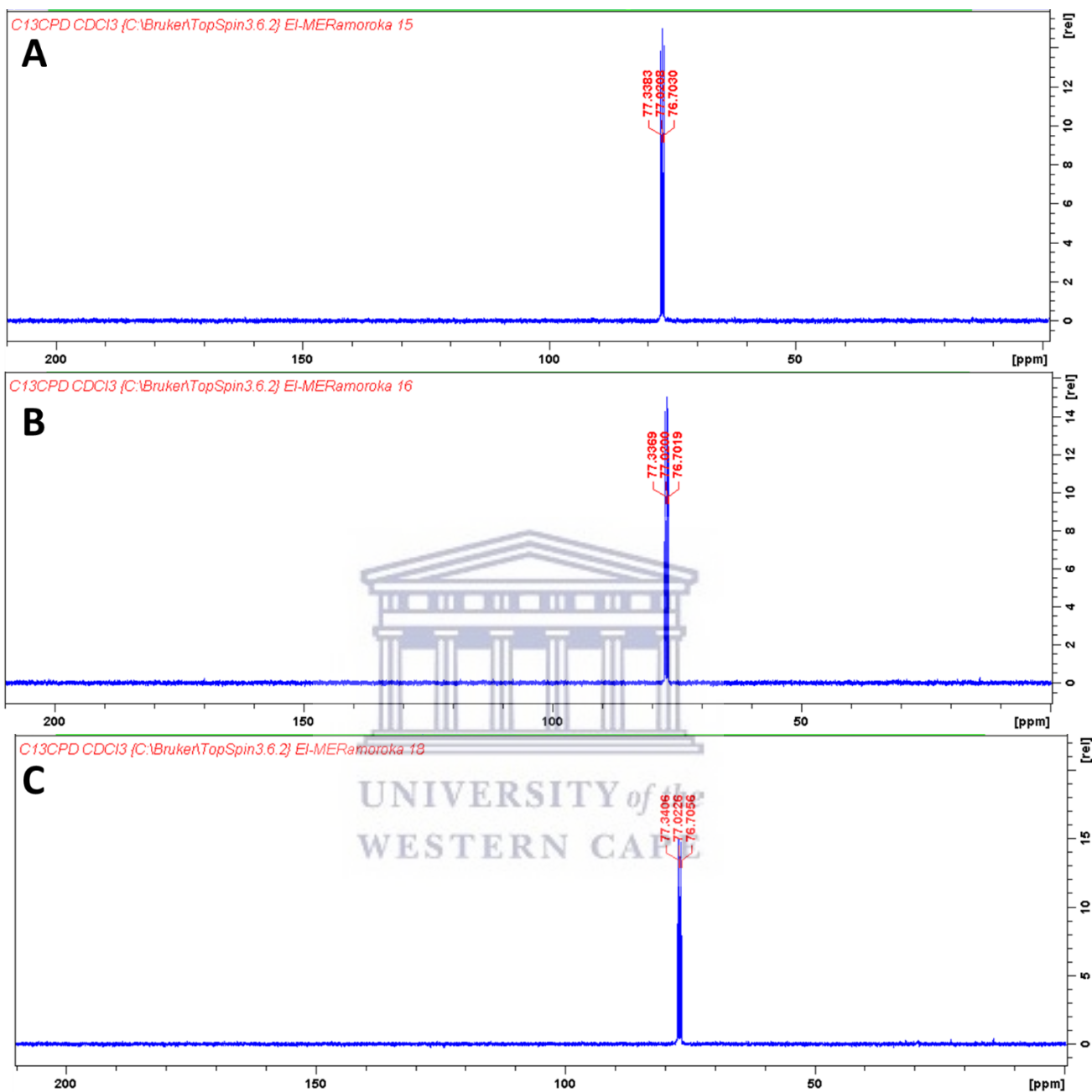


Figure 4.3: ^{13}C -NMR of PPI-Th-co-P3HT (A) 1:40, (B)1:60 and (C) 1:80.

4.3.2. FTIR analysis

FTIR was used to study the structure of the synthesized PPI-Th and PPI-Th-co-P3HT. Figure 4.4 shows the FTIR spectra of PPI-Th and PPI-Th-co-P3HT synthesized using different molar ratios. The vibration bands at 3070 , 2939 and 2833 cm^{-1} are attributed to C–H groups of the imine group, thiophene ring and methylene groups, respectively [21,30]. The band at 1634 cm^{-1} is ascribed to

C=N vibrations, while the peaks at 1432, 1216, 857 and 710 cm^{-1} are due to the vibrations of C=C, C-C, C-H and C-S-C bonds of the thiophene ring, respectively [31]. The band at 1081 cm^{-1} is due to C-N bond vibration. From the spectra of PPI-Th-co-P3HT, the band at 3070 cm^{-1} disappears and the intensity of the bands decreased in all spectra. The band at 1432 cm^{-1} shifts to 1461 cm^{-1} for all PPI-Th-co-P3HT synthesized using different molar ratios. According to literature, these shift of bands, disappearance of bands and decrease in intensity of bands confirm that P3HT is successfully developed on the surface of PPI-Th [32–34]. The change in molar ratios of PPI-Th and 3-hexylthiophene does not have an effect on the spectrum of PPI-Th-co-P3HT.

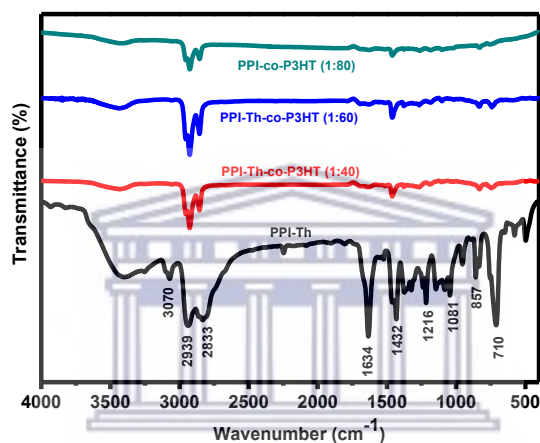


Figure 4.4: FTIR spectra of PPI-Th and PPI-Th-co-P3HT synthesized using 1:40, 1:60 and 1:80 molar ratios.

4.3.3. TGA analysis

Figure 4.5 shows the thermograms of PPI-Th-co-P3HT synthesized at molar ratios of 1:40, 1:60 and 1:80 and PPI-Th. Thermal decomposition of these materials take place in two stages. In the first stage, thermogram of PPI-Th shows a 4% weight loss taking place in the temperature range of 65-130°C, PPI-Th-co-P3HT (1:40) shows a 9% weight loss in the temperature range of 145-337°C, PPI-Th-co-P3HT (1:60) shows a 14% weight loss in the temperature range of 68-365°C and PPI-Th-co-P3HT (1:80) shows a 2% weight loss in the temperature range of 172-303°C. Weight loss in this first stage is usually due to the evaporation of water and solvent such as MeOH and chloroform in the samples except for PPI-Th-co-P3HT synthesized using molar ratio of 1:40 and 1:80 [35]. The first stage weight loss in all PPI-Th-co-P3HT samples was due to small molecular weight PPI-Th-co-P3HT [36]. In the second stage, 77% (216-425°C) weight loss has been observed

on the thermogram of PPI-Th due to the partial decomposition of PPI-Th. PPI-Th-co-P3HT thermograms shows a weight loss of 38 (439-505°C), 28 (447-493°C) and 30% (438-499°C) for 1:40, 1:60 and 1:80, respectively. This weight loss is due to decomposition of PPI-Th-co-P3HT. Thermograms shows that all samples still retain certain amount of weight (%) at 650°C. This can be due to the presence of residual solids and larger molecular weight PPI-Th-co-P3HT [37,38]. From the results, the presence of P3HT on the surface of PPI-Th improves its thermal stability with PPI-Th-co-P3HT 1:80 being the most thermally stable.

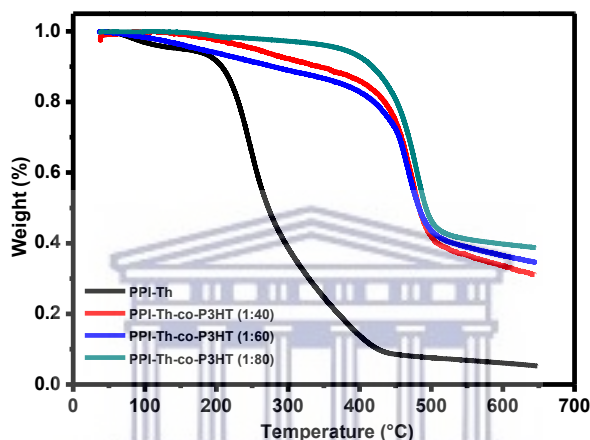


Figure 4.5: TGA thermograms of PPI-Th and PPI-Th-co-P3HT synthesized using different molar ratio.

4.3.4. UV-Vis studies

UV-Vis spectra of PPI-Th and three PPI-Th-co-P3HT (1:40, 1:60 and 1:80) thin film are shown in Figure 4.6. The PPI-Th spectrum shows no absorption band in the wavelength of 385-700 nm, while PPI-Th-co-P3HT compounds show one band. This band is attributed to the $\pi \rightarrow \pi^*$ transition which shows the conjugation double bonds of the conducting polymer [39,40]. The maxima absorption wavelengths of PPI-Th-co-P3HT were determined to be 416 nm for 1:40, 394 nm for 1:60 and 412 nm for 1:80. These onset wavelengths were determined from Figure 4.6 (B, C and D). The optical band gaps (E_g) of PPI-Th-co-P3HT were estimated using Equation 4.1 below:

$$E_g = \frac{1240}{\lambda_{onset}} \text{ eV} \dots\dots\dots 4.1$$

where λ_{onset} is an onset wavelength [28]. Therefore, the onset wavelengths were found to be 614, 556 and 583 nm corresponding to the optical band gap of 2.02, 2.23 and 2.13 eV for PPI-Th-co-P3HT synthesized using a ratio of 1:40, 1:60 and 1:80, respectively. This change in maximum absorption wavelength and optical band gap as the molar ratio of 3HT and PPI-Th changes is ascribed to the difference in molecular weight of PPI-Th-co-P3HT [41,42]. Therefore, this could be that as the molar ratio changes, the length of the P3HT attached to the four sides of PPI-Th changes which alters with the absorption response of PPI-Th-co-P3HT.

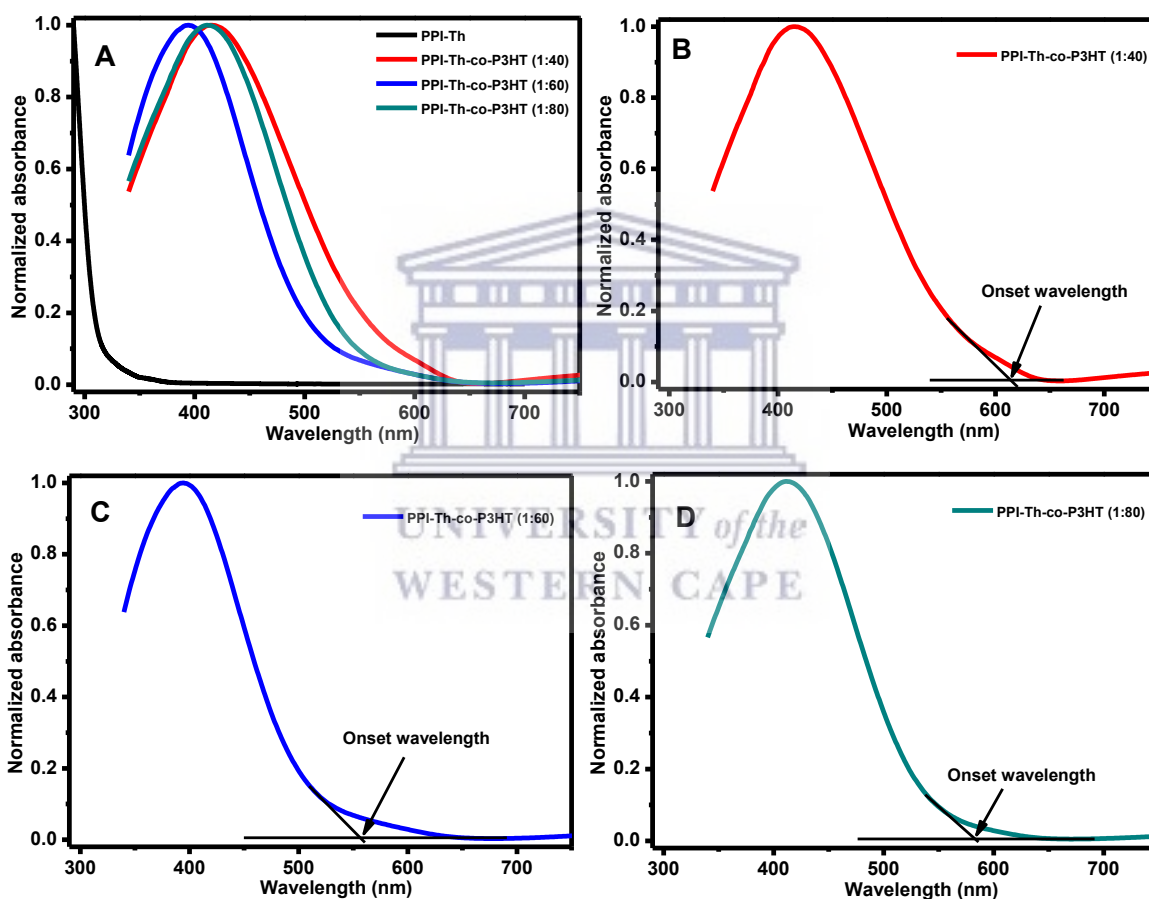


Figure 4.6: UV-Vis absorption spectra of PPI-Th and PPI-Th-co-P3HT synthesized using different molar ratios. Onset wavelength of PPI-Th-co-P3HT synthesized using molar ratio of 1:40, 1:60 and 1:80 are determined on spectra B, C and D, respectively.

4.3.5. TEM studies

Figure 4.7 shows the TEM micrographs of PPI-Th-co-P3HT for different synthesis molar ratios of PPI-Th and 3HT (1:40, 1:60 and 1:80). The TEM micrographs show that the particles are spherical

with the present of agglomeration. The particles were measured to be 35.92, 17.46 and 9.93 nm for molar ratios of 1:40, 1:60 and 1:80, respectively. This reveals that as the molar concentration of 3HT increases, the particles size decreases. At low concentration of 3HT, agglomeration provokes and lead to an increase in particle size. This is due to the fact that at low concentration of 3HT, the rate of reaction is slow and a smaller number of nuclei are formed. Therefore, there will be a collision between the particles that are formed later with the nuclei that are newly formed leading to agglomeration and larger particle size. While at high concentration of 3HT, a large number of nuclei is formed due to an increase in the rate of reaction leading to small particle size [43].

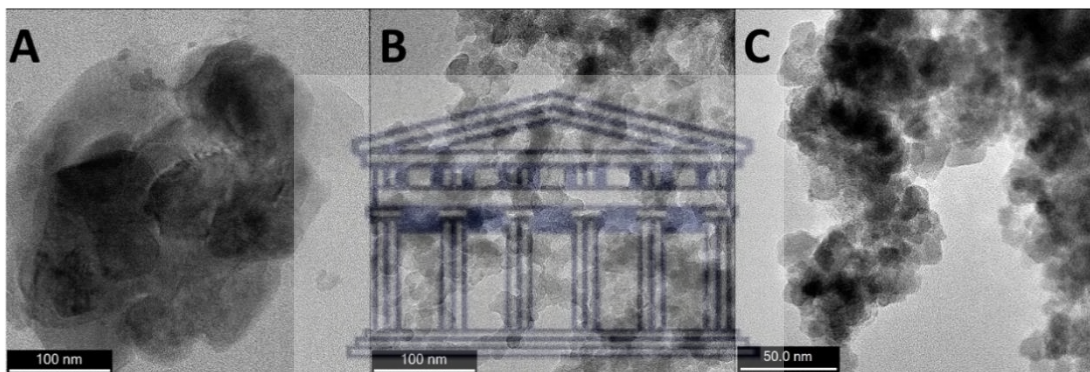


Figure 4.7: TEM micrographs of PPI-Th-co-P3HT synthesized using different ratios of (A) 1:40, (B) 1:60 and (C) 1:80 molar ratios.

4.3.6. SEM and elemental analysis of PPI-Th-co-P3HT

Figure 4.8 shows the SEM images of PPI-Th-co-P3HT synthesized using different molar ratios. SEM images revealed that the PPI-Th-co-P3HT has spherical shape, and it does not change as the molar ratio changes. At the molar ratio of 1:80, aggregation of PPI-Th-co-P3HT particles was observed. Table 4.1 shows the EDS data of PPI-Th-co-P3HT obtained at the different spots of the samples during analysis. An average of 80.00% carbon, 14.03% sulphur and 5.97% chlorine were detected for PPI-Th-co-P3HT synthesized using 1:40 molar ratio, 78.23% carbon, 13.70% sulphur and 8.07% chlorine were detected when 1:60 molar ratio was used. Finally, 81.10% carbon, 13.49% sulphur and 5.41% chlorine were obtained for PPI-Th-co-P3HT synthesized using molar ratio of 1:80. The chlorine detected is attributed to the FeCl_3 used during synthesis of PPI-Th-co-P3HT.

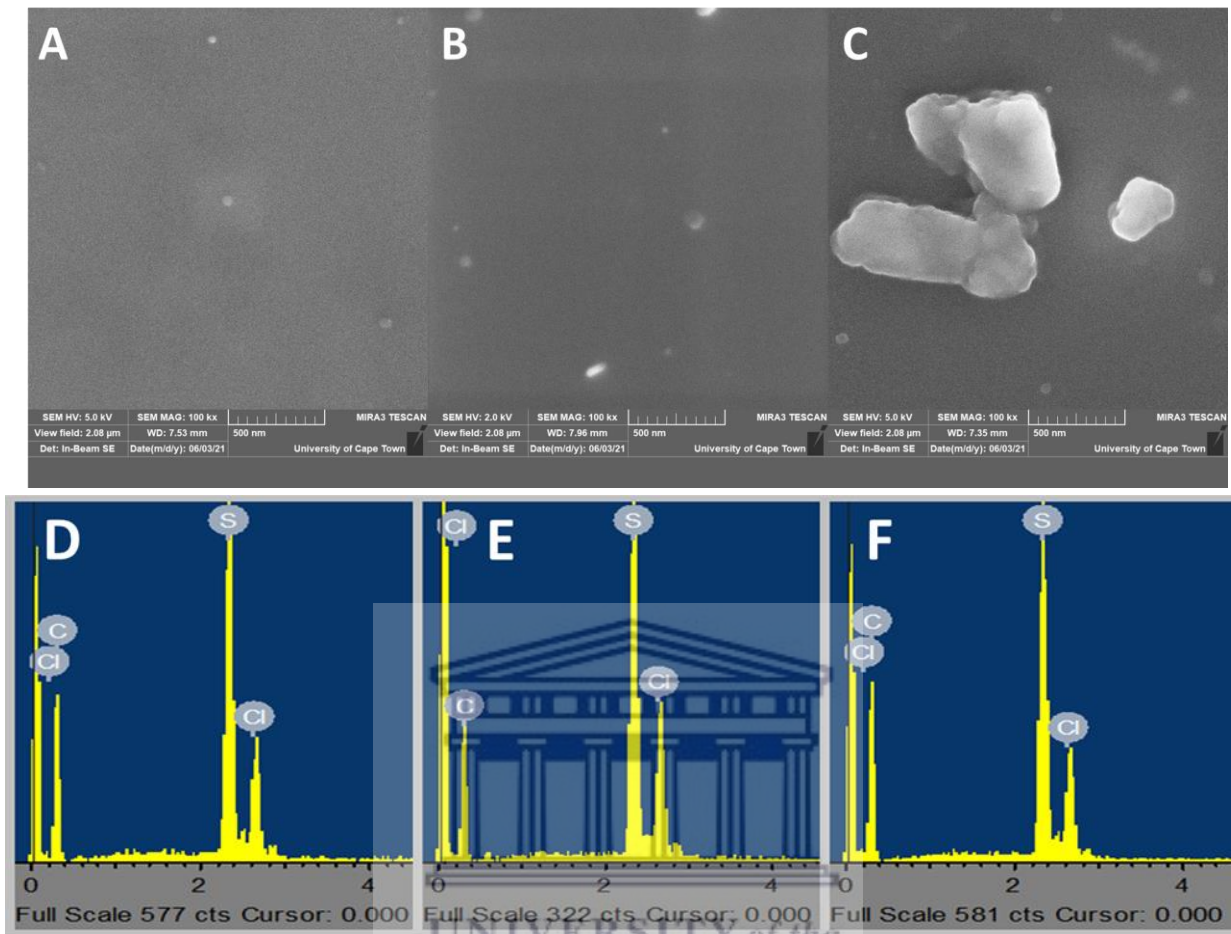


Figure 4.8: SEM images of PPI-Th-co-P3HT synthesized using molar ratio A) 1:40, B) 1:60 and C) 1:80 with their EDS spectra on D, E and F, respectively.

Table 4.1: EDS data of PPI-Th-co-P3HT synthesized using different molar ratios.

Sample	Spot	Carbon (%)	Sulphur (%)	Chlorine (%)	Total (%)
PPI-Th-co-P3HT 1:40	1	79.60	14.39	6.01	100
	2	80.18	13.87	5.95	100
	3	80.19	13.95	5.86	100
	4	80.46	13.78	5.76	100
	5	79.57	14.17	6.25	100
	average	80.00	14.03	5.97	100
PPI-Th-co-P3HT 1:60	1	79.55	12.82	7.63	100
	2	77.16	14.63	8.22	100
	3	78.06	13.60	8.34	100
	4	78.63	13.17	8.21	100
	5	77.74	14.29	7.97	100
	Average	78.23	13.7	8.07	100
PPI-Th-co-P3HT 1:80	1	81.04	13.4	5.56	100
	2	81.56	13.26	5.18	100
	3	81.06	13.74	5.20	100
	4	80.56	13.71	5.73	100
	5	81.25	13.34	5.41	100
	Average	81.10	13.49	5.41	100

4.3.7. CV studies

In order to investigate the effect of molar ratios on the energy levels, CV measurements were performed in 0.1 M TBAFP₆. The voltammograms of PPI-Th-co-P3HT obtained using different molar ratios are presented in Figure 4.9A. The electrochemical properties of PPI-Th-co-P3HT synthesized using different molar ratios are listed in Table 4.2. The HOMO/LUMO energy levels were determined to be $-3.18/-5.50$, $-3.07/-5.63$ and $-3.12/-5.58$ eV for PPI-Th-co-P3HT synthesized using molar ratios 1:40, 1:60 and 1:80 with the LUMO of PPI-Th-co-P3HT positioned 0.52, 0.62 and 0.58 eV above the LUMO of PC₆₁BM (shown in Figure 4.9B), respectively. These values are more than the threshold of 0.3 eV indicating possible occurrence of the energy loss at the PPI-Th-co-P3HT/PC₆₁BM interface [28]. Therefore, electrochemical band gaps (E_g^{CV}) are wider and exhibit similar trend with optical band gaps. This is due to the charge transfer barriers between the analyte (PPI-Th-co-P3HT), electrodes and electrolyte, which delays the input voltage and current measurements [44].

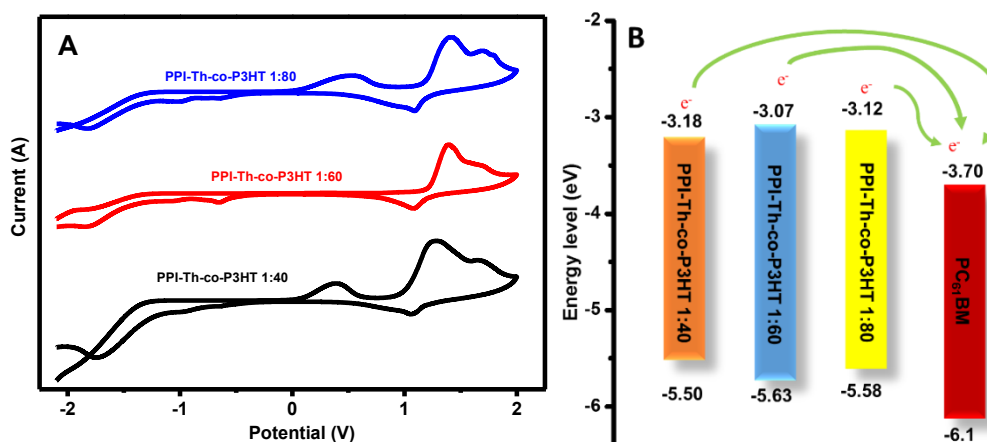


Figure 4.9: (A) CV of PPI-Th-co-P3HT and (B) energy levels diagram.

Table 4.2: Electrochemical responses of PPI-Th-co-P3HT synthesized using different molar ratios.

Compound	Oxidation onset potential (V)	Reduction onset potential (V)	$E_{\text{HOMO}}^{\text{a}}$ (eV)	$E_{\text{LUMO}}^{\text{b}}$ (eV)	$E_{\text{g}}^{\text{CV c}}$ (eV)	$\Delta E_{\text{LUMO}}^{\text{d}}$ (eV)
PPI-Th-co-P3HT 1:40	1.10	-1.22	-5.50	-3.18	2.32	0.52
PPI-Th-co-P3HT 1:60	1.23	-1.33	-5.63	-3.07	2.56	0.62
PPI-Th-co-P3HT 1:80	1.18	-1.28	-5.58	-3.12	2.46	0.58

Obtained with CV method, $^{\text{a}}E_{\text{HOMO}} = -[(E_{\text{oxidation-onset}} - E_{\text{Ferrocene}}) + 4.8]$, $^{\text{b}}E_{\text{LUMO}} = -[(E_{\text{reduction-onset}} - E_{\text{Ferrocene}}) + 4.8]$ eV, $^{\text{c}}E_{\text{g}}^{\text{CV}}$ was estimated using the equation: $E_{\text{g}}^{\text{CV}} = E_{\text{LUMO}} - E_{\text{HOMO}}$ and $^{\text{d}}\Delta E_{\text{LUMO}}$ was estimated using equation: $\Delta E_{\text{LUMO}} = E_{\text{LUMO-donor}} - E_{\text{LUMO-acceptor}}$.

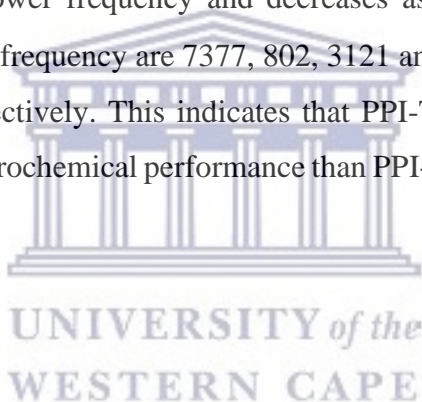
4.3.8. EIS studies

EIS can be used to study the interfacial charge transfer mechanism and characterization of organic semiconductors. Therefore, it was used in this study to investigate the electrochemical behaviour of PPI-Th-co-P3HT synthesized using different molar ratios. Figure 4.10A shows the Nyquist plot of PPI-Th compared with PPI-Th-co-P3HT. Two semicircles were observed from the spectra of PPI-Th and PPI-Th-co-P3HT. The diameter of the first semicircle (at higher frequency) is attributed to electrolyte or electrode resistance and the diameter of the second semicircle (at lower frequency) is attributed to diffusion resistance of the electrolyte or charge transfer resistance [45]. The diameter of the semicircle represents the charge transfer resistance (R_{ct}). It was seen that when the diameter is long, it will have a high the R_{ct} [46]. From Figure 4.10A, the diameter of the semicircle decreases after decorating PPI-Th with P3HT indicating a decrease in R_{ct} . Therefore, the presence of P3HT improves the conducting properties of PPI-Th. When comparing the spectra of the PPI-Th-co-P3HT synthesized using different molar ratios, 1:40 has the smallest diameter of

the semicircle followed by 1:80 whereas 1:60 molar ratio has the largest diameter. Therefore, PPI-Th-co-P3HT synthesized using molar ratio of 1:40 has the smallest R_{ct} , as compared to 1:60 molar ratio having higher R_{ct} . Figure 4.10B shows that P3HT on the surface of PPI-Th causes a shift of the maximum peak to lower frequency. This suggests that the rate of recombination is reduced due to the presence of P3HT. The lifetime (τ) was estimated using the Equation 4.2 below:

$$\tau = \frac{1}{2\pi f_{\max}} \dots \dots \dots 4.2$$

where f_{\max} is maximum peak frequency. The τ values were found to be 1.08, 4.09, 6.05 and 5.91 ms for PPI-Th with 1:40, 1:60 and 1:80 molar ratio, respectively [47]. Figure 4.8C shows the impedance against log (frequency) of the synthesized materials. It is observed that all materials have maximum impedance at lower frequency and decreases as the frequency increases. The impedance values obtain at 0 Hz frequency are 7377, 802, 3121 and 1438 Ω for PPI-Th with 1:40, 1:60 and 1:80 molar ratio, respectively. This indicates that PPI-Th-co-P3HT synthesized using 1:40 molar ratio has the best electrochemical performance than PPI-Th-co-P3HT synthesized using other molar ratios.



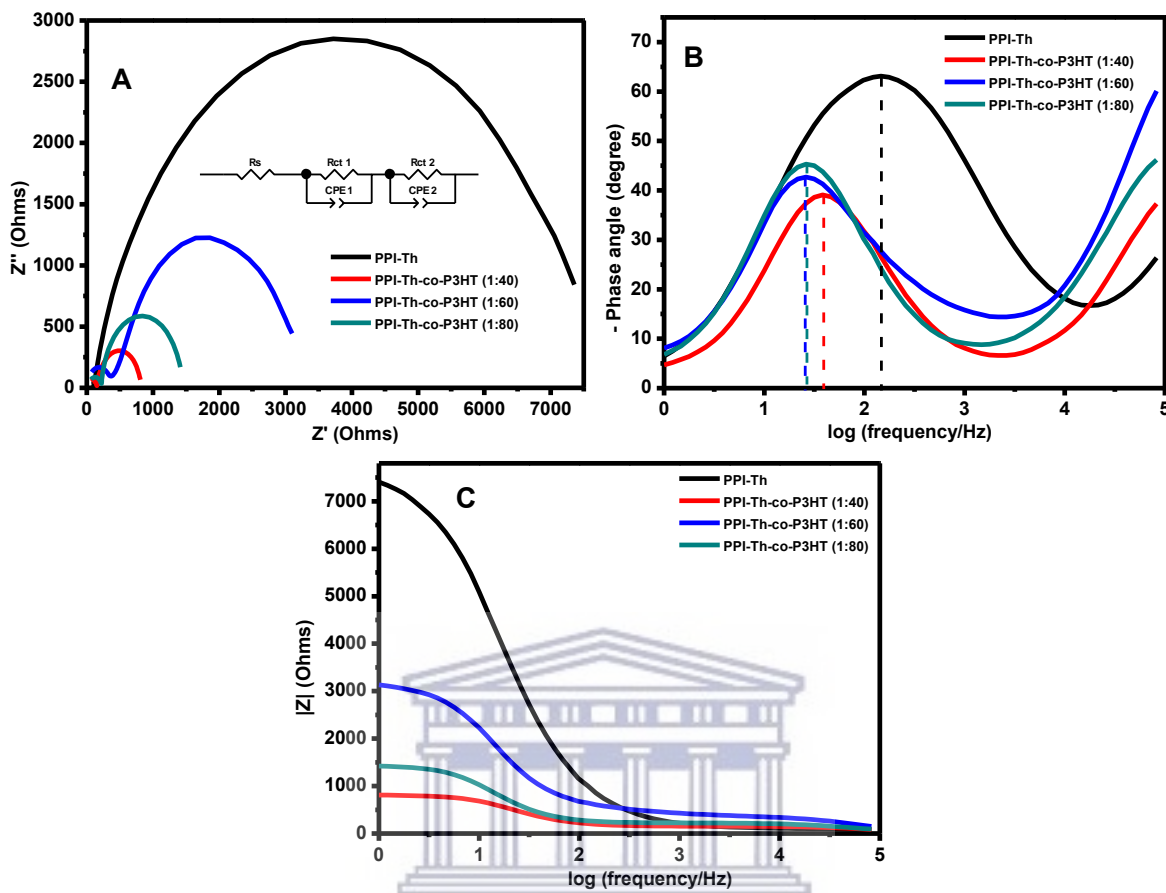


Figure 4.10: (A) Nyquist plot, (B) Bode-phase plots and (C) Bode-impedance of PPI-Th compared PPI-Th-co-P3HT synthesized using molar ratios.

To further investigate the electrochemical behaviour of synthesized PPI-Th-co-P3HT, it was blended with $PC_{61}BM$. The EIS results obtained are displayed in Figure 4.11. After blending with $PC_{61}BM$, the diameter of the semicircle of PPI-Th-co-P3HT: $PC_{61}BM$ is smaller than that of PPI-Th-co-P3HT, suggesting that the composite have a smaller R_{ct} contributing to faster electron transfer from PPI-Th-co-P3HT to $PC_{61}BM$ (Figure 4.11A). The composite of PPI-Th-co-P3HT synthesized using 1:40 molar ratio has the smallest semicircle indicating that it has the lowest R_{ct} . Figure 4.11B shows the phase angle against log (frequency) plot of PPI-Th-co-P3HT with and without $PC_{61}BM$. After introduction of $PC_{61}BM$, the maximum peak frequency shifts to higher frequency indicating the increase in the recombination rate and shorter electron lifetime [47]. Figure 4.11B shows that the impedance decreases after introduction of $PC_{61}BM$, this could be due to successful electron transfer from PPI-Th-co-P3HT to $PC_{61}BM$. The composite containing PPI-

Th-co-P3HT synthesized using 1:40 molar ratio has the lowest impedance of 527 Ω at lower frequency indicating that is the most conductive.

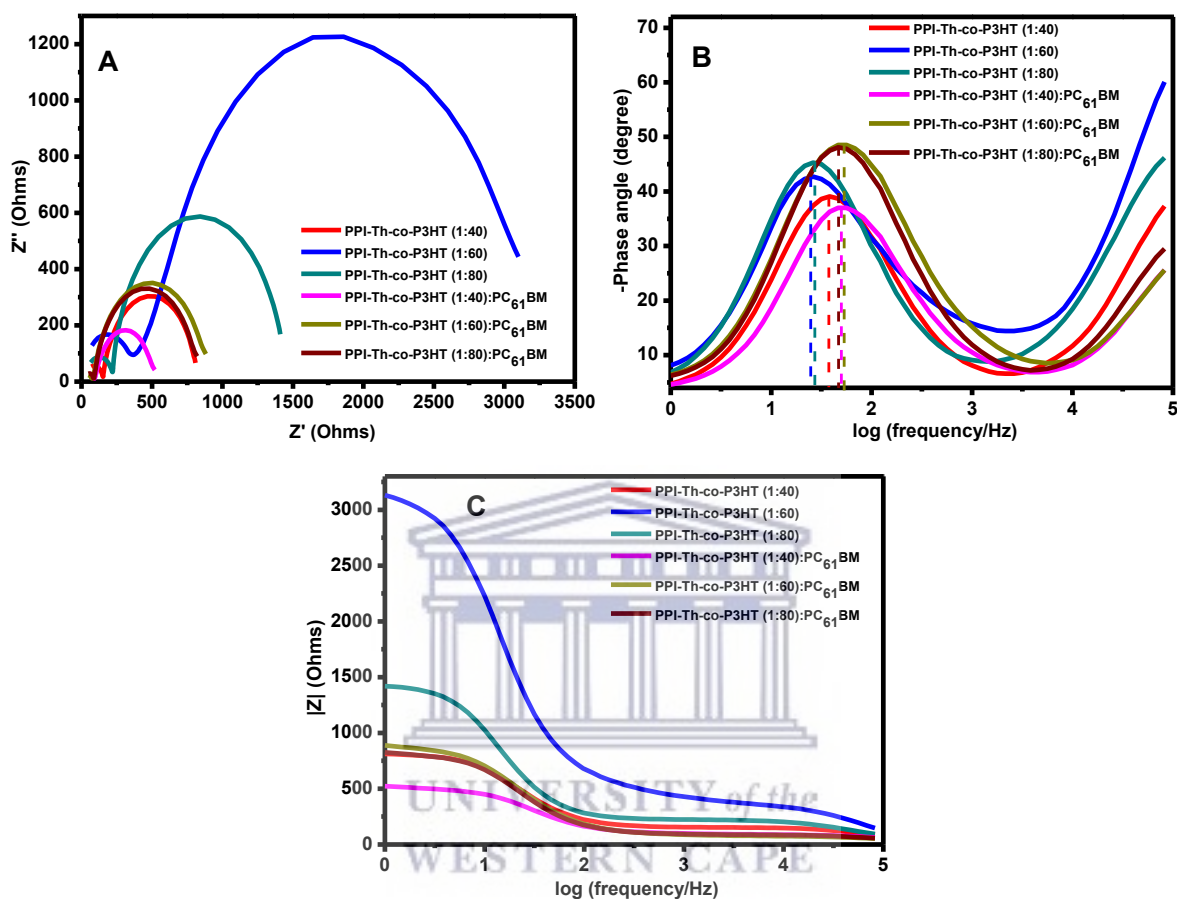


Figure 4.11: (A) Nyquist plots, (B) Bode-phase plots and (C) Bode-impedance of PPI-Th-co-P3HT compared with and without PC₆₁BM.

4.3.9. Photoluminescence studies of PPI-Th-co-P3HT

Photoluminescence is a useful technique for studying emission of light properties of polymers and their composites [49]. The photoluminescence spectra of PPI-Th-co-P3HT synthesized using different molar ratios and their blends with PC₆₁BM are shown in Figure 4.12. PPI-Th-co-P3HT synthesized using molar ratio of 1:40, 1:60 and 1:80 emitted a green light with maximum emission wavelength at 558, 542 and 555 nm, respectively. These results show the blue-shift of the maximum emission peaks in the following order: 1:60 > 1:80 > 1:40 (Figure 4.12D). Wang *et al.* [50] studied between the photoluminescence response and crystallinity of the donor polymers. Their findings revealed that the donor polymer with high crystallinity has the most intense

emission peak and is the most red-shifted peak. Therefore, the PPI-Th-co-P3HT synthesized using molar ratio of 1:40 has higher crystallinity, while 1:60 gave a polymer with the least crystallinity. Photoluminescence was also used to study the charge transfer process between PPI-Th-co-P3HT and PC₆₁BM. From Figure 4.12 (A, B and C), photoluminescence intensity of PPI-Th-co-P3HT decreased after blending with PC₆₁BM. This photoluminescence quenching is associated with transfer of charges between PPI-Th-co-P3HT and PC₆₁BM [51]. Consequently, the carrier charges which were meant to return from excited state to ground state are transferred to PC₆₁BM leading to the reduction in photoluminescence intensity. About 82, 57 and 79 % of photoluminescence intensity for PPI-Th-co-P3HT synthesized using molar ratio of 1:40, 1:60 and 1:80 was quenched, respectively. Therefore, sufficient charge transfer occurs between PPI-Th-co-P3HT synthesized using molar ratio of 1:40 and PC₆₁BM.



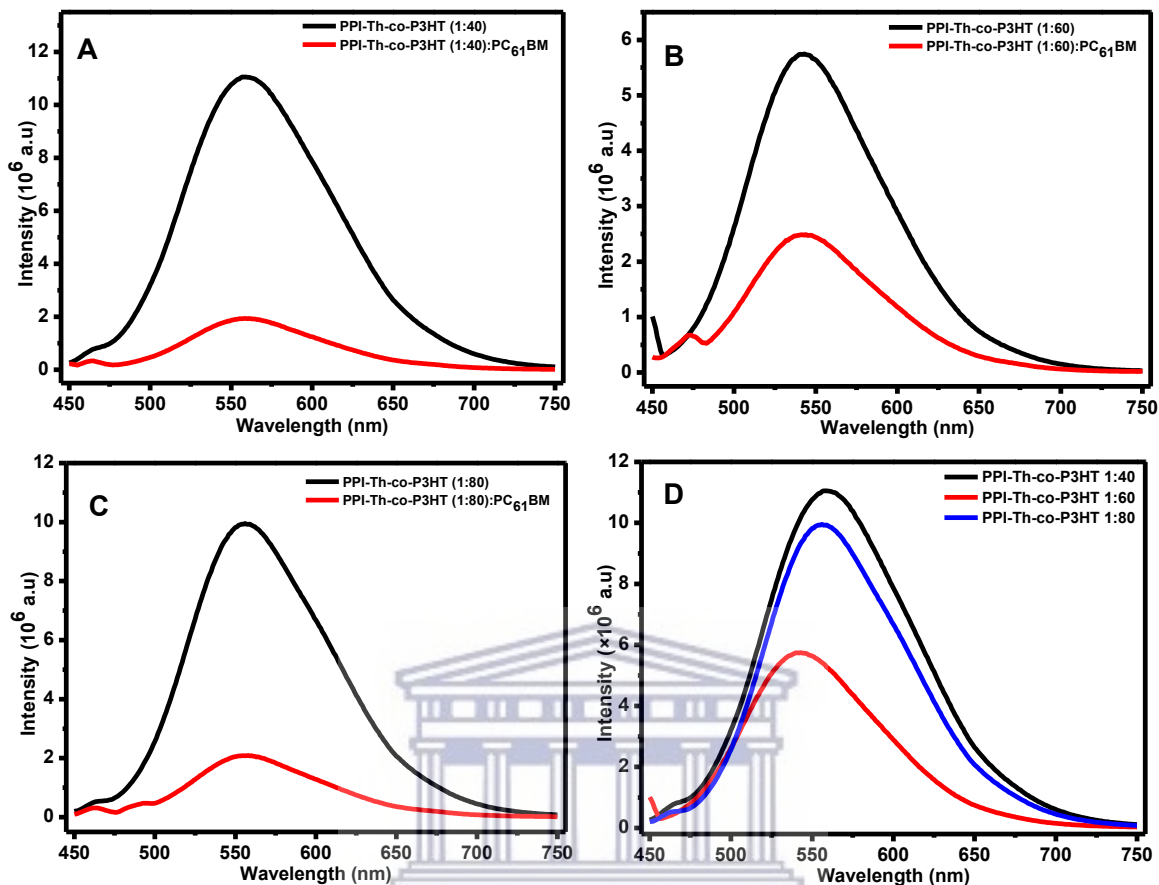


Figure 4.12: Photoluminescence spectra of PPI-Th-co-P3HT synthesized using molar ratios of (A) 1:40, (B) 1:60 and (C) 1:80. D) Comparison of emission spectra of PPI-Th-co-P3HT synthesized using different molar ratios.

4.3.10. XRD analysis of PPI-Th-co-P3HT

Crystallinity studies of PPI-Th-co-P3HT synthesized using different molar ratios were performed using XRD. Figure 4.13 illustrates the comparison of the XRD patterns for PPI-Th-co-P3HT. XRD diffraction pattern of PPI-Th-co-P3HT synthesized using molar ratio of 1:40 and 1:80 showed a diffraction peak at 5.6° and 5.7° , respectively. This diffraction peak corresponds to lamellae structure [49] and it is not present on the XRD pattern of PPI-Th-co-P3HT synthesized using molar ratio of 1:60. This confirms the amorphous nature of PPI-Th-co-P3HT (1:60) [50]. The diffraction peak of PPI-Th-co-P3HT synthesized using 1:40 molar ratio is the most intense indicating that is the most crystalline [49]. These results agree with the photoluminescence studies.

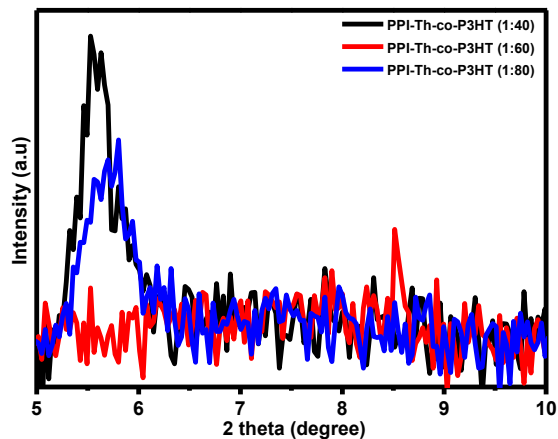


Figure 4.13: XRD pattern of PPI-Th-co-P3HT with different molar ratios.

4.3.11. Photovoltaic performance of PPI-Th-co-P3HT

Figure 4.14 shows the current density-voltage (J-V) characteristics of PPI-Th-co-P3HT synthesized using different molar ratios as donor materials. The OPVs parameters determined from the J-V curve are summarized in Table 4.3. These OPVs parameters are the maximum values obtained from multiple devices fabricated with the J-V curves in Figure A2 with their response in Table A(1-3). The architecture of the fabricated OPVs made of ITO coated glass substrate as bottom electrode, PEDOT:PSS as hole extraction layer, PPI-Th-co-P3HT:PC₆₁BM as an active layer and silver paste as top electrode. The maximum performance was achieved when PPI-Th-co-P3HT synthesized using molar ratio of 1:40 was used as a donor material with PCE of 0.034 %, fill factor (FF) of 31.24%, short circuit current (J_{SC}) of 1.26 A.cm⁻² and open circuit voltage (V_{OC}) of 0.085 V. This performance is due to narrow optical band gap of PPI-Th-co-P3HT synthesized using 1:40 molar ratio allowing generation of sufficient electron-hole pair, also has smaller distance between its LUMO levels and those of PC₆₁BM allowing efficient charge transfer and finally, has lower R_{ct} which indicate that charges are freely transferred at the donor:acceptor interface resulting in higher V_{OC}. These findings are discussed in comparison with the results of PPI-Th-co-P3HT synthesized using molar ratios of 1:60 and 1:80. All the fabricated devices gave low PCE. This is due to the environment in which the devices were fabricated. They were fabricated in air. Previously, studies have been conducted to investigate effect of oxygen on the performance of OPVs. The studies revealed that exposure of the OPVs to oxygen creates non-conductive metal oxide layer between active layer and electrode [52]. These affect the performance

of the OPVs and affect the shape of the J-V curve [52,53]. Penetration of oxygen through the active layer causes the photo-oxidation reaction of the acceptor and donor materials which affect the charge carrier mobilities and energy levels. These also reduce PCE of OPVs [54]. The presence of oxygen in the active layer increases the hole concentration. This leads to the formation of electron traps which reduces FF and V_{OC} [55]. Oxygen is also responsible for the loss of J_{SC} because of exciton quenching [54].

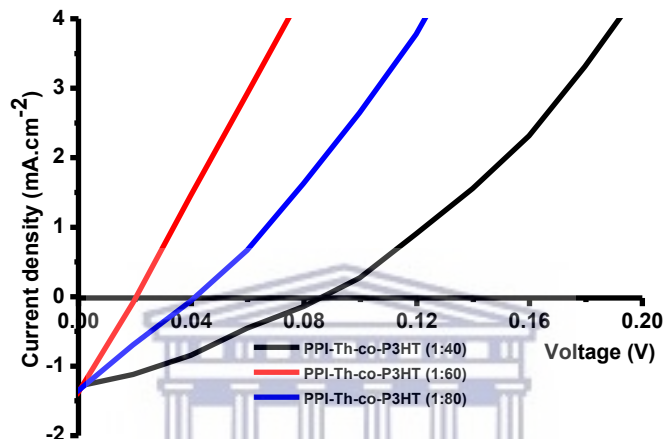


Figure 4.14: J–V characteristics of the fabricated OPVs using PPI-Th-co-P3HT synthesized using different molar ratio as donor materials.

Table 4.3: Photovoltaic performance of PPI-Th-co-P3HT as donor material.

Donor material	PCE ($\times 10^{-2}\%$)	FF (%)	J_{sc} ($\text{mA}\cdot\text{cm}^{-2}$)	V_{oc} ($\times 10^{-2}\text{V}$)
PPI-Th-co-P3HT 1:40	3.40	31.24	1.26	8.50
PPI-Th-co-P3HT 1:60	0.16	6.45	1.26	1.94
PPI-Th-co-P3HT 1:80	0.13	27.68	1.18	4.10

4.4. Conclusion

In summary, we synthesized PPI-Th-co-P3HT successfully by chemical oxidation copolymerization method and characterized their blend with PC_{61}BM using EIS. The structures of the synthesized compounds were confirmed by NMR and FTIR. The TGA studies revealed that the PPI-Th-co-P3HT synthesized using the molar ratio of 1 PPI-Th:80 3HT is the most thermally stable. The optical bandgaps determined from the UV-vis spectroscopy revealed that synthesized PPI-Th-co-P3HT polymers have wider band gaps for use as donor materials in organic

photovoltaic cells. Therefore, for them to be successful and more efficient, they must be blended with an acceptor material that can absorb sufficient light. In this study, we have blended PPI-Th-co-P3HT with PC₆₁BM (which also have poor light absorption properties) to investigate the charge transfer mechanism using EIS. The Nyquist and bode plots revealed that the size of the semi-circle and the impedance decreases after blending PPI-Th-co-P3HT and PC₆₁BM, respectively. This is an indication that the conductivity has improved revealing successful transfer of charges from PPI-Th-co-P3HT to PC₆₁BM. The highest PCE was achieved for PPI-Th-co-P3HT synthesized using molar ratio of 1:40. These performances were attributed to high crystallinity of PPI-Th-co-P3HT synthesized using molar ratio of 1:40 confirmed by XRD and PL along with higher conductivity confirmed by EIS.



References

- [1] Sorrentino, R., Kozma, E., Luzzati, S. and Po, R., 2021. Interlayers for non-fullerene based polymer solar cells: distinctive features and challenges. *Energy & Environmental Science*, 14, pp.180-223.
- [2] Yan, L. and Ma, C.Q., 2021. Degradation of Polymer Solar Cells: Knowledge Learned from the Polymer: Fullerene Solar Cells. *Energy Technology*, p.2000920.
- [3] Chen, J., Zhu, Y., Huang, J., Zhang, J., Pan, D., Zhou, J., Ryu, J.E., Umar, A. and Guo, Z., 2021. Advances in responsively conductive polymer composites and sensing applications. *Polymer Reviews*, 61, pp.157-193.
- [4] Inglev, R., Møller, E., Højgaard, J., Bang, O. and Janting, J., 2021. Optimization of All-Polymer Optical Fiber Oxygen Sensors with Antenna Dyes and Improved Solvent Selection Using Hansen Solubility Parameters. *Sensors*, 21, p.5.
- [5] Lee, T., Song, C.E., Lee, S.K., Shin, W.S. and Lim, E., 2021. Alkyl-Side-Chain Engineering of Nonfused Nonfullerene Acceptors with Simultaneously Improved Material Solubility and Device Performance for Organic Solar Cells. *ACS Omega*, 6, 4562–4573.
- [6] Jiang, K., Wei, Q., Lai, J.Y.L., Peng, Z., Kim, H.K., Yuan, J., Ye, L., Ade, H., Zou, Y. and Yan, H., 2019. Alkyl chain tuning of small molecule acceptors for efficient organic solar cells. *Joule*, 3, pp.3020-3033.
- [7] Pang, S., Zhang, R., Duan, C., Zhang, S., Gu, X., Liu, X., Huang, F. and Cao, Y., 2019. Alkyl chain length effects of polymer donors on the morphology and device performance of polymer solar cells with different acceptors. *Advanced Energy Materials*, 9, p.1901740.
- [8] Chen, M., Nian, Y., Hu, Z. and Zhang, L., 2021. Alkyl side chain engineering for difluorinated benzothiadiazole flanked non-fullerene acceptors toward efficient polymer solar cells. *Journal of Materials Science: Materials in Electronics*, 32, pp.219-231.
- [9] Zeng, L., Ma, R., Zhang, Q., Liu, T., Xiao, Y., Zhang, K., Cui, S., Zhu, W., Lu, X., Yan, H. and Liu, Y., 2021. Synergy strategy to the flexible alkyl and chloride side-chain engineered quinoxaline-based D–A conjugated polymers for efficient non-fullerene polymer solar cells.

Materials Chemistry Frontiers, 5, pp.1906-1916.

- [10] Wang, Y., Zhang, Y., Qiu, N., Feng, H., Gao, H., Kan, B., Ma, Y., Li, C., Wan, X. and Chen, Y., 2018. A halogenation strategy for over 12% efficiency nonfullerene organic solar cells. *Advanced Energy Materials*, 8, p.1702870.
- [11] Sun, S.X., Huo, Y., Li, M.M., Hu, X., Zhang, H.J., Zhang, Y.W., Zhang, Y.D., Chen, X.L., Shi, Z.F., Gong, X. and Chen, Y., 2015. Understanding the halogenation effects in diketopyrrolopyrrole-based small molecule photovoltaics. *ACS Applied Materials & Interfaces*, 7, pp.19914-19922.
- [12] Shin, J., Kim, M., Kang, B., Lee, J., Kim, H.G. and Cho, K., 2017. Impact of side-chain fluorination on photovoltaic properties: fine tuning of the microstructure and energy levels of 2D-conjugated copolymers. *Journal of Materials Chemistry A*, 5, pp.16702-16711.
- [13] Zhao, W., Li, S., Yao, H., Zhang, S., Zhang, Y., Yang, B. and Hou, J., 2017. Molecular optimization enables over 13% efficiency in organic solar cells. *Journal of the American Chemical Society*, 139, pp.7148-7151.
- [14] Fan, Q., Méndez-Romero, U.A., Guo, X., Wang, E., Zhang, M. and Li, Y., 2019. Fluorinated Photovoltaic Materials for High-Performance Organic Solar Cells. *Chemistry—An Asian Journal*, 14, pp.3085-3095.
- [15] Zhao, F., Dai, S., Wu, Y., Zhang, Q., Wang, J., Jiang, L., Ling, Q., Wei, Z., Ma, W., You, W. and Wang, C., 2017. Single-junction binary-blend nonfullerene polymer solar cells with 12.1% efficiency. *Advanced Materials*, 29, p.1700144.
- [16] Kan, B., Feng, H., Wan, X., Liu, F., Ke, X., Wang, Y., Wang, Y., Zhang, H., Li, C., Hou, J. and Chen, Y., 2017. Small-molecule acceptor based on the heptacyclic benzodi (cyclopentadithiophene) unit for highly efficient nonfullerene organic solar cells. *Journal of the American Chemical Society*, 139, pp.4929-4934.
- [17] Gupta, A., Akhtar, A.J. and Saha, S.K., 2013. In-situ growth of P3HT/graphene composites for supercapacitor application. *Materials Chemistry and Physics*, 140, pp.616-621.
- [18] Zhao, S., Wang, Y., Huang, W., Jin, H., Huang, P., Wang, H., Wang, K., Li, D., Xu, M., Yang, D. and Pi, X., 2019. Developing near-infrared quantum-dot light-emitting diodes to

- mimic synaptic plasticity. *Science China Materials*, 62, pp.1470-1478.
- [19] Brixi, S., Melville, O.A., Boileau, N.T. and Lessard, B.H., 2018. The influence of air and temperature on the performance of PBDB-T and P3HT in organic thin film transistors. *Journal of Materials Chemistry C*, 6, pp.11972-11979.
- [20] Çaldıran, Z., Erkem, Ü., Baltakesmez, A. and Biber, M., 2021. Effects of the PENTACENE as doping material on the power conversion efficiency of P3HT:PCBM based ternary organic solar cells. *Physica B: Condensed Matter*, 607, p.412859.
- [21] Ansari, M.A., Mohiuddin, S., Kandemirli, F. and Malik, M.I., 2018. Synthesis and characterization of poly(3-hexylthiophene): improvement of regioregularity and energy band gap. *RSC Advances*, 8, pp.8319-8328.
- [22] Ahmad, S., Berger, R., Khan, H.U. and Butt, H.J., 2010. Electrical field assisted growth of poly(3-hexylthiophene) layers employing ionic liquids: microstructure elucidated by scanning force and electron microscopy. *Journal of Materials Chemistry*, 20, pp.5325-5334.
- [23] Bannock, J.H., Xu, W., Baïssas, T., Heeney, M. and de Mello, J.C., 2016. Rapid flow-based synthesis of poly(3-hexylthiophene) using 2-methyltetrahydrofuran as a bio-derived reaction solvent. *European Polymer Journal*, 80, pp.240-246.
- [24] Facchinatto, W.M., Torres, B.B.M. and Balogh, D.T., 2016. One-pot synthesis of poly-(3-hexylthiophene) with variable degrees of molar mass and regioregularity. *Journal of Polymer Research*, 23, pp.1-8.
- [25] Marrocchi, A., Lanari, D., Facchetti, A. and Vaccaro, L., 2012. Poly(3-hexylthiophene): synthetic methodologies and properties in bulk heterojunction solar cells. *Energy & Environmental Science*, 5, pp.8457-8474.
- [26] Torres, B.B.M. and Balogh, D.T., 2012. Regioregular improvement on the oxidative polymerization of poly-3-octylthiophenes by slow addition of oxidant at low temperature. *Journal of Applied Polymer Science*, 124, pp.3222-3228.
- [27] Gonçalves, V.C., Costa, L.M., Cardoso, M.R., Mendonca, C.R. and Balogh, D.T., 2009. Synthesis and characterization of copolymers of alkyl-and azo-thiophenes: Chromic properties and photoinduced birefringence. *Journal of Applied Polymer Science*, 114,

pp.680-687.

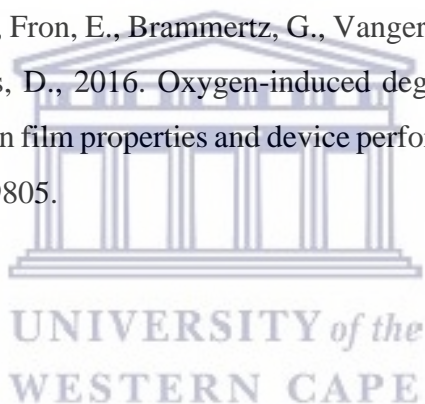
- [28] Ramoroka, M.E., Mdluli, S.B., John-Denk, V.S., Modibane, K.D., Arendse, C.J. and Iwuoha, E.I., 2021. Synthesis and Photovoltaics of Novel 2, 3, 4, 5-Tetrathienylthiophene-co-poly (3-hexylthiophene-2, 5-diyl) Donor Polymer for Organic Solar Cell. *Polymers*, *13*, p.2.
- [29] Memela, M., Feleni, U., Mdluli, S., Ramoroka, M.E., Ekwere, P., Douman, S. and Iwuoha, E., 2020. Electro-photovoltaics of Polymer-stabilized Copper–Indium Selenide Quantum Dot. *Electroanalysis*, *32*, pp.3086-3097.
- [30] Agrawal, V., Jain, K., Arora, L. and Chand, S., 2013. Synthesis of CdS nanocrystals in poly (3-hexylthiophene) polymer matrix: optical and structural studies. *Journal of Nanoparticle Research*, *15*, pp.1-14.
- [31] Sun, C.J., Zhao, X.Q., Wang, P.F., Wang, H. and Han, B.H., 2017. Thiophene-based conjugated microporous polymers: synthesis, characterization and efficient gas storage. *Science China Chemistry*, *60*, pp.1067-1074.
- [32] Ismail, B.A., Nassar, D.A., Abd El-Wahab, Z.H. and Ali, O.A., 2021. Synthesis, characterization, thermal, DFT computational studies and anticancer activity of furfural-type schiff base complexes. *Journal of Molecular Structure*, *1227*, p.129393.
- [33] Ahmed, Y.M., Mahmoud, W.H., Omar, M.M. and Mohamed, G.G., 2021. Synthesis, Characterization and Biological Activity of Transition Metals Schiff Base Complexes Derived from 4, 6-Diacetylresorcinol and 1, 8-Naphthalenediamine. *Journal of Inorganic and Organometallic Polymers and Materials*, pp.1-21.
- [34] Kareem, M.J., Al-Hamdani, A.A.S., Ko, Y.G., Al Zoubi, W. and Mohammed, S.G., 2021. Synthesis, characterization, and determination antioxidant activities for new Schiff base complexes derived from 2-(1H-indol-3-yl)-ethylamine and metal ion complexes. *Journal of Molecular Structure*, *1231*, p.129669.
- [35] Fuentes-Pérez, M., Nicho, M.E., Sotelo-Lerma, M., Fuentes-Ríos, J.L., Castrellón-Uribe, J., León-Silva, U., Hernández-Guzmán, F. and García-Carvajal, S., 2018. Influence of the FeO(OH) nanoparticles concentration in the in-situ synthesis of P3HT. *European Polymer*

Journal, 99, pp.172-179.

- [36] Cui, Z., Coletta, C., Dazzi, A., Lefrancois, P., Gervais, M., Néron, S. and Remita, S., 2014. Radiolytic method as a novel approach for the synthesis of nanostructured conducting polypyrrole. *Langmuir*, 30, pp.14086-14094.
- [37] Fuentes-Pérez, M., Nicho, M.E., Hu, H., Martínez-Alonso, C. and Cadenas-Pliego, G., 2018. Effect of Sb₂S₃ micro-rod incorporation on the polymerization of 3-hexylthiophene. *Journal of Materials Science: Materials in Electronics*, 29, pp.15715-15725.
- [38] Warad, I., Ali, O., Al Ali, A., Jaradat, N.A., Hussein, F., Abdallah, L., Al-Zaqri, N., Alsalmeh, A. and Alharthi, F.A., 2020. Synthesis and spectral Identification of three Schiff bases with a 2-(piperazin-1-yl)-N-(thiophen-2-yl methylene) ethanamine moiety acting as novel pancreatic lipase inhibitors: Thermal, DFT, antioxidant, antibacterial, and molecular docking investigations. *Molecules*, 25, p.2253.
- [39] Magubane, S.S., Muller, T.F.G., Oliphant, C.J. and Arendse, C.J., 2021. Evaluation of rr-P3HT solar cells with low amounts of SiNWs. *Materials Today: Proceedings*, 36, pp.343-348.
- [40] Mahendia, P., Chauhan, G., Wadhwa, H., Kandhol, G., Mahendia, S., Srivastava, R., Sinha, O.P., Clemons, T.D. and Kumar, S., 2021. Study of induced structural, optical and electrochemical properties of Poly (3-hexylthiophene)(P3HT),[6, 6]-phenyl-C61-butyric-acid-methyl-ester (PCBM) and their blend as an effect of graphene doping. *Journal of Physics and Chemistry of Solids*, 148, p.109644.
- [41] Holmes, N.P., Ullum, S., Sista, P., Burke, K.B., Wilson, M.G., Stefan, M.C., Zhou, X., Dastoor, P.C. and Belcher, W.J., 2014. The effect of polymer molecular weight on P3HT: PCBM nanoparticulate organic photovoltaic device performance. *Solar Energy Materials and Solar Cells*, 128, pp.369-377.
- [42] Nicho, M.E., García-Escobar, C.H., Arenas, M.C., Altuzar-Coello, P., Cruz-Silva, R. and Güizado-Rodríguez, M., 2011. Influence of P3HT concentration on morphological, optical and electrical properties of P3HT/PS and P3HT/PMMA binary blends. *Materials Science and Engineering: B*, 176, pp.1393-1400.

- [43] Liou, Y.H., Lo, S.L., Kuan, W.H., Lin, C.J. and Weng, S.C., 2006. Effect of precursor concentration on the characteristics of nanoscale zerovalent iron and its reactivity of nitrate. *Water Research*, 40, pp.2485-2492.
- [44] Chao, C.Y., Chao, C.H., Chen, L.P., Hung, Y.C., Lin, S.T., Su, W.F. and Lin, C.F., 2012. Band structure engineering for low band gap polymers containing thienopyrazine. *Journal of Materials Chemistry*, 22, pp.7331-7341.
- [45] Mei, B.A., Lau, J., Lin, T., Tolbert, S.H., Dunn, B.S. and Pilon, L., 2018. Physical interpretations of electrochemical impedance spectroscopy of redox active electrodes for electrical energy storage. *The Journal of Physical Chemistry C*, 122, pp.24499-24511.
- [46] Huang, J.H., Ibrahim, M.A. and Chu, C.W., 2013. Interfacial engineering affects the photocatalytic activity of poly(3-hexylthiophene)-modified TiO₂. *RSC Advances*, 3, pp.26438-26442.
- [47] Pei, J., Hao, Y.Z., Lv, H.J., Sun, B., Li, Y.P. and Guo, Z.M., 2016. Optimizing the performance of TiO₂/P3HT hybrid solar cell by effective interfacial modification. *Chemical Physics Letters*, 644, pp.127-131.
- [48] Kobchikova, P.P., Efimov, S.V., Khodov, I.A. and Klochkov, V.V., 2021. Features of spatial structures of cyclosporins D, E and G revealed by NMR and MD simulations. *Journal of Molecular Liquids*, 336, p.116244.
- [49] Bakour, A., Bajjou, O., Baitoul, M., Massuyeau, F., Wéry, J., Maaza, M. and Faulques, E., 2021. A study of the temperature effect on photoluminescence of the P3HT/MWNT nanocomposites. *Materials Today: Proceedings*, 36, pp.549-552.
- [50] Wang, T., Yang, X.Y., Bi, P.Q., Niu, M.S., Feng, L., Liu, J.Q. and Hao, X.T., 2019. Effective Exciton Dissociation and Reduced Charge Recombination in Thick-Film Organic Solar Cells via Incorporation of Insulating Polypropylene. *Solar RRL*, 3, p.1900087.
- [51] Khan, M.T., Almohammed, A., Shkir, M. and Aboud, S.W., 2021. Effect of Ag₂S nanoparticles on optical, photophysical, and electrical properties of P3HT thin films. *Luminescence*, 36, pp.761-768.
- [52] Qin, L., Liu, X., Zhang, X., Yu, J., Yang, L., Zhao, F., Huang, M., Wang, K., Wu, X., Li,

- Y. and Chen, H., 2020. Triplet Acceptors with a D-A Structure and Twisted Conformation for Efficient Organic Solar Cells. *Angewandte Chemie International Edition*, 59, pp.15043-15049.
- [53] Finck, B.Y. and Schwartz, B.J., 2013. Understanding the origin of the S-curve in conjugated polymer/fullerene photovoltaics from drift-diffusion simulations. *Applied Physics Letters*, 103, p.143.
- [54] Rafique, S., Abdullah, S.M., Badieli, N., McGettrick, J., Lai, K.T., Roslan, N.A., Lee, H.K.H., Tsoi, W.C. and Li, L., 2020. An insight into the air stability of the benchmark polymer: fullerene photovoltaic films and devices: A comparative study. *Organic Electronics*, 76, p.105456.
- [55] Bastos, J.P., Voroshazi, E., Fron, E., Brammertz, G., Vangerven, T., Van der Auweraer, M., Poortmans, J. and Cheyns, D., 2016. Oxygen-induced degradation in C60-based organic solar cells: relation between film properties and device performance. *ACS Applied Materials & Interfaces*, 8, pp.9798-9805.



Chapter 5

Effect of Reaction Time on the Optical, Electrochemical and Photovoltaic Properties of Polypropylenimine Tetra(pyrrole)-co-Poly(3-hexylthiophene-2,5-diyl)

Abstract

The energy demand in the current society is increasing continuously and the need for energy resources which are not negative to the environment unlike fossil fuels is growing. Organic photovoltaic cells (OPVs) are possible alternative to fossil fuels and expensive inorganic based photovoltaic cells since they offer advantageous properties such as low cost of fabrication, flexibility, environmentally friendly and ease of fabrication. Currently, there are studies focusing on developing new organic donor material in order to achieve modified performance of OPVs. In this study, we are focusing on developing novel polypropylenimine tetra(pyrrole)-co-poly(3-hexylthiophene-2,5-diyl) (PPI-Py-co-P3HT) using chemical oxidation co-polymerization method. The effect of reaction time (24, 48 and 72 h) on the spectroscopic, thermal and electrochemical properties of PPI-Py-co-P3HT were investigated. The study revealed that as the reaction time changes, all optical, thermal and electrochemical properties of PPI-Py-co-P3HT are affected. PPI-Py-co-P3HT has been blended with [6,6]-Phenyl C71 butyric acid methyl ester (PC₇₁BM) and their electron transfer mechanism were investigated using electrochemical methods. OPVs of PPI-Py-co-P3HT as a donor material were fabricated. The power conversion efficiency (PCE) of PPI-Py-co-P3HT synthesized for 24, 48 and 72 h were measured to be 0.073, 0.001 and 0.026%, respectively.

5.1. Introduction

OPVs based on π -conjugated polymers as donor materials have attracted a lot of attention in research field and in the commercial communities. This type of OPVs is of interest because of their advantageous properties such as low cost, ease to process and flexibility of the thin films. These properties make OPVs to be more preferred than inorganic photovoltaic cells, but OPVs still suffer low PCE [1]. Significant improvement of the overall performance of OPVs have been achieved by modifying the donor or acceptor materials [2–4].

In order to obtain high performing OPVs, factors such as effective light absorption, effective charge collection and separation; and long exciton diffusion length are necessary [5,6]. There are several methods used aiming to improve the performance of OPVs by modifying the structure of the device, such as the use of tandem structure [7–9], bulk heterojunction interface structure [10,11] and introduction of electron blocking or transport layers [12,13]. To date, the use of bulk heterojunction OPVs is very beneficial for achieving high PCE [14,15]. According to the operating mechanism of OPVs, bulk heterojunction device structure allows sufficient excitons to reach the donor/acceptor interface due to the short diffusion length [16]. But generation of excitons depend on the properties of the donor material such as light absorption and excitons transportation ability [17,18]. Also, according to the operating OPVs mechanism, the distance between the HOMO of the donor material and LUMO of the acceptor material should be appropriate to allow sufficient charge transfer resulting in high open circuit voltage and the organic materials used in the active layer should have a good electron and hole transport property [19].

Poly(3-hexylthiophene) (P3HT) is one of the most studied polymer donor material for OPVs application because of its simple chemical structure, it can be easily synthesized and is the cheapest among other polymer donor materials [20]. In most studies, P3HT is mostly used with fullerene-based acceptors to make up the active layer of OPVs [21–25]. However, P3HT-based photovoltaic cells still suffer low PCE due to wide band gap of P3HT which results in low short circuit current, as a results of low excitons production and high LUMO energy levels [26]. It was observed that when used with fullerene-based acceptors leading to low open circuit voltage due to insufficient electron transfer [26]. When comparing the energy levels, the HOMO and LUMO of P3HT are higher than those of PC₇₁BM. This will allow the separation of the excitons into electrons and

holes at the interface of P3HT and PC₇₁BM. Electrons will be transferred to the LUMO of PC₇₁BM, while holes will be transferred to the HOMO of the P3HT. To achieve sufficient charge separation, the HOMO and LUMO energy levels of P3HT should be ~0.2 and 0.3 eV higher than those of PC₇₁BM, respectively. If the distance between the energy levels is too low, it would be very difficult to get sufficient exciton separation and if the distance between the energy levels is too wide, high energy loss will take place [27,28]. Therefore, it is important to understand how the energy levels of the donor materials are affected during synthesis.

In this work, we synthesized PPI-Py-co-P3HT dendritic polymers under different reaction conditions. The polymers were synthesized using Schiff base reaction method with different reaction time (24, 48 and 72 h). Different properties such as spectroscopic, electrochemical and thermal were investigated. The LUMO energy levels of the PPI-Py-co-P3HT synthesized under different reaction times were compared with the LUMO energy levels of PC₇₁BM. The study revealed that as the reaction time changes the position of the energy levels also changes. OPVs of PPI-Py-co-P3HT synthesized using different reaction times were fabricated. The minimum performance of OPVs were achieved for PPI-Py-co-P3HT synthesized for 48 h due to its higher charge transfer resistance.

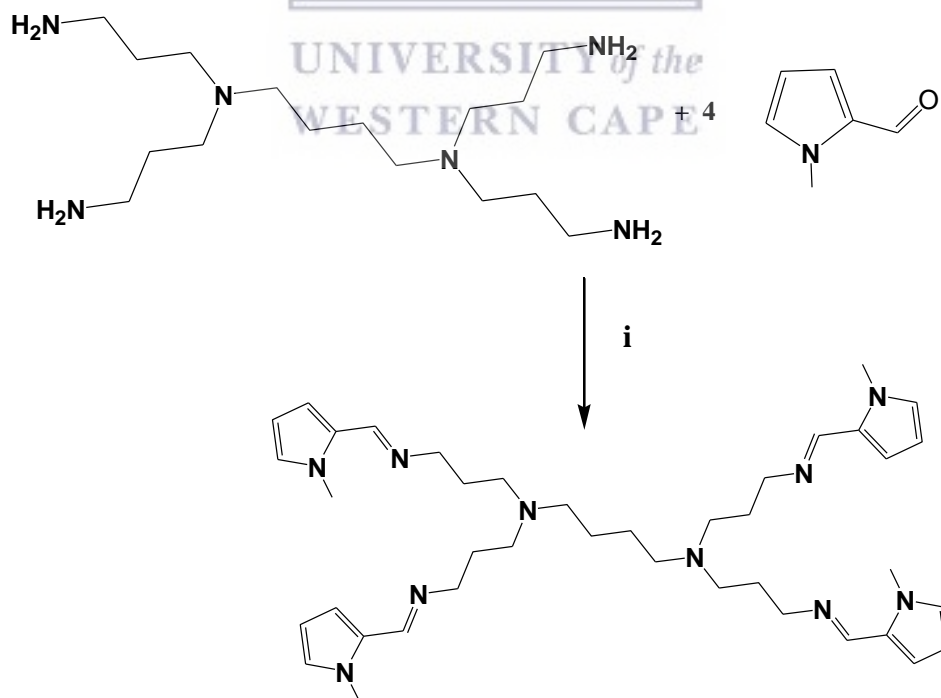
5.2. Materials and Methods

5.2.1. Materials

Generation 1 poly(propylene imine) tetramine (DAB-Am4) dendrimer (pH 12, 25 wt % aq. Soln.), N-Methyl-2-pyrrolicarboxaldehyde (98%), dichloromethane (DCM, 99.9%), deuterated chloroform (CDCl₃, ≥99%), methanol (MeOH, 99.5%), 3-hexylthiophene (≥99%), iron chloride (FeCl₃, ≥99.99%), chloroform (≥99%), acetone (99.3%), tetrabutylammonium hexafluorophosphate (TBAPF₆, ≥99%), PC₇₁BM (99%), poly(3,4-ethylenedioxythiophene) polystyrene sulfonate (PEDOT:PSS, 0.5-1.0% in H₂O, high-conductivity grade), chlorobenzene (99.9%), magnesium sulphate (MgSO₄, ≥99.5%), 2-propylalcohol (99.5%), hellmanex III, silver (Ag) conductive paste and acetonitrile (99.8%) were purchased from Merck (Pty) Ltd., Johannesburg, South Africa and used as received. Indium tin oxide (ITO) substrates were purchased from Ossila Ltd., Sheffield, UK. Deionized water was collected on a Millipore Direct Q3 system from Millipore, Milford, MA, USA.

5.2.2. Synthesis of PPI-Py

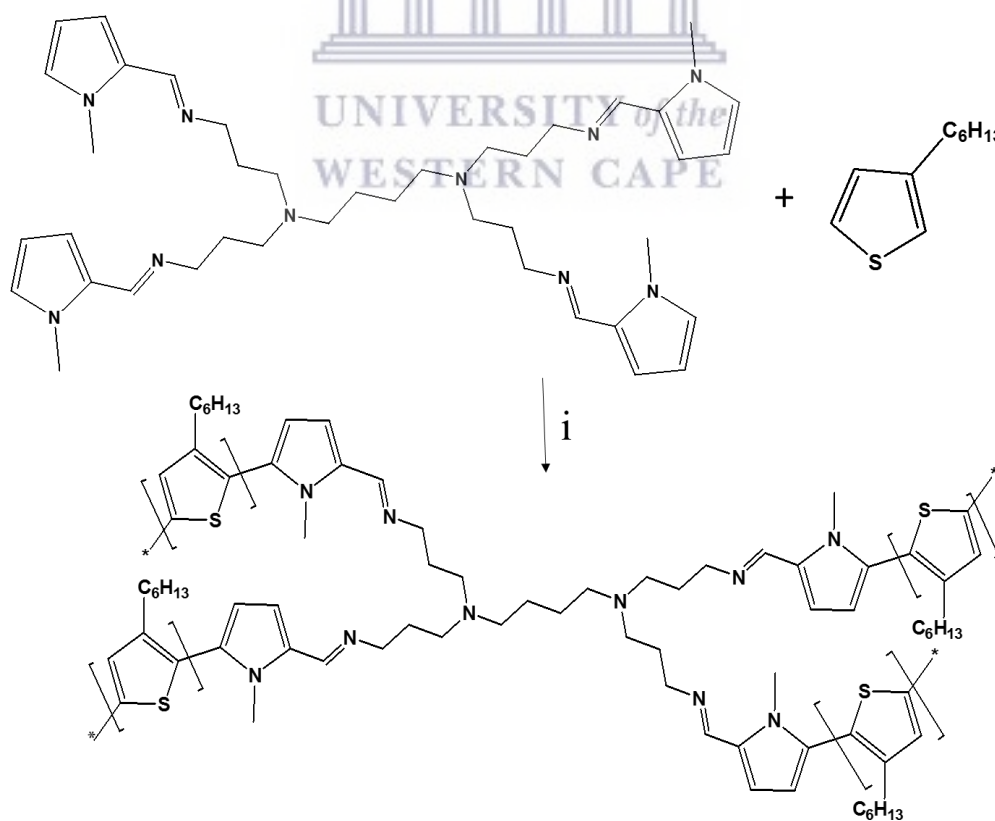
To perform a reaction between primary amines and aldehydes functional groups, Schiff base condensation reaction has been used [29,30]. During synthesis, DAB-Am4 (0.45 g, 1.42 mmol) and N-methylpyrrole-2-carboxaldehyde (0.41 g, 0.95 mmol) were dissolved in 50 mL MeOH. DAB-Am4 was used as limiting reagent and it was in excess. The solution was stirred under nitrogen atmosphere for 48 h at room temperature. Afterwards, the solution was concentrated with rotary evaporator and re-dissolved in 40 mL DCM. The solution was washed three times with deionized water and MgSO_4 was added. Then, the solution was filtered to remove the suspensions of MgSO_4 . The solution was dried using rotary vapor and resulted to a dark brown oily product with actual weight of 0.25 g and percentage yield of 39%. This reaction method is shown schematically in Scheme 5.1. $^1\text{H-NMR}$ (CDCl_3 , 400 MHz): δ_{H} 1.42 (tt, 4H), 1.74-1.78 (tt, 8H), 2.41-2.52 (m, 12H), 3.47-3.51 (t, 8H), 3.89 (s, 12H), 6.10 (d, 4H), 6.45 (dd, 4H), 6.66 (d, 4H), 8.11 (s, 8H). $^{13}\text{C-NMR}$ (CDCl_3 , 400 MHz): δ_{C} 25.21 (4C), 28.82 (2C), 36.45 (4C), 51.82 (4C), 53.00 (4C), 60.22 (2C), 107.92 (4C), 109.51 (4C), 115.66 (4C), 129.98 (4C), 152.27 (4C). HRMS (m/z): Calc. 680.987: 70.55% C, 8.88% H, 20.57% N. Exp. 681.505: 70.49% C, 8.87% H, 20.56% N.



Scheme 5.1: Synthetic route of PPI-Py. (i). MeOH, 48 h.

5.2.3. Synthesis of PPI-Py-co-P3HT

PPI-Py-co-P3HT was synthesized using chemical oxidation polymerization as shown in Scheme 5.2 [31,32] and it was synthesized under three different reaction times. In details, synthesized PPI-Py (0.10 g, 0.15 mmol) and 3-hexylthiophene (1.06 mL, 0.99 g, 5.87 mmol) were added into a 250 mL one neck round bottom flask containing 100 mL chloroform. The solution was stirred under nitrogen atmosphere for 30 min. The suspensions of FeCl_3 (3.81 g, 23.5 mmol) in 50 mL were slowly added to the mixture above. The resulting mixture was left to react at different reaction times (24 h, 48 h and 72 h) at 60°C . After the reaction time is complete, the resulting mixture was poured in a thimble and placed in a Soxhlet extractor (size large, 200 mL extractor volume, Merck (Pty) Ltd.). It was washed with MeOH for 24 h and lastly, with acetone for another 24 h. The product was extracted with chloroform for 24 h using Soxhlet extractor. The solvent was removed with rotary evaporator and left in an oven at 50°C for overnight to dry to give a dark purple product. The actual weights of PPI-Py synthesized for 24, 48 and 72 h were found to be 0.42, 0.31 and 0.35 g, respectively.



Scheme 5.2: Synthetic route of PPI-Py-co-P3HT. (i). FeCl_3 , chloroform, 60°C .

5.2.4. Characterization techniques

Nuclear magnetic resonance (NMR) studies were done using A Bruker 400 MHz Avance III HD Nanobay Spectrometer equipped with a 5 mm BBO Probe at 298 K from Bruker, Karlsruhe, Germany. Fourier-transform infrared (FTIR) studies were performed with Spectrum-100 FTIR Spectrometer from PerkinElmer (Pty) Ltd., Midrand, South Africa. Mass spectroscopy analysis was performed using Waters Synapt G2 Quadrupole Time-of-Flight (QTOF) Mass Spectrometer (MS) connected to a Waters Acquity Ultra-Performance Liquid Chromatograph (UPLC) (Waters, Milford, MA, USA). Thermal gravimetric analysis (TGA) studies were performed using The Simultaneous Thermal Analyzer PerkinElmer STA 6000 Instrument (PerkinElmer (Pty) Ltd.). Transmission electron microscope (TEM) images were done using FEI Tecnai T20 TEM from FEI company, Hillsboro, OR, USA. The ultraviolet-visible (UV-Vis) measurements were done using Nicolet Evolution 100 from Thermo Electron Corporation, Altrincham, UK. Scanning electron microscope (SEM) images were obtained using Tescan MIRA3 RISE SEM from Tescan, Brno, Czech Republic and elemental analysis was performed using FEI NovaNano SEM from FEI company, hillsboro, OR, USA. Photoluminescence spectra were obtained using NanoLog from Horiba Jobin Yvon, Edison, NJ, USA. X-ray diffraction (XRD) analysis was obtained using D8-Advanced Diffractometer from Bruker AXS, Billerica, MA, USA. Electrochemical studies were conducted on CHI700E-Potentiostat from CH Instruments, Inc, Bee Cave, TX, USA using indium tin oxide glass substrate (ITO) glass substrate working electrode from Oscilla, Sheffield, UK, platinum wire counter electrode from Goodfellow Cambridge Ltd., Huntingdon, UK, silver/silver chloride reference electrode from BASi® in West Lafayette, IN, USA and electrolyte consisting of 0.1 M TBAPF₆/acetonitrile solution. Device characteristics (current density–voltage) were measured with X200 Source Meter Unit from Ossila, Sheffield, UK using an illumination of AM 1.5G, 100 mW cm⁻² supplied by a SciSun-150 Solar Simulator, Class AAA from Sciencetech Inc., London, ON, Canada.

5.2.5. Fabrication of OPVs

ITO substrates were sonicated for 5 minutes in 1% hellmanex solution, 2-propylalcohol and acetone, separately. PEDOT:PSS was coated onto clean substrates by spin coating method. Spin coated PEDOT:PSS onto ITO substrate was annealed at 150°C for 5 min. PPI-Py-co-P3HT:PC₇₁BM active layer solution was prepared by dissolving PPI-Py-co-P3HT and PC₇₁BM in

chlorobenzene. The resulting solution was stirred for overnight at 60°C. Active layer solution was spun coated onto PEDOT:PSS coated ITO glass substrate. After, the coated substrate was annealed at 100°C for 5 min. Ag conductive paste as cathode electrode was coated and annealed at 100°C for 5 min to complete the device.

5.3. Results and discussion

5.3.1. NMR analysis of PPI-Py and PPI-Py-co-P3HT

The ^1H -NMR of PPI-Py is shown in Figure 5.1A. The integrals indicated the detection of 60 protons which correspond to the number of protons on PPI-Py structure. This confirms a successful synthesis of PPI-Py. The signals at 1.42 and 1.74-1.78 ppm are assigned to $-\text{CH}_2-$ groups that are not directly bonded to nitrogen. The signals at 2.41-2.52 ppm are assigned to the $-\text{CH}_2-$ groups bonded to a nitrogen and the 3.47-3.51 ppm signals are assigned to the $-\text{CH}_2-$ bonded to an imine functional group. The signal at 3.89 ppm assigned to the CH_3- group attached to pyrrole. The signals at 6.10 and 6.45 ppm are assigned to the β -position protons of pyrrole, while the signal at 6.66 ppm is assigned to α -proton. The signal at 8.11 ppm is assigned to the proton attached to the imine functional group. The ^{13}C -NMR of PPI-Py is shown in Figure 5.1B. Signals due to presence of carbon in the structure of PPI-Py are observed and assigned. The signals at 25.21, 28.82, 51.82, 53.0 and 60.22 ppm are owing to the methylene group carbons ($-\text{CH}_2-$) of the poly(polypropylene imine) part of PPI-Py structure. The signal at 36.45 ppm is ascribed to the methyl group carbon (CH_3-N) bonded to pyrrole [33]. The signals at 107.92, 109.51 and 115.66 ppm are consigned to the $-\text{CH}-$ carbons on the thiophene ring. The signals at 129.98 and 152.27 ppm are assigned to the tertiary carbon of thiophene and imine group carbon, respectively. The ^{13}C -NMR spectrum presented additional signals at 54.14, 127.45 and 132.04 ppm. This could be due to the impurities encountered during sample preparation for analysis [33]. Synthesis of PPI-Py was also confirmed by mass spectroscopy with experimental mass found to be close to the theoretical mass (Figure A3). Figure 5.2 shows the ^1H -NMR of PPI-Py-co-P3HT synthesized using different reaction times. The spectra are dominating by the signals of P3HT. This can be explained by the space interactions between hexyl-group of P3HT and PPI-Py protons which turn to affect the detection of PPI-Py signals. The signals of methyl-group attached pyrrole were observed at 3.42, 3.52 and 3.51 ppm for PPI-Py-co-P3HT synthesized for 24, 48 and 72 h, respectively. The signals at 7.45 ppm (24 h),

and 7.54 ppm (for both 48 and 72 h) were assigned to imine-proton. When comparing the $^1\text{H-NMR}$ spectra of PPI-Py and PPI-Py-co-P3HT, the methyl-group attached to pyrrole and imine-proton signals are more de-shielded in PPI-Py-co-P3HT. This is because the presence of P3HT affects the electron cloud around methyl-group attached to pyrrole and imine-proton causing their signals to be de-shielded.



Figure 5.1:(A) $^1\text{H-NMR}$ and (B) $^{13}\text{C-NMR}$ of PPI-Py.

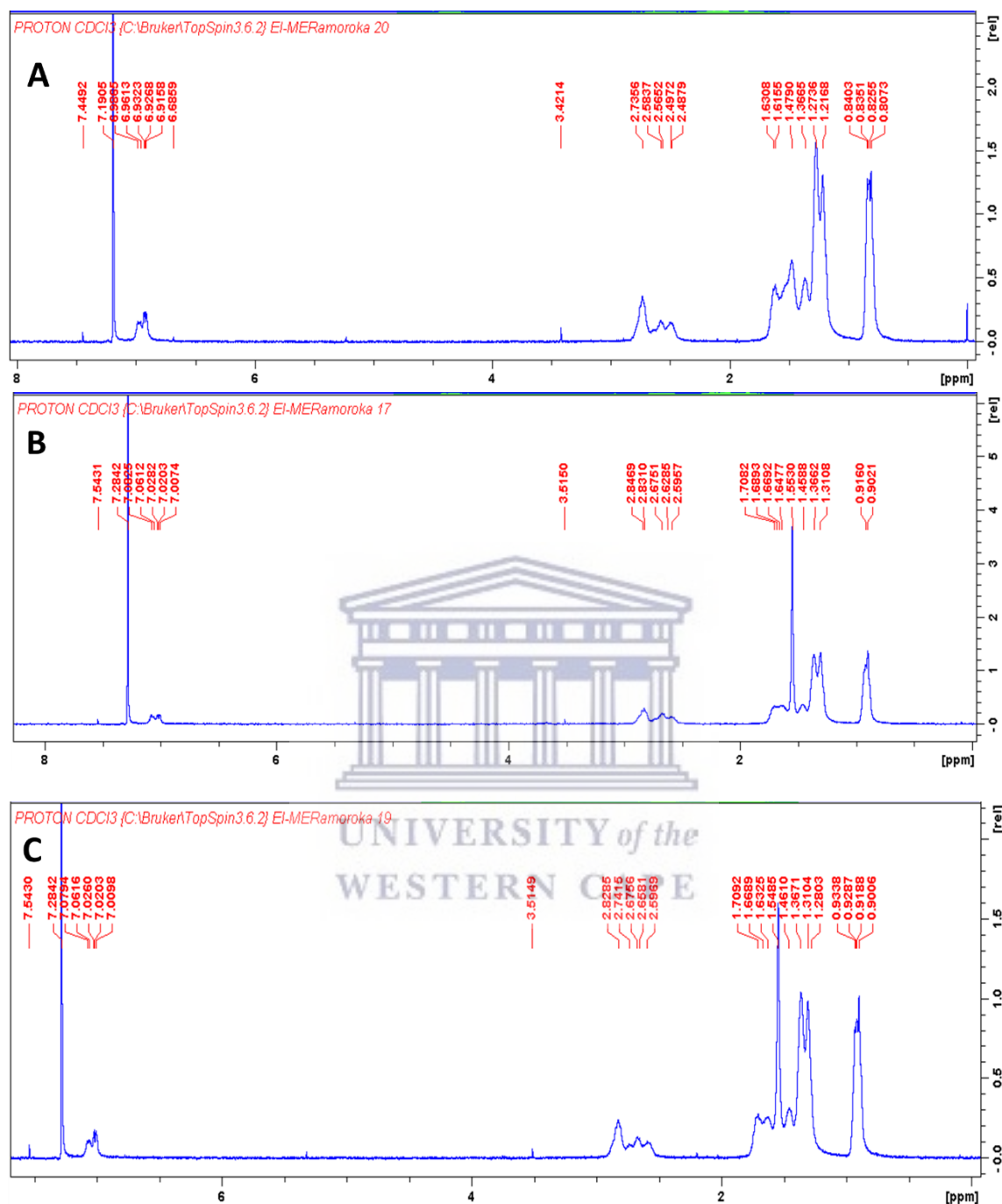


Figure 5.2: ¹H-NMR of PPI-Py-co-P3HT (A) 24 h, (B) 48 h and (C) 72 h.

5.3.2. FTIR studies of PPI-Py and PPI-Py-co-P3HT

The molecular structure of the synthesized PPI-Py and PPI-Py-co-P3HT was studied by FTIR and the results are shown in Figure 5.3. The presence of the bands at 3102, 2940 and 2025 cm^{-1} are attributed to C–H, –CH₃ and –CH₂– group in the structure of PPI-Py [34]. The band at 1642 cm^{-1}

is attributed to C=N stretching mode. The presence of pyrrole ring has been seen by the characteristic vibrational bands at 1483, 1426 and 728 cm^{-1} regions. The bands at 1302 and 1089 cm^{-1} are attributed to the C–C and C–N groups, respectively [35]. All three PPI-Py-co-P3HT synthesized at different reaction times have similar print of their spectra. But the spectra of all three PPI-Py-co-P3HT have weaker bands when compared to the spectra of PPI-Py. This is an indication that polymerization took place and PPI-Py interacted strongly with P3HT. It can be seen that as the reaction time increases from 24 h to 72 h, the intensity of the bands also changes. This is an indication that as the reaction time changes, the chain length of PPI-Py-co-P3HT also changes [36,37].

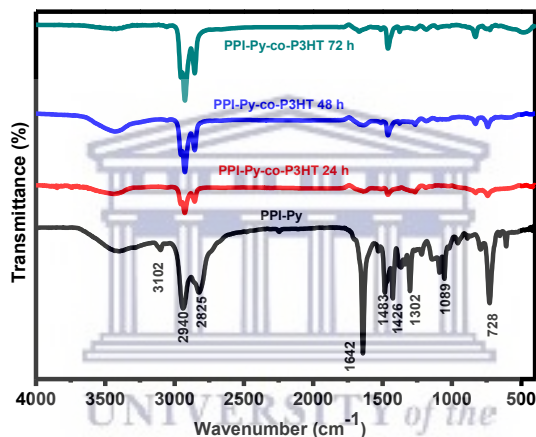


Figure 5.3: FTIR spectra of PPI-Py and PPI-Py-co-P3HT synthesized at 24, 48 and 72 h.

5.3.3. TGA spectra of PPI-Py and PPI-Py-co-P3HT

Figure 5.4 shows the TGA thermograms of PPI-Py-co-P3HT synthesized at different reaction temperatures and PPI-Py in nitrogen atmosphere. As clearly shown by the thermograms, the decomposition of PPI-Py and PPI-Py-co-P3HT occurs through three and two stages mechanism, respectively. In the first stage, PPI-Py shows a weight loss of 5% in the temperature range of 70–120°C, PPI-Py-co-P3HT synthesized for 24, 48 and 72 h show a weight loss of 11 (55–408°C), 16 (71–418°C) and 12% (91–425°C), respectively. This weight loss at first stage is due to the removal of coordinated water and other solvents used during purification such as chloroform and MeOH [38,39]. The temperature ranges of PPI-Py-co-P3HT for the first stage are too wide because they cover the weight loss of small molecular weight PPI-Py-co-P3HT and low linear chain P3HT byproducts. In stage two, PPI-Py thermogram shows a weight loss of 37% (215–296°C) due to

melting and partial decomposition of PPI-Py. PPI-Py-co-P3HT synthesized for 24, 48 and 72 h show a weight loss of 42 (440-498°C), 33 (448-496°C) and 35% (449-500°C), respectively. This represents the decomposition of PPI-Py-co-P3HT and it appears at different temperature range as the reaction time changes. This indicates that PPI-Py-co-P3HT materials with different chain lengths were synthesized at different reaction times. In the third stage, PPI-Py shows a weight loss of 18% (355-466°C) and it represents the decomposition of PPI-Py. At 650°C, PPI-Py still retained weight of 16%, while PPI-Py-co-P3HT still have a weight of 29 (24 h), 34 (48 h) and 37% (72 h). this remaining weight is due to solid residues and high molecular weight PPI-Py-co-P3HT [40,41]. These results revealed that the incorporation of P3HT onto PPI-Py turns to increase thermal stability of PPI-Py and that the reaction time influence thermal stability. The thermal decomposition stability order of PPI-Py < PPI-Py-co-P3HT (48 h) < PPI-Py-co-P3HT (24 h) < PPI-Py-co-P3HT (72 h) was obtained.

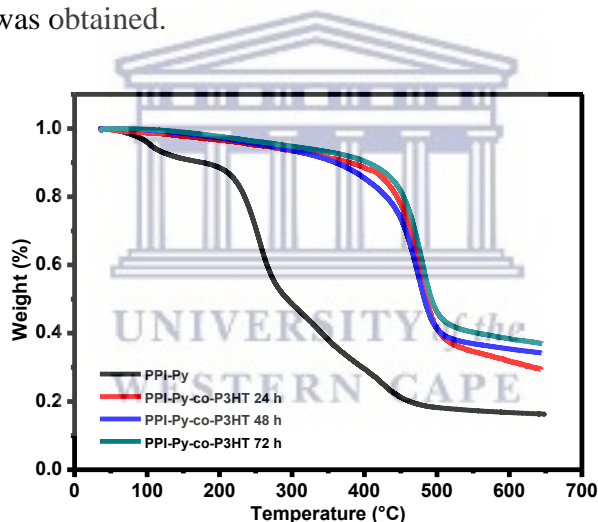


Figure 5.4: TGA thermograms of PPI-Py and PPI-Py-co-P3HT synthesized for 24, 48 and 72 h.

5.3.4. UV-Vis studies of PPI-Py and PPI-Py-co-P3HT

UV-Vis absorption spectra of PPI-Py and three PPI-Py-co-P3HT compounds (which differ in reaction time synthesis) are presented in Figure 5.5A. The band observed at 334 nm on the spectrum of PPI-Py is due to the $n \rightarrow \pi^*$ transition of C=N group [42]. PPI-Py-co-P3HT synthesized for 24, 48 and 72 h showed a maximum absorption at 419, 412 and 417 nm, respectively. This band is related to the $\pi \rightarrow \pi^*$ inter-chain transition of P3HT [43]. But the three PPI-Py-co-P3HT have different wavelength of maximum absorption. Optical bandgaps of PPI-Py and PPI-Py-co-P3HT were determined. This parameter is very important for material which are to

be applied in OPVs. The optical band gaps of PPI-Py and PPI-Py-co-P3HT were determined using Tauc Equation 5.1:

$$\alpha h\nu = A(h\nu - E_g)^n \dots\dots\dots 5.1$$

where h is Planck's constant, ν is frequency, A is a constant, E_g is the band gap and $n=1/2$ [45]. The optical band gap was determined by extrapolating the plot of $\alpha h\nu^2$ vs $h\nu$ to x-axis equal to zero. The optical band gap for PPI-Py was determined from Tauc plot shown in Figure 5.5B to be 4.10 eV and PPI-Py-co-P3HT synthesized for 24, 48 and 72 h (Figure 5.5C, D and E) were found to be 2.29, 2.36 and 2.34 eV, respectively.



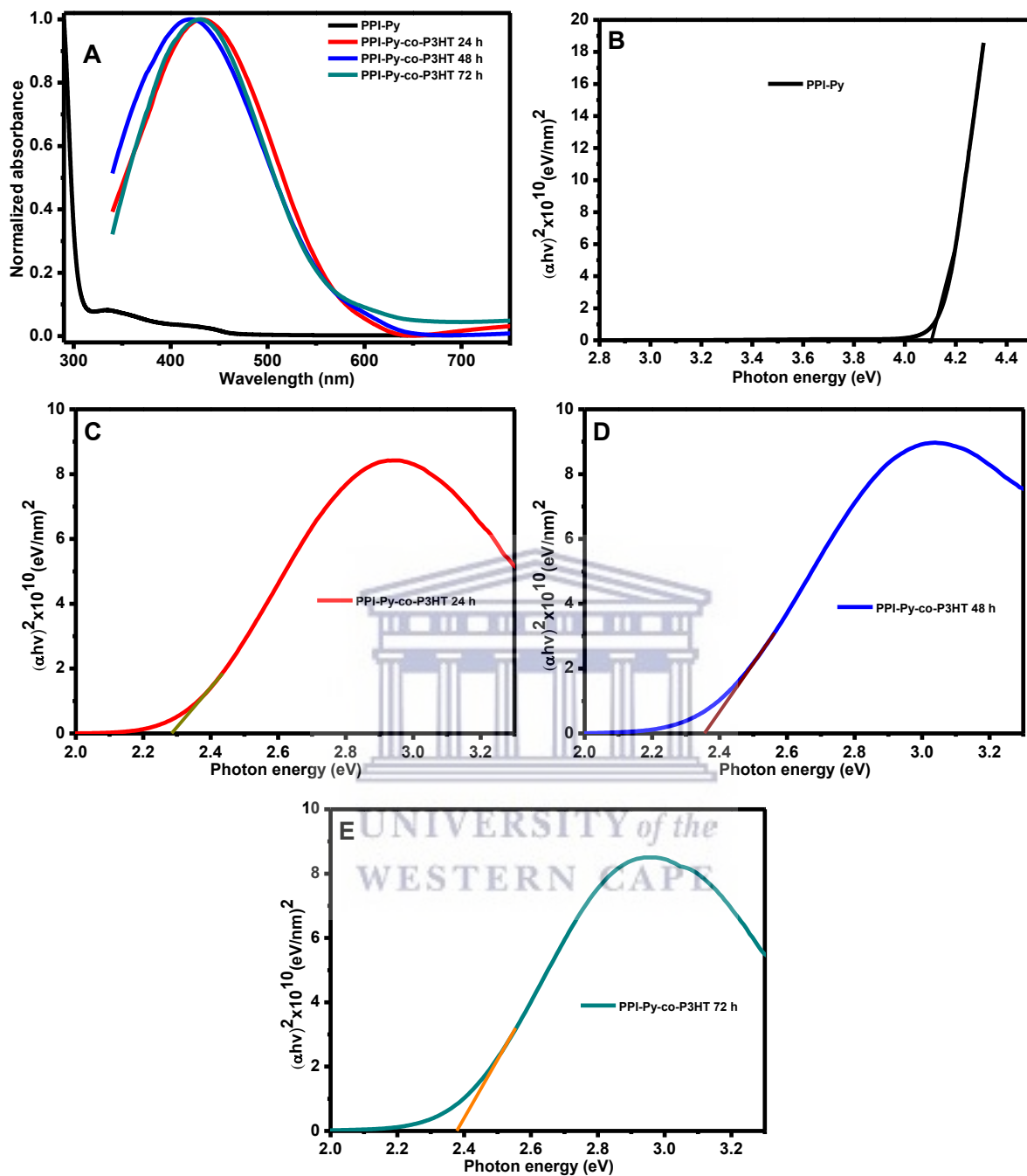


Figure 5.5: (A) UV-Vis absorption spectra and Tauc plots of (B) PPI-Py and PPI-Py-co-P3HT synthesized for (C) 24 h, (D) 48 h and (E) 72 h.

5.3.5. TEM studies of PPI-Py-co-P3HT

Figure 5.6A and Figure 5.6B shows the TEM micrographs of PPI-Py-co-P3HT synthesized for 24 h and 72 h. The micrographs of PPI-Py-co-P3HT shows that the particles are distributed with

different sizes and the presence of agglomeration. Particle sizes were determined to be 11 and 24 nm for 24 and 72 h reaction times, respectively. These findings indicate that the reaction time have an effect on the particle size. The larger sizes of PPI-Py-co-P3HT synthesized for 72 h might be due to coalescing of smaller particles resulting in larger particles. Similar observation of an increase in particle size as the reaction time increases has been reported [46].

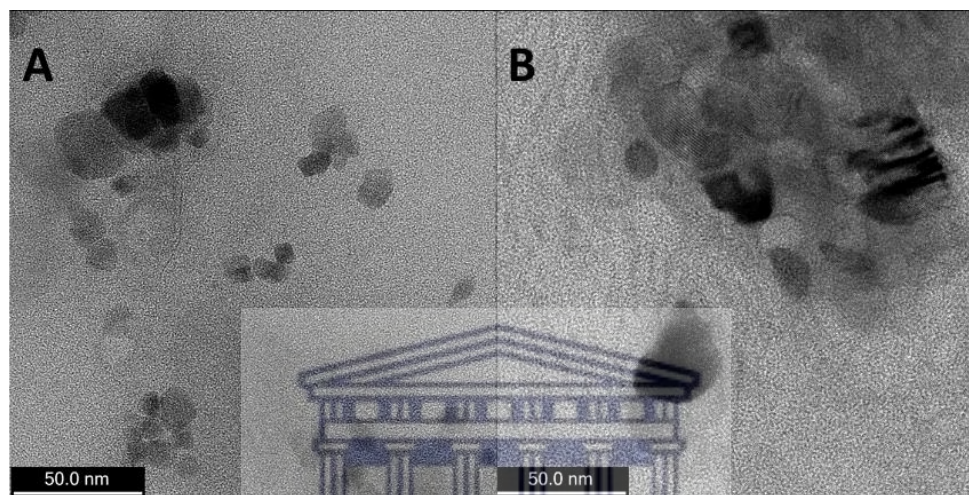


Figure 5.6: TEM micrographs of PPI-Py-co-P3HT synthesized for (A) 24 h and (B) 72 h.

5.3.6. SEM analysis of PPI-Py-co-P3HT

SEM was used to investigate the effect of reaction time on the morphology of PPI-Py-co-P3HT. Obtained SEM images are shown in Figure 5.7 and EDS data is given in Table 5.1. The EDS data in Table 5.1 is the average of five sites measured on each sample. SEM images shows that PPI-Py-co-P3HT synthesized for 48 h has larger particles. All images of PPI-Py-co-P3HT have smooth surface. The chlorine impurity was detected in the samples due to FeCl_3 oxidant used during synthesis.

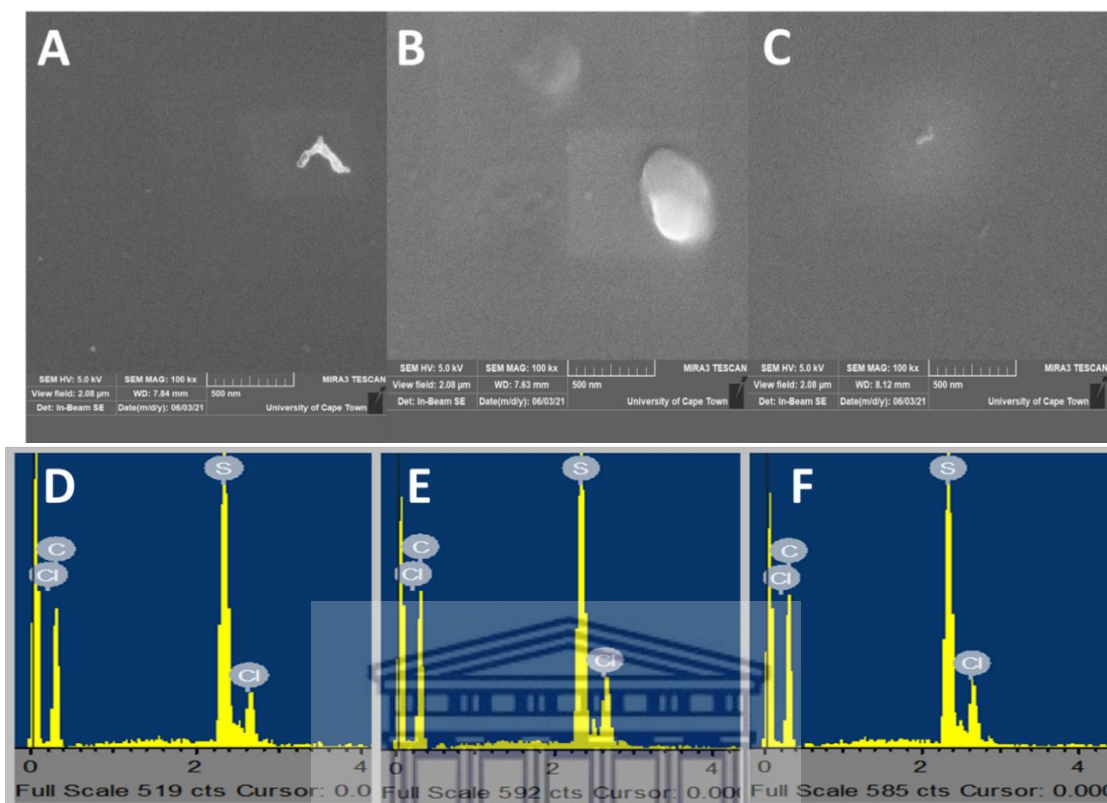


Figure 5.7: SEM images of PPI-Py-co-P3HT synthesized for (A) 24 h, (B) 48 h and (C) 72 h with their EDS spectra D, E and F, respectively.

Table 5.1: EDS data of PPI-Py-co-P3HT synthesized using different reaction times.

Sample	Carbon (%)	Sulphur (%)	Chlorine (%)	Total (%)
PPI-Py-co-P3HT 24h	81.70	14.56	3.74	100
PPI-Py-co-P3HT 48h	81.55	13.92	4.53	100
PPI-Py-co-P3HT 72h	81.68	14.16	4.17	100

5.3.7. CV studies of PPI-Py-co-P3HT

In order to understand the effect of the co-polymerization time on the electrochemical response of newly synthesized PPI-Py-co-P3HT, CV measurements were performed and the voltammograms are shown in Figure 5.8A. As indicated with green shape in Figure 5.8A, as the co-polymerization time changes, the onset oxidation potential also changes. This indicates that PPI-Py-co-P3HT synthesized at different co-polymerization time are oxidized at different rate indicating that they have different electrochemical band gaps and HOMO energy levels [44]. This observation agrees with the band gaps obtained from UV-Vis studies. Cyclic voltammograms of PPI-Py-co-P3HT synthesized using different reaction times were used to determine their HOMO and LUMO energy

levels. The results obtained are given in Table 5.2. Interestingly, as the co-polymerization time changes, both HOMO and LUMO energy levels also changes as shown in Figure 5.8B. When comparing the distance between the LUMO energy levels of PPI-Py-co-P3HT synthesized in this study and the LUMO energy levels of PC₇₁BM (ΔE_{LUMO}), the PPI-Py-co-P3HT synthesized for 48 h gave low value. Therefore, this indicates that efficient electron transfer and high open circuit voltage can take place from PPI-Py-co-P3HT (48 h) to PC₇₁BM than PPI-Py-co-P3HT 24 and 72 h [47].

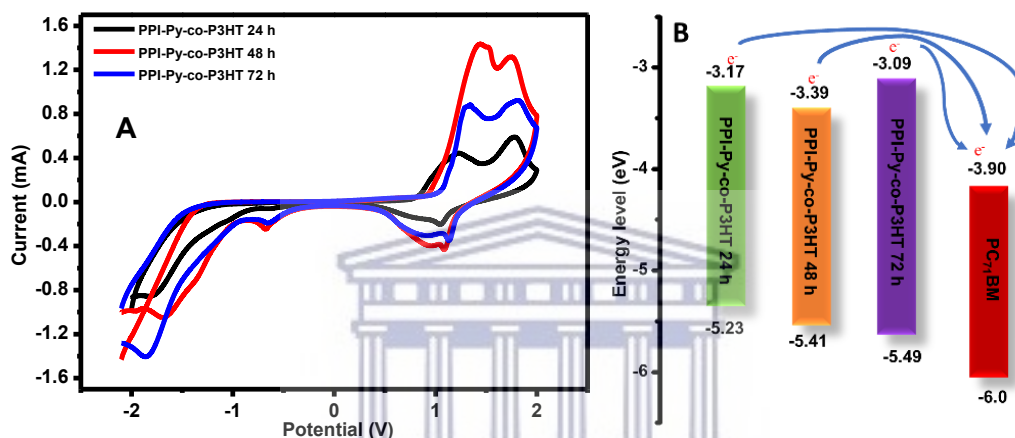


Figure 5.8: (A) CV of PPI-Py-co-P3HT synthesized using different reaction times and (B) energy levels diagram.

Table 5.2: Electrochemical responses of PPI-Py-co-P3HT synthesized at different reaction times.

Compound	Oxidation onset potential (V)	Reduction onset potential (V)	E_{HOMO}^a (eV)	E_{LUMO}^b (eV)	$E_g^{CV}^c$ (eV)	ΔE_{LUMO}^d (eV)
PC ₇₁ BM	-	-	-6.0	-3.90	2.10	-
PPI-Py-co-P3HT 24 h	0.83	-1.23	-5.23	-3.17	2.06	0.73
PPI-Py-co-P3HT 48 h	1.01	-1.01	-5.41	-3.39	2.02	0.51
PPI-Py-co-P3HT 72 h	1.09	-1.09	-5.49	-3.09	2.40	0.81

Obtained with CV method, $^a E_{HOMO} = -(E_{oxidation-onset} - E_{Ferrocene}) + 4.8$, $^b E_{LUMO} = -(E_{reduction-onset} - E_{Ferrocene}) + 4.8$ eV, $^c E_g^{CV}$ was estimated using the equation: $E_g^{CV} = E_{LUMO} - E_{HOMO}$ and $^d \Delta E_{LUMO}$ was estimated using equation: $\Delta E_{LUMO} = E_{LUMO-donor} - E_{LUMO-acceptor}$.

5.3.8. EIS studies of PPI-Py, PPI-Py-co-P3HT and PPI-Py-co-P3HT:PC₇₁BM composite

EIS spectra of PPI-Py and PPI-Py-co-P3HT are shown in Figure 5.9. The circuit used to fit the spectra shown as an inset in Figure 5.9A. The component R_s signifies the ITO glass working electrode resistance, R_{ct1} signifies the charge transfer resistance at the interface of electrolyte and ITO electrode and R_{ct2} signifies the charge transfer resistance at the interface of electrolyte and

PPI-Py-co-P3HT coated on ITO glass electrode [48]. Figure 5.9A shows the Nyquist plots of PPI-Py and different PPI-Py-co-P3HT based on time used during synthesis. The value of R_{ct} was found to be 1005 Ω for PPI-Py and for PPI-Py-co-P3HT synthesized for 24, 48 and 72 h were found to be 325.80, 357.7 and 245.90 Ω , respectively. After modifying PPI-Py with P3HT, R_{ct} drastically decreases with PPI-Py-co-P3HT synthesized for 24 h having the lowest. This is due to the presence of highly conductive P3HT because of its conjugated double bonds [49]. The lower R_{ct} of PPI-Py-co-P3HT (24 h) suggest that it allows faster electron transfer than the ones synthesized for 48 and 72 h. Figure 5.9B presents Nyquist plots showing the comparison of PPI-Py-co-P3HT with and without PC₇₁BM. After blending with PC₇₁BM, R_{ct} decreases to 270.0, 328.80 and 234.6 Ω for PPI-Py-co-P3HT synthesized for 24, 48 and 72 h, respectively. These findings suggest that the PPI-Py-co-P3HT synthesized for 72 h and its composite has the lowest value of R_{ct} . This indicates faster ion diffusion from the electrolyte through the PPI-Py-co-P3HT (72 h) and its composite to the electrode [50]. The lower R_{ct} in PPI-Py-co-P3HT:PC₇₁BM composite shows that PC₇₁BM served as an acceptor for electrons generated by PPI-Py-co-P3HT that successfully decrease recombination of charges. Figure 5.9C present the impedance vs log frequency plot comparing PPI-Py and PPI-Py-co-P3HT. It was observed that PPI-Py showed maximum impedance of 1030 Ω at lower frequency and decreases as the frequency increases. PPI-Py-co-P3HT synthesized for 24, 48 and 72 h showed a maximum impedance of 425, 362 and 331 Ω , respectively, at lower frequency. This decrease in impedance of PPI-Py-co-P3HT as compared to PPI-Py, it indicates fast electron conduction through PPI-Py-co-P3HT and these results agree with the lower value of R_{ct} obtained. Therefore, PPI-Py-co-P3HT (72 h) is the most conductive since it has the lowest value of impedance and R_{ct} . After blending PPI-Py-co-P3HT with PC₇₁BM (Figure 5.9D), the value of impedance decreases further. This decrease in impedance is due to efficient electron transfer from PPI-Py-co-P3HT to PC₇₁BM.

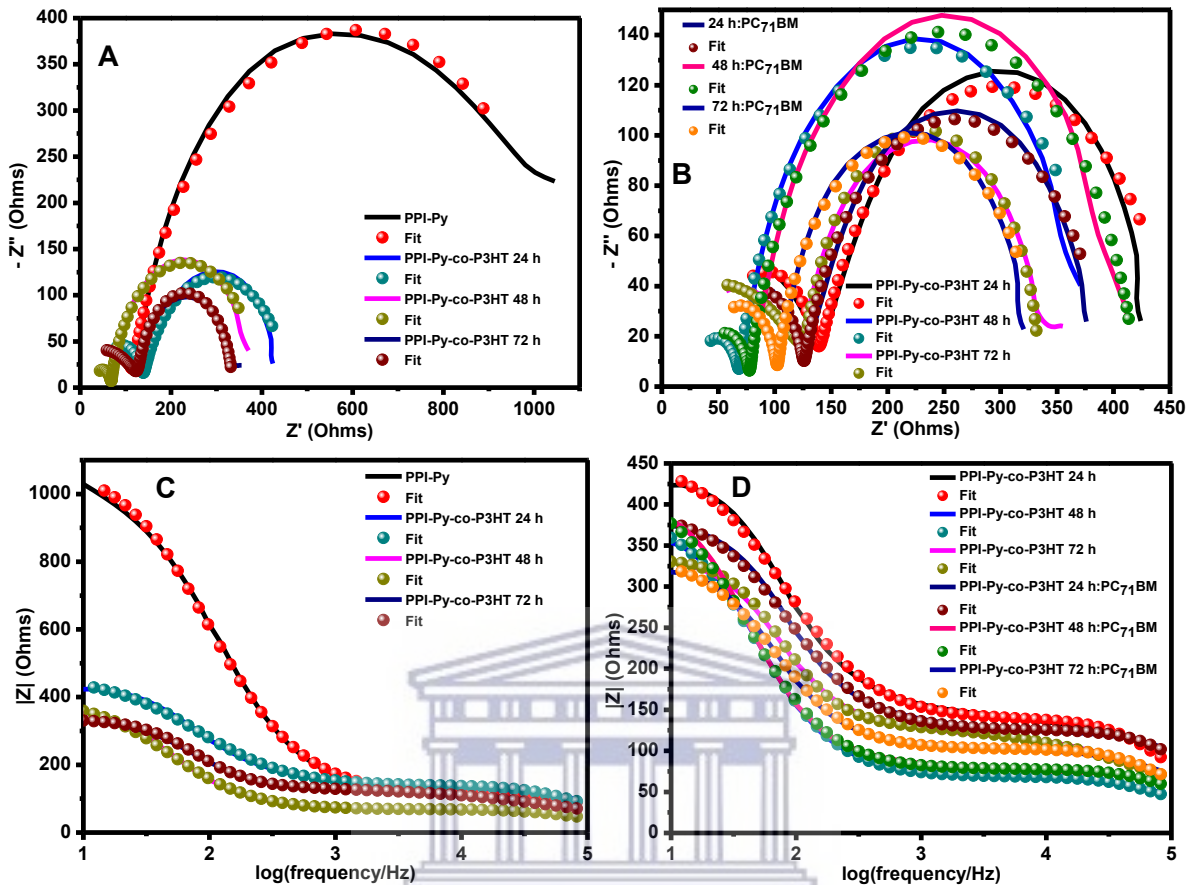


Figure 5.9: Nyquist plot of (A) PPI-Py compared with PPI-Py-co-P3HT and (B) PPI-Py-co-P3HT with and without PC₇₁BM. Bode plot of (C) PPI-Py compared with PPI-Py-co-P3HT and (D) PPI-Py-co-P3HT with and without PC₇₁BM.

5.3.9. Photoluminescence studies of PPI-Py-co-P3HT

Figure 5.10 shows the photoluminescence spectra of different PPI-Py-co-P3HT in chlorobenzene. The emission spectra were obtained using the excitation wavelength of 420 nm. The maximum emission bands for PPI-Py-co-P3HT synthesized for 24, 48, and 72 h appeared at 566, 563 and 563 nm, respectively. These findings revealed that emission bands of PPI-Py-co-P3HT synthesized for 24 h is more red-shifted than 48 and 72 h (shown in Figure 5.10D). The Stokes shifts of PPI-Py-co-P3HT synthesized at 24, 48 and 72 h are 116, 125 and 123 nm. The Stokes shift of the emission band compared to excitation band reveals atomic relaxation upon excitation. When electrons are into the excited states by absorption of light, the P3HT conformation adopts more regular structure to allow stability in the excited state, which is supported by red-shift of the

emission band [51,52]. The smaller Stokes shift in PPI-Py-co-P3HT synthesized for 24 h suggests that its ground state less regiorandom conformation and more regioregular conformation in comparison with PPI-Py-co-P3HT synthesized for 48 and 72 h.

Photoluminescence spectra of PPI-Py-co-P3HT blends with PC₇₁BM are also presented in Figure 5.10. The effect of photoluminescence quenching was used to study the behaviour of electron-hole pair. About 92.42, 89.82 and 90.02% of the photoluminescence intensities of PPI-Py-co-P3HT synthesized for 24, 48 and 72 h, respectively, were quenched in their blends with PC₇₁BM. These quenching of PPI-Py-co-P3HT intensity indicates successful splitting of electron-hole pair and transfer of electrons from PPI-Py-co-P3HT donor to PC₇₁BM. Theoretically, all the intensity of the donor and acceptor blends must not give any intensity to indicate a complete electron-hole pair separation and charge transfer [29]. Therefore, a blend that result to higher quenching percentage has sufficient electron-hole pair separation and charge transfer.



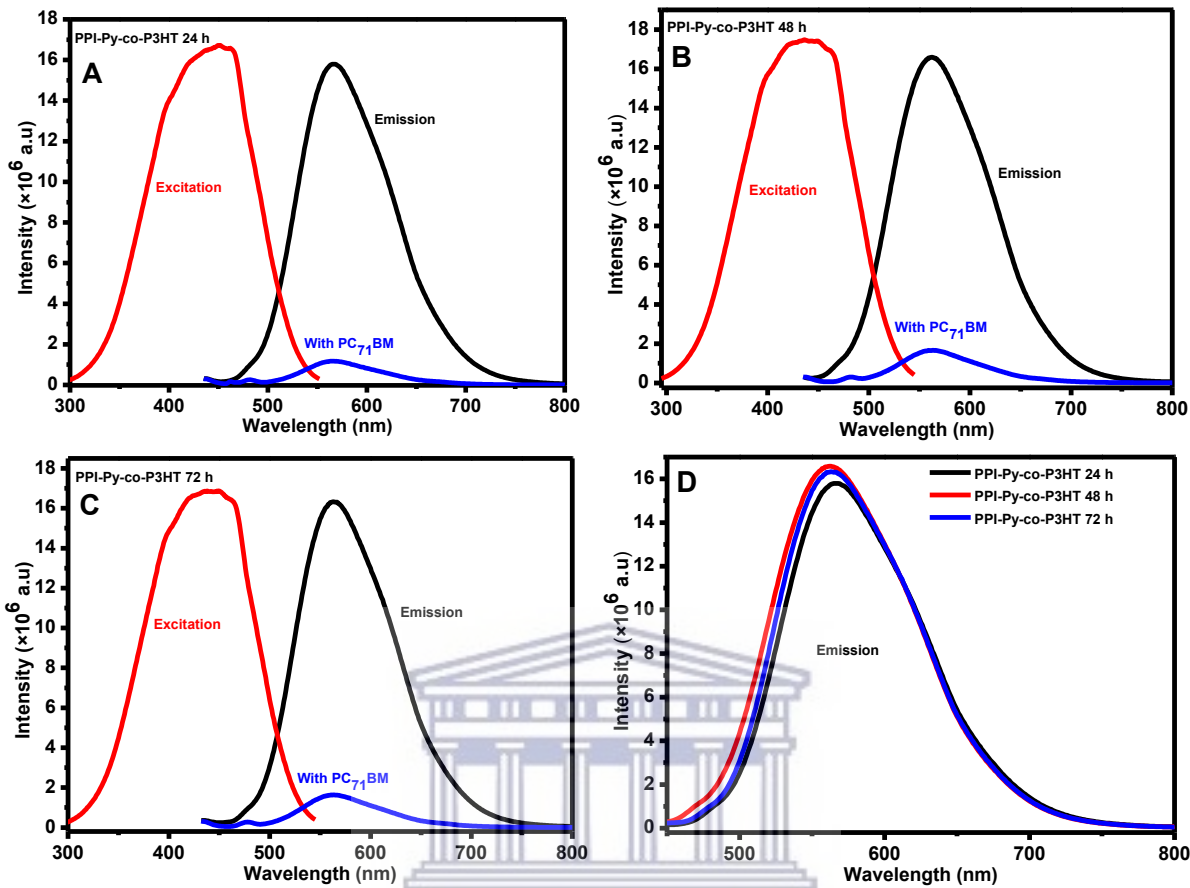


Figure 5.10: Photoluminescence studies of PPI-Py-co-P3HT synthesized for (A) 24, (B) 48 and (C) 72 h. (D) Comparison of emission spectra of PPI-Py-co-P3HT synthesized with different polymerization times.

5.3.10. XRD analysis of PPI-Py-co-P3HT

XRD studies of PPI-Py-co-P3HT were done to investigate the morphology and crystallization as the polymerization time increases. The XRD patterns of PPI-Py-co-P3HT obtained using different polymerization times are shown in Figure 5.11. All PPI-Py-co-P3HT samples exhibited a diffraction peak at 2θ of $\sim 5.6^\circ$ corresponding to the miller indices of (100) [53,54]. This diffraction peak is attributed to the crystalline phase of PPI-Py-co-P3HT [55]. The crystallinity of PPI-Py-co-P3HT is directly related to the intensity and full-width at half maximum (FWHM) of the diffraction peak at 2θ of $\sim 5.6^\circ$ [56]. The FWHM values of PPI-Py-co-P3HT synthesized for 24, 48 and 72h were 0.45° , 0.62° and 0.52° , respectively. The intensity of PPI-Py-co-P3HT synthesized for 24h is

higher than those of 48 and 72 h. These confirm that PPI-Py-co-P3HT synthesized for 24 h is more crystalline since it has smaller FWHM and higher intense diffraction peak.

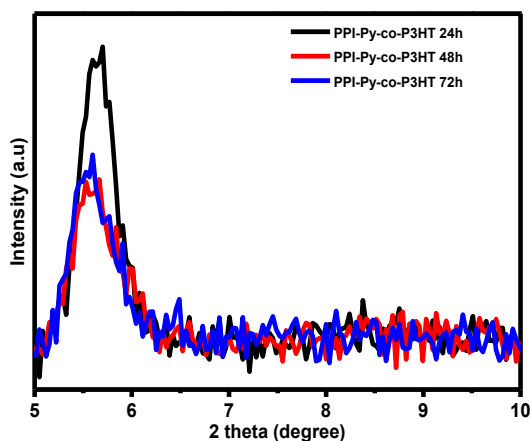


Figure 5.11: XRD pattern of PPI-Py-co-P3HT synthesized using different reaction time.

5.3.11. Photovoltaic performance

OPVs were fabricated with PPI-Py-co-P3HT as a donor material and PC₇₁BM as an electron acceptor material. Multiple devices were fabricated and their results are presented in Figure A4 and Table A(4-6) (Appendix). The current density-voltage (J-V) curves of the devices with maximum PCE are presented in Figure 5.12. The PCE of PPI-Py-co-P3HT synthesized for 24, 48 and 72 h were measured to be 0.073, 0.001 and 0.026 %, respectively (Table 5.3). These PCEs was achieved from OPVs with a geometry of glass|ITO|PEDOT:PSS|PPI-Py-co-P3HT:PC₇₁BM|Ag paste and all the fabrication processes were performed outside the glovebox. The maximum PCE was achieved when PPI-Py-co P3HT synthesized for 24 h was used due to its high crystallinity and sufficient charge separation. PPI-Py-co-P3HT synthesized for 48 h as donor material resulted in lowest PCE and J_{SC}. This is due to its wider optical band gap which lead to lesser generation of excitons. Generally, all these devices have lower PCE due to their low stability in air. PC₇₁BM is photochemically instable [57] and it was found that its exposure to air with the presence of light turns to decrease the overall performance of OPVs [58]. Lee *et al.* [59] studied the photo-oxidation effect of PC₇₁BM on its chemical structure. Their study showed that as the fraction of photo-oxidised PC₇₁BM increases, the performance of OPVs decreases. This is due to formation of photo-oxidized products of PC₇₁BM which turn to trap electrons in the device. The

air exposure affects the electronic structure of PC₇₁BM which have an impact on the OPVs performance [60].

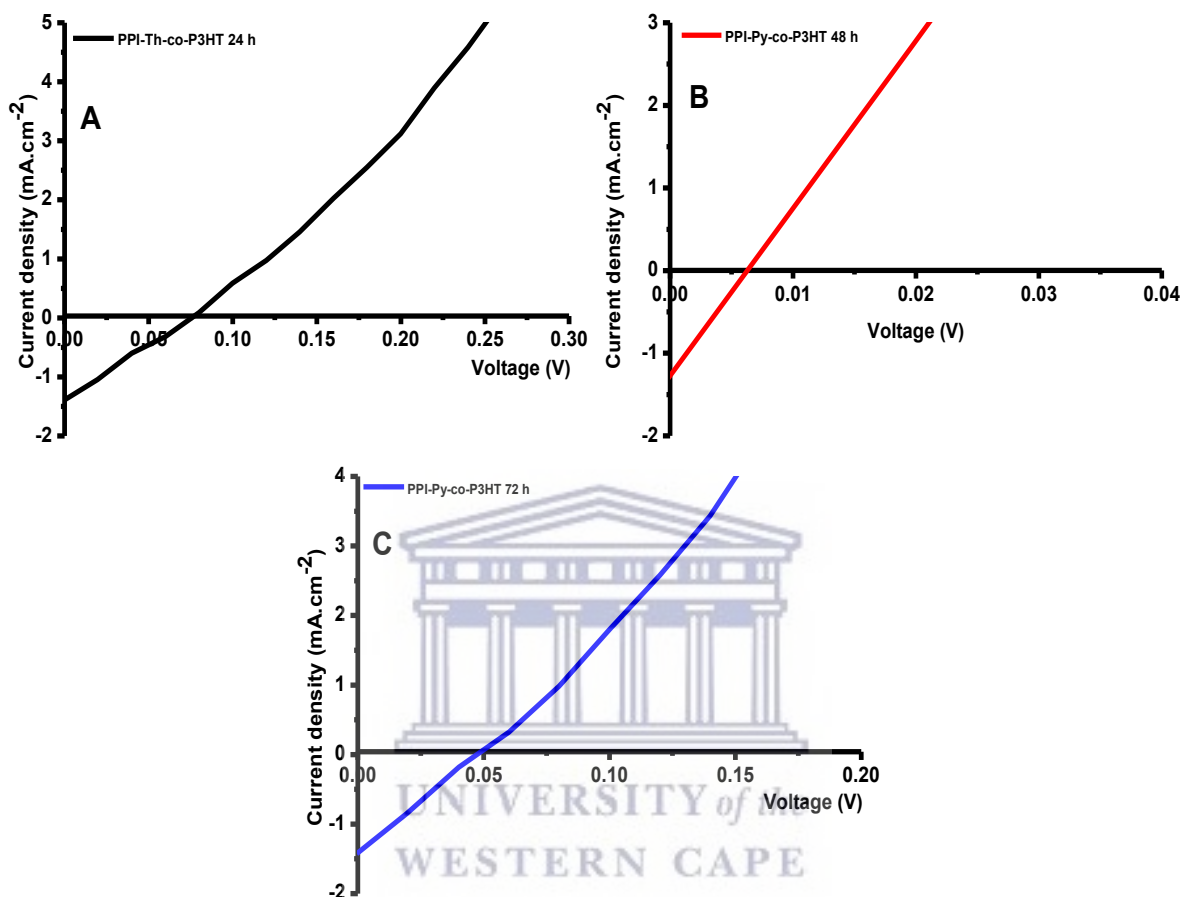


Figure 5.12: J–V characteristics of the fabricated OPVs using PPI-Py-co-P3HT synthesized using different polymerization time as donor materials.

Table 5.3: Photovoltaic performance of PPI-Py-co-P3HT as donor material.

Donor material	PCE (%)	FF (%)	J _{sc} (mA.cm ⁻²)	V _{oc} (V)
PPI-Py-co-P3HT 24h	0.024	24.18	1.34	0.073
PPI-Py-co-P3HT 48h	0.001	8.87	1.21	0.006
PPI-Py-co-P3HT 72h	0.016	25.89	1.34	0.026

5.4. Conclusion

PPI-Py-co-P3HT co-polymer was successfully synthesized using different reaction times. NMR and FTIR were used to confirm the structures of PPI-Py and PPI-Py-co-P3HT. The FTIR band intensities decrease after synthesis of PPI-Py-co-P3HT as compared to the spectrum of PPI-Py

confirming the growth of P3HT on the surface of PPI-Py. From the TGA results, the PPI-Py-co-P3HT synthesized at different reaction times decomposes at different temperatures indicating that they have different molecular weight. The optical band gaps were determined to be 2.29, 2.36 and 2.34 eV for PPI-Py-co-P3HT synthesized for 24, 48 and 72 h, respectively. The ΔE_{LUMO} of PPI-Py-co-P3HT and PC₇₁BM was found to be low for the polymer synthesized for 48 h indicating possible sufficient electron transfer from PPI-Py-co-P3HT donor material to PC₇₁BM acceptor material. When comparing the Nyquist plot of PPI-Py and PPI-Py-co-P3HT, the semi-circle diameters of PPI-Py-co-P3HT are smaller, indicating that they are more conductive. These results were confirmed by the decrease in impedance from the bode plots. The synthesized PPI-Py-co-P3HT were mixed with PC₇₁BM in chlorobenzene and their electrochemical impedance response were record which revealed an increase in charges diffusion and decrease in impedance. Photoluminescence quenching of PPI-Py-co-P3HT intensity was observed which indicate successful separation of electron-hole pair and electron transfer to PC₇₁BM. XRD was used to study crystallinity and the results revealed that PPI-Py-co-P3HT synthesized for 24 h is more crystalline. This study showed that as reaction time changes, the OPV parameters also changes. Maximum PCE was obtained when PPI-Py-co-P3HT synthesized for 24 h was used as a donor material while minimum was achieved when PPI-Py-co-P3HT synthesized for 48 h was used. Maximum PCE of PPI-Py-co-P3HT synthesized for 24 h donor is attributed to sufficient electron-hole separation at the donor:acceptor interface revealed by photoluminescence studies and its high crystallinity. These factors results to an increase in V_{OC} consequently increasing PCE.

References

- [1] Li, S., Li, C.Z., Shi, M. and Chen, H., 2020. New phase for organic solar cell research: emergence of Y-series electron acceptors and their perspectives. *ACS Energy Letters*, 5, pp.1554-1567.
- [2] Chai, G., Chang, Y., Peng, Z., Jia, Y., Zou, X., Yu, D., Yu, H., Chen, Y., Chow, P.C., Wong, K.S. and Zhang, J., 2020. Enhanced hindrance from phenyl outer side chains on nonfullerene acceptor enables unprecedented simultaneous enhancement in organic solar cell performances with 16.7% efficiency. *Nano Energy*, 76, p.105087.
- [3] Choudhury, B.D., Ibarra, B., Cesano, F., Mao, Y., Huda, M.N., Chowdhury, A.R., Olivares, C. and Uddin, M.J., 2020. The photon absorber and interconnecting layers in multijunction organic solar cell. *Solar Energy*, 201, pp.28-44.
- [4] Yu, H., Ma, R., Xiao, Y., Zhang, J., Liu, T., Luo, Z., Chen, Y., Bai, F., Lu, X., Yan, H. and Lin, H., 2020. Improved organic solar cell efficiency based on the regulation of an alkyl chain on chlorinated non-fullerene acceptors. *Materials Chemistry Frontiers*, 4, pp.2428-2434.
- [5] Ji, Y., Xu, L., Hao, X. and Gao, K., 2020. Energy loss in organic solar cells: mechanisms, strategies, and prospects. *Solar RRL*, 4, p.2000130.
- [6] Lee, S.M., Kumari, T., Lee, B., Cho, Y., Lee, J., Oh, J., Jeong, M., Jung, S. and Yang, C., 2020. Horizontal-, Vertical-, and Cross-Conjugated Small Molecules: Conjugated Pathway-Performance Correlations along Operation Mechanisms in Ternary Non-Fullerene Organic Solar Cells. *Small*, 16, p.1905309.
- [7] Jia, Z., Qin, S., Meng, L., Ma, Q., Angunawela, I., Zhang, J., Li, X., He, Y., Lai, W., Li, N. and Ade, H., 2021. High performance tandem organic solar cells via a strongly infrared-absorbing narrow bandgap acceptor. *Nature Communications*, 12, pp.1-10.
- [8] Liyakath, R., Ramaraj, B., Shin, P.K. and Santhakumar, K., 2021. Restructuring and interlayer phenomenon on tandem architecture to improve organic solar cell behaviour. *Journal of Materials Science: Materials in Electronics*, pp.1-10.
- [9] Tavakoli, M.M., Si, H. and Kong, J., 2021. Suppression of Photovoltaic Losses in Efficient Tandem Organic Solar Cells (15.2%) with Efficient Transporting Layers and Light Management Approach. *Energy Technology*, 9, p.2000751.

- [10] Dos Santos, J.M., Neophytou, M., Wiles, A., Howells, C.T., Ashraf, R.S., McCulloch, I. and Cooke, G., 2021. Influence of alkyne spacers on the performance of thiophene-based donors in bulk-heterojunction organic photovoltaic cells. *Dyes and Pigments*, 188, p.109152.
- [11] Ram, K.S., Ompong, D., Rad, H.M., Setsoafia, D.D.Y. and Singh, J., 2021. An Alternative Approach to Simulate the Power Conversion Efficiency of Bulk Heterojunction Organic Solar Cells. *Physica Status Solidi (a)*, 218, p.2000597.
- [12] Chaudhary, D.K., Dhawan, P.K., Patel, S.P. and Bhasker, H.P., 2021. Large area semitransparent inverted organic solar cells with enhanced operational stability using TiO₂ electron transport layer for building integrated photovoltaic devices. *Materials Letters*, 283, p.128725.
- [13] Kang, Q., Zheng, Z., Zu, Y., Liao, Q., Bi, P., Zhang, S., Yang, Y., Xu, B. and Hou, J., 2021. n-doped inorganic molecular clusters as a new type of hole transport material for efficient organic solar cells. *Joule*, 5, pp.1-13.
- [14] Ram, K.S. and Singh, J., 2019. Highly Efficient and Stable Solar Cells with Hybrid of Nanostructures and Bulk Heterojunction Organic Semiconductors. *Advanced Theory and Simulations*, 2, p.1900030.
- [15] Sreedhar Ram, K., Mehdizadeh-Rad, H., Ompong, D., Setsoafia, D.D.Y. and Singh, J., 2021. Characterising Exciton Generation in Bulk-Heterojunction Organic Solar Cells. *Nanomaterials*, 11, p.209.
- [16] Zhang, D., Zhong, W., Ying, L., Fan, B., Li, M., Gan, Z., Zeng, Z., Chen, D., Li, N., Huang, F. and Cao, Y., 2021. Overcoming Incompatibility of Donors and Acceptors by Constructing Planar Heterojunction Organic Solar Cells. *Nano Energy*, 85, p.105957.
- [17] Jiang, K., Zhang, J., Peng, Z., Lin, F., Wu, S., Li, Z., Chen, Y., Yan, H., Ade, H., Zhu, Z. and Jen, A.K.Y., 2021. Pseudo-bilayer architecture enables high-performance organic solar cells with enhanced exciton diffusion length. *Nature Communications*, 12, pp.1-9.
- [18] Park, S.Y., Chandrabose, S., Price, M.B., Ryu, H.S., Lee, T.H., Shin, Y.S., Wu, Z., Lee, W., Chen, K., Dai, S. and Zhu, J., 2021. Photophysical pathways in efficient bilayer organic solar cells: the importance of interlayer energy transfer. *Nano Energy*, 84, p.105924.

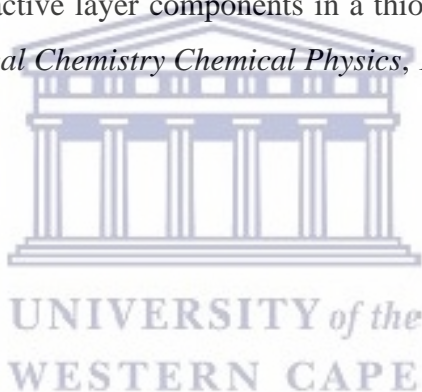
- [19] Gao, J., Li, Y., Li, S., Xia, X., Lu, X., Shi, M. and Chen, H., 2021. Non-fullerene acceptors with nitrogen-containing six-membered heterocycle cores for the applications in organic solar cells. *Solar Energy Materials and Solar Cells*, 225, p.111046.
- [20] Yang, C., Zhang, S., Ren, J., Gao, M., Bi, P., Ye, L. and Hou, J., 2020. Molecular design of a non-fullerene acceptor enables a P3HT-based organic solar cell with 9.46% efficiency. *Energy & Environmental Science*, 13, pp.2864-2869.
- [21] Khairulaman, F.L., Yap, C.C. and Jumali, M.H.H., 2021. Improved performance of inverted type organic solar cell using copper iodide-doped P3HT:PCBM as active layer for low light application. *Materials Letters*, 283, p.128827.
- [22] Kadem, B., Alfahed, R.F., Al-Asadi, A.S. and Badran, H.A., 2020. Morphological, structural, optical, and photovoltaic cell of copolymer P3HT: ICBA and P3HT: PCBM. *Optik*, 204, p.164153.
- [23] Kurukavak, Ç.K., Yılmaz, T., Çetin, Ş., Alqadasi, M.M., Al-Khawlanly, K.M. and Kuş, M., 2021. Synthesis of boron-doped CQDs and its use as an additive in P3HT:PCBM layer for efficiency improvement of organic solar cell. *Microelectronic Engineering*, 235, p.111465.
- [24] Abdallaoui, M., Sengouga, N., Chala, A., Meftah, A.F. and Meftah, A.M., 2020. Comparative study of conventional and inverted P3HT: PCBM organic solar cell. *Optical Materials*, 105, p.109916.
- [25] Ghazy, O., Freisinger, B., Lieberwith, I. and Landfester, K., 2020. Tuning the size and morphology of P3HT/PCBM composite nanoparticles: towards optimized water-processable organic solar cells. *Nanoscale*, 12, pp.22798-22807.
- [26] Fu, P., Yang, D., Zhang, F., Yu, W., Zhang, J. and Li, C., 2015. Efficiency enhancement of P3HT: PCBM polymer solar cells using oligomers DH4T as the third component. *Science China Chemistry*, 58, pp.1169-1175.
- [27] Shen, Y., Scudiero, L. and Gupta, M.C., 2011. Temperature dependence of HOMO-LUMO levels and open circuit voltage for P3HT: PCBM organic solar cells. *MRS Online Proceedings Library*, 1360, pp.080601-080604.
- [28] Hou, J. and Guo, X., 2013. Active layer materials for organic solar cells. *Green Energy and Technology*, 128, pp. 17–42.
- [29] Ramoroka, M.E., Mdluli, S.B., John-Denk, V.S., Modibane, K.D., Arendse, C.J. and Iwuoha, E.I., 2021. Synthesis and Photovoltaics of Novel 2, 3, 4, 5-Tetrathienylthiophene-

- co-poly (3-hexylthiophene-2, 5-diyl) Donor Polymer for Organic Solar Cell. *Polymers*, 13, p.2.
- [30] Mondal, M., Ghosh, S., Maity, S., Giri, S. and Ghosh, A., 2020. In situ transformation of a tridentate to a tetradentate unsymmetric Schiff base ligand via deaminative coupling in Ni (II) complexes: crystal structures, magnetic properties and catecholase activity study. *Inorganic Chemistry Frontiers*, 7, pp.247-259.
- [31] Hai, T.A.P. and Sugimoto, R., 2017. The catalytic oxidative polymerization of 3-hexylthiophene by oxidation of Fe^{2+} to Fe^{3+} . *Catalysis Letters*, 147, pp.1955-1965.
- [32] Ansari, M.A., Mohiuddin, S., Kandemirli, F. and Malik, M.I., 2018. Synthesis and characterization of poly (3-hexylthiophene): improvement of regioregularity and energy band gap. *RSC Advances*, 8, pp.8319-8328.
- [33] Mamaghani, M., Ansar, S. and Jahanshahi, P., 2021. A Convergent One-Pot Synthesis of Novel Pyrrole-Pyridopyrimidines Hybrids Using 1-Carboxymethyl-2, 3-Dimethylimidazolium Iodide {[cmdmim]I} as a Recyclable Catalyst. *Polycyclic Aromatic Compounds*, pp.1-14.
- [34] Memela, M., Feleni, U., Mdluli, S., Ramoroka, M.E., Ekwere, P., Douman, S. and Iwuoha, E., 2020. Electro-photovoltaics of Polymer-stabilized Copper–Indium Selenide Quantum Dot. *Electroanalysis*, 32, pp.3086-3097.
- [35] Cui, Z., Coletta, C., Dazzi, A., Lefrancois, P., Gervais, M., Néron, S. and Remita, S., 2014. Radiolytic method as a novel approach for the synthesis of nanostructured conducting polypyrrole. *Langmuir*, 30, pp.14086-14094.
- [36] García-Escobar, C.H., Nicho, M.E., Hu, H., Alvarado-Tenorio, G., Altuzar-Coello, P., Cadenas-Pliego, G. and Hernández-Martínez, D., 2016. Effect of microwave radiation on the synthesis of poly (3-hexylthiophene) and the subsequent photovoltaic performance of CdS/P3HT solar cells. *International Journal of Polymer Science*, 2016, pp.1-12.
- [37] Chen, T.A., Wu, X. and Rieke, R.D., 1995. Regiocontrolled synthesis of poly (3-alkylthiophenes) mediated by Rieke zinc: their characterization and solid-state properties. *Journal of the American Chemical Society*, 117, pp.233-244.
- [38] Ely, F., Cipriano, T.C., da Silva, M.O., Peressinotto, V.S. and Alves, W.A., 2016. Semiconducting polymer–dipeptide nanostructures by ultrasonically-assisted self-assembling. *RSC Advances*, 6, pp.32171-32175.

- [39] Joseyphus, R.S. and Nair, M.S., 2010. Synthesis, characterization and biological studies of some Co(II), Ni(II) and Cu(II) complexes derived from indole-3-carboxaldehyde and glycyglycine as Schiff base ligand. *Arabian Journal of Chemistry*, 3, pp.195-204.
- [40] Fuentes-Pérez, M., Nicho, M.E., Sotelo-Lerma, M., Fuentes-Ríos, J.L., Castrellón-Uribe, J., León-Silva, U., Hernández-Guzmán, F. and García-Carvajal, S., 2018. Influence of the FeO(OH) nanoparticles concentration in the in-situ synthesis of P3HT. *European Polymer Journal*, 99, pp.172-179.
- [41] Bahry, T., Cui, Z., Dazzi, A., Gervais, M., Sollogoub, C., Goubard, F., Bui, T.T. and Remita, S., 2021. Radiation-induced polymerization of 3-hexylthiophene in oxygen-free and oxygen-saturated dichloromethane solvent. *Radiation Physics and Chemistry*, 180, p.109291.
- [42] Aghvami, F., Ghaffari, A., Kucerakova, M., Dusek, M., Karimi-Nami, R., Amini, M. and Behzad, M., 2021. Catalytic oxidation of organic sulfides by new Iron-Chloro Schiff base complexes: the effect of methoxy substitution and ligand isomerism on the electronic, electrochemical and catalytic performance of the complexes. *Polyhedron*, 200, p.115135.
- [43] Lee, Y.H., Yeh, P.S., Hsu, Y.T., Tong, Z.H. and Chiang, C.H., 2021. Effective control of solution self-assembly of P3HT/zinc salt complex for in situ template synthesis of P3HT/ZnO nanohybrids. *Polymer*, 215, p.123385.
- [44] Hayashi, S., Yamamoto, S.I. and Koizumi, T., 2017. Effects of molecular weight on the optical and electrochemical properties of EDOT-based π -conjugated polymers. *Scientific Reports*, 7, pp.1-8.
- [45] Ergun, E.G.C. and Eroglu, D., 2019. An electrochemically and optically stable electrochromic polymer film based on EDOT and 1, 2, 3, 4-tetrahydrophenazine. *Organic Electronics*, 75, p.105398.
- [46] Wasly, H.S., Abd El-Sadek, M.S. and Henini, M., 2018. Influence of reaction time and synthesis temperature on the physical properties of ZnO nanoparticles synthesized by the hydrothermal method. *Applied Physics A*, 124, p.76.
- [47] An, Q., Wang, J., Gao, W., Ma, X., Hu, Z., Gao, J., Xu, C., Hao, M., Zhang, X., Yang, C. and Zhang, F., 2020. Alloy-like ternary polymer solar cells with over 17.2% efficiency. *Science Bulletin*, 65, pp.538-545.

- [48] Mei, B.A., Lau, J., Lin, T., Tolbert, S.H., Dunn, B.S. and Pilon, L., 2018. Physical interpretations of electrochemical impedance spectroscopy of redox active electrodes for electrical energy storage. *The Journal of Physical Chemistry C*, 122, pp.24499-24511.
- [49] Huang, J.H., Ibrahim, M.A. and Chu, C.W., 2013. Interfacial engineering affects the photocatalytic activity of poly(3-hexylthiophene)-modified TiO₂. *RSC Advances*, 3, pp.26438-26442.
- [50] Wang, G., Dong, W., Gurung, A., Chen, K., Wu, F., He, Q., Pathak, R. and Qiao, Q., 2019. Improving photovoltaic performance of carbon-based CsPbBr₃ perovskite solar cells by interfacial engineering using P3HT interlayer. *Journal of Power Sources*, 432, pp.48-54.
- [51] Xu, Y., Wang, X., Zhou, J., Song, B., Jiang, Z., Lee, E.M., Huberman, S., Gleason, K.K. and Chen, G., 2018. Molecular engineered conjugated polymer with high thermal conductivity. *Science Advances*, 4, p.eaar3031.
- [52] Busby, E., Carroll, E.C., Chinn, E.M., Chang, L., Moulé, A.J. and Larsen, D.S., 2011. Excited-state self-trapping and ground-state relaxation dynamics in poly (3-hexylthiophene) resolved with broadband pump–dump–probe spectroscopy. *The Journal of Physical Chemistry Letters*, 2, pp.2764-2769.
- [53] Meftah, S.E., Benhaliliba, M., Kaleli, M., Benouis, C.E., Yavru, C.A. and Bayram, A.B., 2020. Optical and electrical characterization of thin film MSP heterojunction based on organic material Al/p-Si/P3HT/Ag. *Physica B: Condensed Matter*, 593, p.412238.
- [54] Kadem, B., Alfahed, R.F., Al-Asadi, A.S. and Badran, H.A., 2020. Morphological, structural, optical, and photovoltaic cell of copolymer P3HT: ICBA and P3HT: PCBM. *Optik*, 204, p.164153.
- [55] García-Carvajal, S., Hernández-Martínez, D., Linzaga-Elizalde, I., Maldonado, J.L., Altuzar-Coello, P. and Nicho, M.E., 2019. Effect of the functionalization of CdS nanoparticles in the in-situ synthesis of P3HT/CdS composites. *European Polymer Journal*, 116, pp.471-479.
- [56] Shalu, C., Shukla, M., Tiwari, A., Agrawal, J., Bilgaiyan, A. and Singh, V., 2020. Role of solvent used to cast P3HT thin films on the performance of ZnO/P3HT hybrid photo detector. *Physica E: Low-dimensional Systems and Nanostructures*, 115, p.113694.

- [57] Kong, J., Nordlund, D., Jin, J.S., Kim, S.Y., Jin, S.M., Huang, D., Zheng, Y., Karpovich, C., Sertic, G., Wang, H. and Li, J., 2019. Underwater organic solar cells via selective removal of electron acceptors near the top electrode. *ACS Energy Letters*, 4, pp.1034-1041.
- [58] Anselmo, A.S., Dzwilewski, A., Svensson, K. and Moons, E., 2016. Photodegradation of the electronic structure of PCBM and C60 films in air. *Chemical Physics Letters*, 652, pp.220-224.
- [59] Lee, H.K.H., Telford, A.M., Röhr, J.A., Wyatt, M.F., Rice, B., Wu, J., de Castro Maciel, A., Tuladhar, S.M., Speller, E., McGettrick, J. and Searle, J.R., 2018. The role of fullerenes in the environmental stability of polymer: fullerene solar cells. *Energy & Environmental Science*, 11, pp.417-428.
- [60] Hansson, R., Lindqvist, C., Ericsson, L.K., Opitz, A., Wang, E. and Moons, E., 2016. Photodegradation in air of the active layer components in a thiophene–quinoxaline copolymer: fullerene solar cell. *Physical Chemistry Chemical Physics*, 18, pp.11132-11138.



Chapter 6

Electrochemical studies of Polypropylenimine Tetra(salicylaldimine)-co-Poly(3-hexylthiophene-2,5-diyl) Composite Synthesized by Grignard method

Abstract

Novel polypropylenimine tetra(salicylaldimine)-co-poly(3-hexylthiophene-2,5-diyl) (PPI-Sal-co-P3HT) was synthesized following a Grignard reaction method. The synthesized compounds were characterized by nuclear magnetic resonance (NMR) spectroscopy, mass spectroscopy, electrochemical methods (cyclic voltammetry (CV) and electrochemical impedance spectroscopy (EIS)), Fourier-transform infrared (FTIR) spectroscopy, thermal gravimetric analysis (TGA) and ultraviolet-visible (UV-Vis) spectroscopy. The investigations revealed that the presence of poly(3-hexylthiophene-2,5-diyl) (P3HT) on the four branches of polypropylenimine tetra(salicylaldimine) (PPI-Sal) turns to improve the conductivity and also decrease the optical band gap. The lowest unoccupied molecular orbital (LUMO) energy levels of PPI-Sal-co-P3HT were compared to those of [6,6]-Phenyl C71 butyric acid methyl ester (PC₇₁BM). The LUMO offset of 0.32 eV was achieved indicating possible insufficient charge transfer and high energy loss. Photoluminescence studies confirmed that P3HT on the surface of PPI-Sal increases Stokes shift. The EIS studies revealed that PPI-Sal-co-P3HT has a R_{ct} value of 413.10 Ω and PPI-Sal has R_{ct} value of 525.80 Ω . The power conversion efficiency (PCE) of 0.21% was obtained for photovoltaic cell using PPI-Sal-co-P3HT as donor and PC₇₁BM as acceptor material.

6.1. Introduction

Dendrimers are hyperbranched macromolecules presenting a branching assembly that can be defined as a tree-like arms and were discovered in 1978 by Fritz Vögtle [1]. Fritz Vögtle and Donald Tomalia in the early 1980s working together with his co-workers synthesized poly(amidoamine) (PAMAM) dendrimers [2]. They have been widely studied due to their potential applications ranging from materials to biological science [1,3–5]. The discovery of the useful stepwise methods for synthesis of dendrimers, namely convergent and divergent methods, has made it possible to synthesize molecules that are huge as compared to branched or simple linear polymers [6–8]. The design of dendrimers has a huge impact on their properties [9]. As a results, dendrimers deliver a great potential for wide range applications in a research field. They are mostly used in optoelectronic device applications such as organic light emitting diodes [10] and OPVs [11], and in biomedical applications such as photodynamic therapy [12], drug delivery [13] and anti-bacterial material [14].

Dendrimers are categorized by their unique structural features such as peripheral sites density, a spherical-like 3-dimensional shape, and convergent periphery-to-core tree-like structure. Studies have been done on dendrimers for use as light harvesting material due to their features [15,16]. It was revealed that as the generations of dendrimers changes, parameters such as size, shape and flexibility changes resulting in new properties. Dendrimers composed of end-groups that can be easily functionalized with different groups, consequently modifying their properties [11,17]. Photophysical properties of photoactive dendrimers such as exciplex and excimer formation, resonance energy transfers or charge transfers depends on the groups substituted on the end groups of the dendrimers [11].

For use of dendrimers for light harvesting properties, mostly π -conjugated branches are attached to a dendritic core which are used for energy transportation and as light absorbing unit [18]. In most cases, the attachment of π -conjugated branches to the dendritic core requires a linker. The core groups usually contain aromatic rings such as thiophene, pyrrole and benzene; and π -conjugated branches are linked through meta or α -positions depending on the ring present [19,20]. It was reported that family of phenyl-cored dendrimers substituted at meta positions (three-arm dendrimer) has a better charge transportation than four-arm dendrimer, but they suffer from poor

solubility limiting their studies for OPVs application [19–21]. From literature, solubility of an organic compound can be improved by functionalization with a saturated molecule [22,23].

Dendrimers containing π -conjugated groups have demonstrated to be efficient charge transporter in optoelectronics which was ascribed to the high-quality thin films they formed [20,24]. The high-quality thin films morphology of dendrimers is assisted by their monodispersity nature which is advantageous over polymers. It can be very challenging to synthesize polymers with a very low degree of polydispersity. This can be a problem for optoelectronic devices improvement because the charge transportation properties of polymer depend strongly on their molecular weight [25]. Therefore, this makes dendrimers to be good in organic conducting materials and their potential application in OPVs.

In this study, we report synthesis of PPI-Sal-co-P3HT with first generation dendritic structure in which P3HT chains were grown by replacing bromine on a meta position carbon with the benzene carbon attached to azomethine functional group using Grignard reaction method. The properties of PPI-Sal-co-P3HT such as optical, thermal and electrochemical were investigated and the study revealed that after decorating PPI-Sal with P3HT, those properties change drastically. The OPV device of PPI-Sal-co-P3HT as a donor material was fabricated.

6.2. Materials and Methods

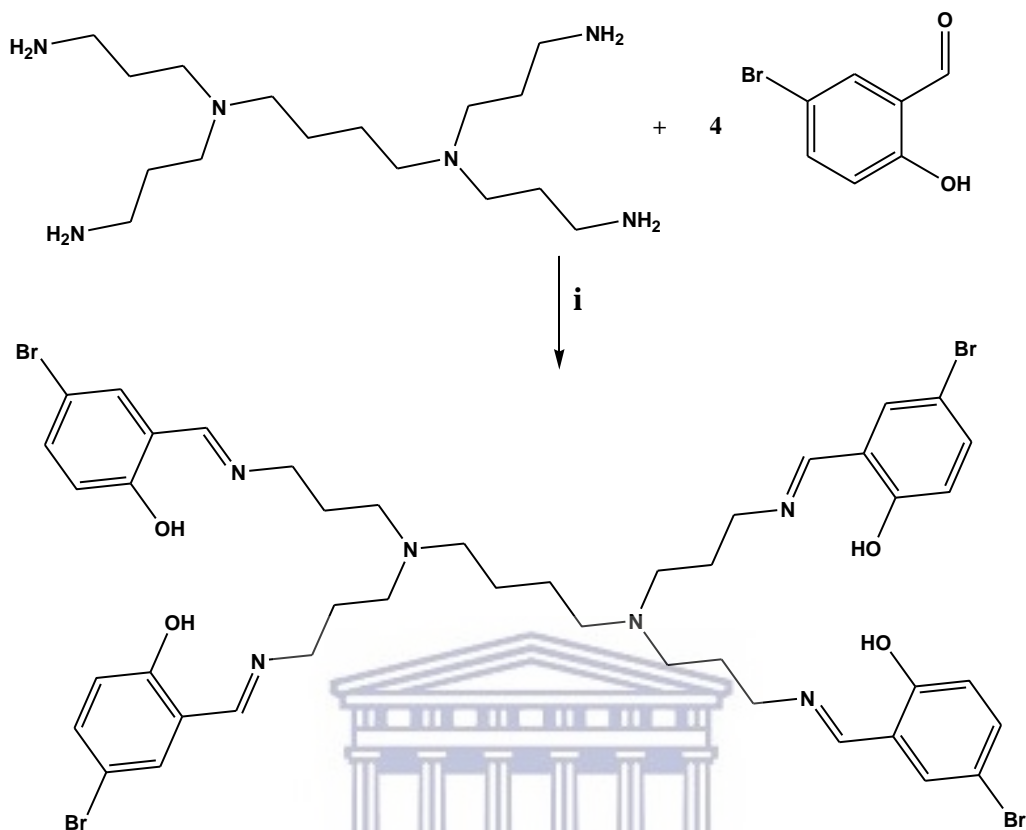
6.2.1. Materials

The reagents were purchased (Merck (Pty) Ltd., Johannesburg, South Africa) and used as received. Generation 1 poly(propylene imine) tetramine (DAB-Am4) dendrimer (pH 12, 25 wt % aq. Soln.), 5-bromosalicylaldehyde (98%), methanol (MeOH, 99.5%), dichloromethane (DCM, 99.9%), diethyl ether ($\geq 99.9\%$), anhydrous tetrahydrofuran ($\geq 99.9\%$), magnesium sulphate (MgSO_4 , $\geq 99.5\%$), 2 M tert-butylmagnesium chloride (2M in diethyl ether), 2,5-bromo-3-hexylthiophene ($\geq 97\%$), [1,3-Bis(diphenylphosphino)propane]dichloronickel(II) ($\text{Ni}(\text{dppp})\text{Cl}_2$), chloroform ($\geq 99\%$), deuterated chloroform (CDCl_3 , $\geq 99\%$), tetrabutyl-ammonium hexafluorophosphate (TBAPF_6 , $\geq 99\%$), acetone (99.3%), PC_{71}BM (99%), 2-propylalcohol ($\geq 99.5\%$), poly(3,4-ethylenedioxythiophene) polystyrene sulfonate (PEDOT:PSS, 0.5-1.0% in H_2O , high-conductivity grade), chlorobenzene (99.9%), acetonitrile anhydrous (99.8%), silver (Ag) conductive paste, zinc

acetate dihydrate ($\geq 98\%$), 2-methoxyethanol (99.8%), ethanolamine ($\geq 99.0\%$) and hellmanex III. Deionized water was collected on a Millipore Direct Q3 system from Millipore, Milford, MA, USA.

6.2.2. Synthesis of PPI-Sal

PPI-Sal was synthesized using synthetic route (Scheme 6.1) previously used by Memela *et. al.* [26]. DAB-Am4 (0.30 g, 0.95 mmol, in excess) and 5-bromosalicylaldehyde (0.76 g, 3.79 mmol) were dissolved in 50 mL MeOH. The solution was stirred under nitrogen gas for 48 h at room temperature. After 48 h, the solution was poured in 100 mL of deionized water and extracted 3 times with DCM and diethyl ether, separately. The MgSO_4 powder was added and the mixture was shaken for 5 min. After, the MgSO_4 suspensions were removed by filtration and solvent was removed with rotary evaporator. The oily yellow product was dried under vacuum overnight and resulted in a percentage yield of 54%. $^1\text{H-NMR}$ (CDCl_3 , 400 MHz): δ_{H} 1.37 (tt, 4H), 1.77-1.81 (tt, 8H), 2.35-2.50 (m, 12H), 3.59-3.62 (t, 8H), 6.83 (dd, 4H), 7.30-7.35 (m, 8H), 8.23 (s, 4H), 13.58 (s, 3H). $^{13}\text{C-NMR}$ (CDCl_3 , 400 MHz): δ_{C} 28.33 (6C), 51.29 (4C), 57.31 (6C), 109.87 (4C), 119.08 (4C), 120.08 (4C), 133.24 (4C), 134.79 (4C), 160.44 (4C), 163.68 (4C). HRMS (m/z): Calc. 1048.554: 50.40% C, 5.00% H, 8.00% N, 6.10% O, 30.50% Br. Exp. 1049.084: 50.37% C, 5.00% H, 8.01% N, 6.10% O, 30.47% Br. (Figure A5)



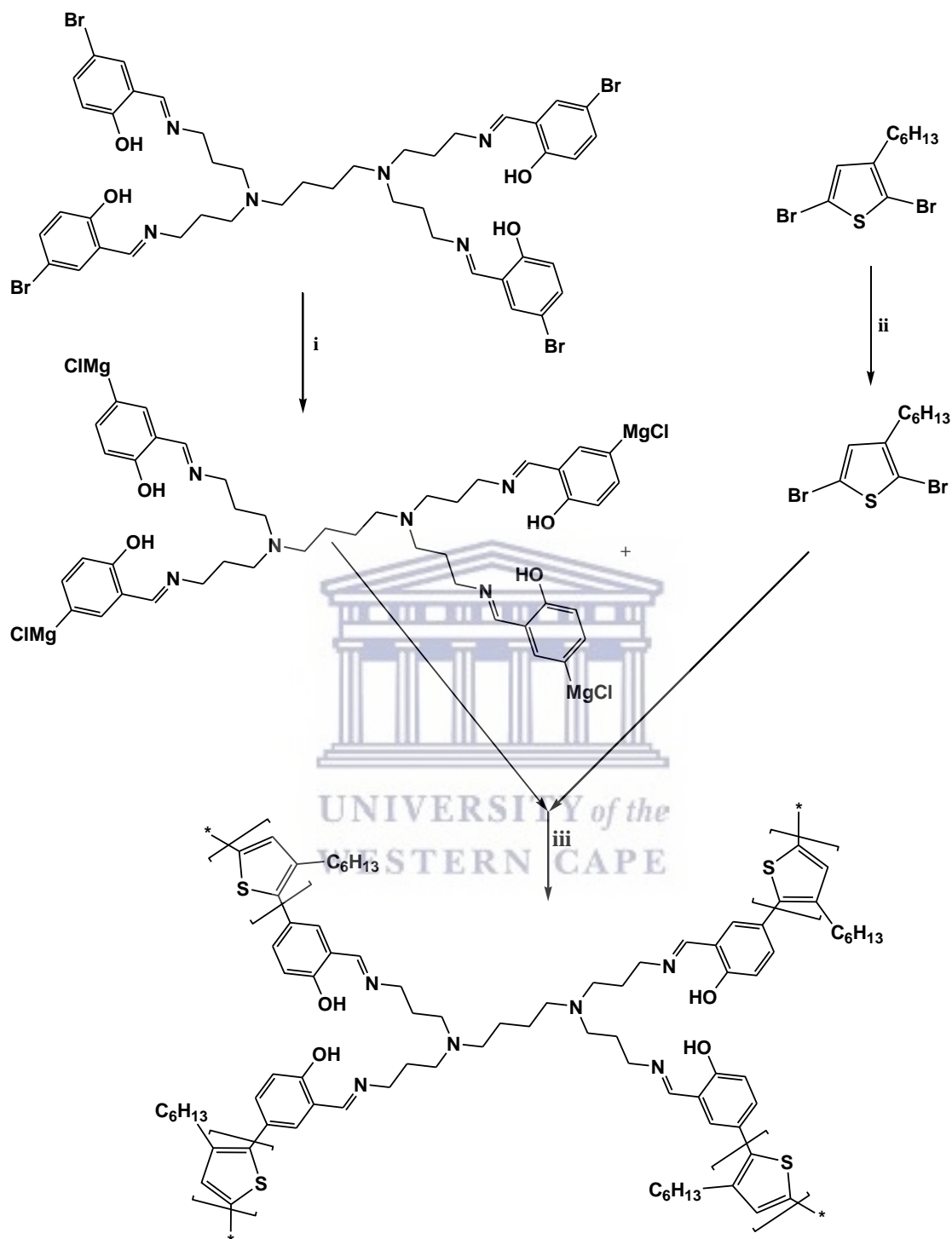
Scheme 6.1: Synthetic route of PPI-Sal. (i). MeOH, 48 h.

6.2.3. Synthesis of PPI-Sal-co-P3HT

PPI-Sal-co-P3HT was synthesized using Grignard reaction method as shown in Scheme 6.2 [27]. The glass wares used for synthesis of PPI-Sal-co-P3HT were dried in an oven overnight at 110°C. A three-necked round-bottom flask was charged with poly(propylene imine) tetra(5-bromosalicylaldehyde) (0.10 g, 95 μ mol) and anhydrous tetrahydrofuran. A solution of 2 M tert-butylmagnesium chloride (0.19 mL, 0.38 mmol) in diethyl ether was added using a deoxygenated syringe. The temperature of the reaction mixture was refluxed at 60°C for 2 h. Another solution of 2,5-bromo-3-hexylthiophene was prepared separately. In details, 2,5-bromo-3-hexylthiophene (0.41 mL, 1.91 mmol) was added in a three-necked round bottom flask containing anhydrous tetrahydrofuran. This was followed by the addition of 2 M tert-butylmagnesium chloride (0.95 mL, 1.91 mmol) in diethyl ether. The resulting reaction mixture was refluxed at 60°C for 2 h. The two reaction mixtures were mixed after 2 h and cooled to room temperature while stirring. The suspensions of Ni(dppp)Cl₂ (0.05 g, 95.37 μ mol) in 3 mL anhydrous tetrahydrofuran were added into the reaction mixture. Polymerization was allowed to take place for 3 h and MeOH was added

to quench the reaction. The precipitates were filter and washed with MeOH and acetone, then, extracted using chloroform in a Soxhlet extractor (size large, 200 mL extractor volume, Merck (Pty) Ltd.). The extract was concentrated using rotary evaporator and re-precipitated using methanol. The precipitate was filtered and dried in an oven overnight resulting to 0.25 g dark purple powder product.





Scheme 6.2: Synthesis of PPI-Sal-co-P3HT. (i) 2 M tertbutylmagnesium chloride solution, THF, 2 h, 60 °C, (ii) 2 M tertbutylmagnesium chloride solution, THF, 2 h, 60 °C, and (iii) Ni(dppp)Cl₂, 3 h, 60 °C.

6.2.4. Characterization techniques

NMR studies were done using A Bruker 400 MHz Avance III HD Nanobay Spectrometer equipped with a 5 mm BBO Probe at 298 K from Bruker, Karlsruhe, Germany. FTIR studies were performed with Spectrum-100 FTIR Spectrometer from PerkinElmer (Pty) Ltd., Midrand, South Africa. Mass spectroscopy analysis was performed using Waters Synapt G2 Quadrupole Time-of-Flight (QTOF) Mass Spectrometer (MS) connected to a Waters Acquity Ultra-Performance Liquid Chromatograph (UPLC) (Waters, Milford, MA, USA). TGA studies were performed using The Thermal Analyzer PerkinElmer STA 6000 Instrument (PerkinElmer (Pty) Ltd.). Scanning electron microscope (SEM) images were obtained using Tescan MIRA3 RISE SEM from Tescan, Brno, Czech Republic and elemental analysis was performed using FEI NovaNano SEM from FEI company, Hillsboro, OR, USA. Transmission electron microscope (TEM) images were obtained using a FEI Tecnai F20 CRYO FEGTEM from FEI company, Hillsboro, OR, USA. Photoluminescence spectra were obtained using NanoLog from Horiba Jobin Yvon, Edison, NJ, USA. The UV-Vis measurements were done using Nicolet Evolution 100 from Thermo Electron Corporation, Altrincham, UK. Electrochemical studies were conducted on CHI700E-Potentiostat from CH Instruments, Inc, Bee Cave, TX, USA using ITO glass substrate working electrode from Oscilla, Sheffield, UK, platinum wire counter electrode from Goodfellow Cambridge Ltd., Huntingdon, UK, silver/silver chloride reference electrode from BASi® in West Lafayette, IN, USA and electrolyte consisting of 0.1 M TBAPF₆/acetonitrile solution. Device characteristics (current density–voltage) were measured with X200 Source Meter Unit from Ossila, Sheffield, UK using an illumination of AM 1.5G, 100 mW cm⁻² supplied by a SciSun-150 Solar Simulator, Class AAA from Sciencetech Inc., London, ON, Canada.

6.2.5. Fabrication of OPVs

OPVs fabrication and measurements were done outside a glovebox. ITO glass substrates were washed with hellmanex solution in hot water, 2-propylalcohol and acetone. After washing the ITO glass substrate, ZnO was spun coated and annealed for 30 min at 100°C. The active layer was prepared by dissolving PPI-Sal-co-P3HT and PC₇₁BM in chlorobenzene with a total concentration of 25 mg/mL. The active layer solution was stirred at 60°C for overnight. It was spun coated onto ZnO/ITO glass substrate and annealed at 100°C for 5 min. After coating with an active layer,

PEDOT:PSS was spun coated and annealed at 150°C for 5 min. Finally, Ag conductive paste was coated as cathode electrode and dried at 100°C for 5 min to complete the OPVs.

6.3. Results and Discussions

6.3.1. NMR analysis of PPI-Sal and PPI-Sal-co-P3HT

The $^1\text{H-NMR}$ and $^{13}\text{C-NMR}$ spectra of PPI-Sal are shown in Figure 6.1A and 6.1B, respectively. From the $^1\text{H-NMR}$, the signals at 1.37 ppm and 1.77-1.81 ppm are assigned to $-\text{C}-\text{CH}_2-\text{C}-$ protons, 2.35-2.50 ppm are due to $-\text{CH}_2-\text{N}-$ protons, 3.59-3.62 ppm are ascribed to $-\text{CH}_2-\text{N}=\text{C}-$ protons, 6.83 ppm and 7.30-7.35 ppm are consigned to protons on the benzene ring, 8.23 ppm is for $-\text{N}=\text{CH}-$ proton and 13.58 ppm is owing to $\text{O}-\text{H}$ protons. An additional signal is observed at 5.30 ppm due to the presence of dichloromethane (CH_2Cl_2). A total of 10 signals were observed from the $^{13}\text{C-NMR}$ of PPI-Sal while they are 44 carbons on the structure. This is due to the presence of the plane symmetry in the structure of PPI-Sal [28]. The signal at 28.33 ppm is assigned to methylene carbon bonded to two carbons ($\text{C}-\text{CH}_2-\text{C}$), 51.29 ppm is for methylene carbon bonded to imine group ($-\text{CH}_2-\text{N}=\text{C}-$), 57.31 ppm is assigned to methylene carbon bonded to nitrogen ($-\text{CH}_2-\text{N}-$), and 109.87 ppm is ascribed to benzene ring carbon bonded to bromine ($-\text{C}-\text{Br}$). Furthermore, the signal at 119.08 ppm is attributed to benzene ring tertiary carbon bonded to an imine group ($-\text{C}-\text{N}=\text{C}$). The signals at 120.08, 133.24 and 134.79 ppm are assigned to benzene ring methine group carbons ($-\text{CH}=\text{C}$), 160.44 ppm is assigned to benzene ring carbon bonded to hydroxyl group ($-\text{C}-\text{OH}$) and 163.68 ppm is assigned to the imine group carbon ($-\text{N}=\text{C}$). The assignment of signals from the NMR results matches well with the structure of PPI-Sal [29–31]. The $^1\text{H-NMR}$ spectrum of PPI-Sal-co-P3HT (Figure 6.2) is dominated by P3HT signals, they are more intense than expected PPI-Sal signals, due to the space interactions [21,26]. The signal at 7.67-7.68 ppm is assigned to imine group proton and is de-shielded and less intense when compared to PPI-Sal spectrum due to the presence of P3HT [32]. The signals at 7.15 ppm and 7.42 ppm are assigned to the methine groups of the benzene ring [30,31].

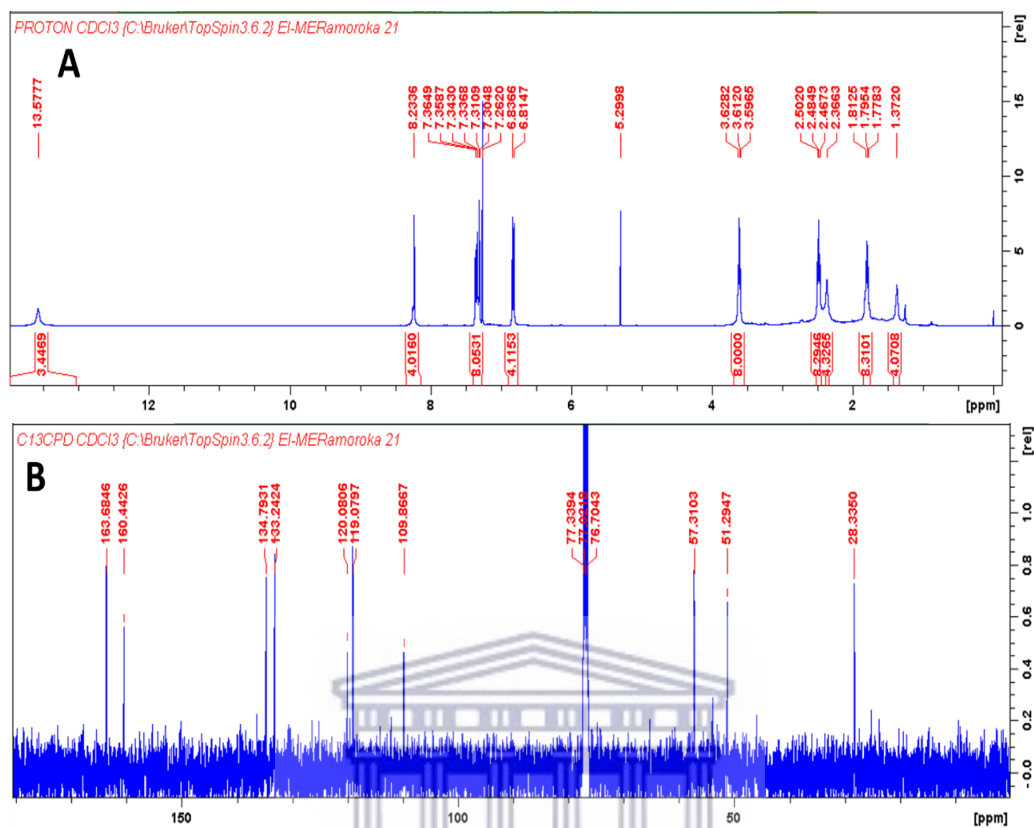


Figure 6.1: (A) ^1H -NMR and (B) ^{13}C -NMR of PPI-Sal.

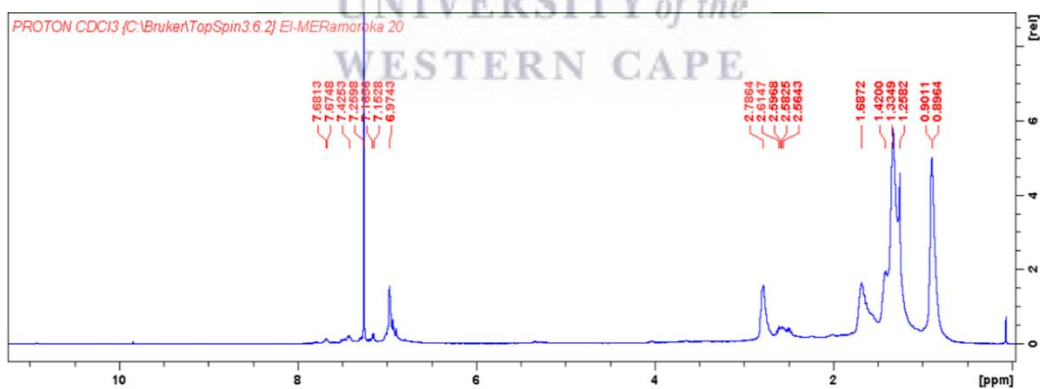


Figure 6.2: ^1H NMR of PPI-Sal-co-P3HT.

6.3.2. FTIR analysis of PPI-Sal and PPI-Sal-co-P3HT

The FTIR spectra of PPI-Sal and PPI-Sal-co-P3HT recorded in the wavenumber range of 4000-450 cm^{-1} are presented in Figure 6.3. From the spectrum of PPI-Sal, strong band can be seen at 2945 cm^{-1} due to the presence of C–H group of the benzene ring and C–H group of the imine group

[33]. The band at 2799 cm^{-1} is attributed to the methylene groups ($-\text{CH}_2-$) present in the PPI-Sal structure [34]. The strong bands at 1634 , 1478 , 1280 , 822 , and 624 cm^{-1} are ascribed to the $\text{C}=\text{N}$, $\text{C}=\text{C}$, $\text{C}-\text{C}$, $\text{C}=\text{C}-\text{H}$ and $\text{C}-\text{Br}$, respectively [35–37]. After modification of PPI-Sal with P3HT, a new strong band is observed at 2927 cm^{-1} due to the presence $-\text{CH}_3$ from the hexyl group. The bands at 2955 and 2856 cm^{-1} are accredited to $-\text{CH}$ and $-\text{CH}_2$ groups [38]. The bands due to $\text{C}=\text{N}$, $\text{C}=\text{C}$ and $\text{C}-\text{N}$ at 1636 , 1461 and 1263 cm^{-1} , respectively, are weak and appear at different wavenumber when compared to their appearance on the spectrum of PPI-Sal. In the literature, it is reported that the decrease in the bands intensity and change in the wavenumber confirm the occurrence of functionalization [39]. Therefore, these observations indicate that PPI-Sal was successfully functionalized with P3HT.

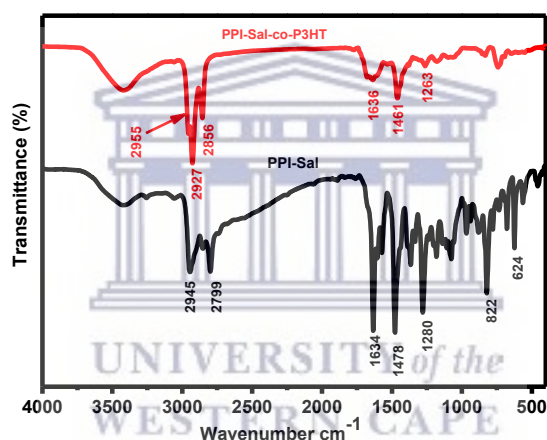


Figure 6.3: FTIR spectra of PPI-Sal and PPI-Sal-co-P3HT.

6.3.3. TGA studies of PPI-Sal and PPI-Sal-co-P3HT

To study the thermal properties of PPI-Sal and PPI-Sal-co-P3HT, thermal gravimetric analysis measurements were performed. The thermograms of PPI-Sal and PPI-Sal-co-P3HT are depicted in Figure 6.4 and were recorded under nitrogen. The weight loss in the temperature range of $50-130^\circ\text{C}$ is associated with the evaporation of moisture present in the samples [40]. But the weight loss in the temperature range of $200-650^\circ\text{C}$ is because of thermal decomposition. Figure 6.4 shows a significant increase in thermal stability after incorporating P3HT on the surface of PPI-Sal. Therefore, PPI-Sal-co-P3HT is more thermally stable than PPI-Sal. At 650°C , the solid residues remaining have the weight percentage of 22 and 29% for PPI-Sal and PPI-Sal-co-P3HT,

respectively. These results show that the incorporation of P3HT for formation of PPI-Sal-co-P3HT improves the thermal stability of PPI-Sal.

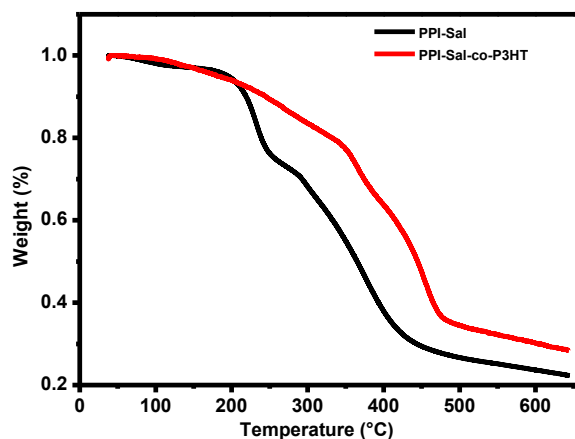


Figure 6.4: TGA thermograms of PPI-Sal and PPI-Sal-co-P3HT.

6.3.4. UV-Vis studies of PPI-Sal and PPI-Sal-co-P3HT

Figure 6.5A shows the UV-Vis absorption spectra of PPI-Sal and PPI-Sal-co-P3HT in chlorobenzene. The PPI-Sal absorption spectrum shows two bands at 328 and 405 nm which correspond to $\pi \rightarrow \pi^*$ transition present in the benzene ring and $n \rightarrow \pi^*$ transition of azomethine group, respectively [41,42]. After decorating PPI-Sal with P3HT, an absorption band appears at 415 nm due to the conjugation of the P3HT chain [43]. From the absorption spectra of PPI-Sal and PPI-Sal-co-P3HT, energy band gap was determined using Tauc plot (Figure 6.5B and C). The absorption spectra were converted to photon energy against absorption coefficient $(\alpha h\nu)^2$ plot. The energy band gap was determined by extrapolating the plot to $\alpha h\nu$ equal to zero. The band gaps were determined to be 3.48 and 2.47 eV for PPI-Sal and PPI-Sal-co-P3HT, respectively.

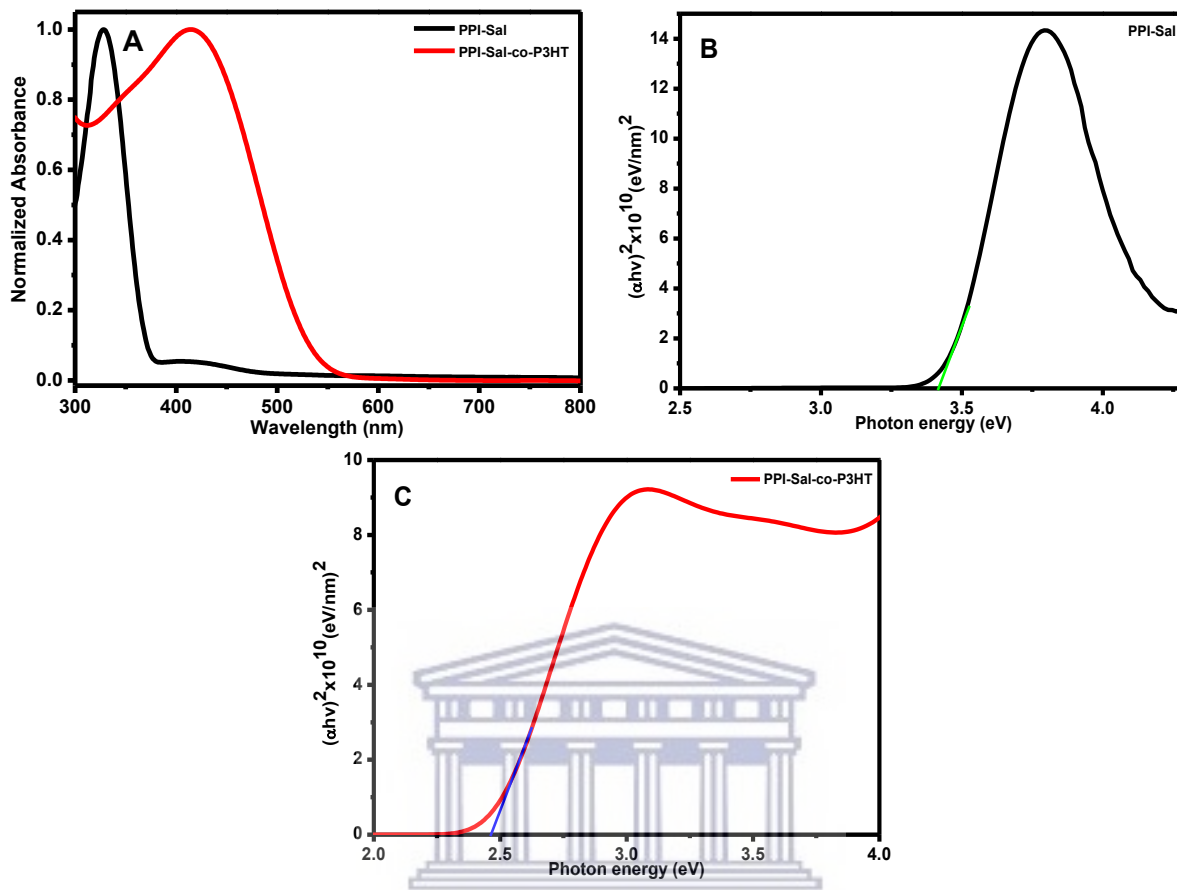


Figure 6.5: (A) UV-Vis spectra and Tauc plots of (B) PPI-Sal and (C) PPI-Sal-co-P3HT.

6.3.5. SEM images of PPI-Sal-co-P3HT

The morphological features of synthesized PPI-Sal-co-P3HT were evaluated by SEM. The SEM images of PPI-Sal-co-P3HT with different magnifications are shown in Figure 6.6. The images of PPI-Sal-co-P3HT demonstrate clusters of microspheres. EDS analysis was also performed to study the composition of PPI-Sal-co-P3HT. The study revealed the presence of 39.27% carbon, 40.75% oxygen, 16.08% magnesium, 1.38% aluminium, 1.81% sulphur, and 0.71% chlorine. The presence of magnesium and chlorine is due to the tetrabutylmagnesium chloride used during synthesis.

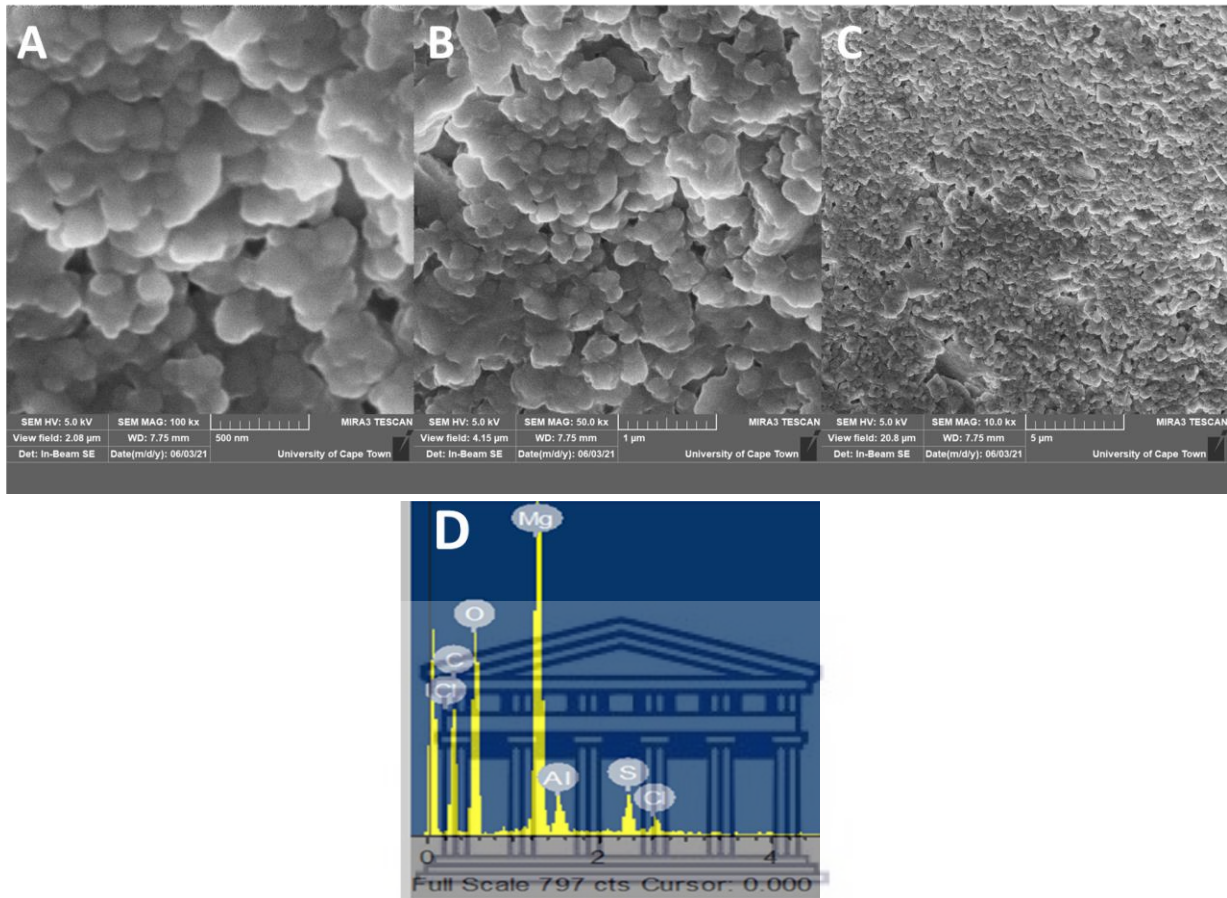


Figure 6.6: SEM images of PPI-Sal-co-P3HT with different magnifications of (A) 500 nm, B) 1 μm and (C) 5 μm. (D) EDS spectrum of PPI-Sal-co-P3HT.

6.3.6. TEM studies of PPI-Sal-co-P3HT

TEM image of PPI-Sal-co-P3HT is shown in Figure 6.7. The TEM image shows that the PPI-Sal-co-P3HT particles are spherical with high level of agglomeration. There are dark and bright regions that can be seen in the image of PPI-Sal-co-P3HT. The dark regions on the image represent the highly agglomerated regions.

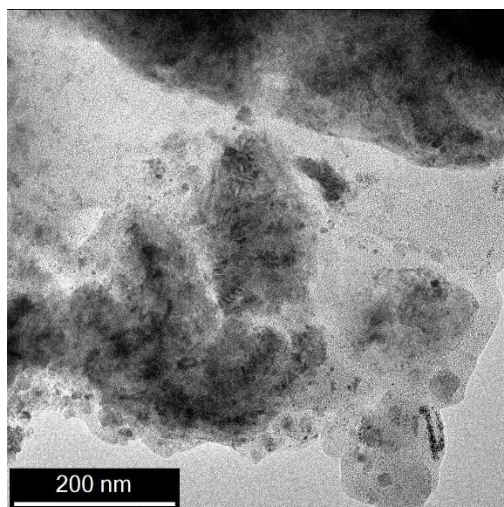


Figure 6.7: TEM image of PPI-Sal-co-P3HT.

6.3.7. CV studies of PPI-Sal and PPI-Sal-co-P3HT

CV measurements of PPI-Sal and PPI-Sal-co-P3HT were performed and obtained voltammograms are presented in Figure 6.8A. It is observed that after decorating PPI-Sal with P3HT the peak current significantly increases. This indicates that PPI-Sal-co-P3HT is more conductive than PPI-Sal [44]. These findings are in agreement with the wider optical band gap estimated for PPI-Sal. CV was used to estimate the energy levels of the newly synthesized PPI-Sal-co-P3HT. The cyclic voltammogram of PPI-Sal-co-P3HT is presented in Figure 6.8B. The HOMO and LUMO energy levels of PPI-Sal-co-P3HT were determined from the onset oxidation potential (E_{ox}) and onset reduction potential (E_{red}) using the equations below:

$$\text{HOMO} = -\left[\left(E_{ox} - E_{\frac{1}{2}(\text{ferrocene})} \right) + 4.8 \right] \dots \dots \dots 6.1$$

$$\text{LUMO} = -\left[\left(E_{red} - E_{\frac{1}{2}(\text{ferrocene})} \right) + 4.8 \right] \dots \dots \dots 6.2$$

where $E_{\frac{1}{2}(\text{ferrocene})}$ is the formal potential of ferrocene (0.4 V) and 4.8 is reference energy level of ferrocene [45]. The HOMO energy level of PPI-Sal was determined (from Figure 6.8A) to check the changes after decoration with P3HT. The results in Table 6.1 show that PPI-Sal has deeper HOMO energy levels than PPI-Sal-co-P3HT. This change is associated with the presence of electron donating P3HT on the surface of PPI-Sal. The HOMO and LUMO energy levels of PPI-

Sal-co-P3HT were determined from Figure 6.8B and the results are given in Table 6.1. Estimated LUMO energy levels of PPI-sal-co-P3HT were compared to those of PC₇₁BM in Figure 6.8C. The distance between the LUMO energy levels (ΔE_{LUMO}) were determined to be 0.72 eV for PPI-Sal-co-P3HT with PC₇₁BM. Consequently, high energy loss and high recombination will take place at the interface of PPI-Sal-co-P3HT and PC₇₁BM. This is because the LUMO offset (ΔE_{LUMO}) obtained (0.72 eV) is twice higher than the empirical threshold of 0.3 eV [46].

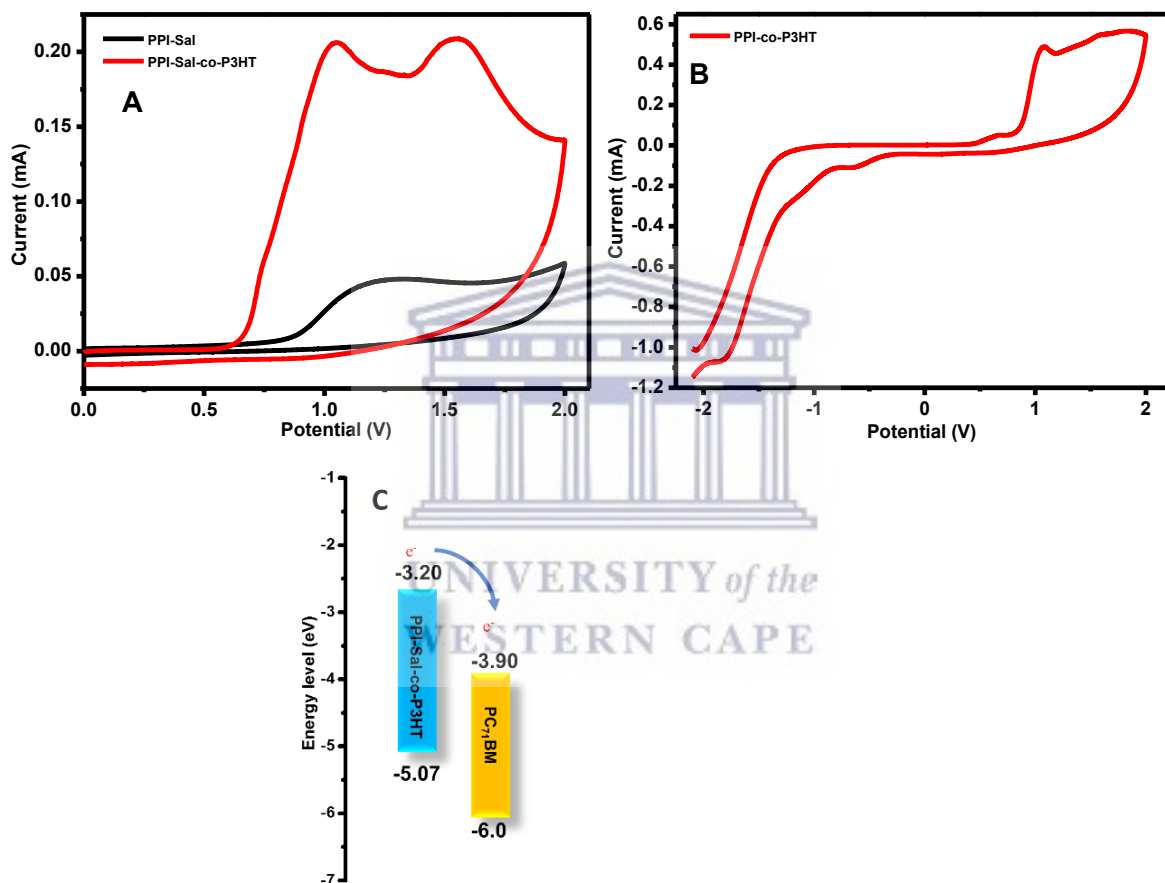


Figure 6.8: (A) CV of PPI-Sal and PPI-Sal-co-P3HT, (B) CV of PPI-Sal-co-P3HT and (C) energy level diagram.

Table 6.1: Electrochemical results of PPI-Sal and PPI-Sal-co-P3HT.

Compound	Onset oxidation potential (V)	Onset Reduction potential (V)	HOMO (eV)	LUMO (eV)	ΔE_{LUMO} (PC ₇₁ BM) (eV)
PPI-Sal	0.85	–	–5.26	–	–
PPI-Sal-co-P3HT	0.67	–1.24	–5.07	–3.18	0.72

6.3.8. EIS studies of PPI-Sal and PPI-Sal-co-P3HT

Electrochemical impedance spectra obtained for PPI-Sal and PPI-Sal-co-P3HT are shown in Figure 6.9. The Nyquist plot depicted in Figure 6.9A is used to study the charge carrier migration in the electrochemical cell. The semicircle of the Nyquist plots corresponds to the charge transfer at the interface of the analyte and electrode. The circuit used to fit the experimental data is given as an inset in Figure 6.9A. It is composed of series resistance, (R_s), accounting for the overall resistance between electrode and supporting electrolyte [47]. The values of R_s were determined to be 60.03 and 80.95 Ω , respectively. The second component is constant phase element (CPE) which corresponds to the double-layer capacitance. The third component is the interfacial charge transfer resistance (R_{ct}) and it is attributed to the inter-particle and intra-particle resistance [47,48]. When comparing the Nyquist plot of PPI-Sal-co-P3HT and PPI-Sal, the semi-circle of PPI-Sal-co-P3HT is smaller. This is an indication that the interfacial charge transfer is faster in PPI-Sal-co-P3HT than in PPI-Sal. This faster interfacial charge transfer could be due to the presence of highly conductive P3HT chain allowing easy charge transfer between the electrode and electrolyte interface. The Nyquist plot fit results revealed the smaller R_{ct} value of 413.10 Ω for PPI-Sal-co-P3HT compared to 525.80 Ω of PPI-Sal. These values also show faster interfacial charge transfer and reduced charge carrier recombination at the PPI-Sal-co-P3HT electrode and electrolyte interface. It is observed that the peak of PPI-Sal-co-P3HT shifts to lower frequency range in Figure 6.9B. This observation confirms the reduction of recombination rate and longer electron lifetime (τ) [49]. The values of τ were estimated using the Equation 6.3 below:

$$\tau = \frac{1}{2\pi f_{\max}} \dots\dots\dots 6.3$$

where f_{\max} is the frequency of the maximum peaks from the bode-phase plot. The values of τ were estimated to be 0.59 and 1.00 ms for PPI-Sal and PPI-Sal-co-P3HT, respectively. Figure 6.9C depicts the bode plot of impedance against frequency for PPI-Sal and PPI-Sal-co-P3HT. It was observed that PPI-Sal has maximum impedance at lower frequency than PPI-Sal-co-P3HT. These findings suggest good conduction of PPI-Sal-co-P3HT and are in agreement with the lower R_{ct} value obtained.

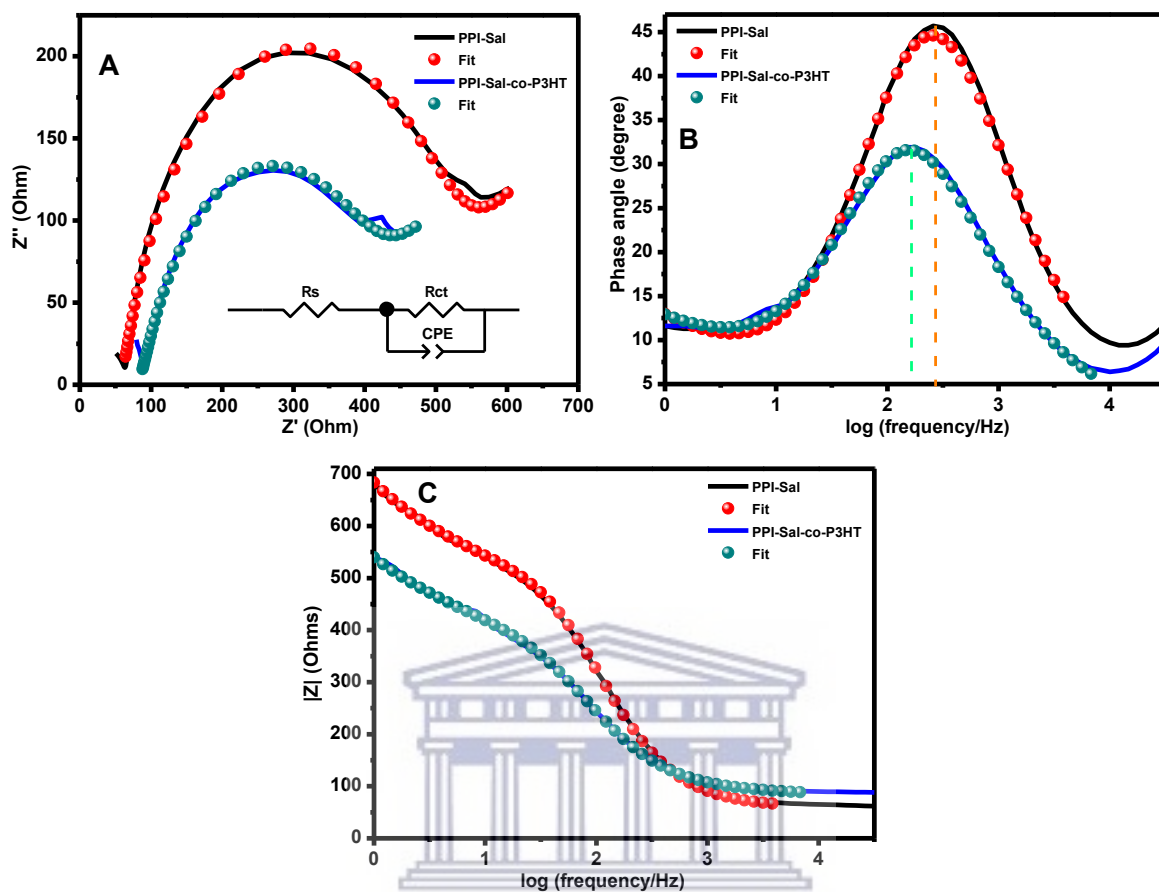


Figure 6.9: (A) Nyquist plots, (B) Bode-phase plots and (C) Bode-impedance of PPI-Sal and PPI-Sal-co-P3HT obtained at bias potential of -1.5 V.

The electrochemical impedance studies of PPI-Sal-co-P3HT were further studied at different bias potentials as shown in Figure 6.10. The fitting results of PPI-Sal-co-P3HT electrochemical impedance experimental data obtained at different bias potentials are summarized in Table 6.2. Figure 6.10A shows that as the bias potential becomes more negative, the diameter of the semicircle decreases and R_{ct} also decreases. This indicates that at more negative bias potential, the charge transfers between the PPI-Sal-co-P3HT coated electrode and electrolyte interface becomes faster. The maximum peak shift to higher frequency as the bias potential becomes more negative (Figure 6.10B). From the maximum peak frequency, the τ were estimated to be 3.18, 1.79, 1.01 and 1.0 ms for bias potential of -1.2, -1.3, -1.4 and -1.5 V, respectively. This result indicates that τ decreases as the bias potential becomes more negative (Figure 6.10D). Therefore, the recombination rate becomes faster at more negative bias potential. Figure 6.10C shows the bode-phase plot of PPI-Sal-P3HT at different bias potentials and the spectra showed similar trend. The

impedance obtained from Figure 6.10C at lower frequency (10 Hz) are 823.56, 637.86, 465.76 and 415.02 Ω for -1.2 , -1.3 , -1.4 and -1.5 V, respectively. The impedance decreases as the bias potential becomes more negative. This trend is consistent with the trend obtained from the Figure 6.10A. Therefore, the faster charge conduction of PPI-Sal-co-P3HT is achieved at bias potential of -1.5 V.

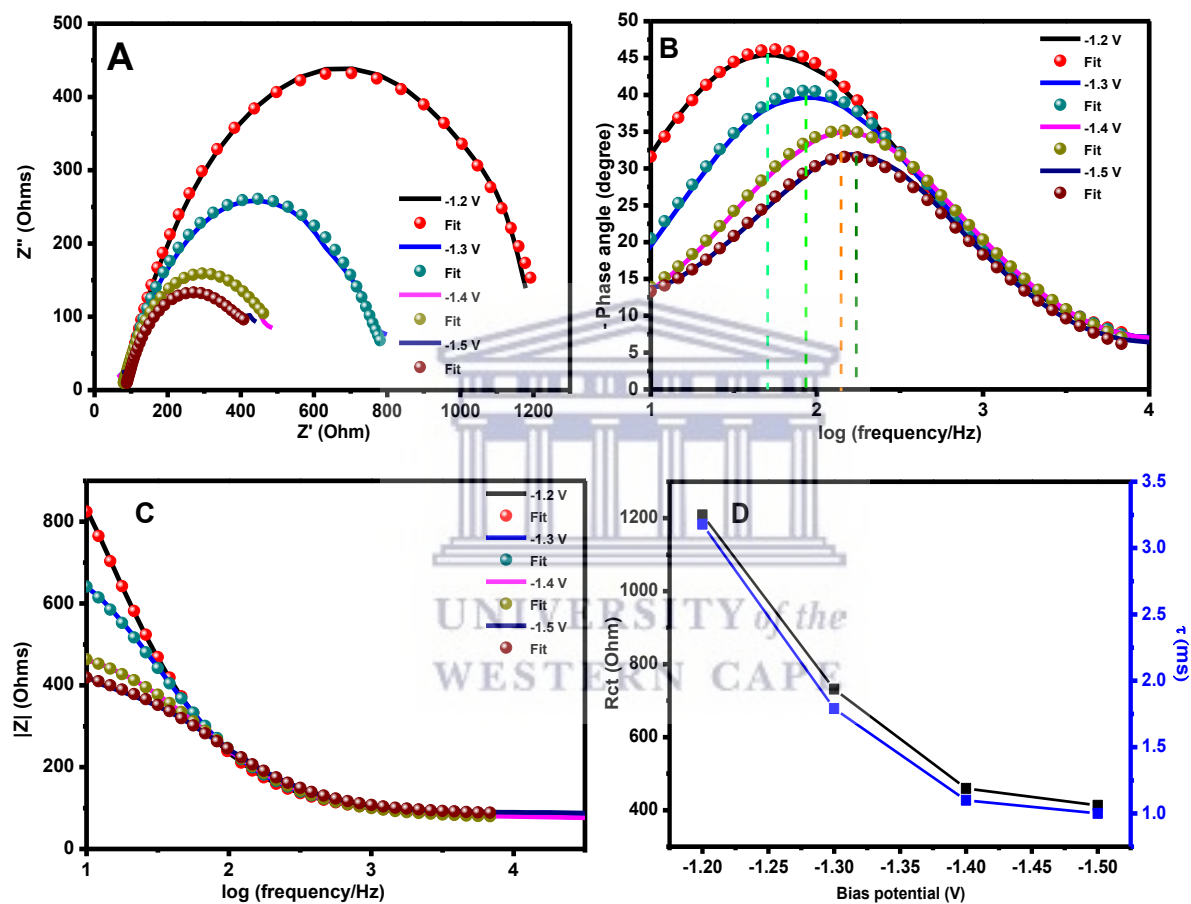


Figure 6.10: (A) Nyquist plots, (B) Bode-phase plots and (C) Bode-impedance of PPI-Sal-co-P3HT obtained at different bias potentials. (D) plot of R_{ct} and τ against bias potential.

Table 6.2: Electrochemical data of PPI-Sal and PPI-Sal-co-P3HT.

Compound	Bais potential (V)	R _s (Ohms)	R _{ct} (Ohms)	τ (ms)
PPI-Sal	-1.5	60.03 ± 0.70	525.80 ± 5.81	0.59
PPI-Sal-co-P3HT	-1.2	80.95 ± 0.59	1209.00 ± 9.96	3.18
	-1.3	80.02 ± 0.51	731.50 ± 4.63	1.79
	-1.4	75.84 ± 0.42	459.70 ± 2.89	1.10
	-1.5	82.79 ± 1.02	413.10 ± 6.09	1.0

6.3.9. Photoluminescence of PPI-Sal-co-P3HT

Photoluminescence spectra of PPI-Sal and PPI-Sal-co-P3HT are shown in Figure 6.11. Both excitation and emission spectra of PPI-Sal and PPI-Sal-co-P3HT are sensitive to the structure of chemical compounds. PPI-Sal and PPI-Sal-co-P3HT exhibited maximum excitation peak at 443 and 429 nm, while emitted green luminescence at 512 nm and orange luminescence at 566 nm, respectively. From literature, the blue-shift of the excitation peak indicates that the polymer chain is twisted or coil-like in chlorobenzene [50,51]. This is the reason why the excitation peak of PPI-Sal-co-P3HT is blue-shifted. Emission peak of PPI-Sal-co-P3HT shows a strong red-shift relative to PPI-Sal due to efficient charge migration to ground state energy levels and the presence of conjugated P3HT [52]. In addition, the Stokes shift of PPI-Sal-co-P3HT (137 nm) is larger than that of PPI-Sal (69 nm). Zheng *et al.* [53] investigated the effect of electron-donating and electron-withdrawing groups as substituents on photoluminescence properties. The presence of electron-donating substituents results to larger Stokes shift, while electron-withdrawing substituents turn to quench photoluminescence. Therefore, the presence of electron-donating group P3HT on the surface of PPI-Sal increases the Stokes shift.

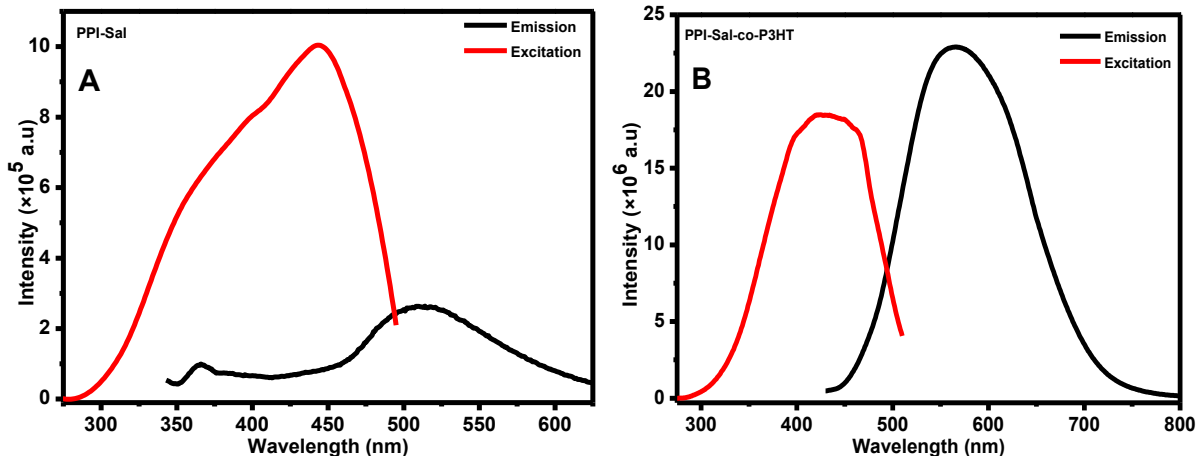


Figure 6.11: Photoluminescence spectra of (A) PPI-Sal and (B) PPI-Sal-co-P3HT in chlorobenzene.

6.3.10. Photovoltaic properties of PPI-Sal-co-P3HT

The current density-voltage (J-V) curves of the OPV device with the structure of glass|ITO|ZnO|PPI-Sal-co-P3HT:PC₇₁BM|PEDOT:PSS|Ag conductive paste are shown in Figure 6.12. The J-V curves and results of different devices fabricated are given in Figure A6 and Table A7, respectively. The maximum performance of the device gave PCE of 0.21%, short circuit current (J_{SC}) of 1.74 mA.cm⁻², fill factor (FF) of 39.34% and open circuit voltage (V_{OC}) of 0.31 V. These OPVs were fabricated outside glovebox. Ag conductive paste used as metal contact can diffuse through the PEDOT:PSS layer to the active layer. This will alter the semiconducting properties of a polymer [54,55]. The exposure of the device to air can result in active layer degradation and oxidation of the electrode [55]. These factors explain why low PCE is achieved for PPI-Sal-co-P3HT based OPV device.

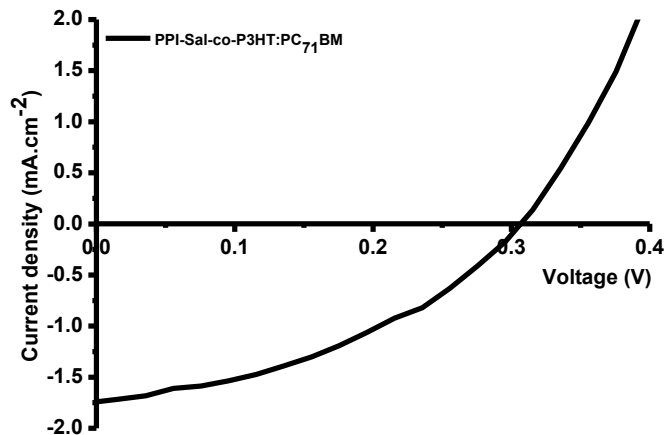


Figure 6.12: J–V characteristics of the fabricated OPVs using PPI-Sal-co-P3HT as donor materials.

6.4. Conclusion

In this work, PPI-Sal was synthesized using Schiff base condensation reaction and PPI-Sal-co-P3HT was synthesized using Grignard reaction method. The spectroscopic, thermal and electrochemical properties of the synthesized PPI-Sal and PPI-Sal-co-P3HT were compared. The UV-vis studies revealed that the optical band gap of PPI-Sal is wider than that of PPI-Sal-co-P3HT. TGA studies revealed that PPI-Sal has poor thermal stability than PPI-Sal-co-P3HT. These findings were attributed to the presence of P3HT chains on the four branches of PPI-Sal. The presence of the P3HT on the branches of PPI-Sal was confirmed by FTIR using change in wavenumber of the azomethine functional group band from 1634 cm^{-1} for PPI-Sal to 1636 cm^{-1} for PPI-Sal-co-P3HT and the reduction in the signal intensity in PPI-Sal-co-P3HT. The LUMO energy level of PPI-Sal-co-P3HT was determined and compared with those of PC₇₁BM. It was found that the LUMO offset is higher than the empirical value indicating high energy loss. The EIS studies revealed that PPI-Sal-co-P3HT is more conductive than PPI-Sal. The bias potential studies showed that as the bias potential becomes more negative, the R_{ct} and τ decreases exponentially. Maximum PCE of 0.21% has been obtained for PPI-Sal-co-P3HT based OPVs.

Reference

- [1] Cevallos-Vallejo, A., Vonlanthen, M., Porcu, P., Ruiu, A. and Rivera, E., 2017. New cyclen-cored dendrimers functionalized with pyrene: Synthesis characterization, optical and photophysical properties. *Tetrahedron Letters*, 58, pp.1319-1323.
- [2] Lyu, Z., Ding, L., Tintaru, A. and Peng, L., 2020. Self-assembling supramolecular dendrimers for biomedical applications: lessons learned from poly (amidoamine) dendrimers. *Accounts of Chemical Research*, 53, pp.3667-3676.
- [3] Astruc, D., Boisselier, E. and Ornelas, C., 2010. Dendrimers designed for functions: from physical, photophysical, and supramolecular properties to applications in sensing, catalysis, molecular electronics, photonics, and nanomedicine. *Chemical Reviews*, 110, pp.1857-1959.
- [4] Dias, A.P., da Silva Santos, S., da Silva, J.V., Parise-Filho, R., Ferreira, E.I., El Seoud, O. and Giarolla, J., 2020. Dendrimers in the context of nanomedicine. *International Journal of Pharmaceutics*, 573, p.118814.
- [5] Golshan, M., Rostami-Tapeh-Esmail, E., Salami-Kalajahi, M. and Roghani-Mamaqani, H., 2020. A review on synthesis, photophysical properties, and applications of dendrimers with perylene core. *European Polymer Journal*, 137, p.109933.
- [6] Bondareva, J., Kolotylo, M., Rozhkov, V., Burirov, V. and Lukin, O., 2020. A convergent approach to sulfonimide-based dendrimers and dendrons. *Tetrahedron Letters*, 61, p.152011.
- [7] Rauch, F., Endres, P., Friedrich, A., Sieh, D., Hähnel, M., Krummenacher, I., Braunschweig, H., Finze, M., Ji, L. and Marder, T.B., 2020. An iterative divergent approach to conjugated starburst borane dendrimers. *Chemistry (Weinheim an der Bergstrasse, Germany)*, 26, p.12951.
- [8] Saviano, F., Lovato, T., Russo, A., Russo, G., Bouton, C.R., Shattock, R.J., Alexander, C., Quaglia, F., Blakney, A.K., Gurnani, P. and Conte, C., 2020. Ornithine-derived oligomers and dendrimers for in vitro delivery of DNA and ex vivo transfection of skin cells via saRNA. *Journal of Materials Chemistry B*, 8, pp.4940-4949.
- [9] Tokarczyk, K. and Jachimska, B., 2017. Quantitative interpretation of PAMAM dendrimers adsorption on silica surface. *Journal of Colloid and Interface Science*, 503, pp.86-94.

- [10] Zhao, L., Wang, S., Ding, J. and Wang, L., 2018. Solution processible distyrylarylene-based fluorescent dendrimers: Tuning of carbazole-dendron generation leads to nondoped deep-blue electroluminescence. *Organic Electronics*, 53, pp.43-49.
- [11] Organista-Mateos, U., Martínez-Klimov, M.E., Pedro-Hernández, L.D., Borja-Miranda, A., Cortez-Maya, S., Hernández-Ortega, S. and Martínez-García, M., 2017. Synthesis of porphyrin dendrimers via Heck reaction and their photovoltaic properties. *Journal of Photochemistry and Photobiology A: Chemistry*, 343, pp.58-65.
- [12] Militello, M.P., Hernández-Ramírez, R.E., Lijanová, I.V., Previtali, C.M., Bertolotti, S.G. and Arbeloa, E.M., 2018. Novel PAMAM dendrimers with porphyrin core as potential photosensitizers for PDT applications. *Journal of Photochemistry and Photobiology A: Chemistry*, 353, pp.71-76.
- [13] Manikkath, J., Hegde, A.R., Kalthur, G., Parekh, H.S. and Mutalik, S., 2017. Influence of peptide dendrimers and sonophoresis on the transdermal delivery of ketoprofen. *International Journal of Pharmaceutics*, 521, pp.110-119.
- [14] He, G., Zhu, C., Ye, S., Cai, W., Yin, Y., Zheng, H. and Yi, Y., 2016. Preparation and properties of novel hydrogel based on chitosan modified by poly (amidoamine) dendrimer. *International Journal of Biological Macromolecules*, 91, pp.828-837.
- [15] Jiang, W., Stolterfoht, M., Jin, H. and Burn, P.L., 2020. Hole-transporting poly (dendrimer)s as electron donors for low donor organic solar cells with efficient charge transport. *Macromolecules*, 53, pp.2902-2911.
- [16] Zhang, X., Zeng, Y., Yu, T., Chen, J., Yang, G. and Li, Y., 2014. Advances in photofunctional dendrimers for solar energy conversion. *The Journal of Physical Chemistry Letters*, 5, pp.2340-2350.
- [17] Abbasi, E., Aval, S.F., Akbarzadeh, A., Milani, M., Nasrabadi, H.T., Joo, S.W., Hanifehpour, Y., Nejati-Koshki, K. and Pashaei-Asl, R., 2014. Dendrimers: synthesis, applications, and properties. *Nanoscale Research Letters*, 9, pp.1-10.
- [18] Pan, Y., Peng, Z. and Melinger, J.S., 2003. Synthesis and optical properties of conjugated dendrimers with unsymmetrical branching. *Tetrahedron*, 59, pp.5495-5506.
- [19] Ravivarma, M., Satheeshkumar, C., Ganesan, S. and Rajakumar, P., 2017. Synthesis and application of stilbenoid phenothiazine dendrimers as additives for dye-sensitized solar cells. *Materials Chemistry Frontiers*, 1, pp.2117-2124.

- [20] Kopidakis, N., Mitchell, W.J., Van De Lagemaat, J., Ginley, D.S., Rumbles, G., Shaheen, S.E. and Rance, W.L., 2006. Bulk heterojunction organic photovoltaic devices based on phenyl-cored thiophene dendrimers. *Applied Physics Letters*, 89, p.103524.
- [21] Ramoroka, M.E., Mdluli, S.B., John-Denk, V.S., Modibane, K.D., Arendse, C.J. and Iwuoha, E.I., 2021. Synthesis and Photovoltaics of Novel 2, 3, 4, 5-Tetrathienylthiophene-co-poly (3-hexylthiophene-2,5-diyl) Donor Polymer for Organic Solar Cell. *Polymers*, 13, p.2.
- [22] Lee, J., Kim, G.W., Kim, M., Park, S.A. and Park, T., 2020. Nonaromatic Green-Solvent-Processable, Dopant-Free, and Lead-Capturable Hole Transport Polymers in Perovskite Solar Cells with High Efficiency. *Advanced Energy Materials*, 10, p.1902662.
- [23] Liu, Y., Li, M., Zhou, X., Jia, Q.Q., Feng, S., Jiang, P., Xu, X., Ma, W., Li, H.B. and Bo, Z., 2018. Nonfullerene acceptors with enhanced solubility and ordered packing for high-efficiency polymer solar cells. *ACS Energy Letters*, 3, pp.1832-1839.
- [24] Anthopoulos, T.D., Markham, J.P., Namdas, E.B., Samuel, I.D., Lo, S.C. and Burn, P.L., 2003. Highly efficient single-layer dendrimer light-emitting diodes with balanced charge transport. *Applied Physics Letters*, 82, pp.4824-4826.
- [25] Schilinsky, P., Asawapirom, U., Scherf, U., Biele, M. and Brabec, C.J., 2005. Influence of the molecular weight of poly (3-hexylthiophene) on the performance of bulk heterojunction solar cells. *Chemistry of Materials*, 17, pp.2175-2180.
- [26] Memela, M., Feleni, U., Mdluli, S., Ramoroka, M.E., Ekwere, P., Douman, S. and Iwuoha, E., 2020. Electro-photovoltaics of Polymer-stabilized Copper-Indium Selenide Quantum Dot. *Electroanalysis*, 32, pp.3086-3097.
- [27] Iovu, M.C., Sheina, E.E., Gil, R.R. and McCullough, R.D., 2005. Experimental evidence for the quasi-“living” nature of the grignard metathesis method for the synthesis of regioregular poly (3-alkylthiophenes). *Macromolecules*, 38, pp.8649-8656.
- [28] Kraikin, V.A., Fatykhov, A.A., Gileva, N.G., Kravchenko, A.A. and Salazkin, S.N., 2021. NMR study of dyadic and triadic splitting in copoly (arylene) phthalides based on diphenyl oxide and diphenyl sulfide. *Magnetic Resonance in Chemistry*, 59, pp.61-73.
- [29] Kuang, S.P., Wang, Z.Z., Liu, J. and Wu, Z.C., 2013. Preparation of triethylene-tetramine grafted magnetic chitosan for adsorption of Pb (II) ion from aqueous solutions. *Journal of Hazardous Materials*, 260, pp.210-219.

- [30] Wei, B.Y., Cao, C.Z. and Cao, C.T., 2021. Influences of polarizability effect of alkyl group and homoring competition effect of substituents on the NMR spectra of salen-type Schiff base. *Magnetic Resonance in Chemistry*, 59, pp.701-712.
- [31] Zhang, X., Wu, S.T., Yang, X.J., Shen, L.Y., Huang, Y.L., Xu, H., Zhang, Q.L., Sun, T., Redshaw, C. and Feng, X., 2021. Dynamic Coordination between a Triphenylamine-Functionalized Salicylaldehyde Schiff Base and a Copper (II) Ion. *Inorganic Chemistry*, 60, 8581–8591.
- [32] Saleem, S.S., Sankarganesh, M., Jose, P.A. and Raja, J.D., 2021. Design, synthesis, antioxidant, antimicrobial, DNA binding and molecular docking studies of morpholine based Schiff base ligand and its metal (II) complexes. *Inorganic Chemistry Communications*, 124, p.108396.
- [33] Mashao, G., Ramohlola, K.E., Mdluli, S.B., Monama, G.R., Hato, M.J., Makgopa, K., Molapo, K.M., Ramoroka, M.E., Iwuoha, E.I. and Modibane, K.D., 2019. Zinc-based zeolitic benzimidazolate framework/polyaniline nanocomposite for electrochemical sensing of hydrogen gas. *Materials Chemistry and Physics*, 230, pp.287-298.
- [34] John, S.V., Mayedwa, N., Ikpo, C., Molefe, L.Y., Ndipingwi, M.M., Dywili, N.R., Van Wyk, J., Mapolie, S.F., Baker, P. and Iwuoha, E., 2016. Photoluminescence quenching of poly(octylfluorenylbenzothiadiazole) luminophore by n-type cobalt(II) salicylaldimine metallodendrimer. *Synthetic Metals*, 220, pp.114-122.
- [35] Cui, Z., Coletta, C., Dazzi, A., Lefrancois, P., Gervais, M., Néron, S. and Remita, S., 2014. Radiolytic method as a novel approach for the synthesis of nanostructured conducting polypyrrole. *Langmuir*, 30, pp.14086-14094.
- [36] Saini, V., Abdulrazzaq, O., Bourdo, S., Dervishi, E., Petre, A., Bairi, V.G., Mustafa, T., Schnackenberg, L., Viswanathan, T. and Biris, A.S., 2012. Structural and optoelectronic properties of P3HT-graphene composites prepared by in situ oxidative polymerization. *Journal of Applied Physics*, 112, p.054327.
- [37] Sun, C.J., Zhao, X.Q., Wang, P.F., Wang, H. and Han, B.H., 2017. Thiophene-based conjugated microporous polymers: synthesis, characterization and efficient gas storage. *Science China Chemistry*, 60, pp.1067-1074.

- [38] Ansari, M.A., Mohiuddin, S., Kandemirli, F. and Malik, M.I., 2018. Synthesis and characterization of poly (3-hexylthiophene): improvement of regioregularity and energy band gap. *RSC Advances*, 8, pp.8319-8328.
- [39] García-Escobar, C.H., Nicho, M.E., Hu, H., Alvarado-Tenorio, G., Altuzar-Coello, P., Cadenas-Pliego, G. and Hernández-Martínez, D., 2016. Effect of microwave radiation on the synthesis of poly(3-hexylthiophene) and the subsequent photovoltaic performance of CdS/P3HT solar cells. *International Journal of Polymer Science*, 2016, pp.1-9.
- [40] Xia, H., Ye, Z., Liu, X., Peng, J. and Qiu, F., 2014. Synthesis, characterization, and solution structure of all-conjugated polyelectrolyte diblock copoly (3-hexylthiophene) s. *RSC Advances*, 4, pp.19646-19653.
- [41] El-Gammal, O.A., Mohamed, F.S., Rezk, G.N. and El-Bindary, A.A., 2021. Synthesis, characterization, catalytic, DNA binding and antibacterial activities of Co(II), Ni(II) and Cu(II) complexes with new Schiff base ligand. *Journal of Molecular Liquids*, 326, p.115223.
- [42] Rani, J.J., Jayaseeli, A.M.I., Rajagopal, S., Seenithurai, S., Chai, J.D., Raja, J.D. and Rajasekaran, R., 2021. Synthesis, characterization, antimicrobial, BSA binding, DFT calculation, molecular docking and cytotoxicity of Ni(II) complexes with Schiff base ligands. *Journal of Molecular Liquids*, 328, p.115457.
- [43] Lee, Y.H., Yeh, P.S., Hsu, Y.T., Tong, Z.H. and Chiang, C.H., 2021. Effective control of solution self-assembly of P3HT/zinc salt complex for in situ template synthesis of P3HT/ZnO nanohybrids. *Polymer*, 215, p.123385.
- [44] Bai, R., Sun, Y., Zhao, M., Han, Z., Zhang, J., Sun, Y., Dong, W. and Li, S., 2021. Preparation of IgG imprinted polymers by metal-free visible-light-induced ATRP and its application in biosensor. *Talanta*, 226, p.122160.
- [45] Chao, C.Y., Chao, C.H., Chen, L.P., Hung, Y.C., Lin, S.T., Su, W.F. and Lin, C.F., 2012. Band structure engineering for low band gap polymers containing thienopyrazine. *Journal of Materials Chemistry*, 22, pp.7331-7341.
- [46] Nakano, K., Chen, Y., Xiao, B., Han, W., Huang, J., Yoshida, H., Zhou, E. and Tajima, K., 2019. Anatomy of the energetic driving force for charge generation in organic solar cells. *Nature Communications*, 10, pp.1-10.

- [47] Mei, B.A., Lau, J., Lin, T., Tolbert, S.H., Dunn, B.S. and Pilon, L., 2018. Physical interpretations of electrochemical impedance spectroscopy of redox active electrodes for electrical energy storage. *The Journal of Physical Chemistry C*, 122, pp.24499-24511.
- [48] Zhang, J., Zheng, X., Yang, X. and Cao, W., 2011. The Effects of Co-Sensitization and Electronic Structure of Nanocrystalline N/TiO₂ Anode on the Performance of Dye-Sensitized Solar Cells. *Journal of Inorganic and Organometallic Polymers and Materials*, 21, pp.150-156.
- [49] Alamelu, K., Raja, V., Shiamala, L. and Ali, B.J., 2018. Biphasic TiO₂ nanoparticles decorated graphene nanosheets for visible light driven photocatalytic degradation of organic dyes. *Applied Surface Science*, 430, pp.145-154.
- [50] Chang, Y.M., Su, W.F. and Wang, L., 2008. Photoactive polythiophene: titania hybrids with excellent miscibility for use in polymer photovoltaic cells. *Macromolecular Rapid Communications*, 29, pp.1303-1308.
- [51] Xu, T., Yan, M., Hoefelmeyer, J.D. and Qiao, Q., 2012. Exciton migration and charge transfer in chemically linked P3HT–TiO₂ nanorod composite. *RSC Advances*, 2, pp.854-862.
- [52] Hu, Z., Willard, A.P., Ono, R.J., Bielawski, C.W., Rossky, P.J. and Bout, D.A.V., 2015. An insight into non-emissive excited states in conjugated polymers. *Nature Communications*, 6, pp.1-9.
- [53] Zheng, J., Li, Y., Cui, Y., Jia, J., Ye, Q., Han, L. and Gao, J., 2015. Isatin-phenylhydrazone dyes and boron complexes with large Stokes shifts: Synthesis and solid-state fluorescence characteristics. *Tetrahedron*, 71, pp.3802-3809.
- [54] Hau, S.K., Yip, H.L., Baek, N.S., Zou, J., O'Malley, K. and Jen, A.K.Y., 2008. Air-stable inverted flexible polymer solar cells using zinc oxide nanoparticles as an electron selective layer. *Applied Physics Letters*, 92, p.225.
- [55] Krebs, F.C. and Norrman, K., 2007. Analysis of the failure mechanism for a stable organic photovoltaic during 10 000 h of testing. *Progress in Photovoltaics: Research and Applications*, 15, pp.697-712.

CHAPTER 7

Hexathienylthiophene-co-Poly(3-hexylthiophene) as Donor Material for Organic Photovoltaic Cell

Abstract

The hexathienylbenzene-co-poly(3-hexylthiophene-2,5diyl) (HTB-co-P3HT) conducting polymer was synthesized by co-polymerization of hexathienylbenzene (HTB) and 3-hexylthiophene using iron chloride (FeCl_3) as an oxidant. The effect of solvent was studied using chlorobenzene, toluene and chloroform. The study revealed that spectroscopic and electrochemical response are affected as the solvent changed. The lowest unoccupied molecular orbital (LUMO) and highest occupied molecular orbital (HOMO) energy levels of HTB-co-P3HT were determined from cyclic voltammetry and were compared to those of [6,6]-phenyl C71 butyric acid methyl ester (PC_{71}BM). The study revealed that the LUMO energy levels of HTB-co-P3HT determined in toluene were deeper than those determined in chlorobenzene and chloroform. The electrochemical impedance spectroscopy (EIS) analysis also revealed that the thin film of HTB-co-P3HT prepared using toluene is the most conductive. Photovoltaic parameters of HTB-co-P3HT were determined in different solvents. We obtained power conversion efficiency (PCE) of 0.48%, fill factor (FF) of 27.84%, current density (J_{SC}) of $4.93 \text{ mA}\cdot\text{cm}^{-2}$ and open circuit voltage (V_{OC}) of 0.35 V in chlorobenzene, PCE of 0.30%, FF of 26.08%, J_{SC} of $5.00 \text{ mA}\cdot\text{cm}^{-2}$ and V_{OC} of 0.23 V in chloroform and finally, PCE of 0.33%, FF of 25.45%, J_{SC} of $5.70 \text{ mA}\cdot\text{cm}^{-2}$ and V_{OC} of 0.23 V in toluene. Different values obtained for photovoltaic parameters of HTB-co-P3HT indicate that solvent have an effect.

7.1. Introduction

The use of organic polymers was restricted to insulators in electrical applications before conducting polymers were discovered due to their high resistivity [1]. After a great work of research, first conducting organic polymer was discovered having a good conductivity [2,3]. It was discovered that the conductivity of the conducting polymers arises from alternating single and double bonds along the polymer chain. To date, many conducting polymers such as polypyrroles [4], polycarbozoles [5], polythiophenes [6], polyaniline [7] and polynaphthylamine [8] have been developed. The conducting polymers have been attracting a lot of attention from researchers in different research fields such as organic light emitting diodes [9], organic field-effect transmitters [10], supercapacitors [11], biosensors [12] and organic photovoltaics [13].

Conducting polymers have gained a lot of interest in the optoelectronics research field because of their advantages such as low cost of materials, tenability of optical properties, light weight and their flexible compatibility [14]. The properties of conjugated polymers are modified by either modification of the side chains or the main chain [15]. The studies showed that polymerization of monomeric fused rings turn to narrow the optical band gap, increase the conjugation length and increase the limits of light absorption [16–20]. Modification of either main chain or side chain with an alkyl group turn to improve the solubility of the polymer, reduce recombination rate and turns to lower LUMO energy levels of the donor material to ensure sufficient electrons transfer to the acceptor material [21,22]. Studies showed that modification of conjugated polymers with electron withdrawing group turn to tune the molecular energy levels and control aggregation morphologies leading to higher charge carrier mobility [23].

Poly(3-hexylthiophene) (P3HT) is one of the conjugated polymers as a donor material in OPVs because of its advantageous properties such as easy to synthesize and high charge carrier mobility. However, it has wider band gap of ~1.9 eV which limit its photon absorption properties. The low power conversion efficiency of P3HT based photovoltaic cell is mostly due to low value of open circuit voltage due to high position of HOMO energy levels of P3HT [24]. There are many efforts done to try to tune the HOMO energy level to a position that can allow sufficient charge transfer. The hexyl group on the 3-position of thiophene ring was replaced by an alkoxy group; but, the introduction of alkoxy group on thiophene turns to improve photon absorption properties by

reducing band gap, while decreasing oxidation potential resulting in higher HOMO energy level for use in OPVs as a donor material [25]. P3HT was also modified at the α -position of the last thiophene in the polymer chain with bromine. It was found that the presence of bromine end-group turn to decrease the overall performance of the device. Due to high electronegativity of bromine, charges are trapped and more disordered morphology was obtained [26]. The presence of bromine on the P3HT also causes a blue shift on the absorption spectrum [27].

In this work, we synthesize novel HTB-co-P3HT dendritic co-polymer using hexathienylbenzene (HTB) as a core. HTB was synthesized using Stille condensation reaction and co-polymerization was performed using chemical oxidation polymerization method. The effect of P3HT on the surface of HTB was studied in chlorobenzene, toluene and chloroform using different characterization techniques. The energy levels of HTB-co-P3HT in different solvents were compared to those of PC₇₁BM. OPVs devices of HTB-co-P3HT were fabricated in different solvents. It was revealed that as solvent changes, photovoltaic parameters of HTB-co-P3HT as a donor material also changes. High PCE was obtained when chlorobenzene was used as a solvent, while low PCE was obtained in chloroform.

7.2. Materials and Methods

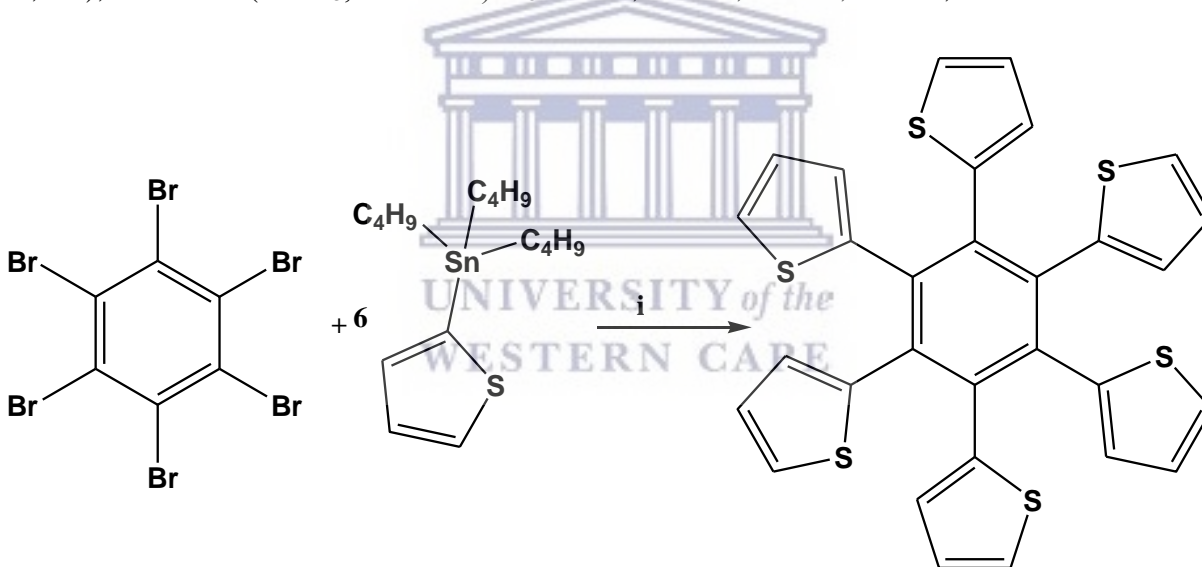
7.2.1. Materials

Chemicals and solvents were used without any further purification and were bought from commercial sources. Silica gel 60 Å (230–400 mesh, Merck (Pty) Ltd., Johannesburg, South Africa) was used for purification. Deionized water used in this study was obtained from a Millipore Direct Q3 system (Millipore, Milford, MA, USA).

7.2.2. Synthesis of HTB

One of the most prominent methods for synthesis of carbon-carbon bonds is the Stille condensation reaction [28,29]. For synthesis of HTB, Stille condensation reaction method was used. In details, hexabromobenzene (0.50 g, 0.91 mmol, 98%, Merck (Pty) Ltd.), 2-(tributylstannyl)-thiophene (2.04 g, 5.46 mmol, 97%, Merck (Pty) Ltd.), copper(I) iodide (1.04 g, 5.46 mmol, 98%, Merck (Pty) Ltd.) and potassium carbonate anhydrous (1.51 g, 10.92 mmol, K₂CO₃, 99.5%, Merck (Pty) Ltd.) were dissolved in toluene (100 mL, 99.8%, Merck (Pty) Ltd.) and stirred for 30 min at room

temperature. After 30 min, palladium tetrakis(triphenylphosphine) (5% mol, 0.31 g, 0.27 mmol, Pd(PPh₃)₄, 99%, Merck (Pty) Ltd.) was added into the solution. The solution was stirred at 110°C for 120 h under nitrogen gas. After 120 h, the solvent of the resulting solution was removed and re-dissolved in dichloromethane (DCM, 99.9%, Merck (Pty) Ltd.). The resulting solution was washed 3 times with deionized water. Magnesium sulphate (MgSO₄, ≥99.5%, Merck (Pty) Ltd.) powder was added into the washed solution. The suspensions of MgSO₄ were removed by filtration. The resulting solution was concentrated by rotary evaporator, followed by purification with column chromatography using DCM and petroleum ether (PE, 95%, Merck (Pty) Ltd.) as an eluent (DCM:PE = 1:2, v/v) and silica gel as stationary phase. The resulting yellow powder (0.33 g) was obtained with 64% yield. The synthetic pathway is shown schematically in scheme 7.1. ¹H-NMR (CDCl₃, Merck (Pty) Ltd., 400 MHz): δ_H 6.93–6.95 (dd, 6H), 7.09–7.11 (dd, 6H), 7.13–7.15 (dd, 6H); ¹³C-NMR (CDCl₃, 400 MHz): δ_C 123.77, 124.36, 127.77, 128.24, 129.05.

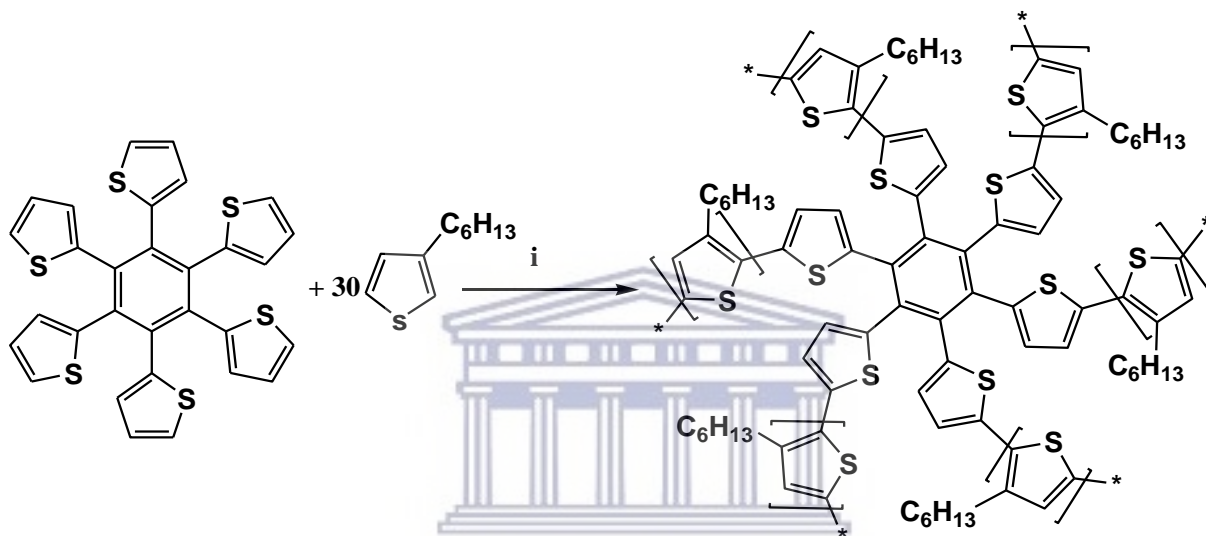


Scheme 7.1: Synthetic route of HTB. (i). 5% Pd(PPh₃)₄, K₂CO₃, CuI, Toluene, 120 h, 110°C.

7.2.3. Synthesis of HTB-co-P3HT

HTB-co-P3HT was synthesized using chemical oxidation polymerization [30,31]. HTB (0.15 g, 0.26 mmol) and 3-hexylthiophene (1.42 mL, 1.33 g, 7.89 mmol, ≥99.0%, Merck (Pty) Ltd.) were added in chloroform (80 mL, ≥99.0%, Merck (Pty) Ltd.). The solution was stirred under nitrogen for 30 minutes and followed by addition of iron chloride anhydrous (5.12 g, 0.03 mol, FeCl₃, ≥99.99%, Merck (Pty) Ltd.) suspensions in chloroform. The mixture was refluxed for 24 h at 60

°C under nitrogen gas. Then, polymerization was terminated by addition of methanol anhydrous (MeOH, 99.8%, Merck (Pty) Ltd.). The precipitates formed after addition of MeOH, filtered and washed with Soxhlet extractor (size large, 200 mL extractor volume, Merck (Pty) Ltd.) using acetone (99.3%, Merck (Pty) Ltd.) for 24 h and MeOH for another 24 h. HTB-co-P3HT was extracted with DCM for 24 h resulting in a 0.28 g dark purple solid. This procedure is shown schematically in scheme 7.2.



Scheme 7.2: Synthetic route of HTB-co-P3HT. (i) FeCl_3 , chloroform, 24 h, 60°C .

7.2.4. Characterization Techniques

Nuclear magnetic resonance (NMR) spectra (Bruker 400 MHz Avance III HD Nanobay Spectrometer, Karlsruhe, Germany) and Fourier-transform infrared spectroscopy (FTIR) spectroscopy (Spectrum-100 FTIR Spectrometer from PerkinElmer (Pty) Ltd., Midrand, South Africa) were used for structural characterization of the synthesized compounds. The thermal gravimetric measurements were done by The Thermal Analyzer Perkin Elmer STA 6000 Instrument (PerkinElmer (Pty) Ltd.) at a rate of $10^\circ\text{C}/\text{min}$ under N_2 flow rate of 20 ml/min. The ultraviolet-visible (UV-Vis) spectra (Nicolet Evolution 100 from Thermo Electron Corporation, Altrincham, UK) were obtained at room temperature. Transmission electron microscope (TEM) images were (FEI Tecnai T20 TEM from FEI company, Hillsboro, OR, USA) obtained for synthesized polymers. Scanning electron microscope (SEM) images (Tescan MIRA3 RISE SEM from Tescan, Brno, Czech Republic) and elemental analysis (FEI NovaNano SEM from FEI

company, Hillsboro, OR, USA) were investigated. Photoluminescence spectra (NanoLog from Horiba Jobin Yvon, Edison, NJ, USA) were obtained. Cyclic voltammetry (CV) and electrochemical impedance spectroscopy (EIS) studies were conducted on a CHI700E-Potentiostat (CH Instruments, Inc, Bee Cave, TX, USA). The measurements were performed using indium tin oxide (ITO) glass substrate (14–16 Ω /square resistance, Oscilla, Sheffield, UK) as working electrode, platinum wire (Goodfellow Cambridge Ltd., Huntingdon, UK) as counter electrode and silver/silver chloride (Ag/AgCl, from BASi® in West Lafayette, IN, USA) as reference electrode in 0.1 M of tetrabutylammonium hexafluorophosphate (TBAPF₆, \geq 99.0%, Merck (Pty) Ltd.)/acetonitrile (99.8%, Merck (Pty) Ltd.) solution as an electrolyte. Before using ITO glass substrate, it was washed with 1% (by volume) hellmanex III (Merck (Pty) Ltd.) solution, acetone and 2-propylalcohol (99.5%, Merck (Pty) Ltd.). Device characteristics (current density–voltage) were measured with X200 Source Meter Unit (Ossila, Sheffield, UK) using an illumination of AM 1.5G, 100 mW cm⁻² supplied by a SciSun-150 Solar Simulator, Class AAA (Sciencetech Inc., London, ON, Canada).

7.2.5. OPVs fabrication

OPVs fabrication and measurements were done outside a glovebox. ITO glass substrates were washed with hellmanex III solution in hot water, 2-propylalcohol and acetone. After washing the ITO glass substrate, zinc oxide (ZnO) was spun coated and annealed for 30 min at 100°C. The active layer was prepared by dissolving PPI-Sal-co-P3HT and PC₇₁BM (mixture of isomers, 99%, Merck (Pty) Ltd.) in chlorobenzene (99.9%, Merck (Pty) Ltd.) with a total concentration of 25 mg/mL. The active layer solution was stirred at 60°C for overnight. It was spun coated onto ZnO/ITO glass substrate and annealed at 100°C for 5 min. After coating with an active layer, poly(3,4-ethylenedioxythiophene) polystyrene sulfonate (PEDOT:PSS (0.5–1.0 wt % in water, Merck (Pty) Ltd.) was spun coated and annealed at 150°C for 5 min. Finally, silver conductive paste (Ag, Merck (Pty) Ltd.) was coated as cathode electrode and dried at 100°C for 5 min to complete the OPVs.

7.3. Results and Discussions

7.3.1. NMR studies of HTB and HTB-co-P3HT

The structure of HTB was confirmed by NMR spectroscopy. Figure 7.1A and 7.1B show the ^1H -NMR and ^{13}C -NMR spectra of HTB, respectively. The integrals on the ^1H -NMR spectra indicate that a total of 18 protons detected which correspond to a total number of protons from HTB structure. The signals at 6.93–6.95 and 7.09–7.11 ppm correspond to protons at the β -position of thiophene. While protons at the α -position of thiophene have a signal at 7.13–7.15 ppm. The ^{13}C -NMR spectra of HTB showed five signals at different chemical shifts. HTB has more than five carbons. This can be explained by the structural symmetry of HTB, which causes carbon signals to appear at the same chemical shift. The signals at 123.77 and 127.77 ppm are assigned to thiophene β -carbons, 124.36 ppm is assigned to the thiophene α -carbon, 128.24 ppm is assigned to the benzene carbons and 129.05 ppm is assigned to the tertiary carbon on thiophene. These finds were interpreted while consulting literature and are in agreement [32–34]. The ^1H -NMR spectrum of HTB-co-P3HT is shown in Figure 7.2. The signal at 0.88 ppm is assigned to the CH_3 - from the hexyl group, 1.28-1.45, 1.56 and 2.57-2.80 ppm are attributed to the $-\text{CH}_2-$ from the hexyl group and 7.00-7.06 ppm is ascribed to the β -protons from the thiophene groups [35,36].

UNIVERSITY OF
WESTERN CAPE

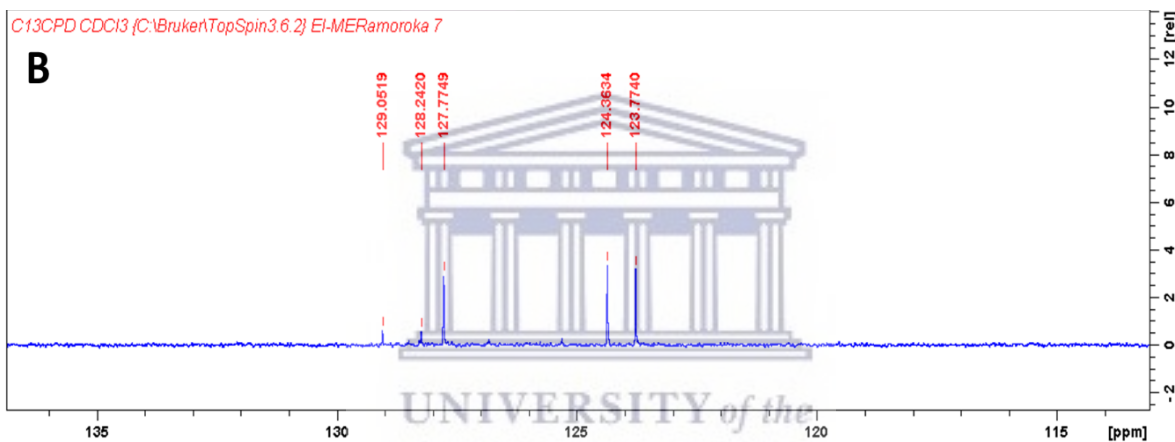
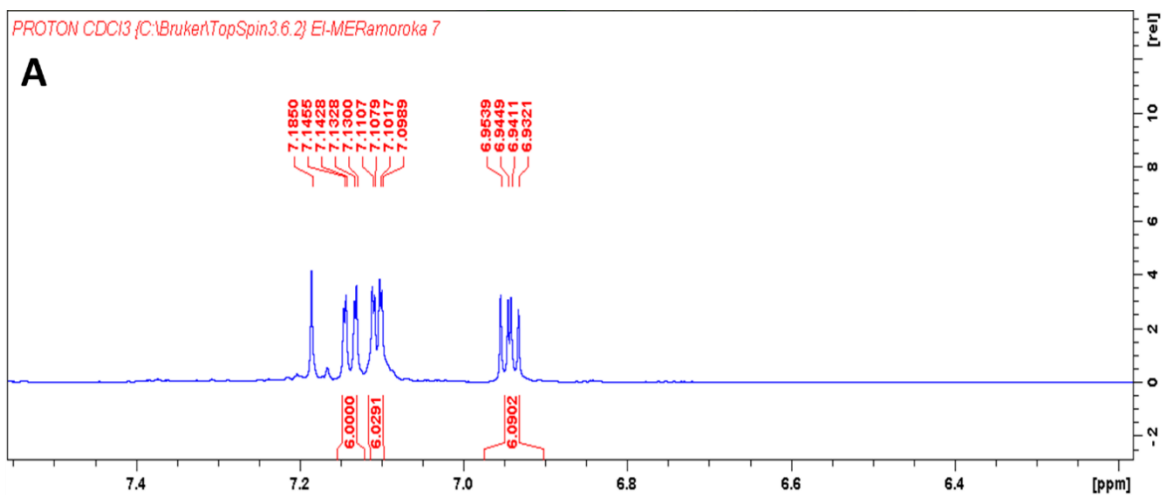


Figure 7.1: (A) ¹H-NMR and (B) ¹³C-NMR of HTB.

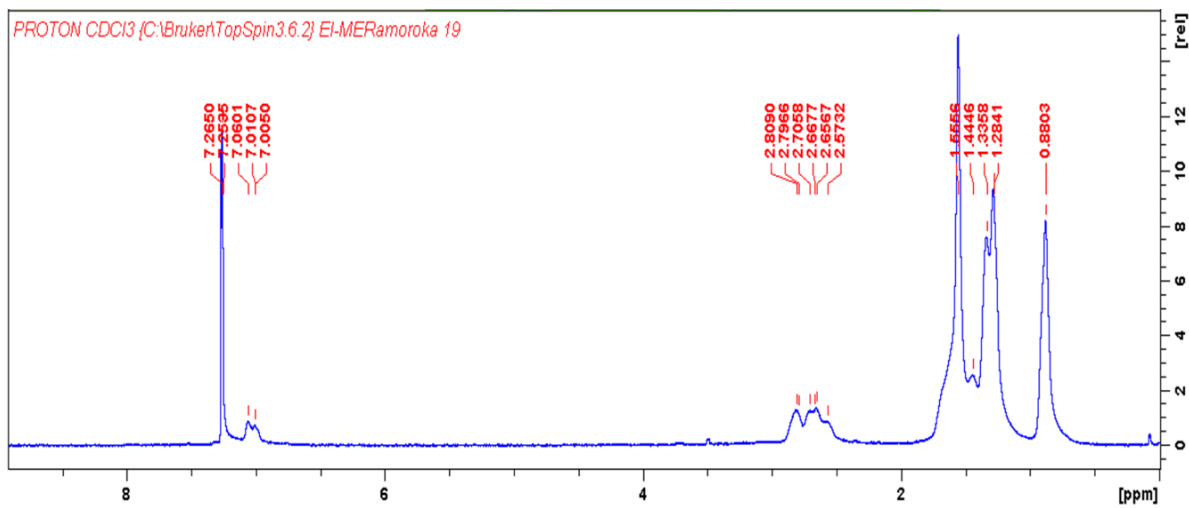


Figure 7.2: ¹H-NMR of HTB-co-P3HT.

7.3.2. FTIR analysis of HTB and HTB-co-P3HT

The synthesized HTB and HTB-co-P3HT were characterized by FTIR (Figure 7.3). The bands at 3104 and 2919 cm^{-1} in the spectrum of HTB are attributed to the C–H stretching, while the band at 816 cm^{-1} is ascribed to the in-plane bending vibration of the aromatic ring. The band at 1094 cm^{-1} is attributed to C–S vibrations. Additionally, the band at 694 cm^{-1} is due to the in-plane bend of the C–S–C of thiophene. Bands at 1435 and 1301 cm^{-1} are assigned to the C=C and C–C of thiophene ring, respectively [37]. After formation of HTB-co-P3HT, strong bands at 2926 and 2855 cm^{-1} appears owing to the vibration of C–H of hexyl group [38]. The band due to C=C stretching vibration shift to 1461 cm^{-1} and this shift is attributed to the attachment of P3HT at the α -position of thiophene [39]. This shift indicates the attachment of P3HT on HTB, since its presence affect the vibration of the bonds in HTB.

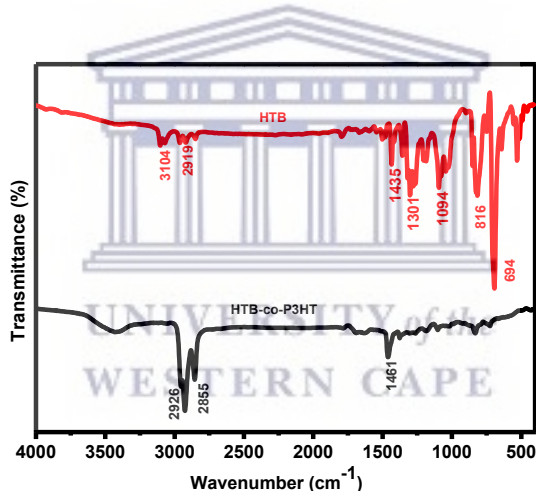


Figure 7.3: FTIR spectra of HTB and HTB-co-P3HT.

7.3.3. TGA studies of HBT-co-P3HT

Figure 7.4 shows a TGA thermogram of HTB-co-P3HT obtained from the co-polymerization of HTB and 3HT. The decomposition of HTB-co-P3HT takes place in two stages. No weight loss was observed at a temperature range between 50 and 130°C [40]. This indicates that there is no water absorbed on the surface of the sample. In the second stage, weight loss of 8% occurred in the temperature range of 138-312°C. This could be due to the decomposition of small molecular weight HTB-co-P3HT and HTB. In the second stage, 25% of the weight loss in the temperature

range of 379-455°C was observed. This weight loss represents the decomposition of HTB-co-P3HT. The remaining weight of 50% was observed and is attributed to solid residues [41,42].

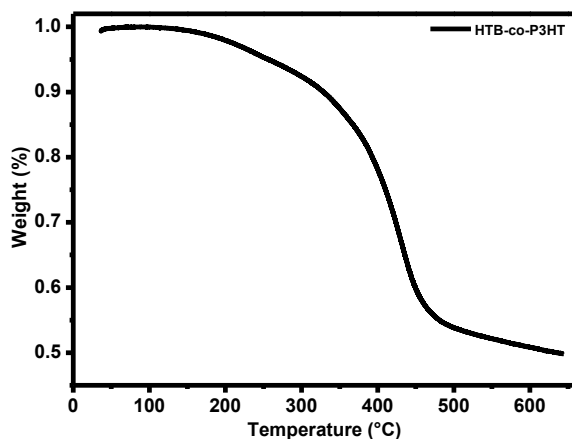


Figure 7.4: TGA thermogram of HTB-co-P3HT.

7.3.4. UV-Vis studies of HTB and HTB-co-P3HT in different solvents

The UV-Vis spectra of HTB and HTB-co-P3HT were recorded in different solvents at room temperature as depicted in Figure 7.5. One and two bands were observed in the absorption spectra of HTB and HTB-co-P3HT in all different solvents. The first band in the spectrum of HTB is due to $\pi \rightarrow \pi^*$ transition and the second band is due to $n \rightarrow \pi^*$ transition [43]. The band in the spectrum of HTB-co-P3HT is due to the extensive conjugated P3HT chain on the surface of HTB. The absorption response of the two compounds are different (as given in Table 7.1) because of the difference in the polarity of the solvents used to perform analysis. The maximum wavelength and lower band gap were obtained in halogen free solvent (toluene). Onset wavelengths were used to estimate the optical band gaps of HTB and HTB-co-P3HT. The onset wavelengths of HTB solutions, HTB-co-P3HT solutions and HTB-co-P3HT were determined from Figure A8, Figure A9 and Figure A10, respectively. The relationship between onset wavelength and optical band gap is given by Equation 7.1 below:

$$E_g = \frac{1240}{\lambda_{\text{onset}}} \text{eV} \dots \dots \dots 7.1$$

where E_g is optical band gap and λ_{onset} is onset wavelength [30]. Optical band gaps for HTB were determined to be 3.55, 3.54 and 3.56 eV, while for HTB-co-P3HT were determined to be 2.38,

2.34 and 2.36 eV in chlorobenzene, toluene and chloroform, respectively. As for thin film, the optical band gaps for HTB-co-P3HT were determined to be 2.15, 2.12 and 2.13 eV for thin films prepared in chlorobenzene, toluene and chloroform, respectively. This study indicated that bathochromic shift occurs as the chlorine atoms are absent on the solvent molecules. Since J_{SC} is inversely proportional to optical band gap, therefore, high J_{SC} can be achieved in toluene since small value of the optical bandgap was obtained [44]. This also indicates that high generation of electron-hole pair in HTB-co-P3HT will occur in toluene [45].

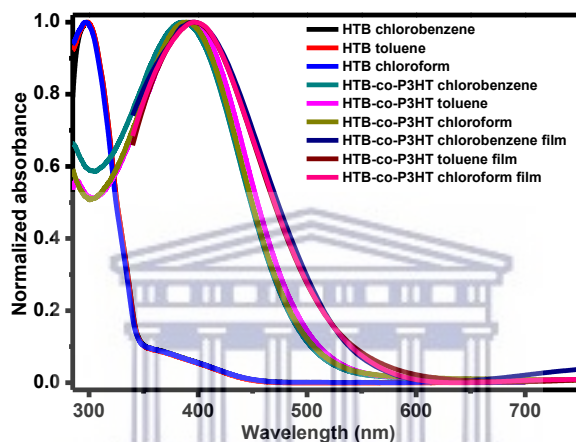


Figure 7.5: UV-Vis spectra of HTB and HTB-co-P3HT in different solvents.

Table 7.1: UV-Vis response of HTB and HTB-co-P3HT in various solvents.

Compound	Solvent	Maximum wavelength (nm)	Onset Wavelength (nm)	Optical band gap (eV) ^a	Onset Wavelength film (nm)	Optical band gap film (eV) ^a
HTB	chlorobenzene	298	349	3.55	-	-
HTB	toluene	299	350	3.54	-	-
HTB	chloroform	296	348	3.56	-	-
HTB-co-P3HT	chlorobenzene	386	520	2.38	578	2.15
HTB-co-P3HT	toluene	393	530	2.34	589	2.12
HTB-co-P3HT	chloroform	389	525	2.36	583	2.13

^aOptical band gap = $1240/\lambda_{\text{onset}}$

7.3.5. TEM studies of HTB-co-P3HT

The morphology of HTB-co-P3HT in different solvents was also characterized using TEM. Obtained TEM images of HTB-co-P3HT in different solvents are presented in Figure 7.6. The images are dark in the region where appears to be HTB-co-P3HT. This is due to high concentration of HTB-co-P3HT particles. Therefore, it is difficult to observe the effect of solvent on the morphology of HTB-co-P3HT. It was expected that when chloroform is used as a solvent to

prepare a sample for TEM analysis, the resulting images will show agglomeration of particles because of its low boiling point and lower surface tension [46,47]. This is because chloroform evaporate fast when compared to toluene and chlorobenzene. It does not give particles enough time to settle, therefore, agglomeration take place which may severely cause high recombination resulting to a decrease in V_{oc} [48].

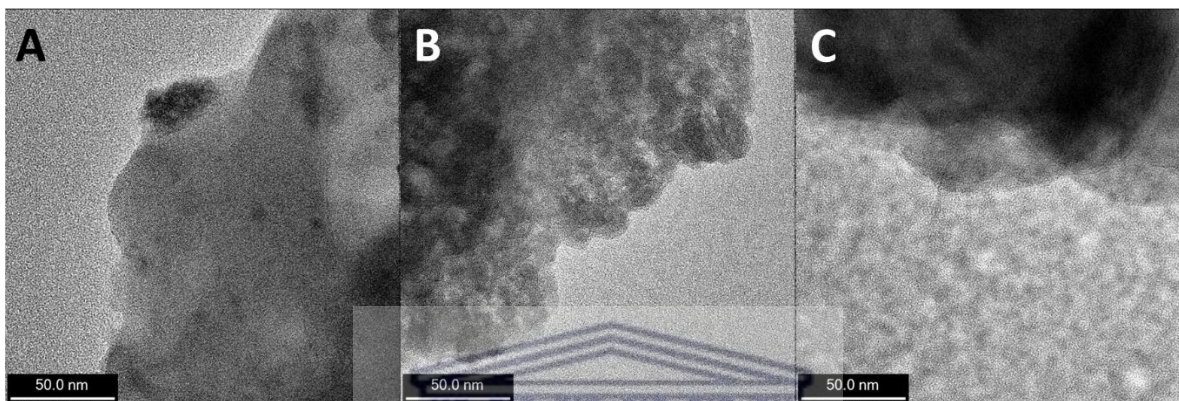


Figure 7.6: TEM images of HTB-co-P3HT prepared using (A) chlorobenzene, (B) chloroform and (C) toluene as solvents.

7.3.6. SEM studies of HTB-co-P3HT

Figure 7.7 shows the SEM images of HTB-co-P3HT films prepared using different solvents. The HTB-co-P3HT film were prepared by drop coating onto an ITO coated glass substrate. The SEM images revealed that the surface of HTB-co-P3HT is smooth, and the morphology changes are the solvent changes. In chlorobenzene, there are same agglomeration of HTB-co-P3HT particles. While in chloroform, HTB-co-P3HT particles with rod and spherical shape were observed. In toluene, the particles with spherical shape were observed. Figure 7.8 shows the spectra of HTB-co-P3HT in different solvents. The spectra revealed the presence of carbon (C) and sulphur (S) which are from synthesized HTB-co-P3HT polymer. The presence of impurities (aluminium (Al) and chlorine (Cl)) were detected. An impurity Cl is attributed to an oxidant $FeCl_3$ used during polymerization.

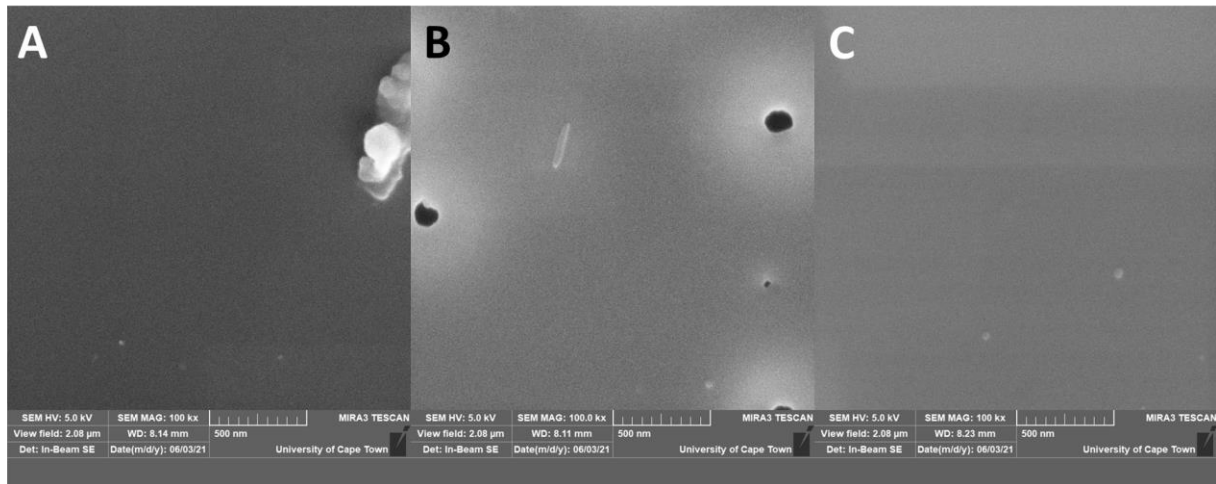


Figure 7.7: SEM images of HTB-co-P3HT films prepared using (A) chlorobenzene, (B) chloroform and (C) toluene.

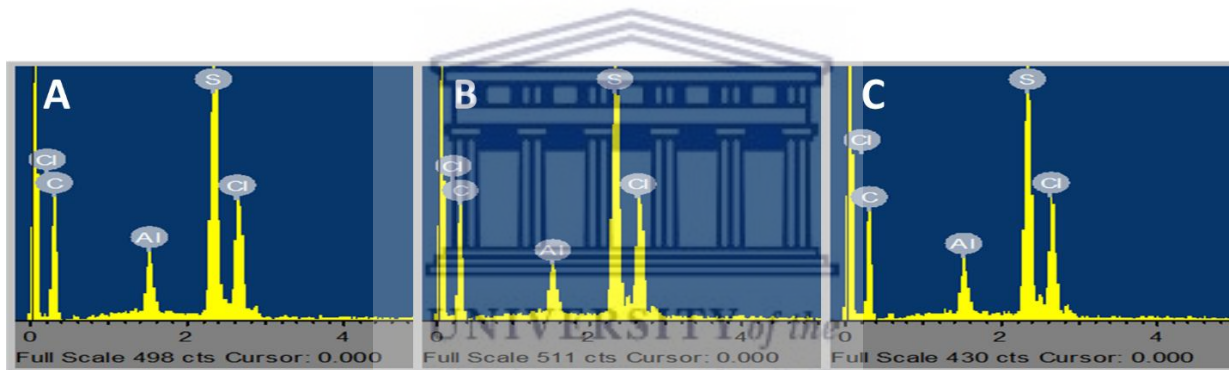


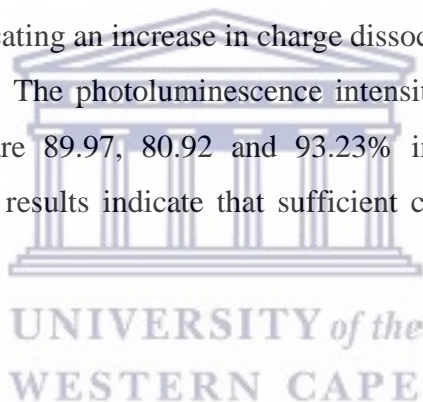
Figure 7.8: EDS spectra of HTB-co-P3HT films prepared using (A) chlorobenzene, (B) chloroform and (C) toluene as solvents.

7.3.7. Photoluminescence of HTB-co-P3HT

Photoluminescence studies of HTB and HTB-co-P3HT in different solvents are shown in Figure 7.9. From the spectra of both samples, the excitation spectra are blue-shifted compared with the emission spectra due to Stokes shift. This suggests that the photogenerated excitons lose energy by means of either nonradiative or radiative processes before recombination [49]. The emission spectra of HTB exhibited peaks at 365, 364 and 366 nm while excitation spectra of HTB exhibited peaks at 329, 331 and 331 nm resulting to Stokes shift of 36, 33 and 35 nm in chlorobenzene, toluene and chloroform, respectively. The Stokes shift for HTB-co-P3HT were determined to be 130, 133 and 131 nm in chlorobenzene, toluene and chloroform, respectively. The Stokes shifts of HTB-co-P3HT are wider than those of HTB. This is attributed to efficient energy transfer to

lower energy levels and planarity enhancement of P3HT polymer chain in HTB-co-P3HT [50]. The emission spectra of HTB-co-P3HT exhibited peaks at 545 nm in chlorobenzene, 546 nm in toluene and 543 nm in chloroform. The difference between the wavelengths of the emission peaks in different solvents are low indicating weak solvatochromism and suggesting that the ground state energy levels of HTB-co-P3HT are independent of the solvent polarity [51]. The emission peak of HTB-co-P3HT is more red-shifted and the Stokes shift is wider in toluene. This is because of high polarity of toluene [50].

Photoexcited charge transfer in the heterojunction between HTB-co-P3HT and PC₇₁BM was investigated using photoluminescence. Emission spectra of HTB-co-P3HT and PC₇₁BM blends are shown in Figure 7.9. Strong emission peak of HTB-co-P3HT suggests high recombination of holes and electrons [52]. The photoluminescence intensity of HTB-co-P3HT:PC₇₁BM is lower than that of HTB-co-P3HT, indicating an increase in charge dissociation of photoexcited excitons and reduction of recombination. The photoluminescence intensity of HTB-co-P3HT quenched after blending with PC₇₁BM are 89.97, 80.92 and 93.23% in chlorobenzene, toluene and chloroform, respectively. These results indicate that sufficient charge separation take place in chloroform.



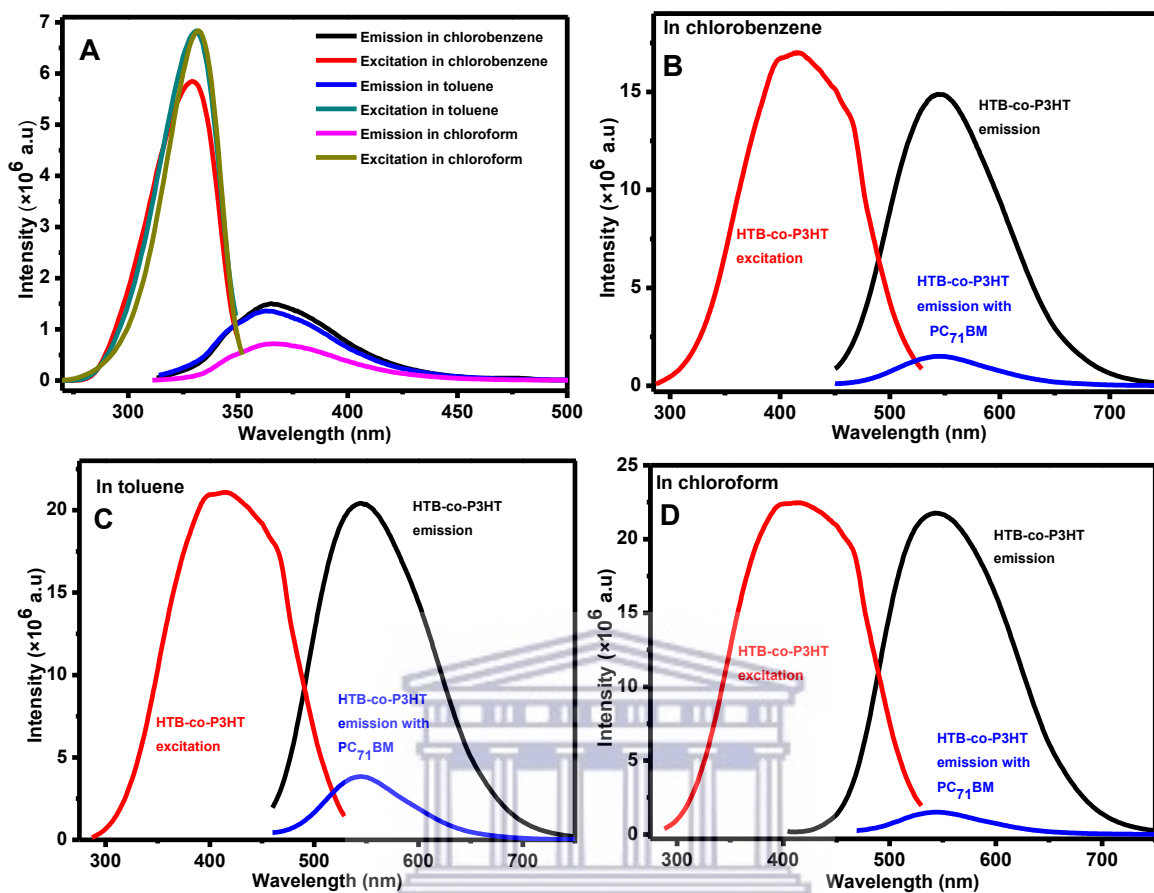


Figure 7.9: (A) Photoluminescence spectra of HTB in different solvents. Photoluminescence spectra of HTB-co-P3HT in (B) chlorobenzene, (C) toluene and (D) chloroform.

7.3.8. CV studies of HTB-co-P3HT

The effect of solvent used to prepare the thin film was studied using CV. Figure 7.10A shows the cyclic voltammograms of HTB-co-P3HT thin films prepared using three different solvents. The HOMO and LUMO energy levels were determined and compared with the energy levels of P3HT and PC₇₁BM. The results obtained from the voltammograms of HTB-co-P3HT in different solvents are listed in Table 7.2. Both HOMO and LUMO energy levels of HTB-co-P3HT in toluene are deeper than those in chlorinated solvent and gave a narrow electrochemical band gap. This change can be attributed to the boiling point and polarity of the solvent. Due to low boiling point of chloroform, the polymer chain is not granted more time to arrange in more crystalline structure leading to aggregation [53]. The difference in polarity of chloroform, toluene and chlorobenzene solvents might cause the difference in their interaction with the aromatic backbone of the polymer

chain causing the difference in the degree of aggregation [54,55]. This might be the factors that caused high LUMO energy levels and wide electrochemical band gaps in chloroform and chlorobenzene. The LUMO energy levels of HTB-co-P3HT in toluene, chloroform and chlorobenzene are -0.61 , -0.73 and -0.83 eV above the LUMO energy levels of PC₇₁BM, respectively. These LUMO offset (ΔE_{LUMO}) values are smaller in toluene than in chlorobenzene and chloroform. This indicate that the charge transfer from LUMO of HTB-co-P3HT in toluene can occur sufficiently than HTB-co-P3HT in chlorobenzene and chloroform. But they will still suffer high energy loss resulting to lower V_{OC} since ΔE_{LUMO} values are much higher than the threshold value of 0.3 eV [56].

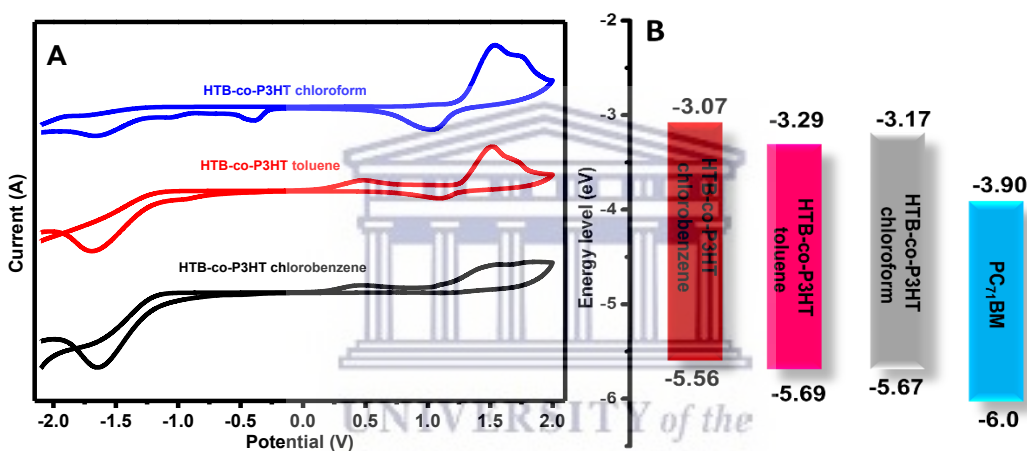


Figure 7.10: (A) Cyclic voltammograms and (B) energy levels HTB-co-P3HT obtained in different solvents compared with PC₇₁BM energy levels.

Table 7.2: Electrochemical properties of HTB and HTB-co-P3HT in different solvents.

Compound	E_{HOMO} (eV)	E_{LUMO} (eV)	ΔE_{LUMO} (eV)	E_{g}^{CV} (eV)
PC ₇₁ BM	-6.0	-3.90	-	-
HTB-co-P3HT chlorobenzene	-5.56	-3.07	-0.83	2.49
HTB-co-P3HT toluene	-5.69	-3.29	-0.61	2.40
HTB-co-P3HT chloroform	-5.67	-3.17	-0.73	2.50

7.3.9. EIS studies of HTB and HTB-co-P3HT

Electrochemical impedance spectra obtained for HTB and HTB-co-P3HT in different solvents are depicted in Figure 7.11. Nyquist plot (Figure 7.11A) is used to study charge carrier migration in an electrochemical cell. The charge transfers resistance (R_{ct}) is related to the diameter of the

semicircle at the interface of an electrode and sample. The smaller the diameter of the semicircle, the faster the diffusion of charges through the sample to the electroactive surface of the electrode. The Nyquist plot showed two semicircles, where the semicircle at the higher frequency corresponds to the resistance of the electrode and the semicircle at the lower frequency corresponds to the ionic diffusion resistance of the electrolyte, charge transfer resistance or the resistance of the sample/electrolyte interphase layer [57]. Both semicircles from the Nyquist spectra were fitted and the results of the semicircle at lower frequency are given in Table 7.3. This study revealed that HTB and HTB-co-P3HT each have different electrochemical behavior in different solvents. The smallest R_{ct} of 939.70 and 109.70 Ω were obtained for HTB and HTB-co-P3HT in chlorobenzene, respectively. This result indicates that the sufficient electron-hole pairs separation and fastest electron transfer at the sample/electrode interface take place in chlorobenzene [58]. The presence of P3HT chain on the surface of HTB promotes electron transfer between the electrode and electrolyte. This is observed by the small semicircle and small value of R_{ct} of HTB-co-P3HT when compared to HTB in chlorobenzene. It is noted that the frequency of the maximum peak shifts to the left after modifying HTB with P3HT in toluene and chloroform but remains on the same frequency in chlorobenzene (Figure 7.11B). This shift indicates the reduction of the recombination rate in chloroform and toluene [59]. The electron lifetime was estimated and the highest values of 1.91 and 2.30 ms were obtained for HTB and HTB-co-P3HT in chloroform. Therefore, the reduced rate of recombination and longer electron lifetime were obtained in chloroform. Figure 7.11C shows the impedance vs frequency plot of HTB and HTB-co-P3HT prepared in different solvents. It was observed that HTB-co-P3HT has minimum impedance at lower frequency than HTB. This indicates fast electron conduction in HTB-co-P3HT than in HTB and this observation is consistent with the lower R_{ct} obtained for HTB-co-P3HT.

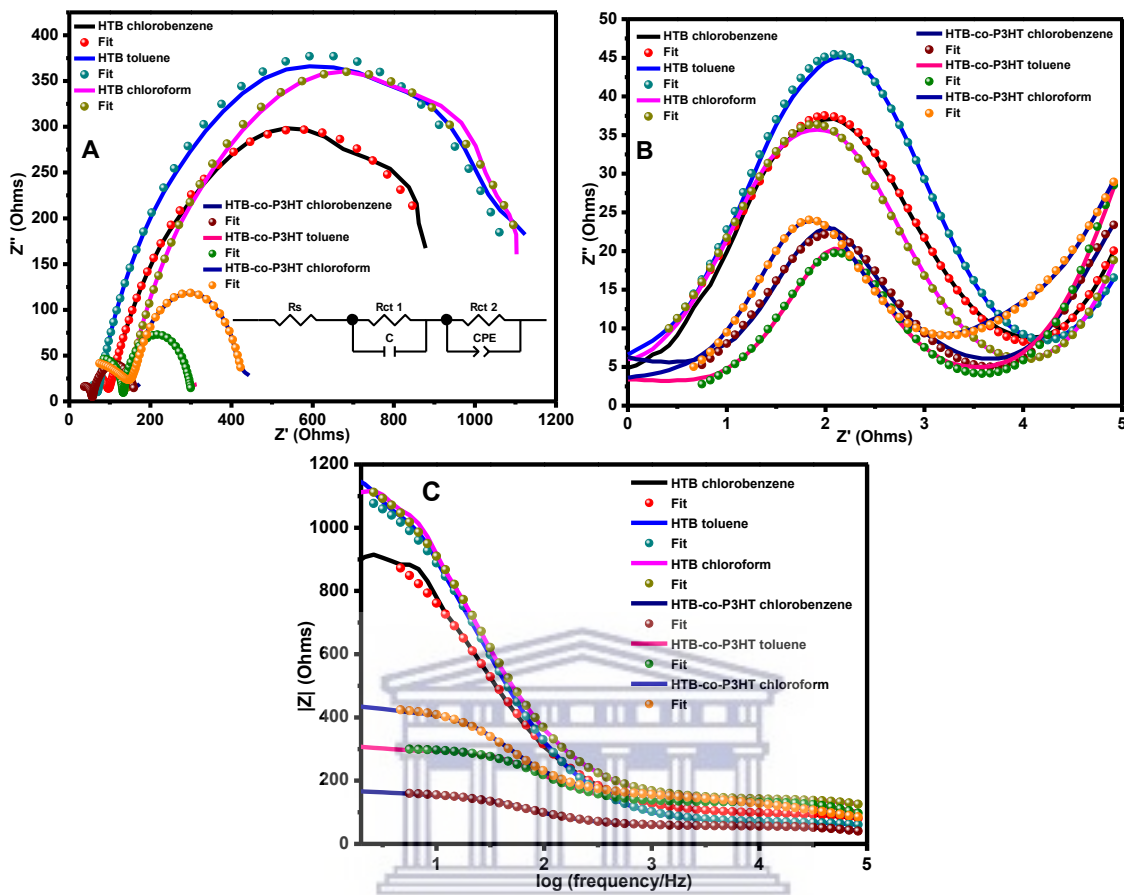


Figure 7.11: (A) Nyquist plot, (B) Bode-phase plot and (C) Bode-impedance plot of HTB and HTB-co-P3HT prepared in different solvents

Table 7.3: EIS results of HTB and HTB-co-P3HT prepared in various solvents.

Compounds	R_s (Ω)	$R_{ct, 2}$ (Ω)	CPE-T	CPE-P	τ (ms)
HTB chlorobenzene	41.16±1.95	939.70±7.41	$3.44 \times 10^{-5} \pm 6.78 \times 10^{-7}$	$0.72 \pm 2.95 \times 10^{-3}$	1.52
HTB toluene	31.55 ±1.57	1109.0±4.33	$2.31 \times 10^{-5} \pm 2.4 \times 10^{-7}$	$0.76 \pm 1.54 \times 10^{-3}$	1.13
HTB chloroform	43.46±3.16	1090.0±3.89	$2.75 \times 10^{-5} \pm 2.82 \times 10^{-7}$	$0.74 \pm 1.60 \times 10^{-3}$	1.91
HTB-co-P3HT chlorobenzene	23.96±0.52	109.70±0.89	$7.88 \times 10^{-5} \pm 2.91 \times 10^{-6}$	$0.81 \pm 5.70 \times 10^{-3}$	1.52
HTB-co-P3HT toluene	40.56±1.36	170.50±1.24	$2.13 \times 10^{-5} \pm 8.50 \times 10^{-7}$	$0.90 \pm 6.10 \times 10^{-3}$	1.29
HTB-co-P3HT chloroform	54.89±2.29	327.80±10.543	$5.18 \times 10^{-5} \pm 6.25 \times 10^{-6}$	$0.75 \pm 19.3 \times 10^{-3}$	2.30

7.3.10. Photovoltaic properties of HTB-co-P3HT

Figure 7.12 shows the current density-voltage (J-V) curves of HTB-co-P3HT as a donor material in different solvents. The maximum key photovoltaic parameters for batch of OPVs fabricated in ambient atmosphere are presented in Table 7.4. The maximum PCE was obtained in chlorobenzene, followed by toluene and then chloroform. This maximum performance in chlorobenzene is due to fast electron transfer confirmed by EIS studies. All OPVs were fabricated

using silver paste as top electrode and outside glovebox. The architecture of the OPVs fabricated in this study was as follows: glass|ITO|ZnO|HTB-co-P3HT:PC₇₁BM|PEDOT:PSS|Ag paste. It was revealed that spin coating PEDOT:PSS results in presence of pinholes [30]. Direct contact between Ag paste and HTB-co-P3HT:PC₇₁BM lead to diffusion of Ag paste into HTB-co-P3HT:PC₇₁BM active layer resulting in an increase in charge recombination [60]. Since devices were fabricated in air, oxidized species such as oxidation of sulphur in the active layer are formed [61]. Such oxidative species in the active layer may act as charge carrier trapping sites [62]. This may lead to an increase in series resistance which consequently reduces the FF [63].

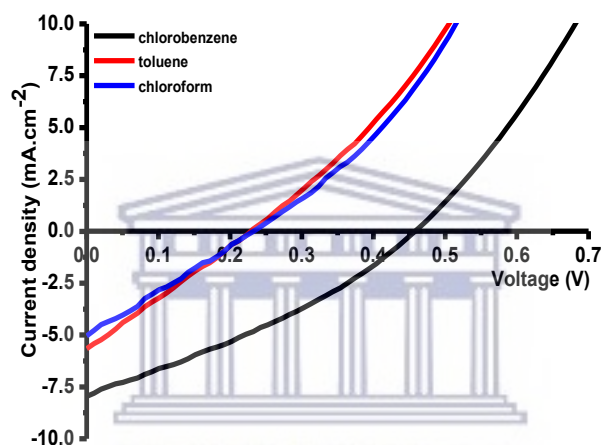


Figure 7.12: J–V characteristics of the fabricated OPVs using HTB-co-P3HT as donor material in different solvents.

Table 7.4: Photovoltaic performance of HTB-co-P3HT as donor material.

Donor material and solvent	PCE (%)	FF (%)	J _{sc} (mA.cm ⁻²)	V _{oc} (V)
HTB-co-P3HT chlorobenzene	0.48	27.84	7.93	0.35
HTB-co-P3HT chloroform	0.30	26.08	5.00	0.23
HTB-co-P3HT toluene	0.33	25.45	5.70	0.23

7.4. Conclusion

In this report, HTB and HTB-co-P3HT were successfully synthesized using Stille condensation reaction and chemical oxidation polymerization method, respectively. The structure of HTB was confirmed by NMR studies as the number of protons detected from the ¹H-NMR through integration of the spectrum corresponds to the number of protons of the structure of HTB and only five signals appeared on the ¹³C-NMR spectrum of HTB due to the presence of structural

symmetry. FTIR was used to confirm the successful decoration of HTB by P3HT. It showed the new bands at 2926 and 2855 cm^{-1} because of the vibrations of C–H for hexyl groups from P3HT and also shift in wavenumber of the C=C vibration after polymerization took place. The UV-vis studies were performed in different solvents (chlorobenzene, toluene and chloroform) and narrow band gaps were achieved in toluene. CV investigations revealed that the LUMO energy level of HTB-co-P3HT are deeper in toluene than other solvents used to prepare thin films. This finding was due to the difference in the boiling point and polarity of the solvent. The EIS revealed that the diameter of the semi-circle is wider and higher impedance for HTB in all solvents than HTB-co-P3HT. These indicate that HTB-co-P3HT is more conductive than HTB due to the presence of highly conductive P3HT especially in chlorobenzene. The highest PCE of 0.45% was achieved in chlorobenzene because of faster electron mobility confirmed by EIS studies.



References

- [1] Le, T.H., Kim, Y. and Yoon, H., 2017. Electrical and electrochemical properties of conducting polymers. *Polymers*, 9, p.150.
- [2] Khokhar, D., Jadoun, S., Arif, R. and Jabin, S., 2021. Functionalization of conducting polymers and their applications in optoelectronics. *Polymer-Plastics Technology and Materials*, 60, pp.463-485.
- [3] Bahceci, S. and Esat, B., 2013. A polyacetylene derivative with pendant TEMPO group as cathode material for rechargeable batteries. *Journal of Power Sources*, 242, pp.33-40.
- [4] Chan, D.H., Millet, A., Fisher, C.R., Price, M.C., Burchell, M.J. and Armes, S.P., 2021. Synthesis and Characterization of Polypyrrole-Coated Anthracene Microparticles: A New Synthetic Mimic for Polyaromatic Hydrocarbon-Based Cosmic Dust. *ACS Applied Materials & Interfaces*, 13, pp.3175-3185.
- [5] Nayana, V. and Kandasubramanian, B., 2020. Polycarbazole and its derivatives: progress, synthesis, and applications. *Journal of Polymer Research*, 27, pp.1-24.
- [6] Valderrama-García, B.X., Rodríguez-Alba, E., Morales-Espinoza, E.G., Moineau Chane-Ching, K. and Rivera, E., 2016. Synthesis and characterization of novel polythiophenes containing pyrene chromophores: thermal, optical and electrochemical properties. *Molecules*, 21, p.172.
- [7] Boeva, Z.A. and Sergeyev, V.G., 2014. Polyaniline: Synthesis, properties, and application. *Polymer Science Series C*, 56, pp.144-153.
- [8] Pei, L.Z., Ma, Y., Qiu, F.L., Lin, F.F., Fan, C.G. and Ling, X.Z., 2018. In-situ synthesis of polynaphthylamine/graphene composites for the electrochemical sensing of benzoic acid. *Materials Research Express*, 6, p.015053.
- [9] Chen, F., Liu, Y., Pan, J., Zhu, A., Bao, J., Yue, X., Li, Z., Wang, S. and Ban, X., 2020. Carbazole-modified polyphenylene ether as host materials for high efficiency phosphorescent organic light-emitting diodes. *Optical Materials*, 101, p.109781.
- [10] Afraj, S.N., He, G.Y., Lin, C.Y., Velusamy, A., Huang, C.Y., Lin, P.S., Vegiraju, S., Huang, P.Y., Ni, J.S., Yau, S.L. and Tung, S.H., 2021. Solution-Processable Multifused Thiophene Small Molecules and Conjugated Polymer Semiconducting Blend for Organic Field Effect Transistor Application. *Advanced Materials Technologies*, 6, p.2001028.

- [11] Wang, Z., Zhu, M., Pei, Z., Xue, Q., Li, H., Huang, Y. and Zhi, C., 2020. Polymers for supercapacitors: boosting the development of the flexible and wearable energy storage. *Materials Science and Engineering: R: Reports*, 139, p.100520.
- [12] Gupta, S., Sharma, A. and Verma, R.S., 2020. Polymers in biosensor devices for cardiovascular applications. *Current Opinion in Biomedical Engineering*, 13, pp.69-75.
- [13] Liu, X., Liang, Z., Du, S., Tong, J., Li, J., Zhang, R., Shi, X., Yan, L., Bao, X. and Xia, Y., 2021. Non-halogenated polymer donor-based organic solar cells with a nearly 15% efficiency enabled by a classic ternary strategy. *ACS Applied Energy Materials*, 4, pp.1774-1783.
- [14] Dikcal, F., Topal, S., Unal, M. and Ozturk, T., 2020. Synthesis, Characterization and Electrochemical Properties of Polymers Based on Dithienothiophene and Bithiazole. *Asian Journal of Organic Chemistry*, 9, pp.1309-1317.
- [15] Zhou, H., Yang, L. and You, W., 2012. Rational design of high performance conjugated polymers for organic solar cells. *Macromolecules*, 45, pp.607-632.
- [16] Zheng, B., Qi, F., Zhang, Y., Zhang, M., Gao, P., Liu, F., Li, T., Wei, D., Wan, M., Chen, G. and Huo, L., 2021. Over 14% Efficiency Single-Junction Organic Solar Cells Enabled by Reasonable Conformation Modulating in Naphtho [2, 3-b: 6, 7-b'] difuran Based Polymer. *Advanced Energy Materials*, 11, p.2003954.
- [17] Zhang, Z., Liang, L., Deng, L., Ren, L., Zhao, N., Huang, J., Yu, Y. and Gao, P., 2021. Fused Dithienopicenocarbazole Enabling High Mobility Dopant-Free Hole-Transporting Polymers for Efficient and Stable Perovskite Solar Cells. *ACS Applied Materials & Interfaces*, 13, pp.6688-6698.
- [18] Gao, K., Kan, Y., Chen, X., Liu, F., Kan, B., Nian, L., Wan, X., Chen, Y., Peng, X., Russell, T.P. and Cao, Y., 2020. Low-bandgap porphyrins for highly efficient organic solar cells: materials, morphology, and applications. *Advanced Materials*, 32, p.1906129.
- [19] Tang, A., Li, J., Zhang, B., Peng, J. and Zhou, E., 2020. Low-bandgap n-type polymer based on a fused-DAD-type heptacyclic ring for all-polymer solar cell application with a power conversion efficiency of 10.7%. *ACS Macro Letters*, 9, pp.706-712.
- [20] Xiao, L., Mao, H., Li, Z., Yan, C., Liu, J., Liu, Y., Reimer, J.A., Min, Y. and Liu, Y., 2020. Employing a narrow-band-gap mediator in ternary solar cells for enhanced photovoltaic performance. *ACS Applied Materials & Interfaces*, 12, pp.16387-16393.

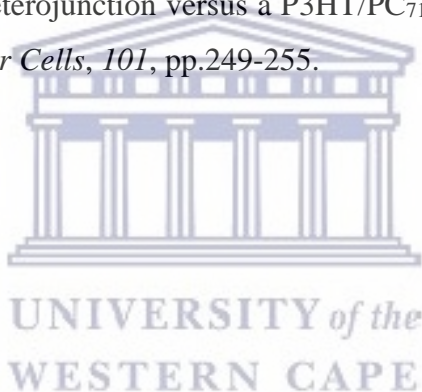
- [21] Ye, D., Li, X., Yan, L., Zhang, W., Hu, Z., Liang, Y., Fang, J., Wong, W.Y. and Wang, X., 2013. Dithienosilole-bridged small molecules with different alkyl group substituents for organic solar cells exhibiting high open-circuit voltage. *Journal of Materials Chemistry A*, *1*, pp.7622-7629.
- [22] Cui, Y., Wu, Y., Lu, X., Zhang, X., Zhou, G., Miapah, F.B., Zhu, W. and Wang, Z.S., 2011. Incorporating benzotriazole moiety to construct D–A– π –A organic sensitizers for solar cells: significant enhancement of open-circuit photovoltage with long alkyl group. *Chemistry of Materials*, *23*, pp.4394-4401.
- [23] Zhang, S., Qin, Y., Zhu, J. and Hou, J., 2018. Over 14% efficiency in polymer solar cells enabled by a chlorinated polymer donor. *Advanced Materials*, *30*, p.1800868.
- [24] Cui, C. and Wong, W.Y., 2016. Effects of alkylthio and alkoxy side chains in polymer donor materials for organic solar cells. *Macromolecular Rapid Communications*, *37*, pp.287-302.
- [25] Shi, C., Yao, Y., Yang, Y. and Pei, Q., 2006. Regioregular copolymers of 3-alkoxythiophene and their photovoltaic application. *Journal of the American Chemical Society*, *128*, pp.8980-8986.
- [26] Tanaka, S., Rosli, S.K.B., Takada, K., Taniai, N., Yoshitomi, T., Ando, H. and Matsumoto, K., 2017. Effects of bromination of poly (3-hexylthiophene) on the performance of bulk heterojunction solar cells. *RSC Advances*, *7*, pp.46874-46880.
- [27] Kim, Y., Cook, S., Kirkpatrick, J., Nelson, J., Durrant, J.R., Bradley, D.D.C., Giles, M., Heeney, M., Hamilton, R. and McCulloch, I., 2007. Effect of the end group of regioregular poly (3-hexylthiophene) polymers on the performance of polymer/fullerene solar cells. *The Journal of Physical Chemistry C*, *111*, pp.8137-8141.
- [28] Zhang, Y., Gao, X., Li, J. and Tu, G., 2015. Highly selective palladium-catalyzed Stille coupling reaction toward chlorine-containing NIR electroluminescent polymers. *Journal of Materials Chemistry C*, *3*, pp.7463-7468.
- [29] Campos, J.F. and Berteina-Raboin, S., 2020. Eucalyptol as bio-based solvent for Migita–Kosugi–Stille coupling reaction on O, S, N-heterocycle. *Catalysis Today*, *358*, pp.138-142.
- [30] Ramoroka, M.E., Mdluli, S.B., John-Denk, V.S., Modibane, K.D., Arendse, C.J. and Iwuoha, E.I., 2021. Synthesis and Photovoltaics of Novel 2, 3, 4, 5-Tetrathienylthiophene-co-poly (3-hexylthiophene-2, 5-diyl) Donor Polymer for Organic Solar Cell. *Polymers*, *13*, p.2.

- [31] Ansari, M.A., Mohiuddin, S., Kandemirli, F. and Malik, M.I., 2018. Synthesis and characterization of poly (3-hexylthiophene): improvement of regioregularity and energy band gap. *RSC Advances*, 8, pp.8319-8328.
- [32] Leitner, T.D., Gmeinder, Y., Röhricht, F., Herges, R., Mena-Osteritz, E. and Bäuerle, P., 2020. Twisted Thienylene–Phenylene Structures: Through-Space Orbital Coupling in Toroidal and Catenated Topologies. *European Journal of Organic Chemistry*, 2020, pp.285-294.
- [33] Yoshida, K., Morimoto, I., Mitsudo, K. and Tanaka, H., 2008. RhCl₃/amine-catalyzed [2+2+2] cyclization of alkynes. *Tetrahedron*, 64, pp.5800-5807.
- [34] Yoshida, K., Morimoto, I., Mitsudo, K. and Tanaka, H., 2008. Facile synthetic procedure for and electrochemical properties of hexa (2-thienyl) benzenes directed toward electroactive materials. *Tetrahedron Letters*, 49, pp.2363-2365.
- [35] Mota, I.C., Santos, B.P.S., dos Santos, R.É.P., Guedes, L.B., Soares, I.T., Arias, J.J.R., de Araújo, F.L., Nogueira, A.F. and Marques, M.D.F.V., 2021. Influence of reaction time on properties of regioregular poly (3-hexylthiophene) by the Grignard metathesis polymerization. *Journal of Thermal Analysis and Calorimetry*, pp.1-12.
- [36] Yadav, P.K., Prakash, O., Ray, B. and Maiti, P., 2021. Functionalized polythiophene for corrosion inhibition and photovoltaic application. *Journal of Applied Polymer Science*, p.51306.
- [37] Agrawal, V., Jain, K., Arora, L. and Chand, S., 2013. Synthesis of CdS nanocrystals in poly (3-hexylthiophene) polymer matrix: optical and structural studies. *Journal of Nanoparticle Research*, 15, pp.1-14.
- [38] Tamanai, A., Beck, S. and Pucci, A., 2013. Mid-infrared characterization of thiophene-based thin polymer films. *Displays*, 34, pp.399-405.
- [39] Naureen, B., Miana, G.A., Shahid, K., Asghar, M., Tanveer, S. and Sarwar, A., 2021. Iron (III) and zinc (II) monodentate Schiff base metal complexes: Synthesis, characterisation and biological activities. *Journal of Molecular Structure*, 1231, p.129946.
- [40] Joseyphus, R.S. and Nair, M.S., 2010. Synthesis, characterization and biological studies of some Co (II), Ni (II) and Cu (II) complexes derived from indole-3-carboxaldehyde and glycyglycine as Schiff base ligand. *Arabian Journal of Chemistry*, 3, pp.195-204.

- [41] Dehno Khalaji, A. and Das, D., 2015. Preparation of CuO nanoparticles by thermal decomposition of double-helical dinuclear copper (II) Schiff-base complexes. *Journal of Ultrafine Grained and Nanostructured Materials*, 48, pp.93-99.
- [42] Warad, I., Ali, O., Al Ali, A., Jaradat, N.A., Hussein, F., Abdallah, L., Al-Zaqri, N., Alsalmeh, A. and Alharthi, F.A., 2020. Synthesis and spectral Identification of three Schiff bases with a 2-(piperazin-1-yl)-N-(thiophen-2-yl methylene) ethanamine moiety acting as novel pancreatic lipase inhibitors: Thermal, DFT, antioxidant, antibacterial, and molecular docking investigations. *Molecules*, 25, p.2253.
- [43] Kargar, H., Behjatmanesh-Ardakani, R., Torabi, V., Kashani, M., Chavoshpour-Natanzi, Z., Kazemi, Z., Mirkhani, V., Sahraei, A., Tahir, M.N., Ashfaq, M. and Munawar, K.S., 2021. Synthesis, characterization, crystal structures, DFT, TD-DFT, molecular docking and DNA binding studies of novel copper (II) and zinc (II) complexes bearing halogenated bidentate N, O-donor Schiff base ligands. *Polyhedron*, 195, p.114988.
- [44] Jeong, C., Nagai, T., Ishizuka, S., Tambo, H., Hajime, S., Kim, S. and Kim, Y., 2021. Examination of Suitable Bandgap Grading of Cu (InGa) Se₂ Bottom Absorber Layers for Tandem Cell Application. *Physica Status Solidi (a)*, 218, p.2000658.
- [45] Fan, Q., Ma, R., Liu, T., Yu, J., Xiao, Y., Su, W., Cai, G., Li, Y., Peng, W., Guo, T. and Luo, Z., 2021. High-performance all-polymer solar cells enabled by a novel low bandgap non-fully conjugated polymer acceptor. *Science China Chemistry*, pp.1-9.
- [46] Zhao, H., Wang, Z., Dong, G. and Duan, L., 2015. Fabrication of highly oriented large-scale TIPS pentacene crystals and transistors by the Marangoni effect-controlled growth method. *Physical Chemistry Chemical Physics*, 17, pp.6274-6279.
- [47] Birnie III, D.P., 2013. A model for drying control cosolvent selection for spin-coating uniformity: The thin film limit. *Langmuir*, 29, pp.9072-9078.
- [48] Liu, X., Zheng, Z., Xu, Y., Wang, J., Wang, Y., Zhang, S. and Hou, J., 2020. Quantifying Alkyl Pendants of Acceptors Induced Voc Loss in Organic Solar Cells. *Journal of Materials*, 8, p.12568.
- [49] Chang, S.H., Chiang, C.H., Cheng, H.M., Tai, C.Y. and Wu, C.G., 2013. Broadband charge transfer dynamics in P3HT: PCBM blended film. *Optics Letters*, 38, pp.5342-5345.

- [50] Hu, Z., Willard, A.P., Ono, R.J., Bielawski, C.W., Rossky, P.J. and Bout, D.A.V., 2015. An insight into non-emissive excited states in conjugated polymers. *Nature Communications*, 6, pp.1-9.
- [51] Ekbote, A., Jadhav, T. and Misra, R., 2017. T-Shaped donor–acceptor–donor type tetraphenylethylene substituted quinoxaline derivatives: aggregation-induced emission and mechanochromism. *New Journal of Chemistry*, 41, pp.9346-9353.
- [52] Liu, F., Nguyen, T.P., Wang, Q., Massuyeau, F., Dan, Y. and Jiang, L., 2019. Construction of Z-scheme g-C₃N₄/Ag/P3HT heterojunction for enhanced visible-light photocatalytic degradation of tetracycline (TC) and methyl orange (MO). *Applied Surface Science*, 496, p.143653.
- [53] Niefind, F., Karande, S., Frost, F., Abel, B. and Kahnt, A., 2019. Solvent influence on the surface morphology of P3HT thin films revealed by photoemission electron microscopy. *Nanoscale Advances*, 1, pp.3883-3886.
- [54] El-Bashir, S.M., 2019. Effect of solvent polarity on the homogeneity and photophysical properties of MDMO-PPV films: towards efficient plastic solar cells. *Journal of King Saud University-Science*, 31, pp.534-540.
- [55] Rahman, M.H., Liao, S.C., Chen, H.L., Chen, J.H., Ivanov, V.A., Chu, P.P. and Chen, S.A., 2009. Aggregation of conjugated polymers in aromatic solvent. *Langmuir*, 25, pp.1667-1674.
- [56] Gautam, P., Sharma, R., Misra, R., Keshtov, M.L., Kuklin, S.A. and Sharma, G.D., 2017. Donor–acceptor–acceptor (D–A–A) type 1, 8-naphthalimides as non-fullerene small molecule acceptors for bulk heterojunction solar cells. *Chemical Science*, 8(3), p.2017.
- [57] Mei, B.A., Lau, J., Lin, T., Tolbert, S.H., Dunn, B.S. and Pilon, L., 2018. Physical interpretations of electrochemical impedance spectroscopy of redox active electrodes for electrical energy storage. *The Journal of Physical Chemistry C*, 122, pp.24499-24511.
- [58] Huang, J.H., Ibrahim, M.A. and Chu, C.W., 2013. Interfacial engineering affects the photocatalytic activity of poly (3-hexylthiophene)-modified TiO₂. *RSC Advances*, 3, pp.26438-26442.
- [59] Pei, J., Hao, Y.Z., Lv, H.J., Sun, B., Li, Y.P. and Guo, Z.M., 2016. Optimizing the performance of TiO₂/P3HT hybrid solar cell by effective interfacial modification. *Chemical Physics Letters*, 644, pp.127-131.

- [60] Kim, J., Duraisamy, N., Lee, T.M., Kim, I. and Choi, K.H., 2015. Screen printed silver top electrode for efficient inverted organic solar cells. *Materials Research Bulletin*, 70, pp.412-415.
- [61] Kettle, J., Ding, Z., Horie, M. and Smith, G.C., 2016. XPS analysis of the chemical degradation of PTB7 polymers for organic photovoltaics. *Organic Electronics*, 39, pp.222-228.
- [62] Rafique, S., Abdullah, S.M., Badiei, N., McGettrick, J., Lai, K.T., Roslan, N.A., Lee, H.K.H., Tsoi, W.C. and Li, L., 2020. An insight into the air stability of the benchmark polymer: fullerene photovoltaic films and devices: A comparative study. *Organic Electronics*, 76, p.105456.
- [63] Wang, D.H., Kim, J.K., Seo, J.H., Park, O.O. and Park, J.H., 2012. Stability comparison: A PCDTBT/PC₇₁BM bulk-heterojunction versus a P3HT/PC₇₁BM bulk-heterojunction. *Solar Energy Materials and Solar Cells*, 101, pp.249-255.



Chapter 8

Synthesis and Photovoltaics of Novel 2,3,4,5-Tetrathienylthiophene-co-poly(3-hexylthiophene-2,5-diyl) Donor Polymer for Organic Photovoltaic cells

Abstract

This report focuses on the synthesis of novel 2,3,4,5-tetrathienylthiophene-co-poly(3-hexylthiophene-2,5-diyl) (TTT-co-P3HT) as a donor material for organic photovoltaic cells (OPVs). The properties of the synthesized TTT-co-P3HT were compared with those of poly(3-hexylthiophene-2,5-diyl) (P3HT). The structure of TTT-co-P3HT was studied using nuclear magnetic resonance spectroscopy (NMR) and Fourier-transform infrared spectroscopy (FTIR). It was seen that TTT-co-P3HT possessed a broader electrochemical and optical band-gap as compared to P3HT. Cyclic voltammetry (CV) was used to determine lowest unoccupied molecular orbital (LUMO) and highest occupied molecular orbital (HOMO) energy gaps of TTT-co-P3HT and P3HT were found to be 2.19 and 1.97 eV, respectively. Photoluminescence revealed that TTT-co-P3HT:PC₇₁BM have insufficient electron/hole separation and charge transfer when compared to P3HT:PC₇₁BM. All devices were fabricated outside a glovebox. Power conversion efficiency (PCE) of 1.15% was obtained for P3HT:PC₇₁BM device and 0.14% was obtained for TTT-co-P3HT:PC₇₁BM device. Further studies were done on fabricated OPVs during this work using electrochemical methods. The studies revealed that the presence of poly(3,4-ethylenedioxythiophene) polystyrene sulfonate (PEDOT:PSS) on the surface of indium tin oxide (ITO) causes a reduction in cyclic voltammogram oxidation/reduction peak current and increases the charge transfer resistance in comparison with a bare ITO. We also examined the ITO/PEDOT:PSS electrode coated with TTT-co-P3HT:PC₇₁BM, TTT-co-P3HT:PC₇₁BM/ZnO, P3HT:PC₇₁BM and P3HT:PC₇₁BM/ZnO. The study revealed that PEDOT:PSS does not completely block electrons from active layer to reach the ITO electrode.

8.1. Introduction

Organic-based solar cells (OPVs) have attained considerable attention in the last decades and have been greatly studied because of their advantageous properties such as light weight, inexpensive, attractive colors and flexibility [1–4]. In comparison with traditional inorganic-based solar cell devices, OPVs have attracted research interest due to their constantly increasing power conversion efficiency (PCE) and solution processability [5]. The continuous improvement of OPVs is because of better understanding of the light conversion mechanism, development of novel materials and architectures of these devices [6–8]. To date, the OPVs with better performance are constructed on bulk heterojunction active layer using conjugated polymers as the electron donor materials and fullerenes as the electron acceptor materials [6,9,10]. The donor and acceptor material interface delivers a pathway for photo-generated charges, transportation and separation. Currently, the research in the OPVs field focuses on designing low energy band gap donor polymers with engineered electrochemical energy levels for better charge separation which lead to an increase in the performance of OPVs [11–13].

Organic donor materials play a crucial part on the overall performance of OPVs and can be easily modified chemically. Polythiophenes based polymers are mostly used as the electron donor materials for OPVs because of their properties such as thermally stable, environmentally friendly, easy to process and less expensive [14,15]. These polythiophenes based polymers are widely reported [14–17]. Katsumata *et al.* [16] reported OPVs with maximum PCE of 2.03% using poly[2,6-(4,4-bis-(2-ethylhexyl)-4H-cyclopenta[2,1-b;3,4-b']dithiophene)-alt-4,7(2,1,3-benzothiadiazole)] (PCPDTBT) as organic donor material. Kesters *et al.* [17] chemically modified PCPDTBT with 4,4-dialkyl-4H-cyclopenta[2,1-b;3,4-b']dithiophene derivative with ester and alcohol moieties to achieve PCE of 2.02% and 1.82% respectively. Whereas the unmodified PCPDTBT possessed PCE of 2.15% [17]. The studies above showed that modification of organic donor materials has an effect on the PCE of OPVs.

Poly(3-hexylthiophene-2,5-diyl (P3HT) is the most widely studied polythiophene-based material as organic donor for solar cells [18–22]. Studies revealed that P3HT properties such as optoelectronic properties and crystallinity and its OPVs performance can be altered by modification of its end groups [18–20]. Seibers *et al.* [21] reported P3HT functionalized with

porphyrin as an end group for use as OPVs donor material. Their findings revealed that porphyrin-functionalized P3HT have similar crystallinity, improved absorption properties and better OPVs performance when compared to pristine P3HT. Lim *et al.* [22] investigated morphological changes and OPVs performance of their synthesized hydrophobic end-functionalized P3HT. Repulsive interactions between hydrophobic end-functionalized P3HT and hydrophilic PCBM provided large continuous interfacial area. As a result, improvement in OPVs performance was achieved because of sufficient electron/hole dissociation. Hydrophobic end-functionalized P3HT maintained the crystallinity of P3HT. Bromo end-functionalized P3HT has a wider optical band gap, different crystallinity and lower OPVs performance as compared to P3HT. Bromo bonded to thiophene acted as exciton quenching and charge trapping sites leading to lower OPVs performance [23]. Properties of P3HT are very sensitive to the presence of the end groups.

In this work, we synthesized a novel TTT-co-P3HT donor material using oxidation polymerization. The performance of TTT-co-P3HT was compared with that of a commercial P3HT. From the conventional device fabricated during this study, the performance of P3HT based device was better than that of TTT-co-P3HT based device due to insufficient electron/hole separation and charge transfer of TTT-co-P3HT material. In both OPVs, PEDOT:PSS was used as an interlayer between ITO and active layer. The OPVs fabricated during this work were further investigated using electrochemical methods.

8.2. Experimental Section

8.2.1. Materials

Chemicals and solvents used in this study were procured from commercial sources and used without any further purification. Silica gel 60 Å (230–400 mesh, Merck (Pty) Ltd., Johannesburg, South Africa) was used for purification.

8.2.2. Synthesis of 2,3,4,5-Tetrathienylthiophene (TTT)

In a 100 mL round bottom flask, 2,3,4,5-tetrabromothiophene (1.00 g, 2.5 mmol, 99.0%, Merck (Pty) Ltd.), 2-thienylboronic acid (1.28 g, 10 mmol, ≥95.0%, Merck (Pty) Ltd.) and potassium carbonate (K₂CO₃, 2.76 g, 20 mmol, 99.5%, Merck (Pty) Ltd.) were stirred for 30 min in 40 mL degassed tetrahydrofuran (THF, 99.0%, Merck (Pty) Ltd.):water solution with a volume ratio of

4:1. In the solution above, palladium tetrakis(triphenylphosphine) (Pd(PPh₃)₄, 0.29 g, 0.20 mmol, 99.0%, Merck (Pty) Ltd.) was added. The mixture was refluxed under nitrogen atmosphere for 24 h at 110 °C before being cooled to room temperature. Afterwards, the resulting solution was poured in a separating funnel containing 50 mL of brine, followed by extraction 3 times with dichloromethane (DCM, 99.9%, Merck (Pty) Ltd.) and 3 times with diethyl ether (≥99.0%, Merck (Pty) Ltd.). The extracts were dried with magnesium sulphate (≥99.5%, Merck (Pty) Ltd.), filtered and rotary evaporator (Buchi AG, Flawil, Switzerland) was used to remove the solvent. Column chromatography was used to purify the residue with DCM and methanol (MeOH, 99.5%, Merck (Pty) Ltd.) as an eluent (DCM:MeOH = 3:1, v/v) resulting to a yellow solid (0.76 g) with a yield of 74%. ¹H-NMR (CDCl₃, Merck (Pty) Ltd., 400 MHz): δ_H 6.89–6.91 (dd, 2H), 6.93–6.96 (m, 4H), 7.09–7.10 (dd, 2H), 7.19–7.21 (dd, 2H), 7.29–7.31 (dd, 2H); ¹³C-NMR (CDCl₃, 400 MHz): δ_C 126.36, 126.42, 126.84, 126.95, 127.15, 129.40, 132.42, 133.33, 135.37, 135.67.

8.2.3. Synthesis of TTT-co-P3HT

In a typical chemical polymerization, TTT (0.12 g, 0.28 mmol) and 3-hexylthiophene (1.87 g, 11.12 mmol, ≥99.0%, Merck (Pty) Ltd.) were added in 50 mL of chloroform (≥99.0%, Merck (Pty) Ltd.). The solution was stirred for 30 min and followed by addition of iron chloride (FeCl₃, 1.8 g, 11.12 mmol, ≥99.99%, Merck (Pty) Ltd.). The mixture was refluxed at 60 °C for 24 h under nitrogen atmosphere, then polymerization was terminated by addition of MeOH. After, the precipitates were collected by filtration and were washed with Soxhlet extractor (size large, 200 mL extractor volume, Merck (Pty) Ltd.) using acetone (99.3%, Merck (Pty) Ltd.) and MeOH as solvents for 24 h with each. Finally, the product was extracted with DCM for another 24 h. The DCM solvent was removed to obtain a dark brown solid (0.36 g).

8.2.4. Characterization Techniques

The ultraviolet-visible (UV-Vis) spectra (Nicolet Evolution 100 from Thermo Electron Corporation, Altrincham, UK), photoluminescence spectra (NanoLog with FluorEssence™ V3 Software from Horiba Jobin Yvon, Edison, NJ, USA), size exclusion chromatogram (Agilent 1260 Infinity Series HPLC Instrument from Agilent Technologies, Waldbronn, Germany), nuclear magnetic resonance spectra (Bruker 400 MHz Avance III HD Nanobay Spectrometer, Karlsruhe, Germany) and attenuated total reflectance-FTIR spectra (Spectrum-100 FTIR Spectrometer from

PerkinElmer (Pty) Ltd., Midrand, South Africa) were recorded with the specified instruments. Device characteristics (current density–voltage) were measured with Keithley 2420 Source Meter (Keithley Instruments B.V., Gorinchem, Netherlands) using an illumination of AM 1.5G, 100 mW cm⁻² supplied by a solar simulator (Sciencetech Inc., London, ON, Canada).

CV and electrochemical impedance spectroscopy (EIS) of the thin films were measured in 0.1 M tetrabutylammonium hexafluorophosphate (TBAPF₆, ≥99.0%, Merck (Pty) Ltd.) in acetonitrile (99.8%, Merck (Pty) Ltd.) as supporting electrolyte. Three electrode cell system consists of ITO (15–25 Ω/square resistance, Merck (Pty) Ltd.), platinum wire (Goodfellow Cambridge Ltd., Huntingdon, UK) and silver/silver chloride (Ag/AgCl, from BASi® in West Lafayette, IN, USA) as working electrode, counter electrode and reference electrode respectively were used. Ferrocene (98%, Merck (Pty) Ltd.) was used as a redox probe molecule. All the electrochemical measurements were conducted using a Bio-Logic VMP-300 (Bio-Logic SAS, Seyssinet-Pariset, France). The zview software (Scribner Associates Inc., Southern Pines, NC, USA) was used to fit EIS results.

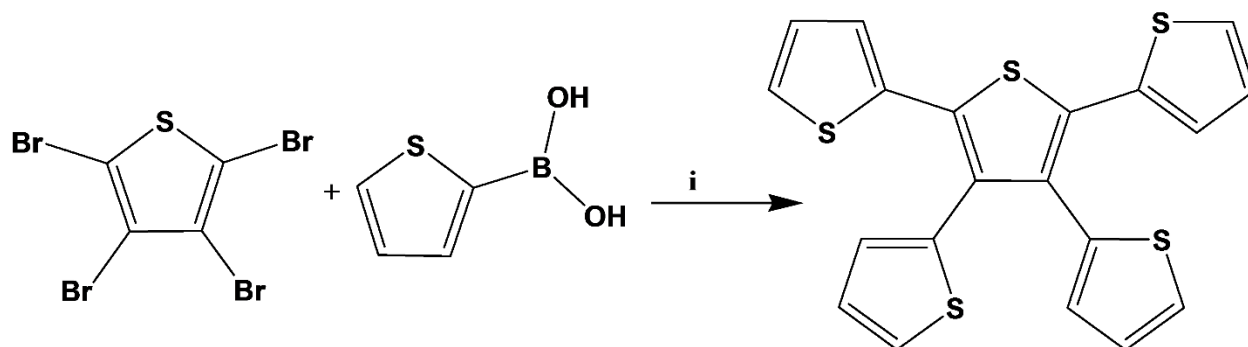
8.2.5. Fabrication of OPVs

Devices fabrication and measurements were conducted in air. ITO (8 pixels, 20 Ω/square resistance, Ossila Ltd., Sheffield, UK) substrates were sonicated in 1% (by volume) hellmanex III (Merck (Pty) Ltd.) solution in hot water, followed by in acetone then 2-propylalcohol for 5 min with each. After every sonication step, the substrate was rinsed with water. PEDOT:PSS (0.5–1.0 wt % in water, Merck (Pty) Ltd.) was sonicated for 3 h then filtered with 0.45 μm filter. It (30 μL PEDOT:PSS) was spun coated on ITO substrate for 30 s at 4000 rpm. The film was baked at 150 °C for 5 min. Active layer was prepared by blending donor material polymer and PC₇₁BM (mixture of isomers, 99%, Merck (Pty) Ltd.) with a total of 25 mg/mL in chlorobenzene (99.9%, Merck (Pty) Ltd.) as a solvent at 60 °C for overnight. The blend ratio of donor: acceptor used is 1:0.8. The solutions of 40 μL were spun at 2000 rpm for 30 s in air. The films were annealed for 5 min at 100 °C. ZnO solution (preparation method is given in supporting document attached in the Appendix) of 30 μL was spun coated at 4000 rpm for 30 s and was annealed at 100 °C for 30 min. Lastly, aluminum metal (Merck (Pty) Ltd.) was thermally evaporated at deposition pressure of about 10⁻⁵ mbar to complete the device.

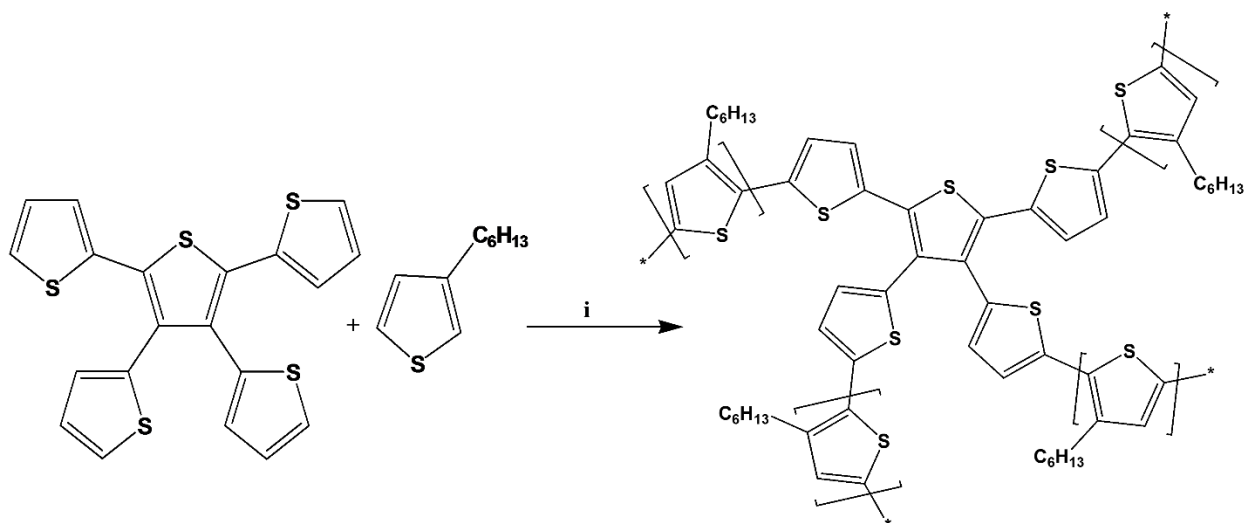
These fabrication conditions were used to prepare thin films for characterization. The deposition of TTT-co-P3HT, TTT-co-P3HT:PC₇₁BM (1:0.8), P3HT (99.995%, Merck (Pty) Ltd.) and P3HT:PC₇₁BM (1:0.8) on ITO substrates with/without PEDOT:PSS were done outside glovebox.

8.3. Results and Discussion

As shown in Scheme 8.1 and Scheme 8.2, synthesis of TTT and TTT-co-P3HT were performed by using Suzuki coupling and oxidation polymerization reaction methods, respectively. Results of size exclusion chromatography are shown in Table 8.1 and the chromatogram of TTT-co-P3HT is shown in Figure A7 (attached in the Appendix). The synthesized polymer, TT-co-P3HT, has a molecular weight M_n of 15,131 g mol^{-1} and a polydispersity index of 3.6. The chemical structure of TTT and TTT-co-P3HT were confirmed by NMR. The ¹H-NMR of TTT in Figure 8.1A reveals no presence of –OH protons from 2-thienylboronic acid confirming successful synthesis. The spectrum was designed at a chemical shift range between 6.74 and 7.38 ppm as an insertion in Figure 8.1A. Number of protons obtained by integrating the signals corresponds to the number of protons from the chemical structure of TTT. Figure 8.1B shows the ¹³C-NMR spectra of TTT and due to structural symmetry, only 10 signals were observed. For TTT-co-P3HT, only ¹H-NMR analysis was performed (Figure 8.1C) and compared with the ¹H-NMR spectrum of P3HT (Figure 8.1D). The ¹H-NMR spectrum of TTT-co-P3HT showed a new signal at 6.75 ppm which is absent on the ¹H-NMR spectrum of P3HT. This signal is due to the present of β-hydrogens from TTT. The signals from ¹H-NMR spectrum of TTT-co-P3HT are broader than those of P3HT. This is due to different P3HT chain lengths attached to TTT.



Scheme 8.1: Synthetic route of 2,3,4,5-tetrathienylthiophene. i) 10% Pd(PPh₃)₄, K₂CO₃, THF/water (4:1), 110 °C, 24 h.



Scheme 8.2: Synthetic of TTT-co-P3HT. i) FeCl_3 , $60\text{ }^\circ\text{C}$, 24 h.

Table 8.1: Size exclusion chromatography analysis of TTT-co-P3HT.

Polymer	Mn (gmol^{-1})	Mw (gmol^{-1})	Mp (gmol^{-1})	Mz (gmol^{-1})	Polydispersity index	Mz/Mw
TTT-co-P3HT	15131	54421	38613	157867	3.60	2.90

UNIVERSITY of the
WESTERN CAPE

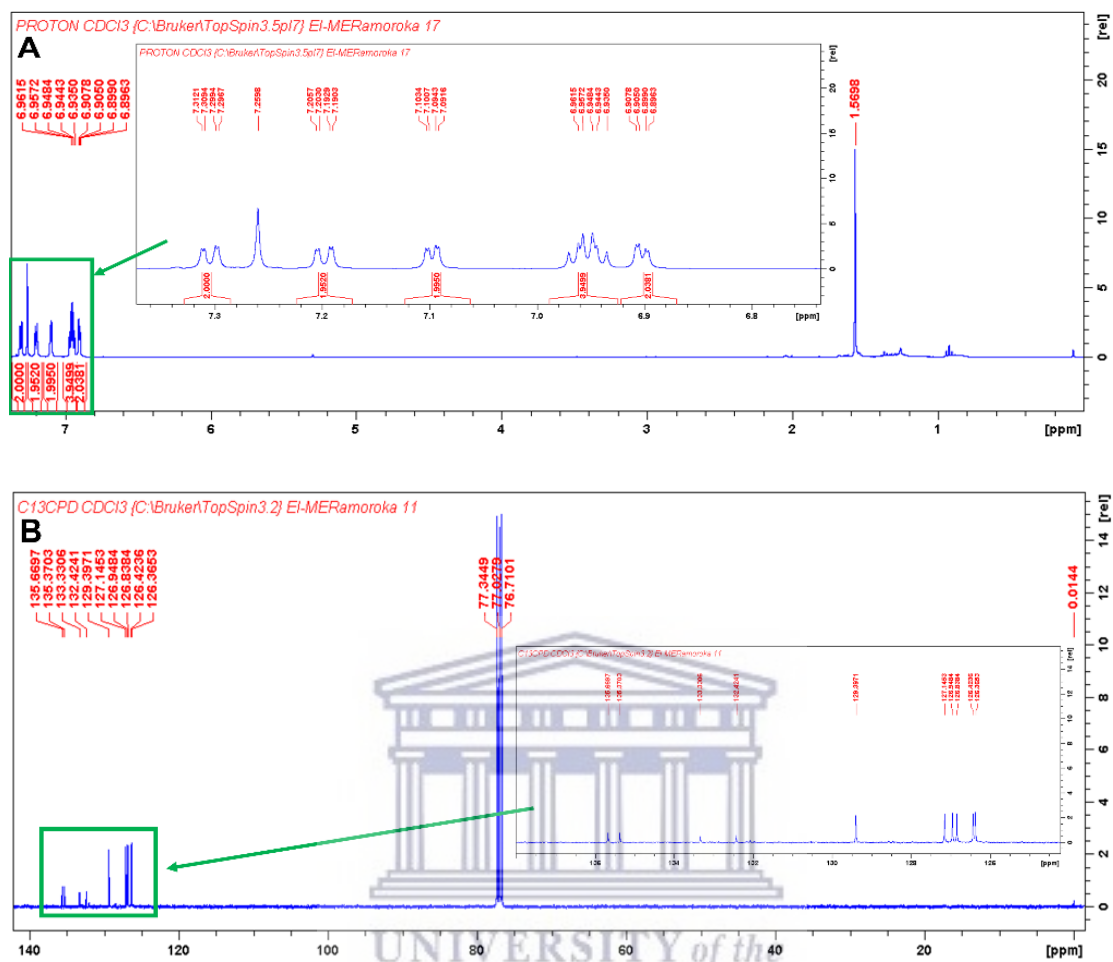


Figure 8.1: (A) ¹H-NMR of TTT in CDCl₃ and the insertion is ¹H-NMR of TTT.

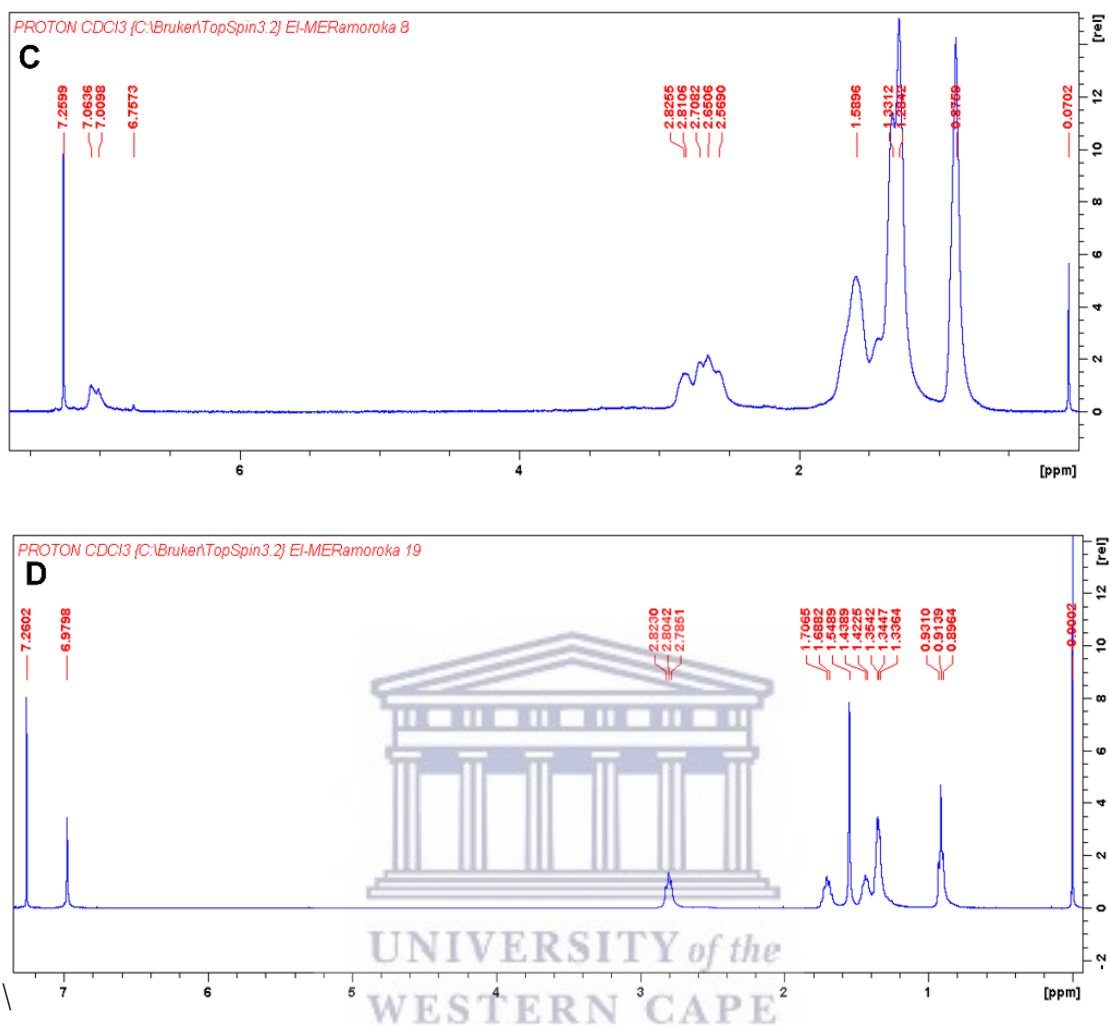


Figure 8.1: (C) $^1\text{H-NMR}$ of TTT-co-P3HT and (D) $^1\text{H-NMR}$ of P3HT in CDCl_3 .

FTIR spectra of TTT, TTT-co-P3HT and P3HT were recorded from 4000 cm^{-1} to 400 cm^{-1} . The spectra are shown in Figure 8.2. Unique vibrational bands can be observed at the wavenumber of 696 cm^{-1} , the range from 2934 to 2844 cm^{-1} and 3085 cm^{-1} on the spectrum of TTT. The vibrational band at 696 cm^{-1} is due to the aromatic C–H out of phase bending vibrations of thiophene [24–26], while the vibrational bands in the range from 2934 to 2844 cm^{-1} are due to the β -position C–H of the thiophene. The presence of the α -position C–H is confirmed by the vibrational band at the wavenumber of 3085 cm^{-1} [26,27]. In comparison with the spectra of P3HT and TTT-co-P3HT, the vibrational bands in the range from 2934 to 2844 cm^{-1} increases in intensity due to the presence of the hexyl group. The vibrational bands at 696 cm^{-1} and 3085 cm^{-1} disappears due to the occurrence of polymerization.

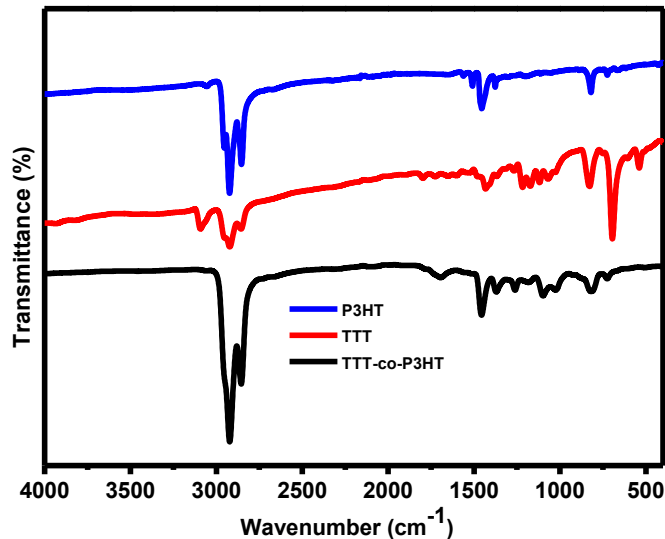


Figure 8.2: FTIR of P3HT, TTT-co-P3HT, and TTT.

8.3.1. Optical and Electrochemical Characterization

UV-Vis spectra of TTT-co-P3HT and P3HT materials are presented in Figure 8.3A and were obtained in chlorobenzene solvent and as thin films. The data obtained from Figure 8.3A is given in Table 8.2. As thin films, TTT-co-P3HT and P3HT materials have maximum absorption at a longer wavelength as compared to the spectra obtained in chlorobenzene. This is an indication that intermolecular π - π stacking is stronger in thin films. In both chlorobenzene and thin films, TTT-co-P3HT showed maximum absorbance at shorter wavelengths. This shows that TTT disturbs the interchain delocalization of π -electrons of P3HT after functionalization [23]. The onset absorption wavelengths determined on Figure A11 were used to estimate the optical band-gaps of TTT-co-P3HT and P3HT. The optical band gaps for TTT-co-P3HT were determined to be 2.32 eV and 1.98 eV in chlorobenzene and thin film, respectively. As for P3HT, they were determined to be 2.21 eV in chlorobenzene and 1.91 eV in thin film. TTT-co-P3HT material has broader band gaps indicating that lower number of photons are absorbed. Therefore, decreased numbers of electron/hole pairs are generated and TTT-co-P3HT OPVs is expected to have a decreased short circuit current-density (J_{sc}).

CV was used to investigate electrochemical response of TTT-co-P3HT and P3HT donor polymers and the voltammograms are shown in Figure 8.3B. Table 8.2 displays the results of

HOMO and LUMO energy levels obtained from Figure 8.3B. These energy level offsets of the donor and acceptor materials are important factors in understanding the electron/hole pair separation dynamics. HOMO offset becomes of importance when the acceptor material absorbs light significantly [28,29]. In this work, we focus only on the LUMO offset. The LUMO offsets between donor and acceptor are determined from Figure 8.3C to be 0.96 eV for TTT-co-P3HT:PC₇₁BM and 0.97 eV for P3HT:PC₇₁BM. The values obtained for LUMO offsets are more than 3 times higher than the commonly known empirical threshold of 0.3 eV [30]. Gadisa *et al.* [31] studied the relationship between onset oxidation potentials of polythiophene derivatives and open circuit voltage (V_{OC}). Their studies revealed that V_{OC} decreases as onset oxidation potential increases. Gao *et al.* [32] reported donor and acceptor materials with LUMO offset less than threshold. They achieved low energy loss and high V_{OC} . Therefore, TTT-co-P3HT:PC₇₁BM and P3HT:PC₇₁BM have high energy loss and this will have an impact on the V_{OC} .



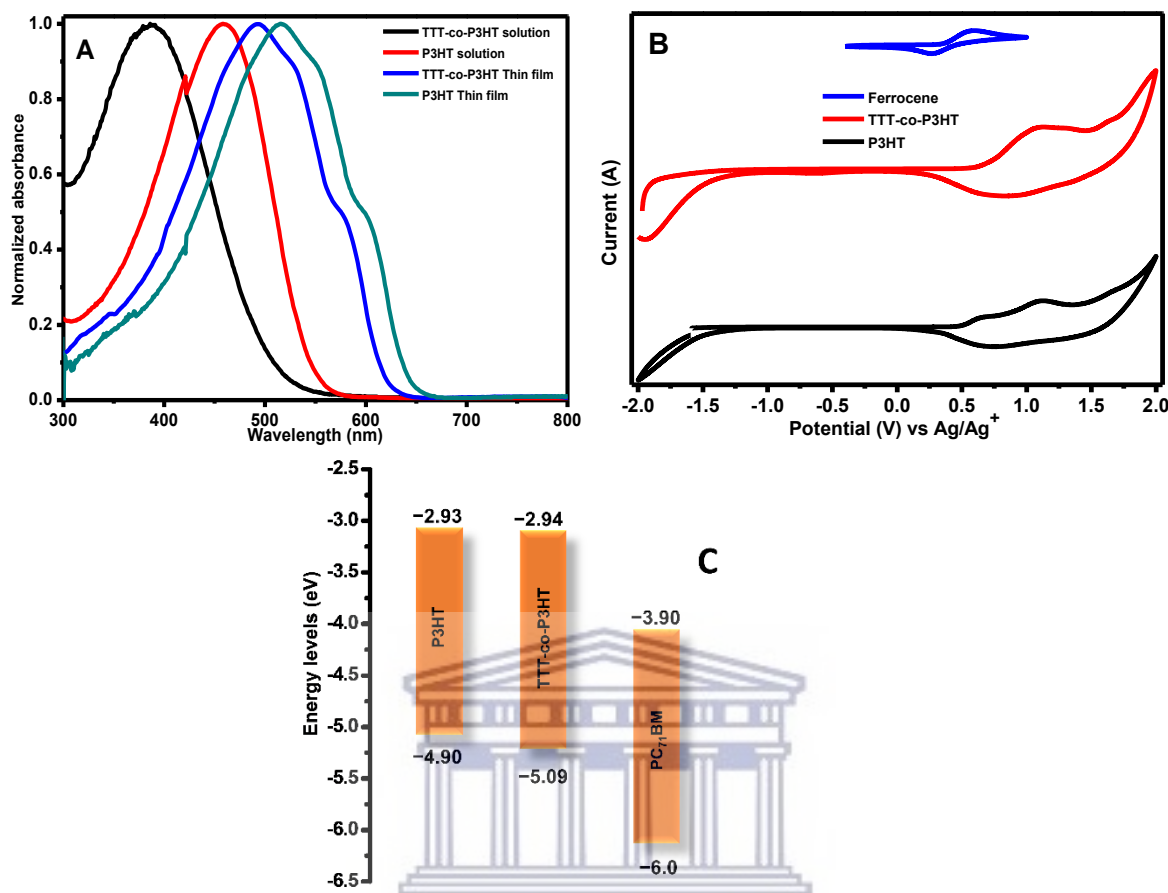


Figure 8.3: (A) Absorption spectra, (B) CV and (C) energy levels diagram of P3HT and TTT-co-P3HT.

Table 8.2: Optical and Electrochemical responses of TTT-co-P3HT and P3HT.

Polymer	^a λ (nm)		^c $E_g^{optical}$ (eV)	^b λ (nm)		^c $E_g^{optical}$ (eV)	^d E_{HOMO} (eV)	^d E_{LUMO} (eV)	^e E_g^{CV} (eV)
	max	onset		max	onset				
TTT-co-P3HT	386	534	2.32	492	626	1.98	-5.09	-2.90	2.19
P3HT	458	561	2.21	516	650	1.91	-4.90	-2.93	1.97

^aIn chlorobenzene solution. ^bIn thin film. ^c $E_g^{opt} = 1240/\lambda_{onset}$ eV in the thin film. ^dObtained with CV method, $E_{LUMO} = -(E_{reduction-onset} - E_{Ferrocene}) + 4.8$ eV and $E_{HOMO} = -(E_{oxidation-onset} - E_{Ferrocene}) + 4.8$. ^e E_g^{CV} was estimated using the equation: $E_g^{CV} = E_{LUMO} - E_{HOMO}$.

Photoluminescence spectroscopy has been widely used to study electron/hole pair separation at the interface of donor and acceptor materials using the quenching effect [33,34,35,36]. Figure 8.4 depicts the photoluminescence results of (A) TTT-co-P3HT and TTT-co-P3HT:PC₇₁BM and (B) P3HT and P3HT:PC₇₁BM obtained using chlorobenzene as a solvent. Photoluminescence quenching was observed in both TTT-co-P3HT:PC₇₁BM and P3HT:PC₇₁BM blends. This quenching can be attributed to charge transfer and electron/hole

pair separation efficiency which corroborates other results in literature [34]. To determine the quenching degree of TTT-co-P3HT:PC₇₁BM and TTT-co-P3HT:PC₇₁BM, Equation 8.1 was used:

$$q(\%) = \frac{I_{\text{donor}} - I_{\text{donor:acceptor}}}{I_{\text{donor}}} \times 100 \dots\dots\dots 8.1$$

This equation was employed to calculate photoluminescence quenching parameter q, where I_{donor} is the intensity of donor material and I_{donor:acceptor} is the intensity of donor:acceptor blend [33]. From Equation 8.1, for an outstanding degree of electron/hole pair separation and charge transfer without any recombination taking place, I_{donor:acceptor} must be equal to zero resulting to q equal to 100%. John *et al.* [35] achieved q of 97.29% and 96.6% indicating excellent electron/hole separation and charge transfer for their blends. The quenching parameter q was found to be 36% in TTT-co-P3HT:PC₇₁BM and 58% in P3HT:PC₇₁BM. This reveals that some of the created electron/hole pair recombine in TTT-co-P3HT and P3HT [36]. When comparing two blends, the results show that electron/hole pair separation and charge transfer is sufficient in P3HT:PC₇₁BM than in TTT-co-P3HT:PC₇₁BM.

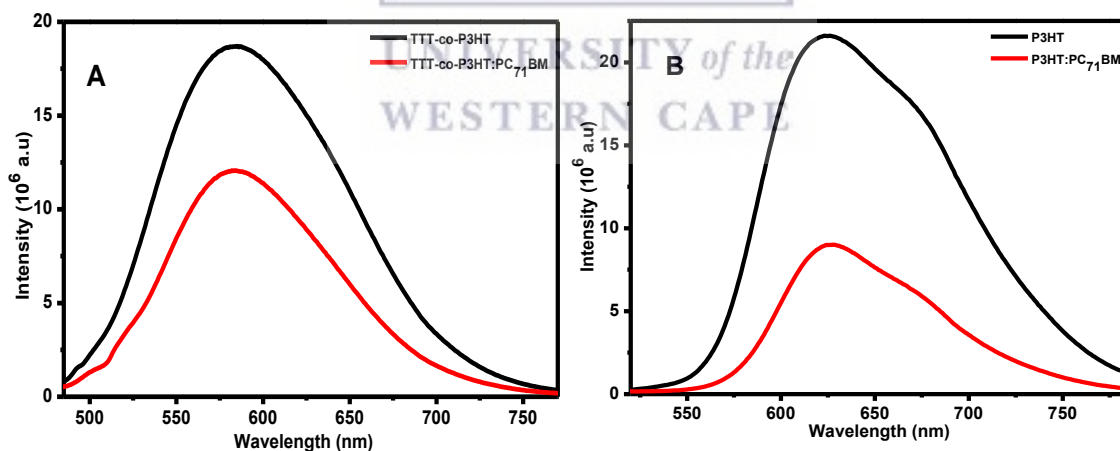


Figure 8.4: Photoluminescence spectra of (A) TTT-co-P3HT and TTT-co-P3HT:PC₇₁BM and (B) P3HT and P3HT:PC₇₁BM.

8.3.2. Photovoltaic Properties

OPVs were fabricated during this study with conventional configuration as follows: ITO/PEDOT:PSS/TTT-co-P3HT:PC₇₁BM/ZnO/Al and

ITO/PEDOT:PSS/P3HT:PC₇₁BM/ZnO/Al. Figure 8.5 depicts the current-density (J) versus voltage (V) plots of (A) P3HT:PC₇₁BM and (B) TTT-co-P3HT:PC₇₁BM as active layers. The solar cell parameters obtained for the devices are recorded in Table 8.3. The organic bulk heterojunction solar cell containing TTT-co-P3HT produced smallest J_{SC} (1.27 mA/cm²), V_{OC} (0.41 V), fill factor, FF (26.78%) and PCE (0.14%) in comparison with the device containing P3HT which produced the largest J_{SC} (7.91 mA/cm²), V_{OC} (0.46 V), FF (31.64%) and PCE (1.15%). The improved performance of the device fabricated using P3HT was ascribed to sufficient electron/hole pair separation confirmed by photoluminescence and lower band-gap in comparison with TTT-co-P3HT. Low J_{SC} and V_{OC} in TTT-co-P3HT based OPV is attributed to the disruption of the ordered lamellar stacking of P3HT by modification with TTT. This disruption results to a decrease in absorption and low hole mobility in TTT-co-P3HT [37,38]. P3HT and TTT-co-P3HT based OPVs were fabricated in air. Therefore, oxygen permeation does occur and will oxidize low work function aluminum electrode. Oxidized aluminum electrode will form a charge transport barrier. This induces S-shaped I–V curve and reduces the performance of the OPVs [39]. Additionally, penetrative oxygen in the active layer lead to different photo-oxidation reactions of an acceptor and donor materials [40,41]. Changes in the structures of an acceptor and donor materials will change their charge carrier mobilities, energy levels and photon absorption properties. The oxygen doping in the active layer will increase the concentration of holes, which results in an increase in trapping of electrons and a decrease in V_{OC} and FF [42,43].

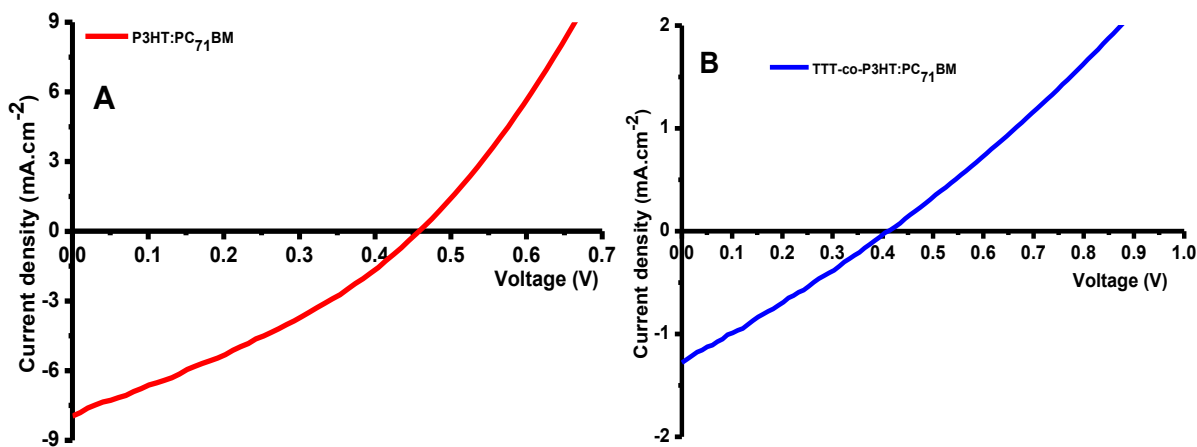


Figure 8.5: J–V plots of (A) P3HT:PC₇₁BM and (B) TTT-co-P3HT:PC₇₁BM devices.

Table 8.3: Response of the TTT-co-P3HT:PC₇₁BM and P3HT:PC₇₁BM devices.

Active layer	J _{sc} (mA/cm ²)	V _{oc} (V)	FF (%)	PCE (%)
TTT-co-P3HT:PC ₇₁ BM	1.27	0.41	26.78	0.14
P3HT:PC ₇₁ BM	7.91	0.46	31.64	1.15

8.3.3. Characterization of OPVs with Electrochemical Methods

In order to further investigate the OPVs fabricated during this work, electrochemical techniques were used. ITO coated substrate was used as working electrode during electrochemical studies. The layers on the ITO substrates were prepared using OPVs fabrication conditions. Electrochemical techniques such as CV and EIS can be used to quantitatively study the electron-blocking ability of PEDOT:PSS interlayer. Parameters such as peak separation and peak current are very useful in evaluating electron-blocking properties because these parameters depend strongly on the amount of electroactive species from the electrolyte that are exposed to electroactive sites of the working electrode. Figure 8.6 depicts CV and Nyquist plots of ITO without/with PEDOT:PSS layer in 1 mM ferrocene prepared using 0.1 M TBAPF₆ in acetonitrile. CV (Figure 8.6A) obtained in the presence of PEDOT:PSS layer show a decrease in the oxidation/reduction peak currents and an increase in peak separations. The peak currents for a bare ITO is 0.27 mA for cathodic peak (I_{pc}) and for anodic peak (I_{pa}) is -0.18 mA, while for ITO/PEDOT:PSS are I_{pc} is 0.17 mA and I_{pa} is -0.07 mA. The extent to which the peak currents decreased after coating PEDOT:PSS onto the ITO substrate were estimated using Equation 8.2:

$$I_{\text{decreased}} = \frac{I_{\text{without}} - I_{\text{with}}}{I_{\text{without}}} \dots\dots\dots 8.2$$

where I_{decreased} is the amount of current decreased, I_{without} is the peak current of bare ITO and I_{with} is the peak current of ITO/PEDOT:PSS [44]. The values of I_{decreased} was found to be 0.54 for cathodic peaks and 0.82 for anodic peaks. The peak separation for bare ITO was determined to be 0.42 V and for ITO/PEDOT:PSS was determined to be 1.17 V. The decrease in peak currents and an increase in peak separation for ITO/PEDOT:PSS suggest a decrease in the ITO electrode activity. These observations indicate that the PEDOT:PSS interlayer does not completely block electroactive species from ferrocene to reach ITO surface since the value of I_{decreased} is not equal to 1. Therefore, PEDOT:PSS interlayer does not completely block electrons when is used as hole transport interlayer in OPVs and this might also be due to the presence of pinholes.

EIS is an important instrument that can be used to research charge transfer processes at the interlayer [45–47] and evaluate the surface coverage at the electrode active area [44,48]. Figure 8.6B shows the Nyquist plots of bare ITO and ITO/PEDOT:PSS with the equivalent circuit as an inset. In the circuit, R_s is an Ohmic resistance, R_{ct} is a resistance of charge transfer processes taking place at the interface and constant phase element (CPE) proposes a non-ideal behavior of the capacitor. CPE is well-defined by two adjustable values (CPE-T and CPE-P) and is mostly used as a capacitor-like element to compensate interfacial inhomogeneity (surface states or defects). In the case where CPE-P is equal to 1, then CPE and ideal capacitor are identical without defects [47,49,50]. The plots were fitted with z-view software and the results of parameters obtained are recorded in Table 8.4. The value of R_{ct} for bare ITO was found to be 655.10 Ω and for ITO/PEDOT:PSS was found to be 2935.00 Ω . These results reveal that PEDOT:PSS block the diffusion of electroactive species from ferrocene containing supporting electrolyte to the ITO surface. The electrode surface coverage (θ) can be estimated from R_{ct} of bare ITO and ITO/PEDOT:PSS using Equation 8.3:

$$\theta = 1 - \frac{R_{ct}^{bare\ ITO}}{R_{ct}^{ITO/PEDOT:PSS}} \dots\dots\dots 8.3$$

where $R_{ct}^{bare\ ITO}$ and $R_{ct}^{ITO/PEDOT:PSS}$ are charge transfer resistances measured at bare ITO and ITO/PEDOT:PSS, respectively [48]. If the surface is completely covered, the value $R_{ct}^{ITO/PEDOT:PSS}$ must be too big in such a way that θ will close to 1 [44]. From the R_{ct} values attained by fitting the Nyquist plots, a value of $\theta = 0.78$ was determined. Therefore, this indicates the presence of pinholes.

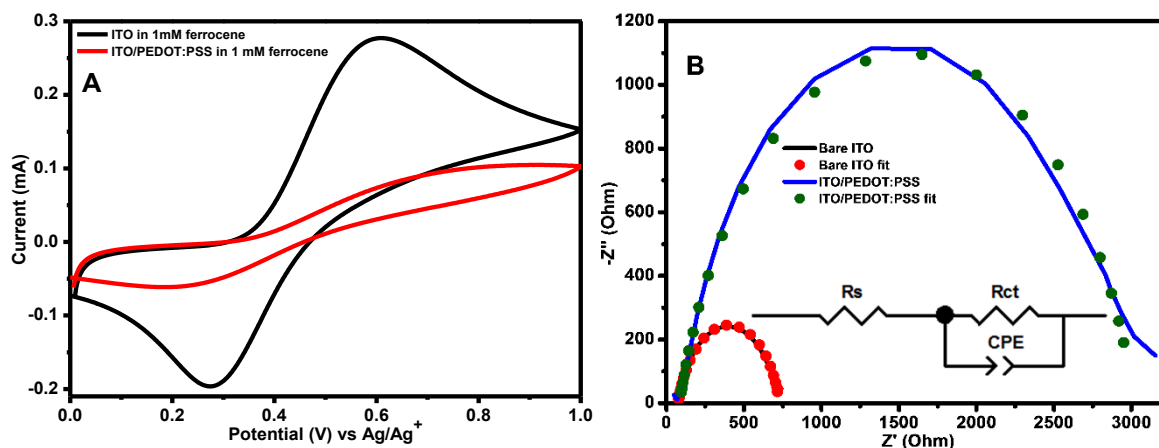


Figure 8.6: (A) CV (measured at 100 mVs⁻¹ scan rate) and (B) Nyquist plots of 1 mM ferrocene obtained using bare ITO and ITO/PEDOT:PSS as working electrodes in 0.1 M TBAPF₆/acetonitrile solution. The Nyquist plots were attained at bias potential of 0.45 V vs Ag/Ag⁺. The equivalent circuit used for impedance data fitting is shown as an inset on B.

Table 8.4: Results obtained from fitting electrochemical impedance data of bare ITO and ITO/PEDOT:PSS.

	R _s (Ω)	R _{ct} (Ω)	CPE-T (μF)	CPE-P (n)
ITO	75.57 ± 0.06	655.10 ± 4.05	19.33 ± 0.51	0.82 ± 0.01
ITO/PEDOT:PSS	85.31 ± 2.15	2935.00 ± 39.65	18.53 ± 0.68	0.82 ± 0.01

Figure 8.7 depicts CV of active layers (TTT-co-P3HT:PC₇₁BM and P3HT:PC₇₁BM) and active layers/ZnO coated onto a bare ITO and ITO/PEDOT:PSS electrodes. The results show that the presence of PEDOT:PSS cause a decrease in the peak currents. Cathodic and anodic peak currents are used to study the degree at which the peak current decreased using Equation 8.2. The results obtained are shown in Table 8.5. The extent at which the cathodic peak current is reduced because of PEDOT:PSS interlayer presence is 0.29 for TTT-co-P3HT:PC₇₁BM, 0.25 for TTT-co-P3HT:PC₇₁BM/ZnO, 0.29 for P3HT:PC₇₁BM and 0.52 for P3HT:PC₇₁BM/ZnO. While amount at which an anodic peak current decreased was determined to be 0.32 for TTT-co-P3HT:PC₇₁BM, 0.25 for TTT-co-P3HT:PC₇₁BM/ZnO, 0.22 for P3HT:PC₇₁BM and 0.48 for P3HT:PC₇₁BM/ZnO. According to Equation 8.2, if an interlayer does completely block electroactive species from reaching the surface of the electrode, the value of I_{decreased} must be equal to 1. These obtained values are low not only because of poor electron blocking properties of PEDOT:PSS, but due to the presence of pinholes on the PEDOT:PSS interlayer which allow active layer to be in direct contact with ITO electrode.

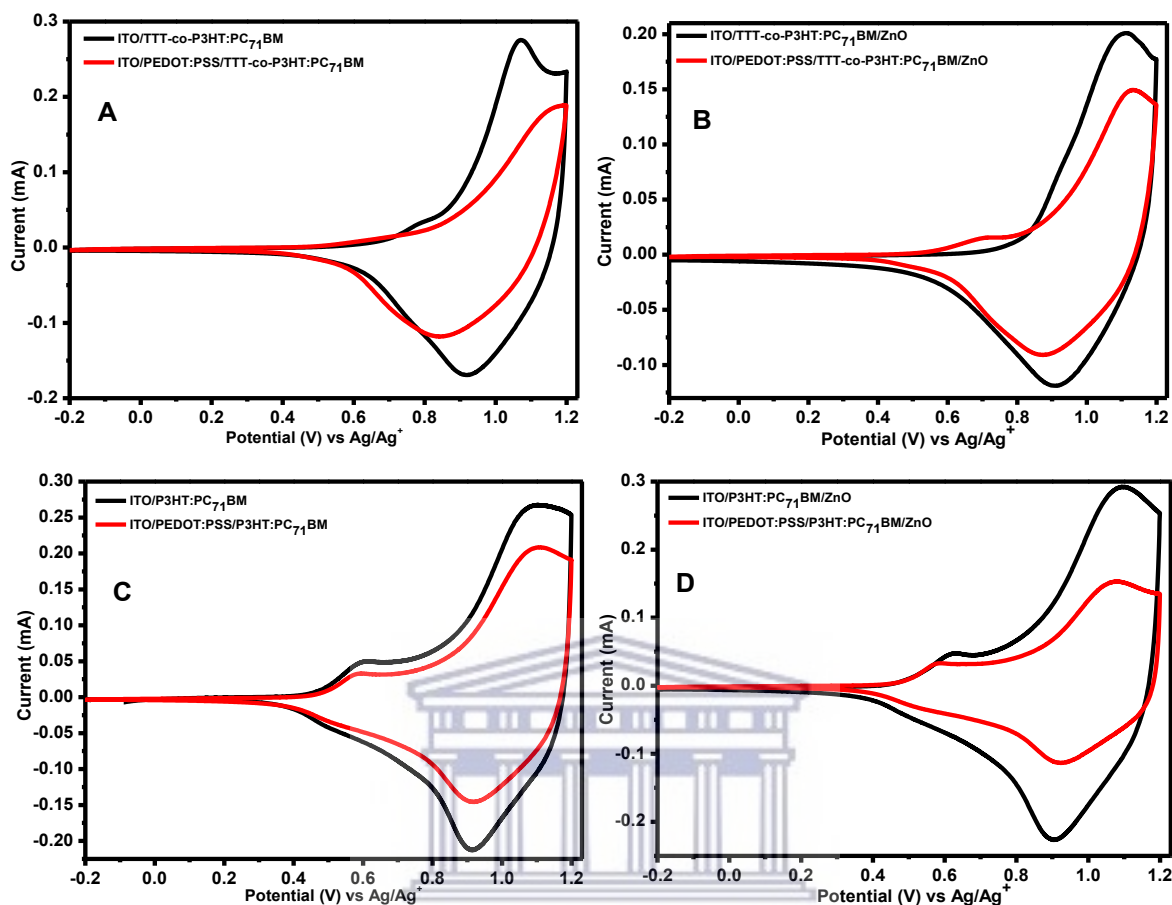


Figure 8.7: CV of (A) TTT-co-P3HT:PC₇₁BM, (B) TTT-co-P3HT:PC₇₁BM/ZnO, (C) P3HT:PC₇₁BM and (D) P3HT:PC₇₁BM/ZnO thin films coated on ITO substrate with/without PEDOT:PSS interlayer at 100 mVs⁻¹ in 0.1 M TBAPF₆/acetonitrile solution.

Table 8.5: Cathodic and anodic peak currents obtained from CV used to study the effect of PEDOT:PSS interlayer.

	^a I _{pa} (without) mA	^b I _{pc} (without) mA	^c I _{pa} (with) mA	^d I _{pc} (with) mA	^e I _{decreased} (pa) mA	^f I _{decreased} (pc) mA
TTT-co-P3HT:PC ₇₁ BM	0.28	-0.17	0.19	-0.12	0.32	0.29
TTT-co-P3HT:PC ₇₁ BM/ZnO	0.20	-0.12	0.15	-0.09	0.25	0.25
P3HT:PC ₇₁ BM	0.27	-0.21	0.21	-0.15	0.22	0.29
P3HT:PC ₇₁ BM/ZnO	0.29	-0.23	0.15	-0.11	0.48	0.52

^aI_{pa} (without) is an anodic peak current obtained without PEDOT:PSS interlayer, ^bI_{pc} (without) is cathodic peak current obtained without PEDOT:PSS interlayer, ^cI_{pa} (with) is an anodic peak current obtained with PEDOT:PSS interlayer, ^dI_{pc} (with) is cathodic peak current obtained with PEDOT:PSS interlayer, ^eI_{decreased} (pa) is the extent at which anodic peak current decreased and ^fI_{decreased} (pc) is an extent at which cathodic peak current decreased.

8.4. Conclusion

In summary, we have successfully synthesized TTT-co-P3HT using chemical oxidation polymerization for use as the donor material in OPVs. The properties of TTT-co-P3HT were compared with those of pristine P3HT. The optical band gaps of TTT-co-P3HT and P3HT in chlorobenzene were found to be 2.32 eV and 2.21 eV respectively. The LUMO offsets of active layers TTT-co-P3HT:PC₇₁BM and P3HT:PC₇₁BM were determined to be 0.96 eV and 0.97 eV, respectively. The TTT-co-P3HT:PC₇₁BM active layer has insufficient electron/hole pair separation and charge transfer at the interface, which was confirmed by photoluminescence quenching studies. The OPVs device of P3HT:PC₇₁BM exhibited a better performance with an efficiency of 1.15%, while TTT-co-P3HT:PC₇₁BM exhibited an efficiency of 0.14%. Poor performance of TTT-co-P3HT in OPV is because of its low hole mobility and decreased photon absorbance due to the disturbance in ordered lamellar stacking of P3HT after functionalization. To further understand the deviation in TTT-co-P3HT:PC₇₁BM and P3HT:PC₇₁BM devices performance, we studied the layers of OPVs fabricated during this work using electrochemical methods. The study revealed that PEDOT:PSS interlayer does not completely block electrons from active layer to the ITO substrate. From cyclic voltammetry results, the diffusion of electrons to the ITO substrate was observed by a decrease in the current of the peaks. Therefore, this study gives an opportunity to further optimize OPVs using cheap and reliable electrochemical methods and also shows the importance of using electrochemical methods in study the interlayers behavior for OPVs use.

References

- [1] Qing, L., Zhong, A., Chen, W., Cao, Y. and Chen, J., 2020. Largely improved bulk-heterojunction morphology in organic solar cells based on a conjugated terpolymer donor via a ternary strategy. *Polymer*, 186, p.122050.
- [2] Genene, Z., Negash, A., Abdulahi, B.A., Eachambadi, R.T., Liu, Z., Van den Brande, N., D'Haen, J., Wang, E., Vandewal, K., Maes, W. and Manca, J., 2020. Comparative study on the effects of alkylsilyl and alkylthio side chains on the performance of fullerene and non-fullerene polymer solar cells. *Organic Electronics*, 77, p.105572.
- [3] Li, X., Li, K., Su, D., Shen, F., Huo, S., Fu, H. and Zhan, C., 2020. Design a thieno [3, 2-b] thiophene bridged nonfullerene acceptor to increase open-circuit voltage, short-circuit current-density and fill factor via the ternary strategy. *Chinese Chemical Letters*, 31, pp.1243-1247.
- [4] Huang, K., Li, M., He, M., Liang, Z. and Geng, Y., 2020. Difluorobenzoxadiazole-based conjugated polymers for efficient non-fullerene polymer solar cells with low voltage loss. *Organic Electronics*, 77, p.105541.
- [5] Li, T., Chen, Z., Wang, Y., Tu, J., Deng, X., Li, Q. and Li, Z., 2019. Materials for interfaces in organic solar cells and photodetectors. *ACS Applied Materials & Interfaces*, 12, pp.3301-3326.
- [6] Chen, T.L., Zhang, Y., Smith, P., Tamayo, A., Liu, Y. and Ma, B., 2011. Diketopyrrolopyrrole-containing oligothiophene-fullerene triads and their use in organic solar cells. *ACS Applied Materials & Interfaces*, 3, pp.2275-2280.
- [7] Niklas, J., Zheng, T., Neshchadin, A., Mardis, K.L., Yu, L. and Poluektov, O.G., 2019. Polaron and exciton delocalization in oligomers of high-performance polymer PTB7. *Journal of the American Chemical Society*, 142, pp.1359-1366.
- [8] Liang, Y., Wu, Y., Feng, D., Tsai, S.T., Son, H.J., Li, G. and Yu, L., 2009. Development of new semiconducting polymers for high performance solar cells. *Journal of the American Chemical Society*, 131, pp.56-57.
- [9] Ranjitha, A., Thambidurai, M., Shini, F., Muthukumarasamy, N. and Velauthapillai, D., 2019. Effect of doped TiO₂ film as electron transport layer for inverted organic solar cell. *Materials Science for Energy Technologies*, 2, pp.385-388.

- [10] Revoju, S., Biswas, S., Eliasson, B. and Sharma, G.D., 2018. Effect of acceptor strength on optical, electrochemical and photovoltaic properties of phenothiazine-based small molecule for bulk heterojunction organic solar cells. *Dyes and Pigments*, 149, pp.830-842.
- [11] Cui, Y., Yao, H., Zhang, J., Zhang, T., Wang, Y., Hong, L., Xian, K., Xu, B., Zhang, S., Peng, J. and Wei, Z., 2019. Over 16% efficiency organic photovoltaic cells enabled by a chlorinated acceptor with increased open-circuit voltages. *Nature Communications*, 10, pp.1-8.
- [12] Zhao, W., Li, S., Yao, H., Zhang, S., Zhang, Y., Yang, B. and Hou, J., 2017. Molecular optimization enables over 13% efficiency in organic solar cells. *Journal of the American Chemical Society*, 139, pp.7148-7151.
- [13] Li, S., Ye, L., Zhao, W., Zhang, S., Mukherjee, S., Ade, H. and Hou, J., 2016. Energy-level modulation of small-molecule electron acceptors to achieve over 12% efficiency in polymer solar cells. *Advanced Materials*, 28, pp.9423-9429.
- [14] Ansari, M.A., Mohiuddin, S., Kandemirli, F. and Malik, M.I., 2018. Synthesis and characterization of poly (3-hexylthiophene): improvement of regioregularity and energy band gap. *RSC Advances*, 8, pp.8319-8328.
- [15] Wang, W., Zhang, G., Guo, J., Gu, Z., Hao, R., Lin, Z., Qian, Y., Zhu, M., Xia, H., Peng, W. and Liu, X., 2019. Medium-Bandgap (Acceptor–Donor) 2Acceptor-Type Small-Molecule Donors Based on an Asymmetric Thieno [3, 2-c] isochromene Building Block for Organic Solar Cells with High Efficiency and Voltage. *ACS Applied Energy Materials*, 2, pp.4730-4736.
- [16] Katsumata, S., Isegawa, T., Okamoto, T. and Kubo, W., 2020. Effect of Metamaterial Perfect Absorber on Device Performance of PCPDTBT: PC₇₁BM Solar Cell. *Physica Status Solidi (a)*, 217, p.1900910.
- [17] Kesters, J., Verstappen, P., Raymakers, J., Vanormelingen, W., Drijkoningen, J., D'Haen, J., Manca, J., Lutsen, L., Vanderzande, D. and Maes, W., 2015. Enhanced organic solar cell stability by polymer (PCPDTBT) side chain functionalization. *Chemistry of Materials*, 27, pp.1332-1341.
- [18] Liu, J., Zhu, X., Li, J., Shen, J. and Tu, G., 2016. Enhancing the thermal stability of the bulk-heterojunction photovoltaics based on P3HT/PCBM by incorporating diblock amphiphatic P3HT–PEO at D/A interface. *RSC Advances*, 6, pp.61934-61943.

- [19] Chen, Y.H., Huang, P.T., Lin, K.C., Huang, Y.J. and Chen, C.T., 2012. Stabilization of poly (3-hexylthiophene)/PCBM morphology by hydroxyl group end-functionalized P3HT and its application to polymer solar cells. *Organic Electronics*, 13, pp.283-289.
- [20] Kim, J.S., Lee, Y., Lee, J.H., Park, J.H., Kim, J.K. and Cho, K., 2010. High-Efficiency Organic Solar Cells Based on End-Functional-Group-Modified Poly(3-hexylthiophene). *Advanced Materials*, 22, pp.1355-1360.
- [21] Seibers, Z.D., Collier, G.S., Hopkins, B.W., Boone, E.S., Le, T.P., Gomez, E.D. and Kilbey, S.M., 2020. Tuning fullerene miscibility with porphyrin-terminated P3HTs in bulk heterojunction blends. *Soft Matter*, 16, pp.9769-9779.
- [22] Lim, B., Jo, J., Na, S.I., Kim, J., Kim, S.S. and Kim, D.Y., 2010. A morphology controller for high-efficiency bulk-heterojunction polymer solar cells. *Journal of Materials Chemistry*, 20, pp.10919-10923.
- [23] Tanaka, S., Rosli, S.K.B., Takada, K., Tani, N., Yoshitomi, T., Ando, H. and Matsumoto, K., 2017. Effects of bromination of poly (3-hexylthiophene) on the performance of bulk heterojunction solar cells. *RSC Advances*, 7, pp.46874-46880.
- [24] Liu, R. and Liu, Z., 2009. Polythiophene: Synthesis in aqueous medium and controllable morphology. *Chinese Science Bulletin*, 54, pp.2028-2032.
- [25] Rassie, C., Olowu, R.A., Waryo, T.T., Wilson, L., Williams, A., Baker, P.G. and Iwuoha, E.I., 2011. Dendritic 7T-polythiophene electro-catalytic sensor system for the determination of polycyclic aromatic hydrocarbons. *International Journal of Electrochemical Science*, 6, pp.1949-1967.
- [26] Tamanai, A., Beck, S. and Pucci, A., 2013. Mid-infrared characterization of thiophene-based thin polymer films. *Displays*, 34, pp.399-405.
- [27] Hotta, S., Rughooputh, S.D.D.V., Heeger, A.J. and Wudl, F., 1987. Spectroscopic studies of soluble poly (3-alkylthienylenes). *Macromolecules*, 20, pp.212-215.
- [28] Li, S., Zhan, L., Sun, C., Zhu, H., Zhou, G., Yang, W., Shi, M., Li, C.Z., Hou, J., Li, Y. and Chen, H., 2019. Highly efficient fullerene-free organic solar cells operate at near zero highest occupied molecular orbital offsets. *Journal of the American Chemical Society*, 141, pp.3073-3082.

- [29] Zhang, J., Liu, W., Zhang, M., Liu, Y., Zhou, G., Xu, S., Zhang, F., Zhu, H., Liu, F. and Zhu, X., 2019. Revealing the critical role of the HOMO alignment on maximizing current extraction and suppressing energy loss in organic solar cells. *IScience*, *19*, pp.883-893.
- [30] Scharber, M.C., Mühlbacher, D., Koppe, M., Denk, P., Waldauf, C., Heeger, A.J. and Brabec, C.J., 2006. Design rules for donors in bulk-heterojunction solar cells—Towards 10% energy-conversion efficiency. *Advanced materials*, *18*, pp.789-794.
- [31] Gadisa, A., Svensson, M., Andersson, M.R. and Inganäs, O., 2004. Correlation between oxidation potential and open-circuit voltage of composite solar cells based on blends of polythiophenes/fullerene derivative. *Applied Physics Letters*, *84*, pp.1609-1611.
- [32] Gao, B., Yao, H., Hong, L. and Hou, J., 2019. Efficient Organic Solar Cells with a High Open-Circuit Voltage of 1.34 V. *Chinese Journal of Chemistry*, *37*, pp.1153-1157.
- [33] Huang, P.T., Huang, P.F., Horng, Y.J. and Yang, C.P., 2013. Photoluminescence Study on Charge Transfer Behavior of Poly (3-hexylthiophene) and PCBM Blends. *Journal of the Chinese Chemical Society*, *60*, pp.467-472.
- [34] Otieno, F., Mutuma, B.K., Airo, M., Ranganathan, K., Erasmus, R., Coville, N. and Wamwangi, D., 2017. Enhancement of organic photovoltaic device performance via P3HT: PCBM solution heat treatment. *Thin Solid Films*, *625*, pp.62-69.
- [35] John, S.V., Mayedwa, N., Ikpo, C., Molefe, L.Y., Ndipingwi, M.M., Dywili, N.R., Van Wyk, J., Mapolie, S.F., Baker, P. and Iwuoha, E., 2016. Photoluminescence quenching of poly (octylfluorenylbenzothiadiazole) luminophore by n-type cobalt (II) salicylaldimine metallodendrimer. *Synthetic Metals*, *220*, pp.114-122.
- [36] Nismy, N.A., Jayawardena, K.I., Adikaari, A.D.T. and Silva, S.R.P., 2011. Photoluminescence Quenching in Carbon Nanotube-Polymer/Fullerene Films: Carbon Nanotubes as Exciton Dissociation Centres in Organic Photovoltaics. *Advanced Materials*, *23*, pp.3796-3800.
- [37] Sun, Y., Han, Y. and Liu, J., 2013. Controlling PCBM aggregation in P3HT/PCBM film by a selective solvent vapor annealing. *Chinese Science Bulletin*, *58*, pp.2767-2774.
- [38] Abu-Zahra, N. and Algazzar, M., 2014. Effect of crystallinity on the performance of P3HT/PC70BM/n-dodecylthiol polymer solar cells. *Journal of Solar Energy Engineering*, *136*, p.021023.

- [39] Glatthaar, M., Riede, M., Keegan, N., Sylvester-Hvid, K., Zimmermann, B., Niggemann, M., Hinsch, A. and Gombert, A., 2007. Efficiency limiting factors of organic bulk heterojunction solar cells identified by electrical impedance spectroscopy. *Solar Energy Materials and Solar Cells*, 91, pp.390-393.
- [40] Norrman, K. and Krebs, F.C., 2006. Lifetimes of organic photovoltaics: using TOF-SIMS and $^{18}\text{O}_2$ isotopic labelling to characterise chemical degradation mechanisms. *Solar Energy Materials and Solar Cells*, 90, pp.213-227.
- [41] Reese, M.O., Nardes, A.M., Rupert, B.L., Larsen, R.E., Olson, D.C., Lloyd, M.T., Shaheen, S.E., Ginley, D.S., Rumbles, G. and Kopidakis, N., 2010. Photoinduced degradation of polymer and polymer–fullerene active layers: experiment and theory. *Advanced Functional Materials*, 20, pp.3476-3483.
- [42] Seemann, A., Sauermann, T., Lungenschmied, C., Armbruster, O., Bauer, S., Egelhaaf, H.J. and Hauch, J., 2011. Reversible and irreversible degradation of organic solar cell performance by oxygen. *Solar Energy*, 85, pp.1238-1249.
- [43] Cheng, P. and Zhan, X., 2016. Stability of organic solar cells: challenges and strategies. *Chemical Society Reviews*, 45, pp.2544-2582.
- [44] Campuzano, S., Pedrero, M., Montemayor, C., Fatás, E. and Pingarrón, J.M., 2006. Characterization of alkanethiol-self-assembled monolayers-modified gold electrodes by electrochemical impedance spectroscopy. *Journal of Electroanalytical Chemistry*, 586, pp.112-121.
- [45] Ma, X., Zhong, J., Li, M., Chen, J., Zhang, Y., Wu, S., Gao, X., Lu, X., Liu, J.M. and Liu, H., 2016. Hybrid solar cells using solution-processed $\text{TiO}_2/\text{Sb}_2\text{S}_3$ bilayer as electron transport layer. *Solar Energy*, 133, pp.103-110.
- [46] Xu, L., Lee, Y.J. and Hsu, J.W., 2014. Charge collection in bulk heterojunction organic photovoltaic devices: An impedance spectroscopy study. *Applied Physics Letters*, 105, p.123904.
- [47] Zhang, Y., Li, L., Yuan, S., Li, G. and Zhang, W., 2013. Electrical properties of the interfaces in bulk heterojunction organic solar cells investigated by electrochemical impedance spectroscopy. *Electrochimica Acta*, 109, pp.221-225.

- [48] Janek, R.P., Fawcett, W.R. and Ulman, A., 1998. Impedance spectroscopy of self-assembled monolayers on Au (111): sodium ferrocyanide charge transfer at modified electrodes. *Langmuir*, *14*, pp.3011-3018.
- [49] Diao, P., Guo, M. and Tong, R., 2001. Characterization of defects in the formation process of self-assembled thiol monolayers by electrochemical impedance spectroscopy. *Journal of Electroanalytical Chemistry*, *495*, pp.98-105.
- [50] Jorcin, J.B., Orazem, M.E., Pébère, N. and Tribollet, B., 2006. CPE analysis by local electrochemical impedance spectroscopy. *Electrochimica Acta*, *51*, pp.1473-1479.



Chapter 9

9.1. Conclusion

We have successfully synthesized PPI-Th-co-P3HT, PPI-Py-co-P3HT, HTB-co-P3HT and TTT-co-P3HT copolymers using chemical oxidation polymerization synthetic method, while PPI-Sal-co-P3HT was synthesized using Grignard reaction method. They were all characterized using different characterization techniques and for each co-polymer a study has been performed. Due to the difference in studies performed for each co-polymer, the findings are discussed below:

- PPI-Th-co-P3HT was synthesized using different molar ratios of PPI-Th and 3HT. The molar ratios used are 1:40, 1:60 and 1:80 for PPI-Th and 3HT, respectively. This study revealed that there is no specific trend on the optical, thermal and electrochemical properties as the molar ratios change. The PPI-Th-co-P3HT synthesized using molar ratios of 1:40 and 1:80 were found to have a narrow optical band gap and most thermally stable, respectively. This is the indication that as the molar ratio changes, PPI-Th-co-P3HT with different molecular weight were synthesized. For TEM image, it was revealed that as the molar ratios increases, the particle size of PPI-Th-co-P3HT decreases. This was attributed to the fact that at higher concentration of 3HT, the rate of reaction is faster leading to smaller particle size. CV was used to determine the energy levels of PPI-Th-co-P3HT synthesized using molar ratios and they were compared to those of PC₆₁BM. The LUMO offset (ΔE_{LUMO}) of molar ratios of 1:40, 1:60 and 1:80 were determined to be 0.52, 0.62 and 0.58 eV, respectively. This is an indication that sufficient electron can occur between the PPI-Th-co-P3HT synthesized using 1:40 molar ratio and PC₆₁BM as compared to other co-polymers. This was confirmed by Nyquist plot which gave a smallest semi-circle and bode plot that gave the smallest value of impedance for PPI-Th-co-P3HT synthesized using 1:40 molar ratio and its composite with PC₆₁BM. Maximum PCE of 0.034% was achieved for PPI-Th-co-P3HT synthesized using molar ratio of 1:40. This performance was attributed to its narrow bandgap determined from UV-Vis, sufficient electron-hole separation at the PPI-Th-co-P3HT (1:40):PC₆₁BM interface observed by

photoluminescence quenching and high conductivity observed from Nyquist and bode plots.

- PPI-Py-co-P3HT was synthesized using different reaction times (24, 48 and 72 h). Their ¹H-NMR showed that the signals of all synthesized PPI-Py-co-P3HT are broad and this is due to the different chain lengths of P3HT attached to PPI-Py. It was revealed that as the reaction time increases, the FTIR vibration bands of PPI-Py-co-P3HT also intensify when comparing 24, 48 and 72 h. This is due to the resulting difference in the chain length of the P3HT branches as the reaction time increases. The optical studies showed that PPI-Py-co-P3HT synthesized for 24, 48 and 72 h have the maximum absorption at 419, 412 and 417 nm, respectively. While TGA showed that they decompose at different temperature range. These findings from optical and TGA studies reveals that there is no trend between them and reaction time. CV studies revealed that as the reaction time increases, the onset oxidation potential increases resulting in deepening of the HOMO energy levels. EIS revealed successful electron transfer between PPI-Py-co-P3HT and PC₇₁BM by showing smaller semi-circle diameter and low value of impedance. Photoluminescence studies revealed that about 92.42, 89,82 and 90.02% photoluminescence intensities of PPI-Py-co-P3HT synthesized for 24, 48 and 72 h, respectively. This indicates successful electron-hole separation at the interface of PPI-Py-co-P3HT:PC₇₁BM. PCE of 0.073, 6.14×10⁻³ and 0.026% were achieved when PPI-Py-co-P3HT synthesized for 24, 48 and 72 h, respectively.
- Effect of P3HT on the surface of PPI-Sal was investigated by comparing the response of PPI-Sal and PPI-Sal-co-P3HT from different characterization techniques. Their structures were confirmed by NMR and FTIR. After decoration PPI-Sal with P3HT, the maximum absorption peak showed a red shift from 328 nm to 415 nm due to the conjugation of the P3HT chain. CV was used to determine the HOMO and LUMO energy levels of PPI-Sal-co-P3HT which were compared to those of PC₇₁BM. The findings revealed that the ΔE_{LUMO} of PPI-Sal-co-P3HT and PC₇₁BM is 0.72eV and is more than twice higher than the empirical value of 0.3eV. Therefore, high energy loss and high recombination will take place at the interface of PPI-Sal-co-P3HT and PC₇₁BM. The τ values for PPI-Sal and PPI-Sal-co-P3HT were estimated from bode plot to be 0.59 and 1.00 ms, respectively. The higher value for PPI-Sal-co-P3HT indicates the suppression the electron-hole

recombination. Photoluminescence studies revealed that P3HT on the surface of PPI-Sal increases Stokes shift. OPVs of PPI-Sal-co-P3HT were fabricated and the photovoltaic parameters were measured. Maximum performing OPV device gave PCE of 0.21%, J_{SC} of $1.74 \text{ mA}\cdot\text{cm}^{-2}$, FF of 39.34% and V_{OC} of 0.31 V.

- Before the effect of solvent on the properties of HTB-co-P3HT were studied, HTB and HTB-co-P3HT were synthesized by Stille condensation and oxidation polymerization methods, respectively. NMR and FTIR were used to confirm their structural properties. FTIR confirmed successful synthesis of HTB-co-P3HT by showing new vibration bands at 2926 and 2855 cm^{-1} appearing due to the vibration of C–H of the P3HT hexyl group. The TGA studies revealed that the decomposition of HTB-co-P3HT occurs in two stages. The first stage was assigned to the decomposition of HTB-co-P3HT with smaller molecular weight and the second stage was assigned to HTB-co-P3HT with higher molecular weight. The effect of solvent on the optical and electrochemical properties of HTB-co-P3HT were studied using chlorobenzene, toluene and chloroform. It was found that narrow optical band gap was achieved in toluene. After performing EIS studies, it was found that the thin film prepared using chlorobenzene have smaller semi-circle and lower impedance than others prepared in toluene and chloroform. This is due to high boiling point of chlorobenzene which granted more time for HTB-co-P3HT to arrange in more crystalline structure. In chlorobenzene, toluene and chloroform, about 89.97, 80.92 and 93.23% of HTB-co-P3HT photoluminescence intensity is quenched after blending with PC₇₁BM, respectively. This indicates transfer of electrons from HTB-co-P3HT to PC₇₁BM. OPVs of HTB-co-P3HT as a donor material were fabricated using chlorobenzene, chloroform and toluene to prepare active layer. PCE of 0.48% was achieved from a device prepared using chlorobenzene, while 0.30 and 0.33% were achieved in chloroform and toluene, respectively. High PCE achieved in chlorobenzene is due to high conductivity of the thin film formed which is confirmed by EIS studies.
- After synthesis of TTT-co-P3HT, its properties were compared to those of P3HT. It was revealed that P3HT has optical band gaps of 2.21 and 1.91 eV, while TTT-co-P3HT has the optical band gaps of 2.32 and 1.98 eV in chlorobenzene and thin films, respectively. The LUMO energy level of TTT-co-P3HT are higher than those of P3HT and the HOMO energy levels are deeper than those of P3HT. This indicates that there is high energy loss

in TTT-co-P3HT than in P3HT containing organic solar cell devices. This was also confirmed by PL the photoluminescence studies based on quenching parameter (q) which was estimated to be 58% in P3HT:PC₇₁BM and 36% in TTT-co-P3HT:PC₇₁BM. This explains why the TTT-co-P3HT has lower Voc value than P3HT. The solar cell efficiency of the TTT-co-P3HT and P3HT device were determined to be 0.14 and 1.15%, respectively. The reason for this low efficiency was due to the fact that the devices were fabricated in air. So, oxygen will oxidize the aluminium electrode which will result to the electron transport barrier affecting the shape of the I–V curve and the performance of the device. The oxygen can also penetrate through the active layer leading to the electrons trapping which will result to lower FF and Voc. We also showed how electrochemical methods can be used in the research field of solar cells. It was revealed that PEDOT:PSS do not completely block electrons. This was attributed to the presence of pinholes generated during spin coating and very thin layer of PEDOT:PSS formed.

9.2. Recommendations

These materials synthesized in this work have some disadvantages such as wide optical band gaps and their devices suffer from low efficiency. There are some recommendations that can be used to improve their disadvantages and they are as follows:

- Materials synthesized in this study such as PPI-Th-co-P3HT, PPI-Sal-co-P3HT and PPI-Py-co-P3HT have functional group such as C=N and OH that can bind to the metallic elements. These allows them to have their complexes using variety of metals which can improve their light absorption properties.
- Materials such as HTB-co-P3HT and TTT-co-P3HT have no functional groups that can be used to form their complexes. Therefore, metallic elements can be introduced into the active layer by blending so that they can improve the absorption properties via surface plasmon effect.
- There is also an option of using acceptor materials with very good absorption properties together with any donor material synthesized in this study to improve light absorption properties and the device performance.

- The OPVs in this study were fabricated in air. This is another factor that contribute to low performance of OPVs fabricated in this study. Therefore, fabricating these devices can results to improved photovoltaic parameters.



Appendix

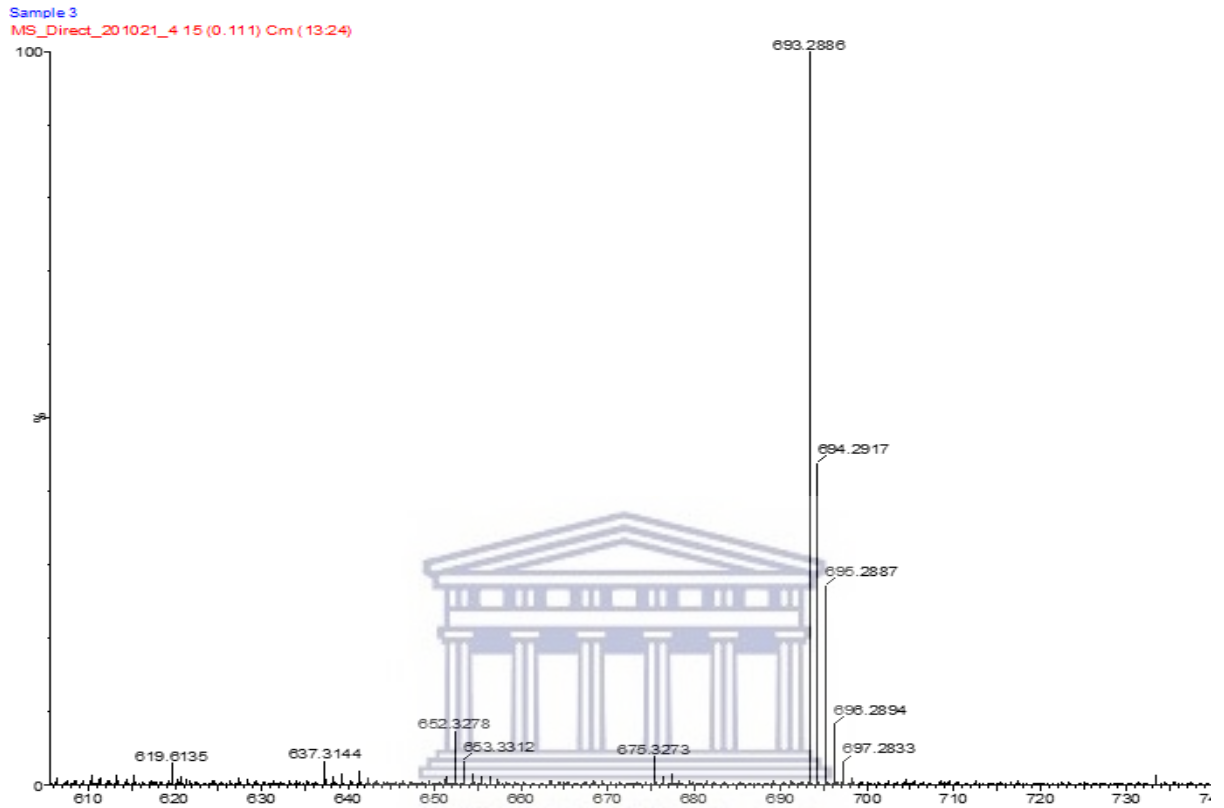


Figure A1: Mass spectrum of PPI-Th.

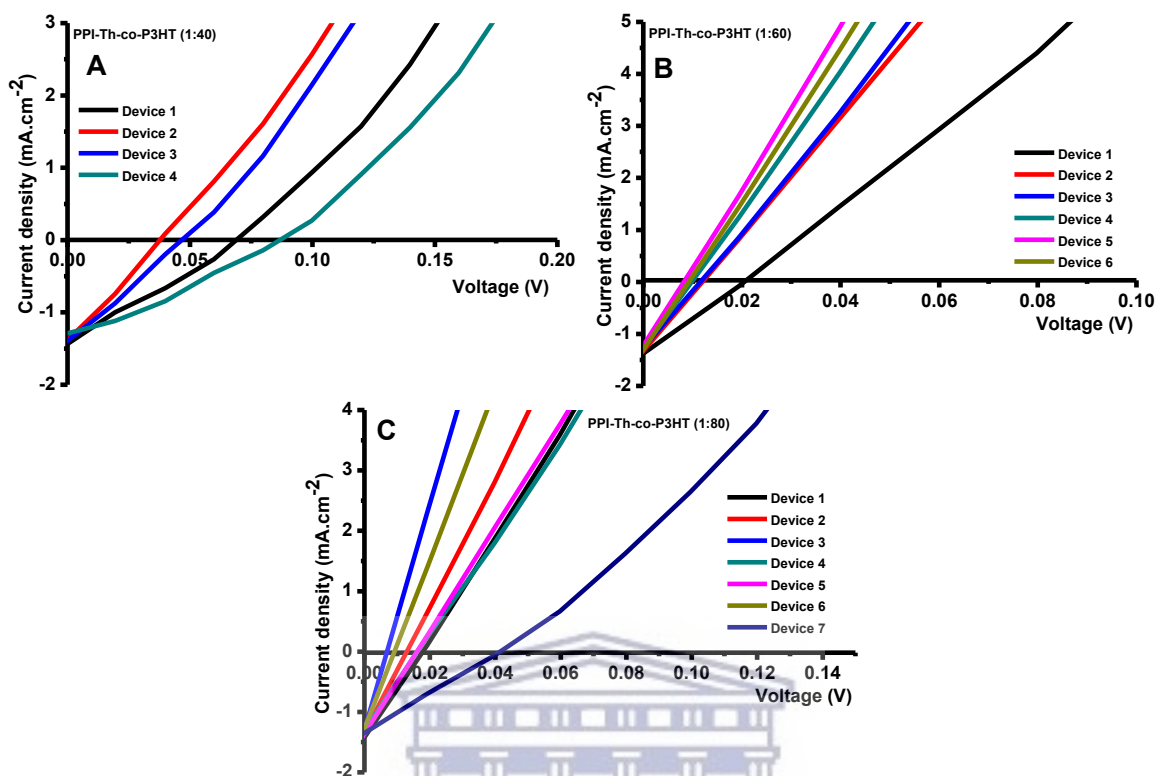


Figure A2: J–V characteristics of the fabricated OPVs using PPI-Th-co-P3HT synthesized using molar ratio of A) 1:40, B) 1:60 and C) 1:80 as donor materials.

Table A1: Photovoltaic performance of PPI-Th-co-P3HT synthesized using molar ratio of 1:40 as donor material.

Device	PCE (%)	FF (%)	J _{sc} (mA.cm ⁻²)	V _{oc} (V)
1	0.027	29.34	1.34	0.027
2	0.014	29.18	1.28	0.014
3	0.017	29.35	1.23	0.017
4	0.034	31.24	1.26	0.085

Table A2: Photovoltaic performance of PPI-Th-co-P3HT synthesized using molar ratio of 1:60 as donor material.

Device	PCE (×10 ⁻³ %)	FF (%)	J _{sc} (mA.cm ⁻²)	V _{oc} (×10 ⁻² V)
1	1.60	6.45	1.26	1.94
2	0.95	6.86	1.17	1.18
3	0.92	6.65	1.18	1.16
4	0.92	8.67	1.09	0.98
5	0.90	10.06	1.10	0.81
6	0.92	9.45	1.10	0.89

Table A3: Photovoltaic performance of PPI-Th-co-P3HT synthesized using molar ratio of 1:80 as donor material.

Device	PCE ($\times 10^{-3}$ %)	FF (%)	J _{sc} (mA.cm ⁻²)	V _{oc} ($\times 10^{-2}$ V)
1	1.24	6.09	1.17	1.74
2	1.12	6.88	1.22	1.33
3	1.14	13.87	1.20	0.68
4	1.03	5.10	1.20	1.68
5	1.09	5.77	1.20	1.57
6	1.06	10.32	1.14	0.89
7	13.41	27.68	1.18	4.10

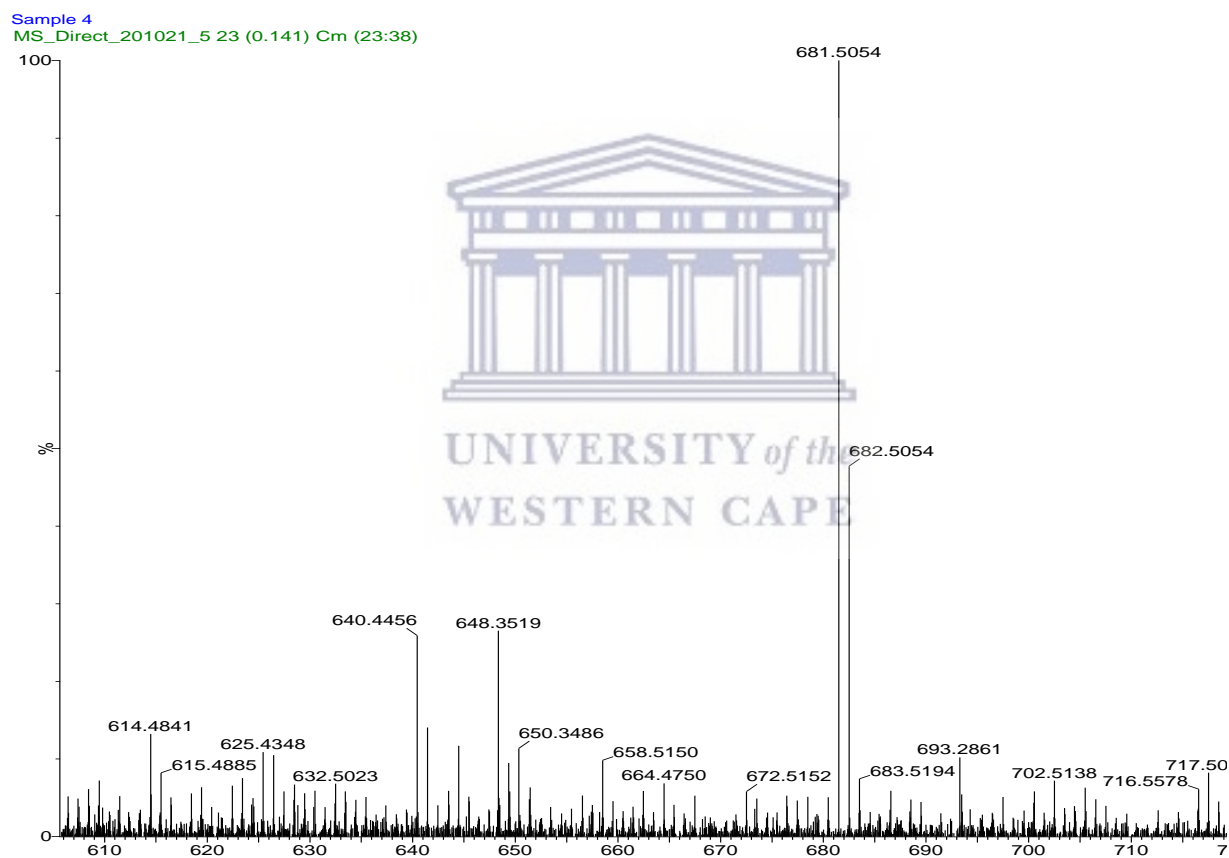


Figure A3: Mass spectrum of PPI-Py.

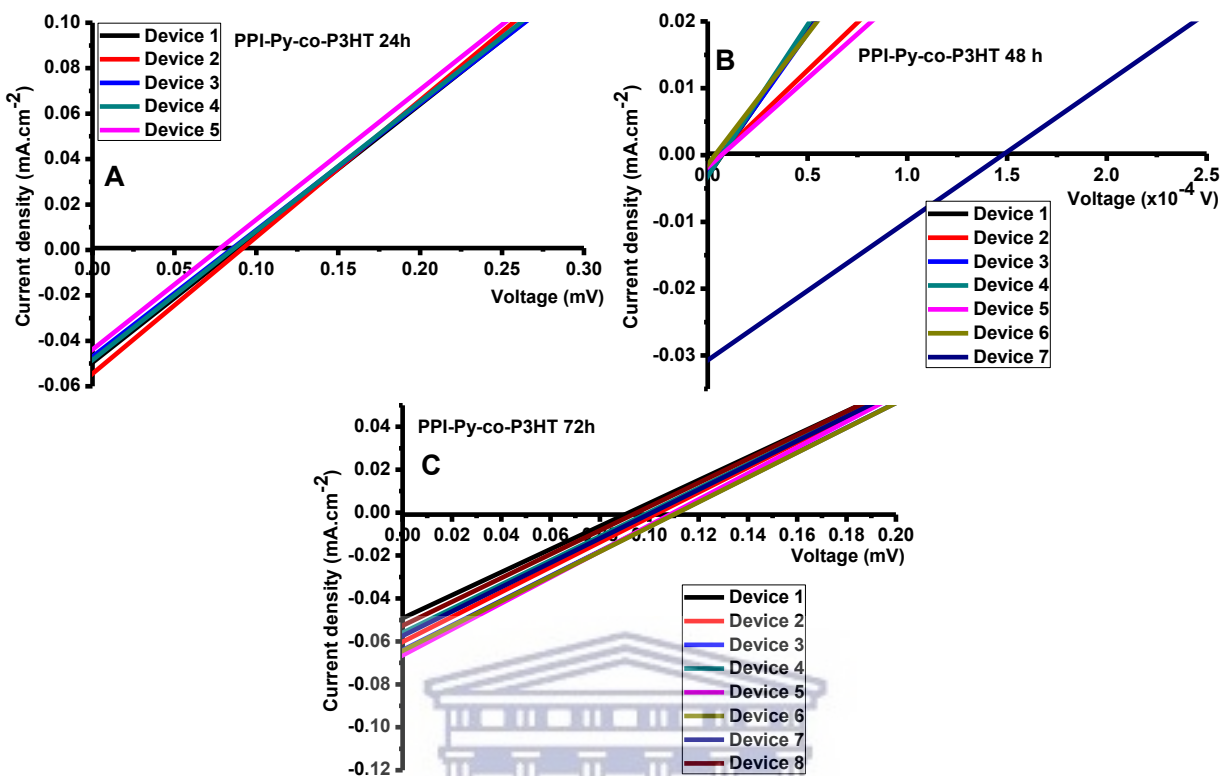


Figure A4: J–V characteristics of the fabricated OPVs using PPI-Py-co-P3HT synthesized for (A) 24h, (B) 48h and (C) 72h as donor materials.

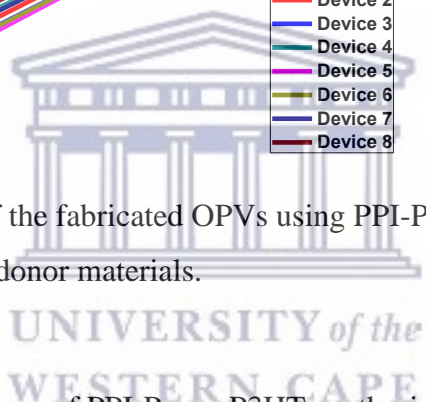


Table A4: Photovoltaic performance of PPI-Py-co-P3HT synthesized for 24h as donor material.

Device	PCE ($\times 10^{-4}$ %)	FF (%)	Jsc ($\times 10^{-2}$ mA.cm $^{-2}$)	Voc ($\times 10^{-5}$ V)
1	2.99	67.22	4.95	9.00
2	2.96	60.07	5.51	9.00
3	2.88	69.21	4.86	8.60
4	2.76	69.43	4.65	8.60
5	2.95	83.25	4.46	8.00

Table A5: Photovoltaic performance of PPI-Py-co-P3HT synthesized for 48h as donor material.

Device	PCE ($\times 10^{-4}$ %)	FF (%)	Jsc ($\times 10^{-2}$ mA.cm $^{-2}$)	Voc ($\times 10^{-5}$ V)
1	0.40	17.27	0.32	0.72
2	0.36	33.32	0.16	0.64
3	0.32	18.54	0.27	0.65
4	0.34	13.97	0.33	0.73
5	0.31	26.02	0.17	0.67
6	0.32	58.67	0.15	0.38
7	2.95	79.86	2.65	13.93

Table A6: Photovoltaic performance of PPI-Py-co-P3HT synthesized for 72h as donor material.

Device	PCE ($\times 10^{-4}\%$)	FF (%)	J _{sc} ($\times 10^{-2}$ mA.cm ⁻²)	V _{oc} ($\times 10^{-5}$ V)
1	3.50	76.47	4.94	9.30
2	3.51	59.65	5.86	10.10
3	3.32	50.08	6.16	10.80
4	3.38	60.23	5.60	10.00
5	3.46	47.22	6.67	11.00
6	3.15	44.49	6.34	11.20
7	3.36	56.75	5.75	10.30
8	3.18	63.20	5.31	9.50

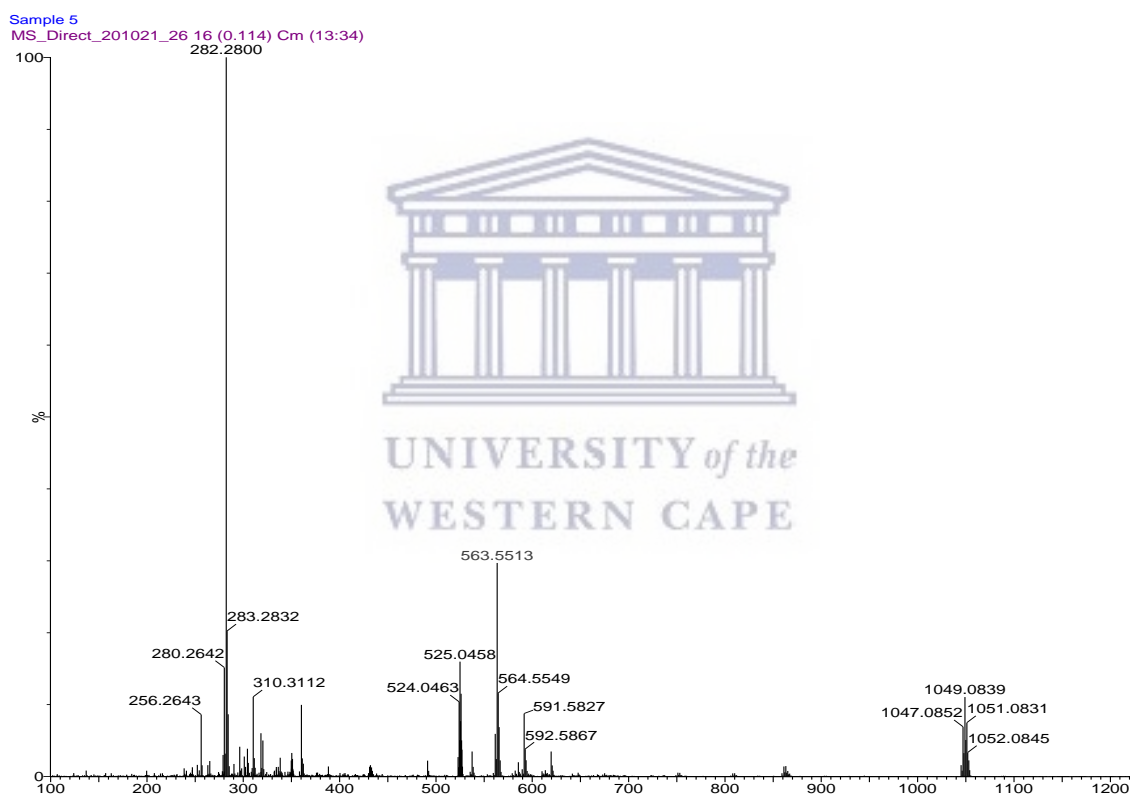


Figure A5: Mass spectrum of PPI-Sal.

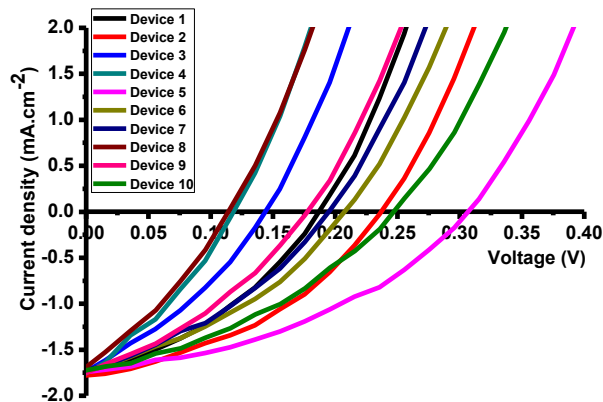


Figure A6: J–V characteristics of the fabricated OPVs using PPI-Sal-co-P3HT as donor materials.

Table A7: Photovoltaic performance of PPI-Sal-co-P3HT as a donor material.

Device	PCE (%)	FF (%)	J _{sc} (mA.cm ⁻²)	V _{oc} (V)
1	0.12	35.81	1.76	0.19
2	0.17	39.67	1.78	0.24
3	0.08	33.34	1.69	0.14
4	0.07	32.24	1.70	0.12
5	0.21	39.34	1.74	0.31
6	0.13	36.27	1.70	0.21
7	0.12	35.68	1.71	0.20
8	0.06	31.42	1.66	0.12
9	0.11	34.50	1.73	0.18
10	0.16	36.70	1.72	0.25

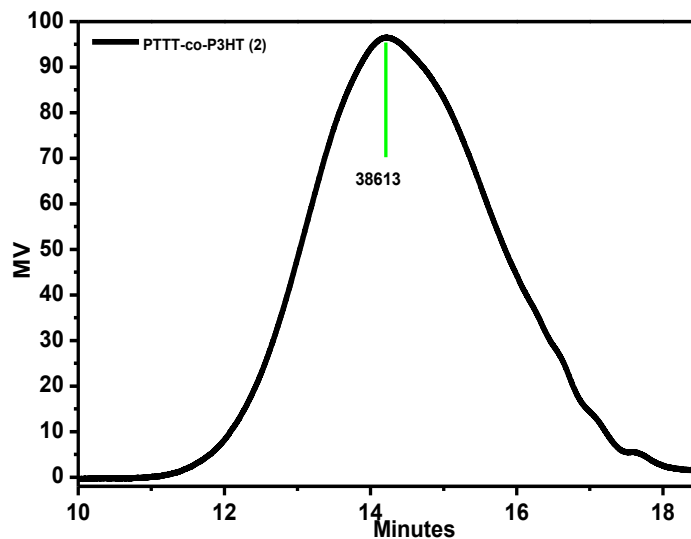


Figure A7: Size-exclusion chromatogram of PTTT-co-P3HT.

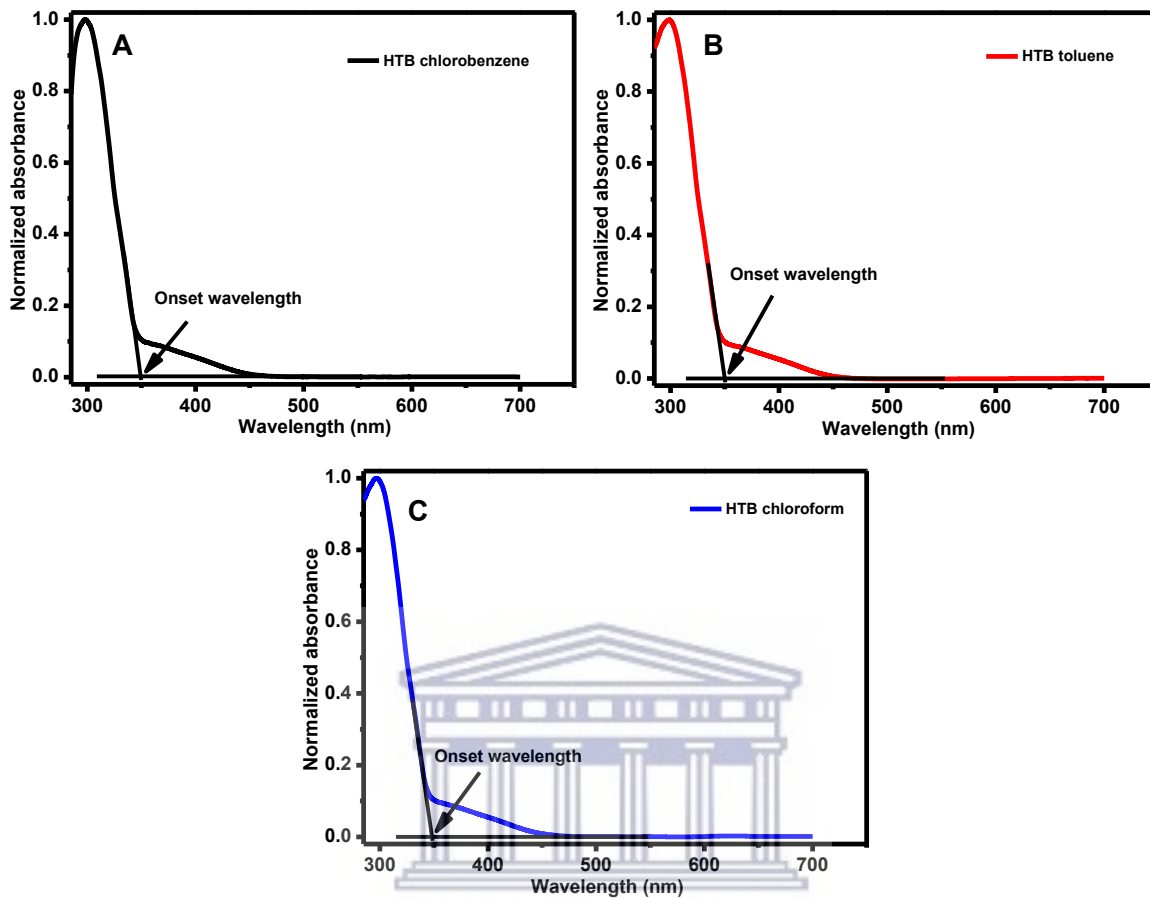


Figure A8: UV-Vis spectra of HTB in different solvents showing how onset wavelength was determined.

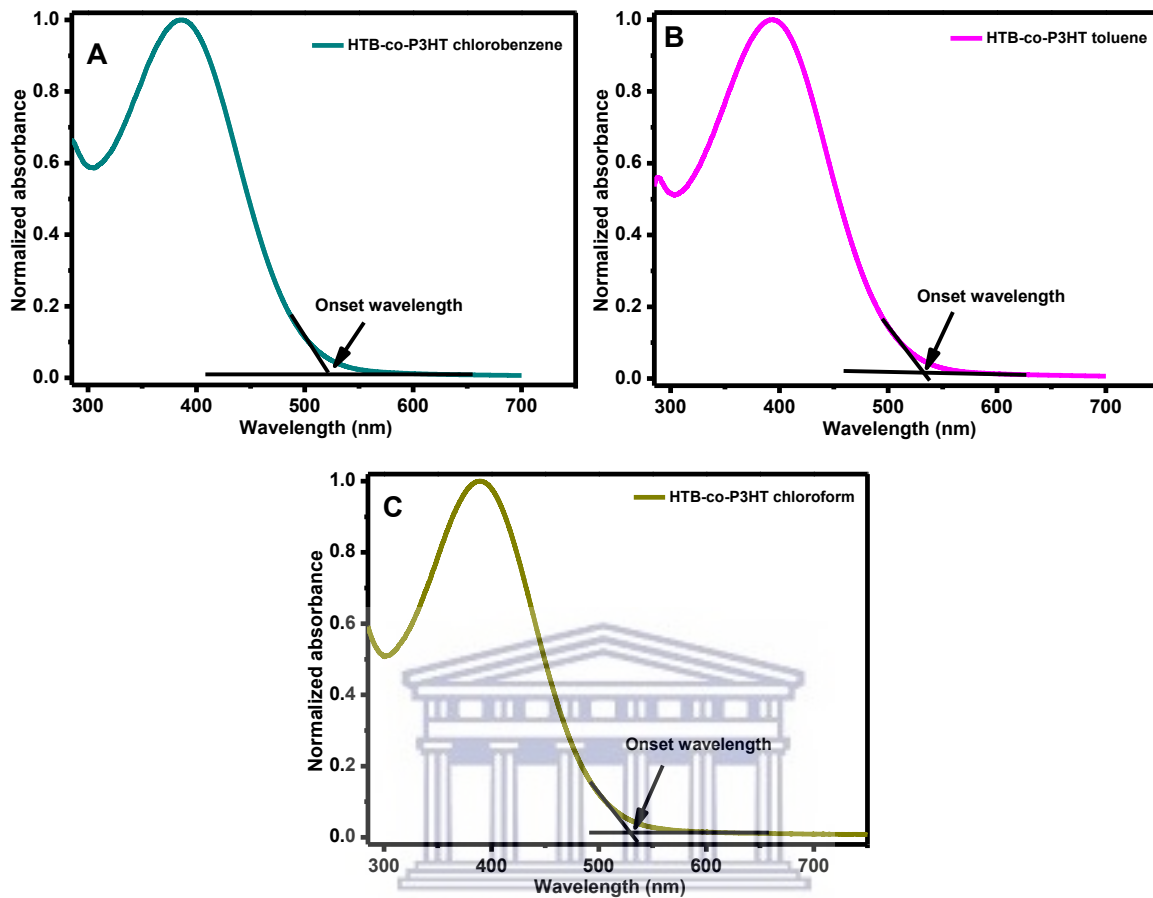


Figure A9: UV-Vis spectra of HTB-co-P3HT in different solvents showing how onset wavelength was determined.

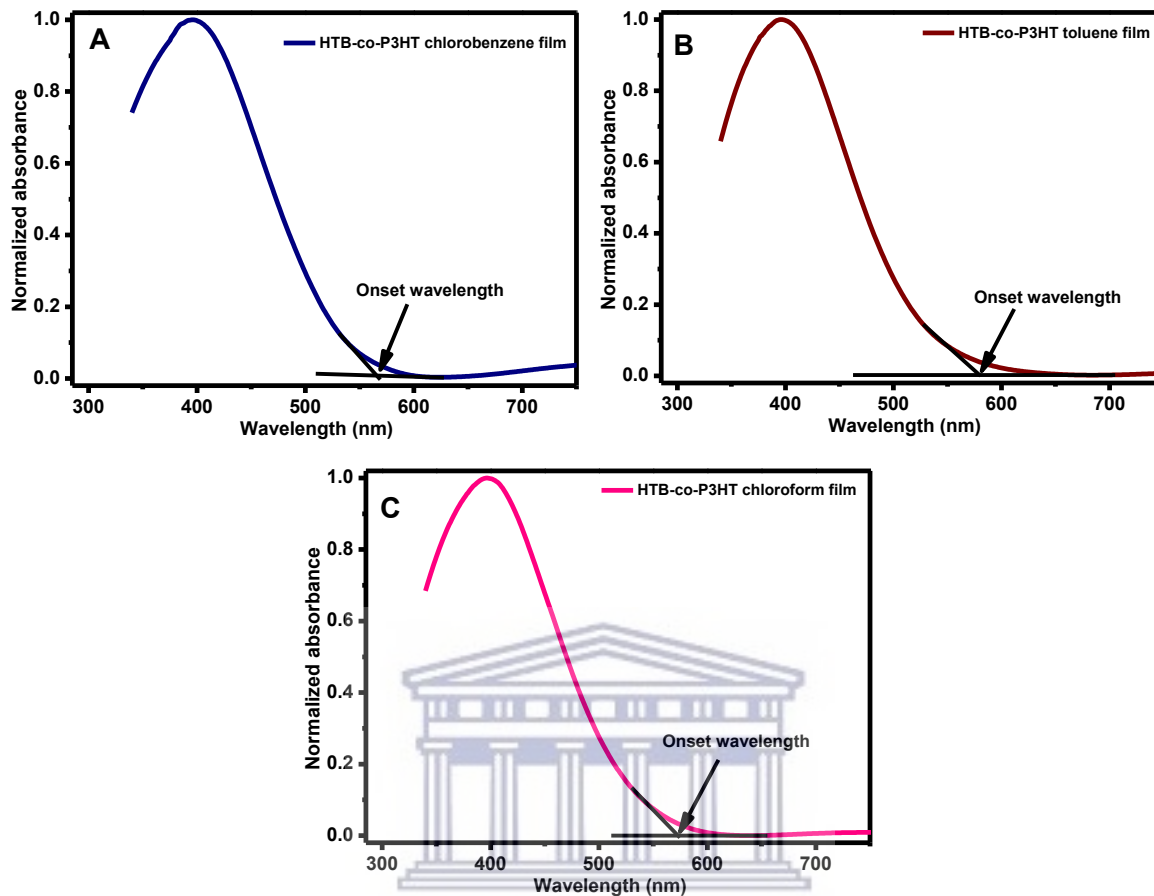


Figure A10: UV-Vis spectra of HTB-co-P3HT films prepared in different solvents showing how onset wavelength was determined.

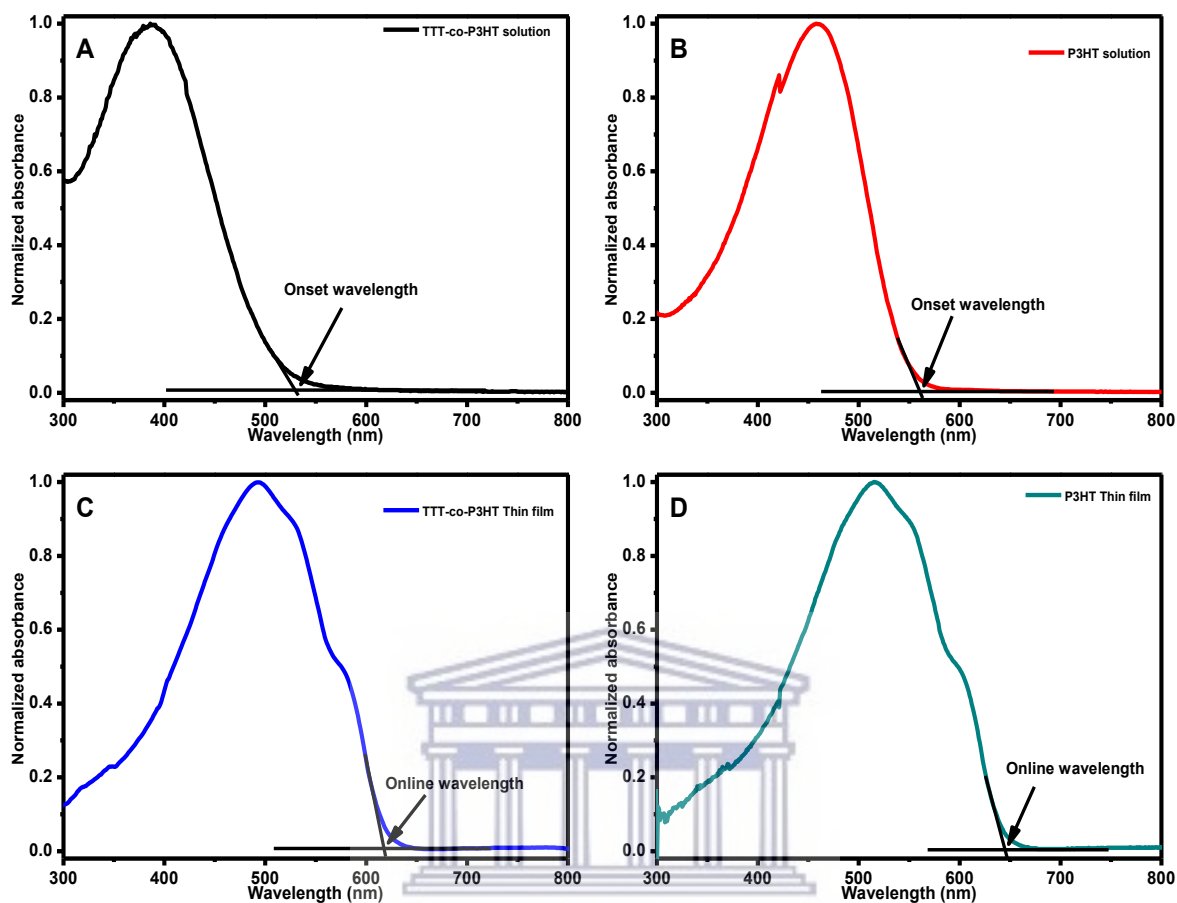


Figure A11: UV-Vis spectra of TTT-co-P3HT and P3HT in chlorobenzene and as thin films showing how onset wavelength was determined.